UNIVERSIDADE DE SANTIAGO
DE COMPOSTELA

FACULTADE DE FÍSICA

Departamento de Física de Partículas

β-delayed γ-ray spectroscopy of heavy neutron-rich nuclei produced by cold-fragmentation of ^{208}Pb

Memoria presentada por:
Ana Isabel Morales López
como requisito para optar al
Título de Doctora en Física
dentro del **Programa de Doctorado**
Interuniversitario en Física Nuclear
4 de Marzo de 2011

UNIVERSIDADE DE SANTIAGO DE COMPOSTELA

José Benlliure Anaya, Profesor Titular de la **Universidade de Santiago de Compostela**,

CERTIFICA:

que la memoria titulada **β-delayed γ-ray spectroscopy of heavy neutron-rich nuclei produced by cold-fragmentation of ^{208}Pb**, ha sido realizada por **Ana Isabel Morales López** en el **Departamento de Física de Partículas de esta Universidad** bajo mi dirección y constituye la **Tesis** dentro del **Programa de Doctorado Interuniversitario en Física Nuclear** que presenta para optar al grado de **Doctora en Física.**

Santiago de Compostela, a 4 de Marzo de 2011

Fdo. Ana Isabel Morales López

Fdo. José Benlliure Anaya

Contents

Contents **1**

Introduction **3**

1 Experimental setup **9**
- 1.1 Experimental technique . . . 10
  - 1.1.1 Projectile fragmentation . . . 10
  - 1.1.2 In-flight separation of residues . . . 11
- 1.2 The GSI accelerator facility . . . 12
  - 1.2.1 The GSI acceleration system . . . 12
  - 1.2.2 The reaction target . . . 13
  - 1.2.3 The FRagment Separator . . . 14
- 1.3 Identification of heavy residues: the detection setup . . . 19
  - 1.3.1 Tracking detectors: multiwire proportional chambers . 21
  - 1.3.2 Position and Time-of-flight detectors: the plastic scintillators . . . 21
  - 1.3.3 Energy-loss detectors: MUlti Sampling Ionization Chambers . . . 23
- 1.4 Identification of heavy residues: charge state selection . . . 27
  - 1.4.1 The MUSIC chambers. Charge state corrections . . . 27
  - 1.4.2 The FRagment Separator. Charge state selection . . . 29
- 1.5 Identification of heavy residues: atomic charge and mass determination . . . 31
- 1.6 β-delayed γ-ray analysis: the implantation setup . . . 33
  - 1.6.1 The implantation procedure . . . 34
  - 1.6.2 The active stopper . . . 36
  - 1.6.3 The advanced RISING γ-ray spectrometer . . . 41
- 1.7 Trigger logic and Data ACquisition (DAC) . . . 51

2 Charge-exchange cross sections **53**
- 2.1 The charge-exchange process . . . 53

2.2 Identification procedure 55
2.3 Measured cross sections 59
    2.3.1 Yield corrections 60
    2.3.2 Experimental results 61
    2.3.3 Discussion of results 62

3 γ-ray spectroscopy 65
3.1 Isomeric spectroscopy 66
    3.1.1 Analysis technique 66
    3.1.2 Verification of the isotopic identification 67
3.2 β-delayed γ-ray spectroscopy 67
    3.2.1 Analysis technique 69
    3.2.2 γ-γ coincidences 75
3.3 Results 75
    3.3.1 β-decay of ^{204}Pt to ^{204}Au 75
    3.3.2 β-decay of ^{203}Pt to ^{203}Au 81
    3.3.3 β-decay of ^{202}Ir to ^{202}Pt 87
    3.3.4 β-decay of ^{201}Ir to ^{201}Pt 92
    3.3.5 β-decay of ^{200}Ir to ^{200}Pt 97
3.4 Discussion 101
    3.4.1 Nuclear β decay 101
    3.4.2 The nuclear shell model 102
    3.4.3 Shell model calculations 104
    3.4.4 Nuclear structure of Au isotopes 105
    3.4.5 Nuclear structure of Pt isotopes 107
    3.4.6 Summary 109

4 γ-labelled β half life measurements 111
4.1 Ion-β correlations 111
    4.1.1 Position correlations 112
    4.1.2 Time correlations 112
    4.1.3 β-prompt γ-ray time correlations 112
4.2 Feasibility of a direct measurement 113
4.3 Evaluation technique of β-decay half lives 114
    4.3.1 Monte-Carlo simulation 115
    4.3.2 The χ^2 test 118
    4.3.3 The fitting procedure 119
    4.3.4 Limits of the procedure 123
    4.3.5 Results 125
4.4 Validation of the analysis procedure 126
    4.4.1 Comparison with analytical techniques 126

4.4.2 Comparison with former data 128
4.4.3 Comparison with theoretical predictions 128

Summary and conclusions **131**

A Beam-line setup at S2 **135**

B Beam-line setup at S4 **137**

C List of layers in the beam line **139**

D Total β-delayed γ-ray energy spectrum **141**

E γ-labelled β-decay half lives **143**

Resumen en castellano **145**

Bibliography **163**

List of figures **i**

List of tables **xii**

Introduction

The RISING project (*Rare ISotopes INvestigations at GSI*) consists in performing different experiments of nuclear physics in order to investigate structural properties of exotic nuclei produced through fragmentation and fission reactions.

Within this context, the current dissertation focuses on two burning subjects in nuclear physics. Firstly, the knowledge of the origin of heavy elements in the Universe represents one of the most relevant questions of nuclear astrophysics in the new century [1]. The theory of nucleosynthesis predicts that approximately half of the neutron-rich nuclei heavier that Fe are formed as a consequence of the rapid neutron-capture process (*r-process*)[2–4]. Secondly, the evolution of shell structure from the nuclei along the valley of stability towards exotic neutron-rich nuclei has been a major theme in the last decades. The scarce experimental information on the extreme nuclei with a few neutron and proton holes out of the doubly magic ^{208}Pb makes this region of the Segrè chart an incredibly valuable piece to understand the r-process and the evolution of shell structure. Furthermore, we have given a step forward towards the study of the robustness of the N=126 shell closure characterising the single (π,ν) charge-exchange interactions of ^{208}Pb on a Be target. As it will be shown, charge-exchange of a ^{208}Pb beam is more adequate than fragmentation of ^{238}U to produce some nuclei with a valence neutron out of the N=126 shell. The measured single (π,ν) charge-exchange cross sections are presented for the first time in this work.

The r-process scenario is represented in figure 1. It is thought to arise in astrophysical sites such as supernovae [5–8] or neutron star mergers [9–11], where a large flux of neutrons becomes available in a very short time scale ($\sim$ 0.01-10 s), for addition of neutron captures to seed nuclei of the Fe group. An equilibrium is reached for the so-called *waiting point* nuclei [2], corresponding to the neutron shell closures N=50, 80 and 126 and responsible for the formation of the three peaks of r-process abundance distribution at A $\simeq$ 80, 130 and 195. At this *bottlenecks*, the neutron capture process is limited by photodisintegration, so that the r-process chain “waits” till the

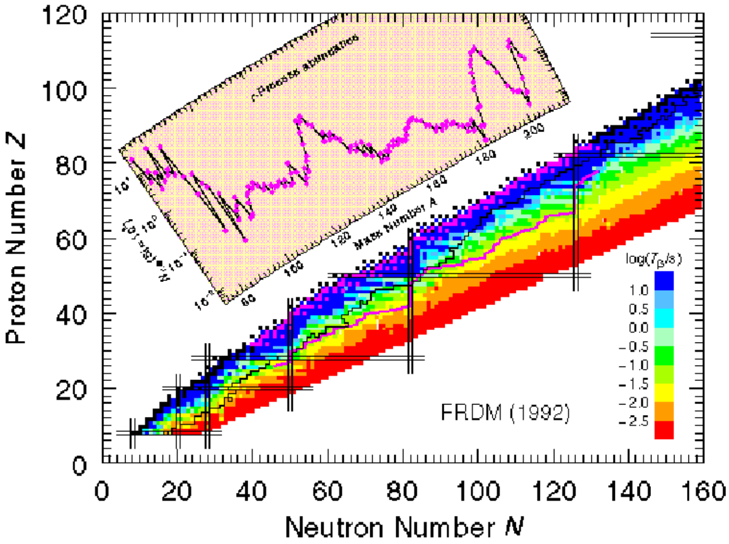

Figure 1: Chart of nuclides showing the abundance patterns drawn from the r-process. The stable nuclides are marked by black boxes. The jagged black line denotes the limit of nuclear properties experimentally determined, whereas the magenta line indicates the r-process path. Colour-shading reveals the different (log) timescales for β-decay. Vertical and horizontal black lines represent the magic closed neutron and proton shells, respectively. Figure taken from [12].

nucleus undergoes a β-decay, then continues until another equilibrium is established. Once the neutron flux is exhausted, the unstable neutron-rich nuclides undergo subsequent β-decays back to the valley of stability to form the stable r-process nuclei.

Experimental data on the r-process unstable nuclei must be available to perform studies of the r-process. A few nuclear properties are particularly important in the calculations, namely, the nuclear mass, the β-decay half lives and the β-delayed neutron-emission probabilities. By determining these properties the nucleosythesis r-process calculations are more reliable, and even the theoretical models may be tested and extrapolated to far-unstable nuclei [13].

Thus far, direct experimental information on the r-process has been focused on the neutron-magic *waiting point* nuclei ^{80}Zn [14, 15] and ^{130}Cd [16]. Nevertheless, most of the very neutron-rich nuclei conforming the r-process path have remained experimentally unaccessible until recently, when the acceleration of heavy projectiles at relativistic energies enabled the production of heavy neutron-rich nuclei through reaction mechanisms such as cold-fragmentation reactions [17] or charge-exchange reactions [18]. In particular, the β-decay half lives of several exotic nuclei surrounding the waiting-point A=195 were measured in a pioneering work developed by Kurtukian et al. [19]. In the present thesis, we continue the work of Kurtukian et al. on the measurement of β-decay half lives of nuclei approaching the r-process path near the 126-neutron shell closure. The importance of these measurements lies not only in having a better knowledge on the path and time-scales of the r-process (which are responsible of the final abundance patterns in the Universe), but also in the benchmarking of nuclear models far from stability.

The testing of theoretical models is further fulfilled studying the low-lying structure of these nuclei. One of the objectives of this work is to address the question of the stiffness of the 82-proton, 126-neutron shell closures as the number of valence holes out of the doubly magic ^{208}Pb core increases. Initially, one expects to observe the development of collective excitations and, consequently, the related ground state quadrupole deformation β_2 [20, 21]. Hitherto, several experimental studies have been performed on the evolution from axially-symmetric deformed prolate shapes in the surroundings of the maximum valence isotope ^{170}Dy [22] towards spherical, single-particle-like excitations nearby the doubly magic nucleus ^{208}Pb. This region of the Segrè chart is predicted to be composed of triaxial γ-soft and oblate nuclei [23–25], also described as prolate-oblate phase transitional systems [26].

In this work, we concentrate on the measurement of the low energy structure of ^{204,203}Au and ^{202,201,200}Pt using β-delayed γ-ray spectroscopy. Such nuclei are expected to have near spherical shape due to their proximity to the Z=82, N=126 shell closures.

The nuclear shell model (SM) [27–29] describes appropriately many properties of spherical nuclei, this is, nuclei with a magic or nearly magic number of protons and neutrons, as the energy, spin and parity of the excited states. Other properties of systems close to doubly magic nuclei are also in good agreement with the shell model approach, as the electromagnetic moments, occupation number, transition rates and Gamow-Teller β-decay. However, the characterisation of nuclear systems within the shell model framework fails as the number of valence holes out of the shell closures increases. Particularly, the nuclei in the transition region "south-west" of ^{208}Pb are better described by collective models such as the Interacting Boson Approximation (IBA) [30–35]. In the IBA theory, the low-lying collective excitations of an even-even nucleus are described in terms of the *s* (L=0) and *d* (L=2) bosons. A wide variety of studies on heavy even-even nuclei [36–41] have been performed in order to determine the limits of geometrical symmetry within the IBA [42]. For instance, the nucleus ^{196}Pt [43, 44] represented an excellent empirical example of the O(6) [45] limiting symmetry of the Interacting Boson Approximation. Heavier Pt isotopes appear to evolve towards a more vibrational character as the N=126 neutron shell is approached [44, 46], although the overall shape may be more oblate rather than the γ-unstable shape of lighter Pt isotopes.

The present dissertation shows the data analysis corresponding to an experiment performed in 2007 at the *Gesellschaft für Schwerionenforschung* (GSI), located in Darmstadt, Germany. A stable primary beam of ^{208}Pb, delivered by the SIS-18 synchrotron [47] at an energy of 1 A·GeV, was directed to a Be target. Nuclei at the current limits of experimental synthesis, with 0 to 3 neutron holes out of the 126-neutron shell closure, were produced using *cold fragmentation* reactions. The magnetic spectrometer Fragment Separator (FRS) allowed for the "in-flight" identification of the exotic nuclei from their mass-over-charge ratio A/Q and their ionic charge Q, quantities determined from the direct measurement on an event-by-event basis of the magnetic rigidity $B\rho$, time-of-flight and energy loss of the fragmentation residues. The degrader energy-loss method [48] was employed to separate the different ionic charge states that arose with the passing of the heavy ions through matter. Additionally, the particle identification was confirmed by the observation of the previously reported isomeric decays in ^{204,203}Pt [49]. Fragments transmitted to the end of the FRS were implanted in an active stopper, consisting of three Double Sided Silicon Strip Detectors (DSSSDs, $5 \times 5 \times 0.1$ cm^3) each with 16 vertical and horizontal strips. The aim of this device was to perform event-by-event position and time correlations between the implanted ions and the electrons emitted in their decay. The Si active stopper was surrounded by the advanced RISING γ-ray spectrometer in its *Stopped Beam* configuration [50]. The RISING array had an efficiency of nearly 15% at 661 keV and allowed for β-prompt γ-ray time correlations, so isomeric and β-delayed γ-ray spectroscopic studies could be performed in the same experiment.

In spite of the state-of-the-art detectors employed for such an analysis, we faced a background contamination in the characteristic β-delayed γ-ray energy spectra due to the simultaneous implantation of several nuclear species in the active stopper with long half lives and high implantation frequencies. The procedure followed to minimise the induced background is described in detail within this work. The experimental β-decay curves were obtained from time and position correlations between the implanted fragments and the subsequent β-like particles detected in coincidence with a characteristic γ-ray of the daughter nuclides. As it happened with the γ-ray spectroscopic analysis, the pulsed structure of the primary beam modulated the rates of implantation and decay with a periodic time structure that seriously spoilt the β-decay curves. In order to disentangle the background from the real time correlations, the method proposed in ref. [19] was adapted and applied to this data with very successful results. It consists in performing sets of Monte Carlo simulations of ion-β time correlations to further apply the χ^2 fit method to both the measured and simulated time distributions.

The structure of the current work is the following: Chapter 1 provides the description of the experimental setup and the technique used for the production, identification and β-delayed γ-ray spectroscopy of exotic nuclei, as well as the identification analysis procedure. Chapter 2 is dedicated to the measurement of the experimental charge-exchange cross sections. Chapter 3 shows the experimental procedure used to perform both the isomeric and β-delayed γ-ray spectroscopy, as well as the corresponding results and discussion. In chapter 4 the modifications on the novel technique developed by T. Kurtukián et al. to determine β-decay half lives are described, and the corresponding results are shown. Finally, the conclusion provides an overview of the outcomes and perspectives derived from this dissertation.

Chapter 1

Experimental setup

In this chapter we provide a general overview of the experimental facility and the detection setup employed in the current experiment. The *Gesellschaft für Schwerionenforschung* (GSI), in Germany, is a unique facility for the production and study of radioactive ion beams [51]. The technique used to produce the exotic fragments is in-flight fragmentation of heavy projectiles in inverse kinematics, which consists in colliding a heavy nucleus against a light target at relativistic energies, such that the reaction residues keep the kinematic properties of the projectile and can further be separated and identified in a magnetic spectrometer.

In this particular experiment, the SIS-18 synchrotron [47] accelerated a stable primary beam of ^{208}Pb up to 1 A·GeV. The relativistic heavy projectile was directed to a ^{9}Be target of thickness 2.5 g/cm^2, where the neutron-rich residues were produced through *cold fragmentation* reactions [17] and forwarded to the FRagment Separator (FRS) to be identified. Due to the ion-optical characteristics of the spectrometer not only fully-stripped nuclei were transmitted through the FRS, but also hydrogen-like and helium-like fragments. To determine the charge state distribution of the reaction products and further identify them according to their masses and atomic numbers, different experimental devices were placed along the separator. The selected fragments were stopped at the exit of the FRS in a state-of-the-art β-delayed spectroscopy system set up to carry out β-decay studies. The active stopper allowed to perform position and time correlations between the implanted fragments and the electrons emitted in their decay. Surrounding this device was the RISING γ-ray spectrometer, which allowed to identify the γ-rays registered after implantations and decays. Note that this scenario is the only where these neutron-rich nuclei, at the current limits of experimental synthesis, can be investigated.

1.1 Experimental technique

1.1.1 Projectile fragmentation

Fragmentation reactions are described as peripheral nuclear collisions at relativistic energies between a heavy projectile and a light target. The process can be characterised in a participant-spectator picture, such that the heavy projectile is sheared off by the target nucleus. We distinguish between two stages [52]. The first step, denominated the *abrasion* stage, occurs in the spur of the impact, within a specific time of 10^{-23} s. The nucleons located in the interaction volume between the projectile and the target are denominated the participants, since they experience the collision with each other and eventually are abraded. The other nucleons of projectile and target, respectively, are referred to as the spectators, since they continue moving almost undisturbed as observers of the process [53]. Their excitation energy is given by the energies of the holes in the single-particle level scheme of the projectile after the collision [54].

The projectile spectators de-excite in a second stage, referred to as the *ablation* stage, through fission, evaporation of α particles, nucleons, and emission of gammas. The neutron-to-proton ratio of the projectile spectator is subject to statistical fluctuations as given by the hypergeometric distribution [55, 56]. The most neutron-rich nuclei are produced when only protons are abraded from the projectile and the excitation energy of the pre-fragment is below the neutron separation energy. The probability of producing an extremely neutron-rich nuclide decreases with the number of abraded nucleons [57].

Several computer codes have been developed to predict the nuclear yields and cross-sections of the residues produced in fragmentation reactions. EPAX [58–60] is a semi-empirical parameterisation of fragment cross sections. It has carefully been adjusted to available experimental data. ABRABLA [54, 55] is a modern version of the abrasion-ablation model based in a participant-spectator picture that describes the fragmentation process for excitation energies well above the Fermi level. The COFRA code [17] is a simplified analytical version of ABRABLA that only considers evaporation of neutrons in the pre-fragment. Because of the neutron-rich nature of the nuclei discussed in this work, this last code has been used to predict the yields of the fragmentation residues.

1.1.2 In-flight separation of residues

The in-flight separation of residues is an extremely effective method to produce secondary beams of radioactive isotopes at high energies without the need for re-acceleration. It consists in separating the selected residues from the primary beam and from other reaction products by the combination of a magnetic spectrometer with other elements, such as a velocity degrader. If the fragments are selected according to their magnetic rigidity, a set of ions with a given mass-over-charge ratio A/Q will pass through the magnetic spectrometer. The resolution of the A/Q ratio is given by the dispersion of the magnetic rigidity of the ions and the acceptance of the spectrometer. The use of a degrader at the intermediate image plane breaks the degeneracy among the fragments that have the same A/Q because the momentum of each nuclear specie is shifted by the energy-loss process in the degrader according to Z/v [61], with Z and v the atomic number and the velocity of the nuclei under study, respectively. Consequently, the ions leave the degrader layer with different momenta and thus magnetic rigidities, and the remaining contaminants can be deflected by an additional bend that depends on the degrader thickness and the ratio of the magnetic rigidities before and behind the degrader. Figure 1.1 shows the resulting residues after the "in-flight" isotopic separation in the FRS for a setting centred in ^{202}Ir.

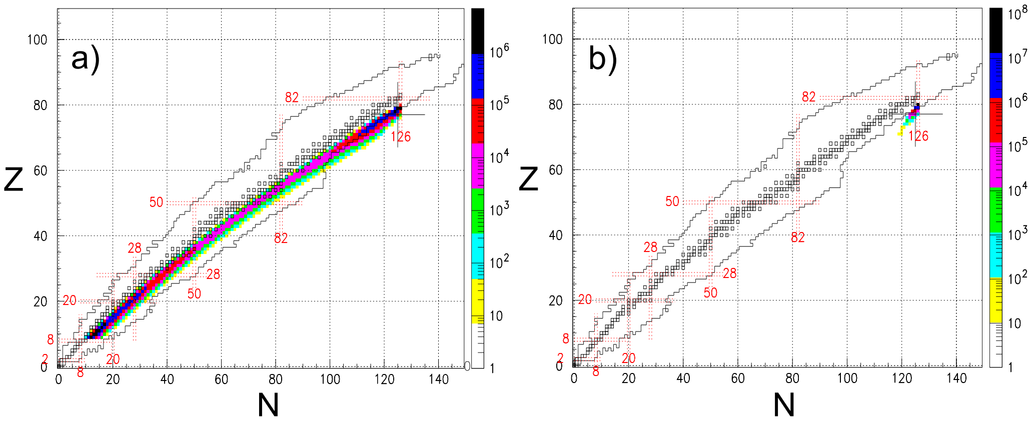

Figure 1.1: Illustration of the two selections performed in the "in-flight" isotopic separation. a) First magnetic selection in A/Q. b) Second magnetic selection in Z/v. The corresponding production rates are on a logarithmic scale. The magnetic FRS setting is optimised to transmit ^{202}Ir.

The main advantage of the in-flight separation technique is the rapid event-by-event identification of the exotic ions, given by their flight time

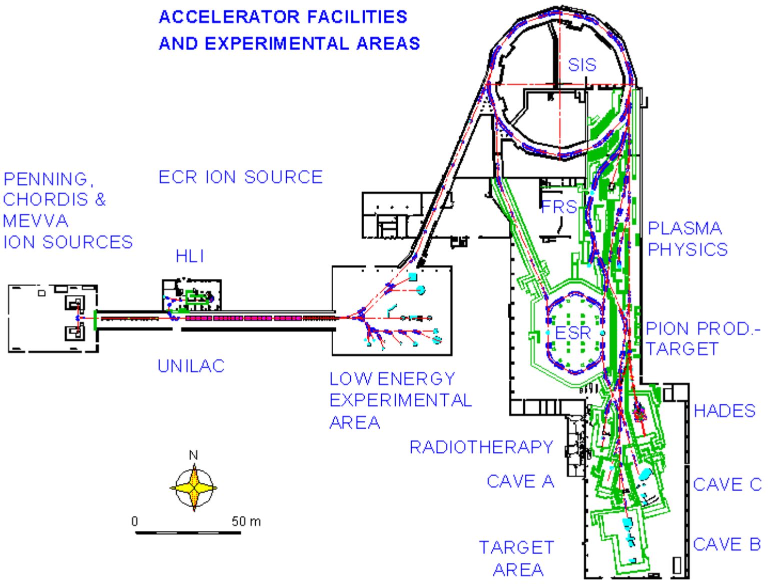
ACCELERATOR FACILITIES
AND EXPERIMENTAL AREAS
SIS
PENNING, CHORDIS & MEVVA ION SOURCES
ECR ION SOURCE
HLI
FRS
PLASMA PHYSICS
ESR
PION PROD.-TARGET
UNILAC
LOW ENERGY EXPERIMENTAL AREA
HADES
RADIOTHERAPY
N
CAVE A
CAVE C
0
50 m
TARGET AREA
CAVE B

Figure 1.2: Schematic view of the GSI accelerator facilities and experimental areas. The primary beams are delivered by the ion sources, pre-accelerated in the UNILAC and injected into the SIS18-synchrotron to be re-accelerated. Eventually, the projectile beam is forwarded to the desired experimental area.

along the FRS (300 ns). This feature allows to perform β-decay studies over the range of the microsecond.

Several programs have been developed to calculate the performance and the expected yields of in-flight separators. LIESCHEN [62] and LISE [63] calculate the first order ion optics of the studied separator. More complex programs can calculate higher order optics, as MOCADI [64]. Others, as AMADEUS [65], evaluate the expected number of nuclear reactions in the elements of the separator, as well as the resulting charge-state distributions.

1.2 The GSI accelerator facility

1.2.1 The GSI acceleration system

The GSI acceleration system consist of three stages [66]: the ion sources, the UNiversal Linear Accelerator (UNILAC) and the heavy-ion synchrotron SIS-18 [47]. In the ion source stage, the primary beam nuclei are produced, firstly ionised and pre-accelerated. After, they are directed to the UNILAC, where their velocity can be adjusted over a range of 2 to 18 A·MeV. The pre-accelerated ions are then injected into the SIS-18 synchrotron through the transfer line. The synchrotron consists of 12 consecutive identical cells, each containing two dipoles, a quadrupole triplet and correction elements to decouple chromatic effects. The maximum magnetic bending power of the SIS-18 is 18 Tm, which provides a maximum energy around 1 A·GeV for $^{238}U^{73+}$. The extraction beam line is located on the opposite side of the injection beam line and connects the synchrotron to the FRagment Separator by a 4.5 μg/cm^2 titanium window that shields the SIS-18 ultrahigh vacuum from the FRS high vacuum. In this experiment, the synchrotron delivered beam spills of 2 s over a period of 10 s.

1.2.2 The reaction target

Thickness (mg/cm^2)	0e (%)	1e (%)	2e (%)	Nuclear reactions (%)
2513	92.6	7.3	0.1	41.5

Table 1.1: Charge state distributions and probability of nuclear reactions in the target for a setting centred in ^{202}Ir, predicted by the code AMADEUS [65].

The selection of the target thickness is based on two features: to maximise the cross section of secondary heavy fragments and to minimise both, the charge exchange processes and the rate of secondary nuclear reactions. It is well known that the optimum target thickness represents the 10% of the beam range at the entrance of the FRS [48].

Since the fully stripped ions can be accurately identified using the technique outlined in section 1.4, we can select a target of double the thickness to increase the production rates of the nuclei of interest. Thus, the target used in this experiment was 2513 mg/cm^2 thick, corresponding to the 21% of the incident beam range [67].

A stripping layer of niobium 221 mg/cm^2 thick was placed at the exit of the target to minimise the number of charge states by reaching the ionic charge state equilibrium[1]. The code AMADEUS [65] was used to calculate the predicted charge state distributions and the expected rate of secondary nuclear reactions. Table 1.1 shows the corresponding percentages of bare, hydrogen-like and helium-like nuclei, as well as the percentage of predicted nuclear reactions after the target for a setting centred in ^{202}Ir. Whilst the probability of nuclear reactions corresponds to that of the projectile beam (^{208}Pb), the charge exchange percentages refer to the reference fragment (^{202}Ir).

---

[1] The ionic charge state equilibrium represents the scenario where the distribution of charge states after traversing a layer of matter does not depend on the initial proportions. The equilibrium is reached by favouring a high number of electron exchanges with the traversed medium.

1.2.3 The FRagment Separator

Design and technical layout

The FRagment separator (FRS) [68] is a high-resolution forward spectrometer with a momentum resolving power of 1500 for an emittance of 20π mm·mrad, designed for experiments of nuclear physics with relativistic heavy ions. This device can analyse heavy-ion beams with magnetic rigidities ranging from 5 to 18 Tm. The system consists of four stages referred to as S1, S2, S3 and S4. Each stage is made up of five quadrupoles, a 30° dipole magnet and a pair of sextupoles (see fig. 1.3).

The three quadrupole magnets in front of each dipole can be adjusted to properly illuminate the field volume of the bending magnets to achieve a high resolving power and to minimise the vertical gap width, whereas the two quadrupoles following the dipole magnets fulfil first-order focussing conditions at the four focal planes, referred to as F1, F2, F3 and F4. The second-order chromatic aberrations in the ion-optical system are corrected by the sextupole magnets fixed in front of and behind each dipole magnet. The fields of the sextupole magnets are relatively low to inhibit induced aberrations of third and higher order. Furthermore, the focal plane at F2 is rotated by the sextupole fields in order to be perpendicular to the optical axis. Each dipole magnet has a nominal curvature radius of 11.25 m and a maximum operation field of 1.6 T. Both features limit the maximum magnetic rigidity accepted by the FRS to 18 Tm. The magnetic fields of the dipoles are calibrated by Hall probes, which allow a precision and stability of about 10^{-4} T.

The FRS is traversed by a vacuum line with a length of 70 m from the entrance to the exit. The apertures in the transversal plane to the optical axis range from ±10 cm to ±18 cm in the horizontal direction and from ±5 cm to ±15 cm in the vertical direction. The acceptance of the device is constrained in momentum and angular acceptance to ± 1.5 % and 15 mrad around the beam direction, respectively.

The FRagment Separator was operated in achromatic mode in the current experiment. In this operation mode, the dispersion due to the momentum

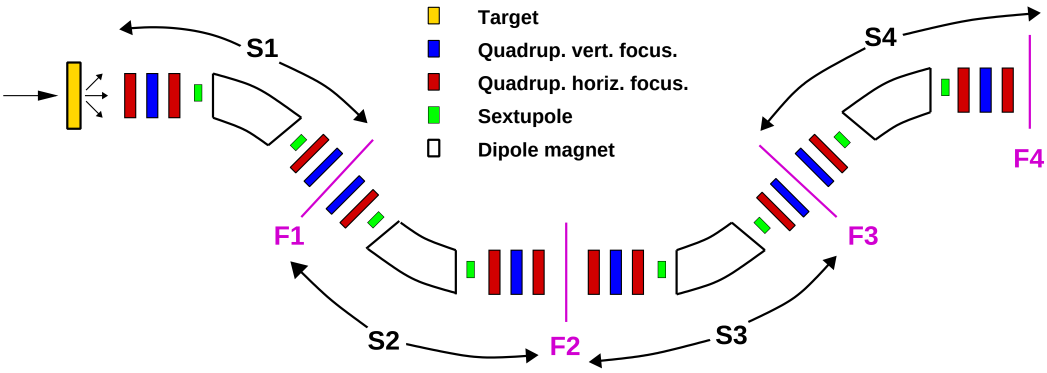

Figure 1.3: Layout of the magnetic spectrometer FRS at GSI. Each dipole magnet can be adapted to fulfil the ion-optical conditions to the specific requirements of different experiments. Blue and red quadrupoles accomplish first-order focussing conditions at each image plane in the vertical and horizontal directions, respectively. Sextupoles correct second-order chromatic aberrations.

spread at the entrance of the FRS reaches a maximum value of -6.47 cm/% at the second focal plane F2, which is designated the dispersive plane. At the final focal plane F4, referred to as the achromatic plane, the momentum deviation δp of the incident beam is independent to first order from the image size x and the angular divergence x' of the secondary fragments at the achromatic plane

$$\left(\frac{\partial x}{\partial(\delta p)}\right)_{F4} = \left(\frac{\partial x'}{\partial(\delta p)}\right)_{F4} = 0 \qquad (1.1)$$

Magnetic selection of secondary fragments

Within the Fragment Separator, the secondary residues follow different trajectories that can be defined by a set of phase-space variables, the most significant of which is the magnetic rigidity $B\rho$

$$B\rho = \left(\frac{A}{Q}\right) \cdot \frac{m_0 c}{e} \cdot \beta\gamma \qquad (1.2)$$

where A is the mass number, Q is the ionic charge, m_0 is the mass unit, c is the speed of light, e is the electron charge and $\beta\gamma$ is the relativistic reduced momentum with $\beta = v/c$, being v the velocity of the selected fragment. The horizontal position of a fragment through the separator depends on the variables that describe its trajectory -the coordinates (x,y), the angles (θ,ϕ)

and the momentum deviation δp-. At the image planes, the x-position of the fragments does not depend on their angular distributions. In addition, we will consider that the incident nuclei are forwarded to the FRS with a central position in the x direction ($x_0 = 0$), this is, the horizontal position at F2 does not depend on the x-coordinate of the fragment at the entrance of the FRS. Eventually, we will consider no charge state difference between the fragment under study and a reference fragment following the central trajectory, so that $\delta p = \delta B\rho$. Then, the transversal x-position of the studied nuclide at the dispersive plane is [69]:

$$x_2 = \left(\frac{\partial x}{\partial(\delta p)}\right)_{02} \delta B\rho \tag{1.3}$$

where the term $(\partial x/\partial(\delta p))_{02}$ is the horizontal dispersion at the central focal plane (referred to as D_2) due to the momentum spread at the entrance of the FRS. From now on, we will denote the fragment coordinates at the focal planes F1, F2, F3 and F4 with the subindexes 1, 2, 3 and 4, and we will refer to the entrance of the FRS with the subindex 0.

At the achromatic plane, however, the horizontal position also depends on the position at F2, since x_2 can take values different from zero:

$$x_4 = \left(\frac{\partial x}{\partial x}\right)_{24} x_2 + \left(\frac{\partial x}{\partial(\delta p)}\right)_{24} \delta B\rho \tag{1.4}$$

The term $(\partial x/\partial x)_{24}$ stands for the horizontal magnification (referred to as M_4) between the dispersive plane and the achromatic plane, and the term $(\partial x/\partial(\delta p))_{24}$ refers to the horizontal dispersion at F4 (henceforth D_4) due to the momentum deviation at F2.

From equations 1.3 and 1.4 we conclude that the transversal x-positions at the image planes F2 and F4 depend on the magnetic rigidity of the studied fragment. Therefore, we can determine the magnetic rigidity of a nuclide traversing the FRS from the dispersions D_2 and D_4, the magnification M_4, and the horizontal position at the dispersive and the achromatic planes:

$$B\rho_2 = (B\rho_0)_2 \left(1 + \frac{x_2}{D_2}\right) \tag{1.5}$$

$$B\rho_4 = (B\rho_0)_4 \left(1 + \frac{x_4 - M_4 \cdot x_2}{D_4}\right) \tag{1.6}$$

where $(B\rho_0)_{2,4}$ are the magnetic rigidities of the central trajectory at F2 and F4, respectively.

First magnetic selection

A momentum-loss achromatic system is divided in two sections in order to perform the magnetic selection of the secondary fragments. The first section embodies all the magnetic elements from the entrance of the FRS to the dispersive plane, whereas the second section covers the magnetic elements from the dispersive plane to $F4$. Since the velocity of the nuclei produced by cold fragmentation reactions is almost preserved, the magnetic fields and curvature radii of the first two dipoles determine the mass-over-charge ratio A/Q of the fragments through their magnetic rigidity $B\rho_2$. Thus, a first magnetic selection is performed according to the A/Q ratio of the residues, with a resolution determined by the deviation of their magnetic rigidities and the acceptance of the spectrometer (± 1.5 %).

Along the first stage of the FRS the projectile beam and its hydrogen-like charge state should be rejected to prevent damages in the detection setup. In the case of the helium-like charge state of the primary beam, the maximum beam intensity acceptable by the experimental devices is approximately 10^6 particles per second. A pair of slits located at both sides of each focal plane are used to stop these ions.

Second magnetic selection

A considerable number of nuclei with mass-over-charge ratios similar to the reference A/Q are forwarded along the first section of the FRS together with the selected nuclei. To eliminate these fragments, a second selection is performed by placing a velocity degrader in the dispersive plane. The fragments passing through the Al degrader experience an energy loss process and, consequently, reduce their velocity and range. The momentum p_4 behind the degrader is then substantially smaller than the momentum p_2 in front of the degrader. The fragments with different p_4 momentum at the second section of the FRS can be separated by a new selection criterion in magnetic rigidity $B\rho_4$, according to the ratio of the momenta of the fragments behind and in front of the degrader:

$$B\rho_4 = \frac{p_4}{p_2} B\rho_2 \tag{1.7}$$

The dipole magnets of the second section can be tuned to accomplish equation 1.7. This second magnetic selection is approximately a selection in the atomic number Z of the nuclei.

Thickness (mg/cm^2)	0e (%)	1e (%)	2e (%)	Nuclear reactions (%)
5200	76.2	22.1	1.6	37.6

Table 1.2: Charge state distributions and probability of nuclear reactions in the intermediate degrader for a setting centred in ^{202}Ir. The selected degrader thickness is about half the range of the reference fragment (^{202}Ir).

The intermediate degrader

In the current work we used an Al degrader with the optimum thickness, correspondent to approximately 50% of the range of the ions at the entrance of the FRS [48]. A Nb foil 107 mg/cm^2 thick was placed behind the degrader to eliminate the maximum amount of charge state contaminants. Table 1.2 shows the percentages of the different cross contaminants in this FRS element for a setting centered in ^{202}Ir.

The intermediate degrader can be profiled in two modes. In the achromatic mode, the horizontal position of the fragments at F4 is an arbitrary function of their momentum at F2, whereas in the monoenergetic mode the energy loss of the fragments at F4 is independent from their horizontal position at F2. In this case, the horizontal angle of the degrader can be increased to bunch the momentum width of the ions at F4 until the spread is barely determined by the energy straggling in the degrader and the FRS resolution. This type of profiled element is employed when an energy bunch is needed at the final focal plane. For instance, when one is interested in stopping the selected fragments in a thin layer of matter at the exit of the FRS, as it is our case. Figure 1.4 illustrates the schematic layouts of the achromatic and monoenergetic degraders. The x-position distributions of the selected fragments at the focal plane F4 are also displayed.

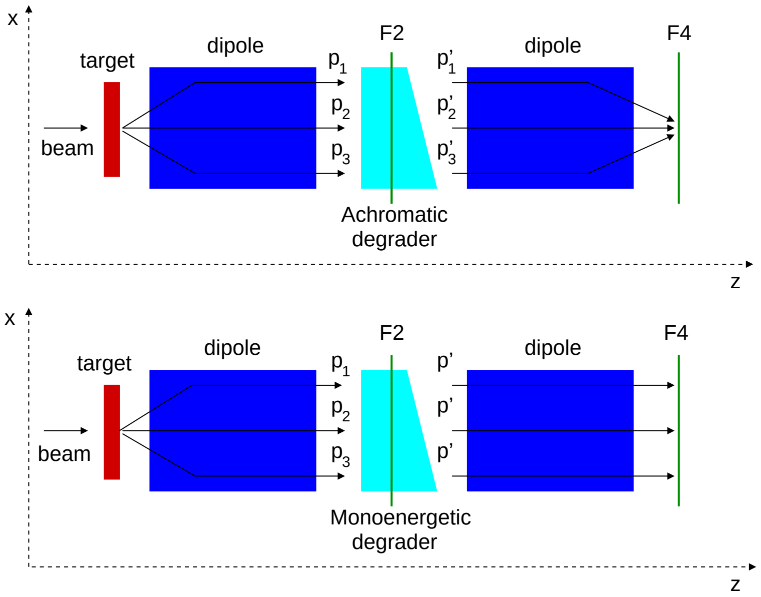

Figure 1.4: Schematic layout of the two FRS degraders. Upper panel: Achromatic mode. The resulting x-transversal position of the ions at F4 is independent from their momentum at the exit of the intermediate degrader. Lower panel: Monoenergetic mode. The final momentum distribution is independent from the horizontal position of the ions at the central focal plane. Note that the horizontal position distribution at F2 is preserved at F4.

1.3 Identification of heavy residues: the detection setup

Heavy neutron-rich nuclei can be separated and identified according to their mass-over-charge ratio A/Q and their atomic charge Q. These physical quantities are determined from the magnetic rigidity ($B\rho$), time-of-flight (ToF) and energy loss of the fragmentation residues. Different experimental devices are placed along the FRS in order to measure these magnitudes: tracking, time-of-flight and energy loss detectors. Figure 1.5 shows the experimental setup used in the current work. The technical drawings of the $S2$ and $S4$ regions are shown in appendixes A and B, respectively.

All the experimental devices located within the FRS, specially those placed in the dispersive image plane, should preserve the ion-optical conditions to keep the achromatism of the system. Throughout this section, we will describe the aim, technical details and calibration methods of each device.

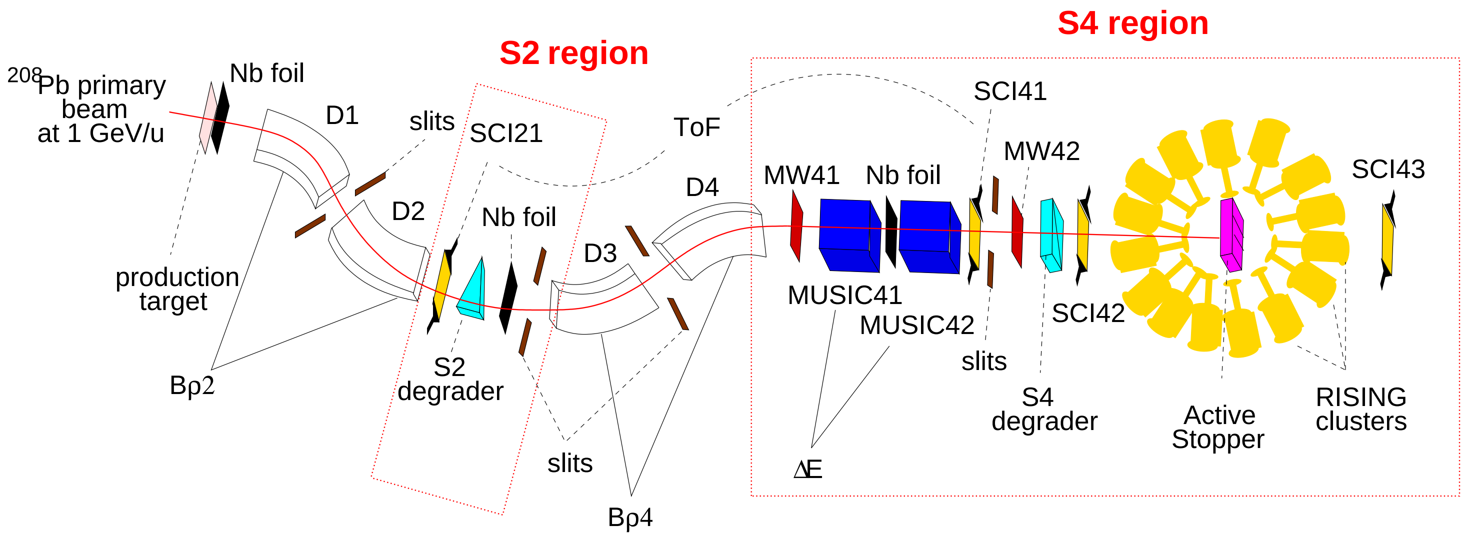
S2 region
S4 region
^{208}Pb primary beam at 1 GeV/u
Nb foil
D1
slits
SCI21
ToF
SCI41
MW42
SCI43
production target
Bρ2
D2
Nb foil
S2 degrader
D3
slits
Bρ4
D4
MW41
Nb foil
MUSIC41
MUSIC42
ΔE
slits
SCI42
S4 degrader
Active Stopper
RISING clusters

Figure 1.5: Schematic view of the FRagment Separator and the detection equipment used for the production, identification and β-delayed γ-ray spectroscopy of heavy neutron-rich nuclei.

1.3.1 Tracking detectors: multiwire proportional chambers

The MWPC detectors provide an accurate measurement of the transversal x and y positions of the traversing ions.

Although figure 1.5 only displays two MWPC at the $S4$ region, another four multiwire chambers were used at the beginning of the experiment to centre the trajectory of the primary beam along the ion-optical axis. These detectors were specifically designed to resist the high intensities of the projectile beam, and they were placed at each focal plane ($MW11$ at $S1$, $MW21$ and $MW22$ at $S2$, and $MW31$ at $S3$). Before proceeding with the fragmentation of ^{208}Pb, they were removed from the beam line as their wire structure could break the achromaticity of the system. The chambers were also used to calibrate the horizontal position of the plastic scintillators. For technicals details on these type of detectors, the reader is referred to ref. [70].

1.3.2 Position and Time-of-flight detectors: the plastic scintillators

Figure 1.5 shows a detector system consisting of two plastic scintillation detectors, SCI21 and SCI41, placed during the whole experiment at the central and final focal planes (their uniformity allows to maintain the achromaticity of the ion-optical system). The aim of this detection system is to provide an accurate event-by-event measurement of the positions and the time-of-flight of the traversing fragments [71].

The scintillation detectors are made of Bicron (BC420). The dimensions of the scintillator SCI21 are $210\times80\times3$ mm^3, whereas those of the scintillator SCI41 are $200\times80\times3$ mm^3. In both cases the sensitive area is the appropriate to cover the entire focal plane.

Two fast photomultipliers were mounted at the left- and right-hand sides of the plastic scintillators in order to register the signals coming from the sensitive area. Figure 1.6 [72] illustrates the electronic scheme of the scintillation detection system. The horizontal positions of the traversing ions at F2 and F4 were determined from the time difference between the scintillator signals arriving at both photomultipliers. This difference can be measured with a resolution of $\Delta t = 40$ ps (FWHM) for ^{40}Ar [71]. The position resolution $\Delta x = c_{scint}\Delta t/2$, being the effective speed of light within the scintillator approximately $c_{scint} = 20$ cm/ns, is then $\Delta x = 4$ mm for ^{40}Ar. The signal of each photomultiplier was then filtered by a constant-fraction discriminator (CFD) and used as the start signal (left hand side) or the stop signal (right hand side) of a time-to-amplitude converter (TAC). The analog output of the

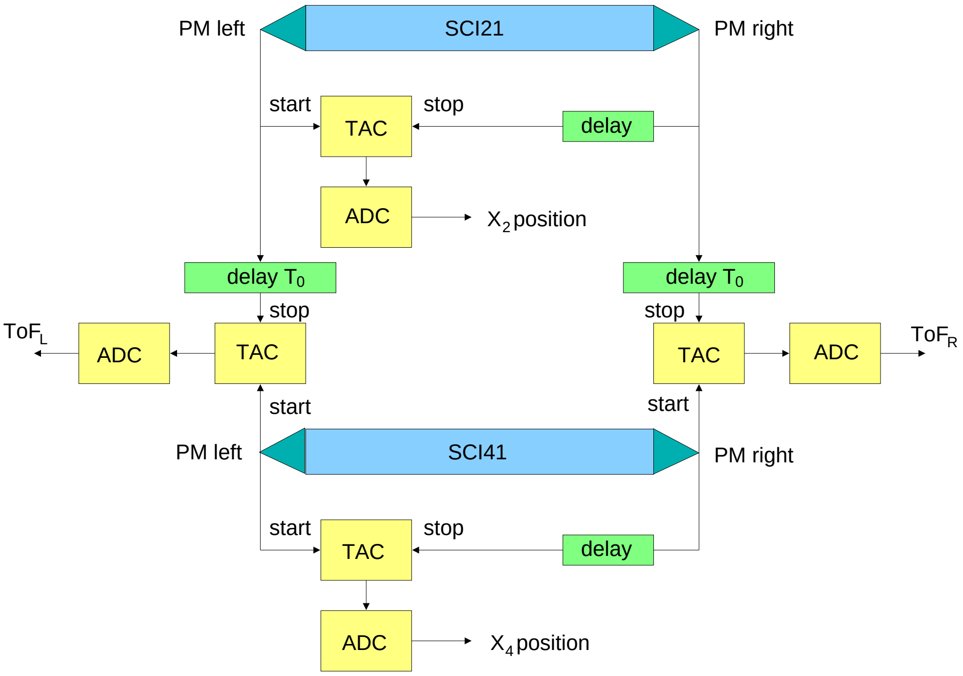
PM left
SCI21
PM right
start
TAC
stop
delay
ADC
X$_2$ position
delay T$_0$
delay T$_0$
stop
stop
ToF$_L$
ADC
TAC
TAC
ADC
ToF$_R$
start
start
PM left
SCI41
PM right
start
TAC
stop
delay
ADC
X$_4$ position

Figure 1.6: Electronic scheme of the plastic scintillators.

TAC was converted by an analog-to-digital converter (ADC). The resulting signal was converted from channels to position with a linear calibration.

With regard to the time-of-flight measurement, the fragments pass through $S2$ at time T_2 and through $S4$ at time T_4. The output of the scintillator SCI41 was selected as the start signal of the TAC and the output of the scintillator SCI21 as the stop to prevent recording signals of fragments stopped in the second stage of the FRS. The time T_2 was delayed a quantity T_0 in order to provide the stop signal from $S2$ later than the start from $S4$.

Each of the TACs provides a signal, ToF_R^* and ToF_L^*, respectively. The measured time-of-flight ToF^* is the average of both:

$$ToF^* = T_2 + T_0 - T_4 = \frac{ToF_L^* \cdot \alpha_L + ToF_R^* \cdot \alpha_R}{2} \tag{1.8}$$

where α_L and α_R are the corresponding calibration factors to transform amplitude to time.

The real time-of-flight is given by:

$$ToF = T_4 - T_2 = T_0 - ToF^* \tag{1.9}$$

where ToF is the ratio between the flight path d along the second half of the FRS (approximately 36 m) and the velocity v of the traversing ion:

$$ToF = \frac{d}{v} \tag{1.10}$$

From equations 1.10 and 1.9 we obtain a first order polynomial from which we can measure the velocity of the residues in the second section of the FRS:

$$\frac{1}{v} = \frac{T_0}{d} - \frac{ToF^*}{d} \tag{1.11}$$

The TAC calibration allows to obtain the factors α_R and α_L that transform the ToF^*_R and ToF^*_L signals from channels to time.

The ToF calibration is performed in order to deduce the offset $a = T_0/d$ and the slope $b = -1/d$ of expression 1.11. The process is the following: the projectile beam of ^{208}Pb is forwarded throughout the FRS and different ToF calibration files are recorded, each of them for a given layer of matter in the dispersive plane. For each layer thickness, the primary beam leaves the S2 region with a particular velocity, and thus with a different time-of-flight.

Each ToF calibration setting had well known effective thicknesses and magnetic rigidities. Hence, it is possible to calculate the corresponding laboratory velocities with the code AMADEUS [65]. By histogramming the inverse of the velocity versus the measured time-of-flight (ToF^*), we can make a linear fit and obtain d and T_0. Figure 1.7 shows the ToF calibration fit of the present experiment. The resulting values of d and T_0 are 37 m and 181 ns, respectively.

1.3.3 Energy-loss detectors: MUlti Sampling Ionization Chambers

According to the Bethe-Bloch formula [73], the energy loss of an ion in matter depends on the square of its charge. For fully stripped ions, the charge is equal to the atomic number Z.

The Bethe-Bloch formula is applied in the working principle of some gas-filled detectors, since the number of electrons generated by a traversing ion in a gaseous medium is proportional to its energy loss and, therefore, to the charge carried by the nuclide. The gas-filled detectors utilised in the present experiment were two MUlti Sampling Ionization Chambers (MUSIC80) [74, 75], placed at the exit of the FRS (see figure 1.5). Henceforth, the front chamber will be referred to as MUSIC41, whereas the rear one will be cited as MUSIC42. A Nb foil of thickness 222.82 mg/cm^2 was located between both

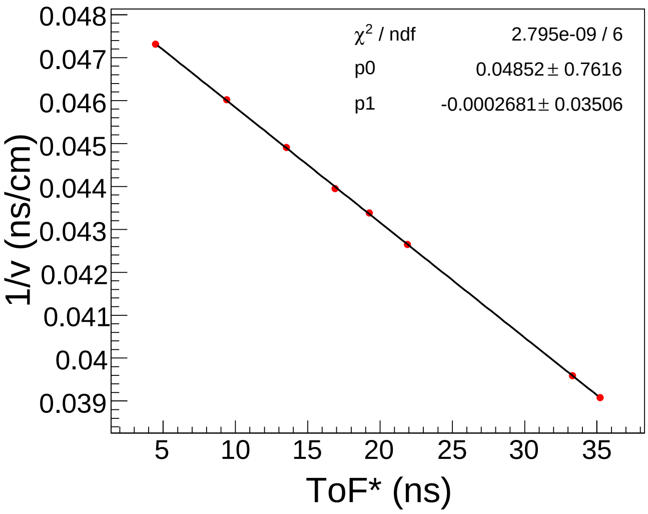

Figure 1.7: Time-of-flight calibration for the present experiment. The linear fit allows to deduce the parameters d and T_0. See text for details.

detectors to strip off the electrons gained by the fragments after crossing the MUSIC41.

The MUSIC80 is a 400mm length detector with an active area of 200×80 mm^2. It consists of 8 anode strips, a cathode and a Frisch grid [76]. The chamber is filled with pure CF_4 at room temperature and atmospheric pressure. The counting gas was renewed during the measurements to preserve the operational conditions of the detector. The entrance windows are made of thin float glass with integrated aluminium strips of thickness 1 μm. The high voltage supplied to the cathode and the Frish grid ensures the correct electric field intensities. Each anode strip collects the electron shower signal, which is read out by a charge sensitive preamplifier connected to a shaping amplifier. The signals are then digitalised by an amplitude-to-digital converter (ADC) and finally sent to the data acquisition system. Each anode provides an independent measurement of the energy loss. Since the gas conditions inside the detector are practically equal, one may consider the energy loss averaged over the eight anodes in order to improve the resolution of the measurement.

The MUSIC signals depend on the ionic charge state of the incoming ions and the charge exchanges due to the collision processes occurred along the chambers. The ionic charge is defined as

$$Q = Z - n_e \tag{1.12}$$

Where n_e is the number of electrons carried by the nuclide.

As figure 1.8 shows, the signals generated in the MUSIC detectors vary according to the transversal x-position of the traversing fragments, probably because of the inhomogeneity of the electromagnetic field in the extremes of the chambers.

The energy loss ΔE registered by these devices is then a function of the ionic charge Q of the traversing fragments, their velocity β and their horizontal position x

$$\Delta E = Q^2 \cdot f(x) \cdot g(\beta) \tag{1.13}$$

Where the dependencies in position and velocity can be factorised and corrected in order to obtain a more realistic measurement of the ionic charge. In order to perform an adequate fit of the energy loss as a function of the transversal x-position, it is worth that the secondary residues cover the whole horizontal range at the final focal plane $F4$. The resulting correction function can be expressed as

$$f(x) = \frac{\Delta E(x_{ref})}{\Delta E(x)} \tag{1.14}$$

Where $\Delta E(x)$ is the position dependence and $\Delta E(x_{ref})$ is the energy loss corresponding to a reference position (for instance, the energy loss of the ions following the central trajectory $x_{ref} = 0$).

The code AMADEUS is used to obtain the correction function $g(\beta)$ from theoretical calculations of the energy loss for different ion velocities. The function $g(\beta)$ is defined as the ratio between the energy loss correspondent to a reference velocity β_{ref} and the velocity dependence obtained with AMADEUS

$$g(\beta) = \frac{\Delta E(\beta_{ref})}{\Delta E(\beta)} \tag{1.15}$$

In the present work, the correction functions in the transversal x-position and the velocity β have been approximated by third order polynomials. Figure 1.8 shows the raw energy loss signals in the chamber MUSIC42 for a setting centred in ^{202}Ir. Note that the horizontal position of the traversing fragments is that of the closest scintillator SCI41, whereas the velocity corresponds to that of the second half of the FRS. Figure 1.9 shows the resulting ΔE spectra after correcting the aforementioned dependences.

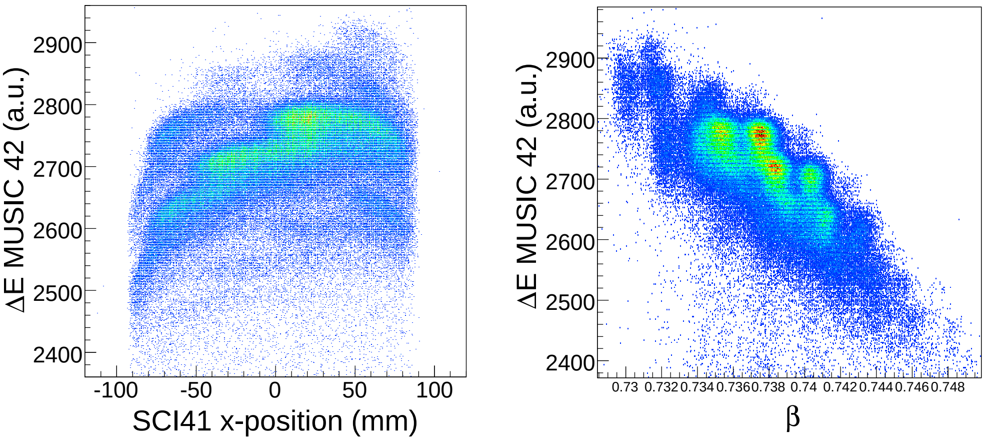

Figure 1.8: Dependences of the energy loss signal in the chamber MUSIC42 for a magnetic setting of the FRS optimised to transmit ^{202}*Ir.*

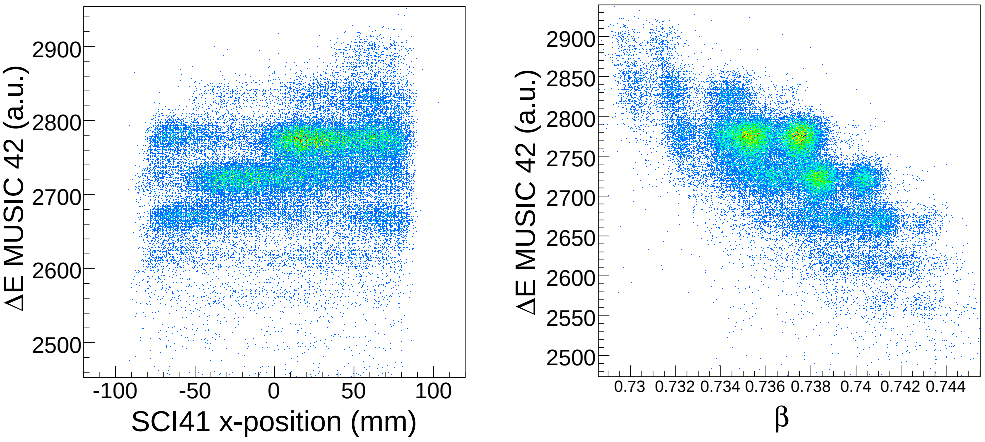

Figure 1.9: Corrected energy loss signals in MUSIC42.

1.4 Identification of heavy residues: charge state selection

The ionic charge states represent a significant challenge to perform an unambiguous identification of the projectile residues, in particular for heavy neutron-rich nuclei. The use of a profiled degrader, placed at the dispersive plane of the FRS, together with the use of two MUSIC detectors allows to identify and select the fully-stripped nuclei for the subsequent β-delayed γ-ray spectroscopic study. In this section we describe the charge state selection technique. For further details on this procedure see refs. [17] and [77].

1.4.1 The MUSIC chambers. Charge state corrections

The stochastic changes of charge states of the incoming nuclei in the gas of the MUSIC detectors lead to a deterioration of the energy loss resolution, which can be improved by combining the energy loss measurements of both chambers. We expect that any ionic charge state observed in a given MUSIC is mainly due to electron exchanges inside the gas detector, since a high percentage of the selected residues enter fully-stripped within the MUSICs. The use of two ionization chambers allows to obtain two independent measurements of the energy loss of the fragments that can be represented in a two-dimensional plot, as shown in figure 1.10.

From the resulting correlation, one can define an ionic charge with an improved resolution. Figure 1.10 reveals different fragment distributions corresponding to different atomic numbers Z. Each distribution shows two wings orthogonal to the x and y axis that intersect in a cluster of spots. The fragments contained in the cluster carry the maximum energy loss ΔE measured by any of the two detectors. Since the maximum ionic charge carried by a fragment is that of its atomic number (Q_{max}=Z), the highest energy loss cluster corresponds to the fully-stripped ions with a maximum probability.

Any variation in the ionic charge in any of the two chambers leads to a reduction of the energy loss in the detector where the fragment collected the electron(s). If there are no charge exchanges in the other chamber, the energy loss is kept constant. For a given fragment distribution, the vertical wing indicates a constant energy loss in the x axis, which corresponds to the bare ions in MUSIC41 that carried one or more electrons in MUSIC42. On the contrary, the horizontal wing indicates a constant energy loss in the y axis, corresponding to the fully stripped ions in MUSIC42 that carried at least one electron in MUSIC41.

A linear fit is performed along the cores of each distribution. The maxi-

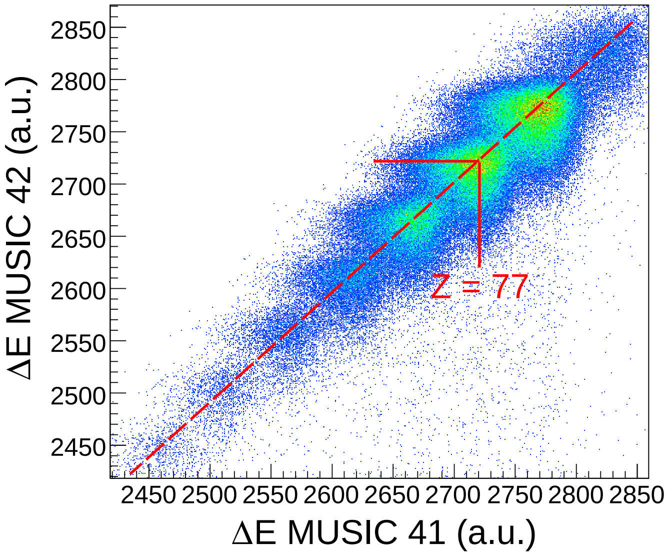

Figure 1.10: Correlation plot of the energy loss signals provided by the two MUSIC chambers used in the present experiment, for a setting centred in ^{202}*Ir. The distribution corresponding to the iridium isotopes* ($Z = 77$) *is marked in the figure.*

mum ionic charge Q_{max} is defined as that traversed by the linear fit (see the dashed line in figure 1.10). In order to improve the energy loss resolution in the analysis, the value ΔE assigned to the fragments over the diagonal corresponds to the energy loss measured in MUSIC42, whereas the value ΔE assigned to the ions laying under the linear fit is the corresponding maximum ionic charge Q_{max} in MUSIC42. Note that the residues which carry the same number of electrons ($n_e \neq 0$) throughout the two chambers cannot be identified. The percentage of this type of events is less than 2% for ^{202}Ir along the central trajectory, as checked with the code AMADEUS. Figure 1.11 shows the effective charge resolution achieved after correcting the position and velocity dependencies, as well as the charge state exchanges in both MUSIC chambers.

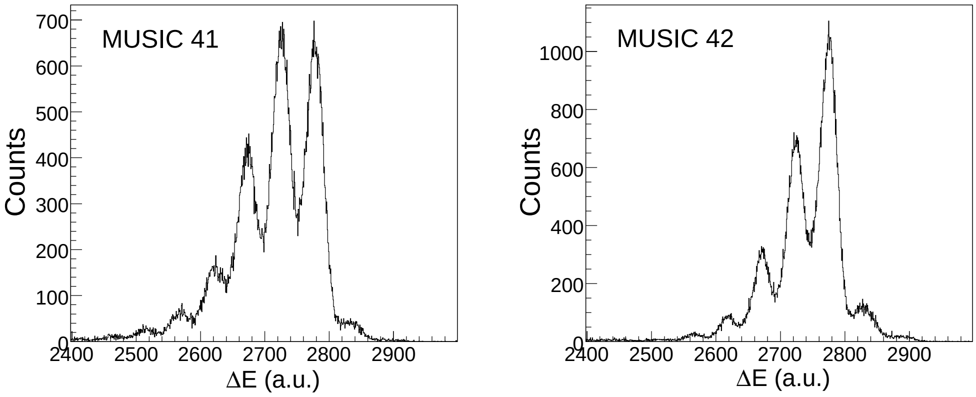

Figure 1.11: Corrected energy loss spectra of the MUSIC chambers. The figures correspond to a magnetic setting centred in ^{202}Ir.

1.4.2 The FRagment Separator. Charge state selection

In the previous section we assumed that the fully stripped ions could be identified and selected along the FRS. The energy loss ΔE_{deg} of an ion in the profiled Al degrader of $S2$ is the key, as we will show subsequently.

The kinetic energy E carried by an ion of mass A and velocity β along the first section of the FRS is defined as

$$E = A \cdot (\gamma - 1) \tag{1.16}$$

being γ the relativistic factor. The alternative magnitude energy-to-charge ratio E/Q is sensitive to changes in the ionic charge of an ion within the FRS

$$\frac{E}{Q} = \frac{A}{Q} \cdot (\gamma - 1) \tag{1.17}$$

The magnitude ΔE_{deg} can be evaluated from the difference between the kinetic energies E_1 and E_2 of a fragment in the first and second halves of the FRS, respectively. The $\Delta E_{deg}/Q$ ratio is, then

$$\frac{\Delta E_{deg}}{Q} = \frac{E_1}{Q} - \frac{E_2}{Q} = \frac{A}{Q} \cdot (\gamma_1 - \gamma_2) \tag{1.18}$$

From equation 1.2, eq. 1.18 can be written as

$$\frac{\Delta E_{deg}}{Q} = \frac{e}{m_0 c}\left(\frac{B\rho_1}{\beta_1} - \frac{B\rho_2}{\beta_2}\right) \tag{1.19}$$

Where e is the electron charge, m_0 is the mass unit and c is the speed of light. The magnitudes $B\rho_1$, $B\rho_2$ are calculated according to equations 1.5 and 1.6, respectively. The relativistic velocity β_2 is directly obtained from the measured time-of-flight, and β_1 is determined from the relations

$$\gamma_1^2 = 1 + \left(\frac{e}{m_0 c}\right)^2 \left(\frac{B\rho_1}{A/Q}\right)^2 \tag{1.20}$$

and

$$\beta_1 = \sqrt{1 - \frac{1}{\gamma_1^2}} \tag{1.21}$$

To determine the velocity β_1 it is essential to consider that the traversing ions do not undergo any ionic charge change along the FRS. This is equivalent to consider the ratio A/Q constant through the FRagment Separator. Any change of ionic charge in a given fragment between both stages of the FRS will imply a significant variation of the $\Delta E_{deg}/Q$ value, thus separating the different distributions of ionic charge states along the spectrometer.

Figure 1.12 shows the resulting $\Delta E_{deg}/Q$ versus Q_{max} matrix for a magnetic setting optimised to transmit ^{202}Ir in the central trajectory. We distinguish three parallel distributions of clusters, each of them corresponding to a certain charge state. In order to determine which line of clusters corresponds to the fully stripped distribution, the fragment production rates have been calculated with the code LIESCHEN [67]. As result, the central distribution is that of the bare nuclei along the FRS ($(0e - 0e)$ in figure 1.12). The upper line of spots corresponds to those ions that carry one electron in the first stage of the FRS and are fully stripped in the second stage $(1e-0e)$, whereas the lower distribution is conformed by the bare nuclei before the degrader that acquire one electron after $(0e - 1e)$. Moreover, one can slightly distinguish a fourth distribution of small clusters lying just over the fully stripped ions, marked as $(1e-1e)$. This distribution is drawn from two contributions: the fragments that are fully stripped along the FRS but carry one electron throughout both MUSIC chambers, and the nuclei that are in their hydrogen-like ionic state along the FRS and are completely bare in the chambers. The only misidentifications left with this charge state selection method are two. First, the nuclei (A-3,Z) that have one electron in the FRS and lose it in one of the two MUSIC chambers. Second, the fragments (A,Z+1) that keep one

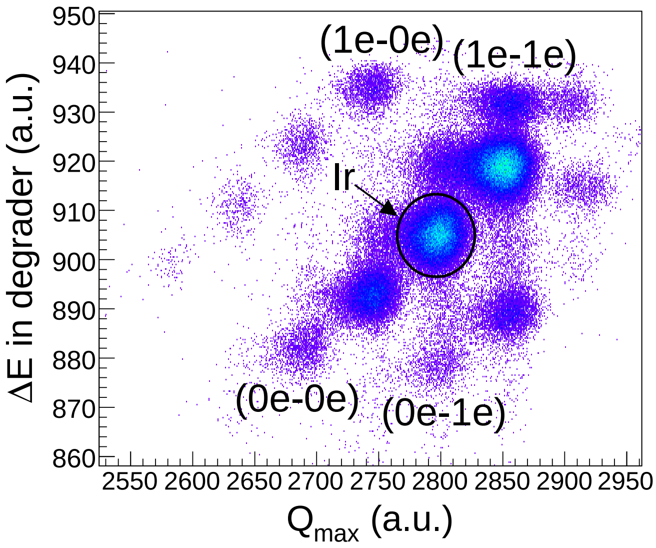

Figure 1.12: Correlation plot between the energy loss in the aluminium intermediate degrader and the maximum ionic charge measured with the two MUSIC chambers for an FRS setting centred in ^{202}Ir. Each labelled distribution of clusters corresponds to a different charge state configuration along the FRS. See text for details.

electron along the entire setup line. In both cases, the assignation of Q and A/Q corresponds to that of the fragment of interest.

1.5 Identification of heavy residues: atomic charge and mass determination

The mass separation is reached in two different ways: by displaying the maximum ionic charge Q_{max} versus the A/Z value (see figure 1.13) or, after a previous selection in Q_{max}, representing the A/Q ratio as a function of the transversal x-position in either, the central or the final focal planes (see figure 1.14). In both cases, each cluster of spots corresponds to a given mass. The high isotopic resolution achieved is demonstrated by the clear separation between clusters.

The isotopic identification is performed comparing the measured values of the A/Q ratio, the transversal positions x_2 and x_4, and the production yields with the theoretical predictions calculated with the code LIESCHEN.

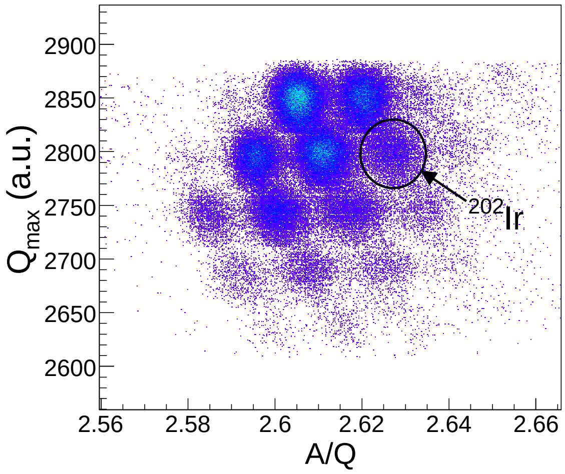

Figure 1.13: Scatter plot of the maximum ionic charge measured in the MUSIC chambers in relation to the A/Q value of the fragments along the FRS for a setting centred in ^{202}*Ir (marked).*

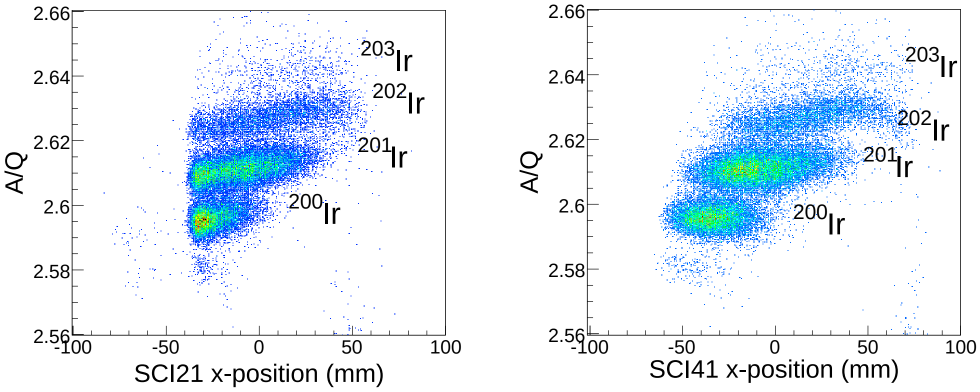

Figure 1.14: Mass identification plot of the different iridium isotopes for an FRS setting centred in ^{202}*Ir. The two-dimensional spectra show the A/Q ratio as a function of the position of the fragments at the central and final focal planes, respectively.*

After leaving the FRS, the selected fragments can be studied without any ambiguity in the mass identification.

1.6 β-delayed γ-ray analysis: the implantation setup

In the $S4$ region the selected ions are decelerated till a few tens of A·MeV and implanted in a β-delayed spectroscopy setup, consisting of a variable-thickness aluminium degrader, two plastic scintillators (henceforth referred to as SCI42 and SCI43), the active stopper and the advanced RISING γ-ray spectrometer. Figure 1.15 provides a schematic view of the slowing-down setup. The extremely neutron-rich nuclei with half lives long enough to survive the flight path of the FRS ($\sim$ 300 ns) are implanted in the Si catcher. Afterwards, they undergo subsequent β-decay processes until a stable fragment is formed.

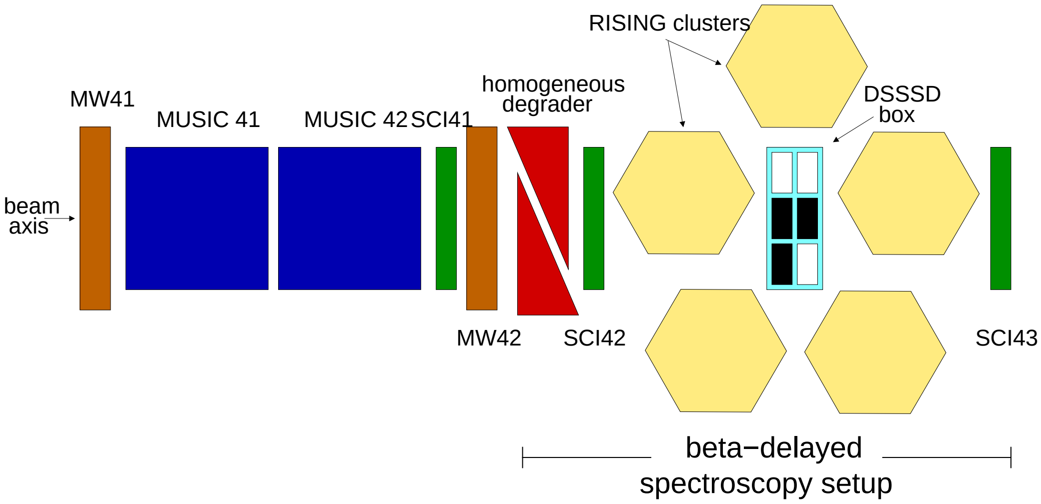

Figure 1.15: Schematic layout of the experimental configuration at the S4 region of the FRS. Selected fragments enter into the slowing-down system after being identified by their A/Q ratio and their ionic charge Q. The nuclei are decelerated in the homogeneous degrader and subsequently implanted into the active stopper. The three positions of the Si catcher occupied by DSSSD detectors are marked with black boxes. The scintillator system (SCI42 + SCI43) allows for the offline suppression of the ions destroyed in the slowing-down process.

Whilst the active stopper allows to determine the half lives by means of position and time correlations between implantations and decays, the advanced RISING γ-ray spectrometer allows to perform isomeric spectroscopy of the fragmentation residues, and β-delayed γ-ray spectroscopy of their

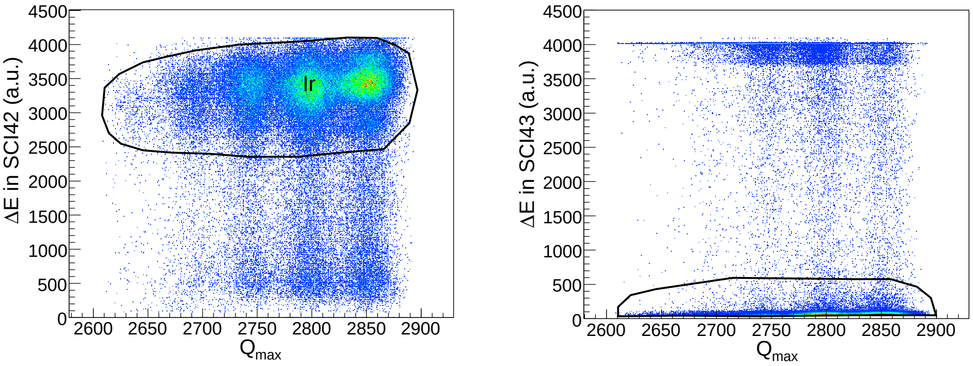

Figure 1.16: Two-dimensional scatter plots of the energy loss in the scintillators located at S4 vs. the effective charge registered in the MUSIC chambers. The gates performed to select the implanted nuclei are shown.

daughter nuclei.

The efficiency of the slowing-down system is enhanced by the use of a monoenergetic intermediate degrader in the FRS. The $S2$ degrader delivers a secondary beam with a range distribution confined in the beam direction and a broad dispersion in the transversal x-direction [78], in such a way that several nuclear species can be implanted in the active stopper at the same time. Furthermore, the thin layer (1 mm thick) of the active stopper is highly pixelated to reduce the probability of multiple implantation in a given cell.

1.6.1 The implantation procedure

The nuclear species transmitted through the FRS reach the $S4$ region with energies ranging between 500 and 600 A·MeV. The Al homogeneous degrader is required to slow the fragments down before their implantation in the active stopper. For every magnetic setting of the FRS, the thickness of the degrader is determined according to the range of the selected fragments.

The plastic scintillators SCI42 and SCI43 provide the energy loss of the traversing ions in front of and behind the active stopper, respectively. These measurements allow to control the implantation of the selected nuclei, since the energy loss signal in the scintillators is proportional to the square of the ionic charge Q, according to the Bethe-Block formula.

If the degrader thickness is smaller than the range of the fragments, the residues will cross the entire slowing-down system, and they will deposit a high energy signal in SCI43. If, on the contrary, the degrader thickness ex-

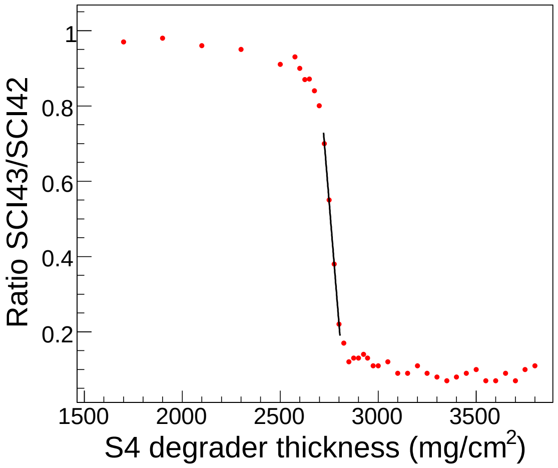

Figure 1.17: Calibration of the S4 degrader thickness. The plot shows the ratio between the number of projectiles registered in SCI42 and the number of projectiles detected in SCI43 as a function of the degrader thickness. The linear fit performed to obtain the required thickness is displayed.

ceeds the range of the fragments, the ions will be stopped before the active stopper. If they are implanted in SCI42, the energy signal of this scintillator will be saturated, whereas if they are stopped before, the energy output of SCI42 will provide the energy loss of the secondary fragments formed in the degrader and the scintillator SCI42. To suppress the secondary reaction products formed during the implantation process, a lower energy threshold is established for SCI42, and an upper energy threshold for SCI43. As an example, figure 1.16 shows the energy loss signals registered in the S4 scintillators as a function of the maximum ionic charge for a setting centred in ^{202}Ir. The gates used to discriminate the secondary fragments are also shown.

The S4 degrader thickness necessary to implant the primary beam in the centre of the active stopper is calibrated in order to calculate the appropriate thickness for each magnetic setting of the FRS. Figure 1.17 represents the ratio between the number of projectiles at SCI42 and the number of projectiles at SCI43 as a function of the degrader thickness. This ratio decreases rapidly when the fragments are stopped at the entrance of the scintillator SCI43. The decreasing region is adjusted to a linear fit, such that the thickness $T_d^{sci43}(^{208}Pb)$ required to stop the projectile beam at the entrance of SCI43 corresponds to the average value of the fit. The matter M_{Si}^{sci43} contained between the middle of the active stopper and the entrance of the veto scintillator is provided in equivalent Al thickness in Appendix C. Thus, we can deduce the Al degrader thickness $T_d^{Si}(^{208}Pb)$ necessary to stop the primary beam in the centre of the active stopper:

$$T_d^{Si}(^{208}Pb) = T_d^{sci43}(^{208}Pb) + M_{Si}^{sci43} \tag{1.22}$$

Referring to d_{Si} as the thickness between the final focal plane F4 and the centre of the front DSSSD detector, one can deduce for each FRS setting the thickness required to implant the nuclide of interest in the middle of the active stopper, since the quantity

$$d_{Si} = R_{F4}(^{208}Pb) - T_d^{Si}(^{208}Pb) \tag{1.23}$$

is constant. $R_{F4}(^{208}Pb)$ refers to the range of the primary beam at the final focal plane. Let $T_d^{Si}(^A_ZX)$ be the degrader thickness required to implant a given nuclear specie in the centre of the active stopper, and $R_{F4}(^A_ZX)$ be its range at F4. Then, the resulting degrader thickness $T_d^{Si}(^A_ZX)$ is

$$T_d^{Si}(^A_ZX) = R_{F4}(^A_ZX) - R_{F4}(^{208}Pb) + T_d^{Si}(^{208}Pb) \tag{1.24}$$

1.6.2 The active stopper

The active stopper is a new β counting system developed to study the β-decay of exotic nuclei within the RISING project [50]. It consists of up to six semiconductor Double Sided Silicon Strip Detectors (DSSSD).

In the present experiment, we employed three DSSSD detectors placed within a light-tight box located in the centre of the RISING γ-ray spectrometer (see figure 1.18). The active stopper box is made up of Pertinax[2] 2 mm thick, with two windows covered by a 20 μm black Polacon C foil [79]. Figure 1.15 shows the position of each DSSSD inside the box. This device is used to determine the position, time and energy of the implanted nuclei and the subsequent β-decays to further perform event-by-event position and time correlations between them. In addition to this, the active stopper can be utilised to perform electron conversion spectroscopy of the fragmentation residues [25].

Technical details

The DSSSDs are Micron Semiconductors Ltd [81] Model W1(DS)-1000 DC, each with a sensitive area of 5×5 cm^2 and 1 mm thickness. The thickness of this device guarantees a detection efficiency for fragmentation residues of $\sim 100\%$. The range of the β-particles, however, is usually larger than 1 mm of

---

[2] Phenolic-formaldehyde cellulose-paper PF CP 2061

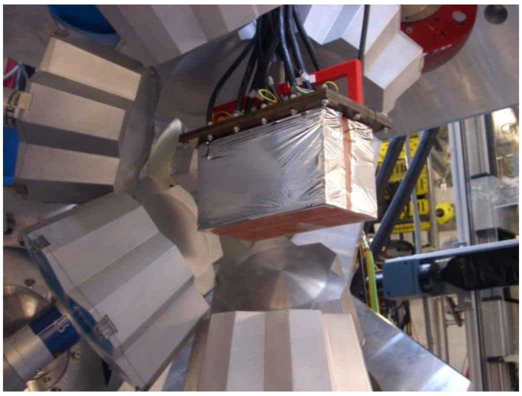

Figure 1.18: Photograph of the active stopper setup. The DSSSDs are contained in the light-tight box, which is placed in the middle of the RISING γ-ray array in its Stopped Beam configuration [80].

silicon. Therefore, the electrons deposit only a fraction of their total kinetic energy in the DSSSDs, resulting in a lower detection efficiency. The portion of energy deposited depends on the path of the β-particle and, consequently, on the implantation depth. The expected efficiency value ranges from 40-50 % for ions implanted in the middle of the DSSSD up to 80-90 % for fragments implanted between two DSSSD detectors (note that the configuration of the active stopper is equivalent to consider the two central DSSSDs as a unique DSSSD with double the thickness).

Each detector is divided in 16 front strips and 16 back strips, which provide the transversal x and y positions by means of 256 pixels, each of them with a sensitive surface of 3.12×3.12 mm^2. By this way, implantations and decays can be spatially correlated within a given pixel or a group of adjacent pixels. The time sequences between fragment implantations and β-decays arisen in the same group of pixels yield the β-decay half life of the nuclide under study. Events are recorded with a time resolution of 20 ns.

The technical complexity related to the active stopper lies in the wide energy range necessary to identify both, the implanted nuclei and the subsequent β-decays. Whereas a fragment implantation may deposit more than 1 GeV when it is stopped in the middle of the DSSSD, an emitted electron deposits less than 1 MeV. In the present experiment, the difficulty is addressed by the use of logarithmic pre-amplifiers coupled with high-gain shaping amplifiers [79].

The *Mesytec* [82] MPR-32 is a logarithmic pre-amplifier with 32 input channels used for the 16 horizontal and vertical strips of a single DSSSD.

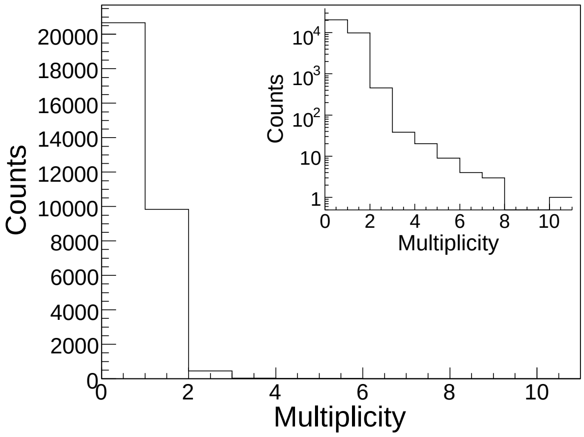

Figure 1.19: X-strips multiplicity distribution of the active stopper for the implantation of ^{204}*Pt. The input shows the graphic in logarithmic scale. Multiplicity 1 indicates that only one pixel (X, Y) has been fired with an energy above the implantation threshold, and so on.*

The MPR-32 pre-amplifier is characterised by a linear response in the low energy range (0-10 MeV) followed by a logarithmic amplification at higher energies (10 MeV-3GeV). The linear response enables the position identification (x,y) and the energy and time measurements of the β-particles and the conversion electrons. The position coordinates (x,y) stand for the x- and y-strip of the detected electron, respectively. The logarithmic part allows for the determination of the time and implantation position in a given pixel (X,Y), where X and Y refer to the horizontal and vertical strip of the implanted fragment, respectively. Due to the high energies involved in the slowing-down process, a cross-talk effect may be induced around the pixel of implantation, giving rise to signals (normally of lower energy) in the neighbouring strips. In order to minimise this effect, an implantation threshold is established. As an example, figure 1.19 shows the multiplicity distribution of x-strips fired by the implantation of ^{204}Pt. Whilst for multiplicity one on each side of the DSSSD the position determination of the implantation is straightforward, for higher multiplicities the x-strip with maximum energy output compared to its adjacents provides the implantation position (X,Y) with a maximum probability.

Each MPR-32 pre-amplifier is combined with two *Mesytec* STM-16 NIM-powered amplifiers with 16 channels each. The STM-16 is controlled by a bus master (a NIM-module MRC-1). An interface allows for the communication with a control PC. The 96 analogue signals are sent via twisted-pair cables and fed into three CAEN VME-ADCs Model V785AF [83] with 32 channels each. In order to start the acquisition, a signal above threshold, typically 150 keV, is required in at least one x- or y-strip. Consequently, the β trigger is provided by a logical OR of the 16 discriminator channels in the STM-16 amplifiers. The trigger is subsequently used to produce the ADC gate.

Energy calibration

The energy resolution of the linear part of the logarithmic pre-amplifier (∼20 keV) is good enough to perform conversion electron spectroscopy. We proceeded with two different calibrations depending on the issue of research, i.e., heavy ion implantations or β (conversion) electrons.

It is not necessary to perform an energy calibration for the logarithmic range of the pre-amplifier, since we are not interested in the quantitative value of the energy deposited by the fragments, but in the X- and Y-strip positions where the ions lose the maximum amount of energy. Nevertheless, we perform an energy correction, which consists in matching up the implantation channel of every x- and y-strip by fitting the highest energy peak (related to the implantation) to a Gaussian function. Subsequently, we apply to the initial energy channelling $E(ch)$ an energy shift given by the alignment of the Gaussian centroid E_c to a constant value C

$$E'(ch) = E(ch) + (C - E_c) \tag{1.25}$$

where $E'(ch)$ stands for the final energy channelling. By this way, we can establish an accurate energy threshold to minimise the implantation strip multiplicity. Figure 1.20 shows the total measured energy spectrum obtained for a setting centred in ^{202}Ir after applying the aforementioned correction to each x- and y-strip. The threshold selected to trigger an implantation event is marked with a dashed line.

The calibration of the low energy range is made with an open ^{207}Bi source positioned at 5 cm from the front face of the active stopper. Each peak of the 32 energy spectra of every DSSSD detector is individually fitted to a Gaussian function. The resulting centroids are used to perform a linear fit of the two energy values.

A β-decay energy threshold is established to improve the DSSSD response for the detection of electrons. In the present experiment, the energy signal of each strip was adjusted until the electron rate achieved 1 count$\cdot$(strip$\cdot$s)$^{-1}$. For the *Mesytec* electronics used in this experiment, the energy threshold can be lowered until ∼150 keV [79]. Any detected energy over this threshold was

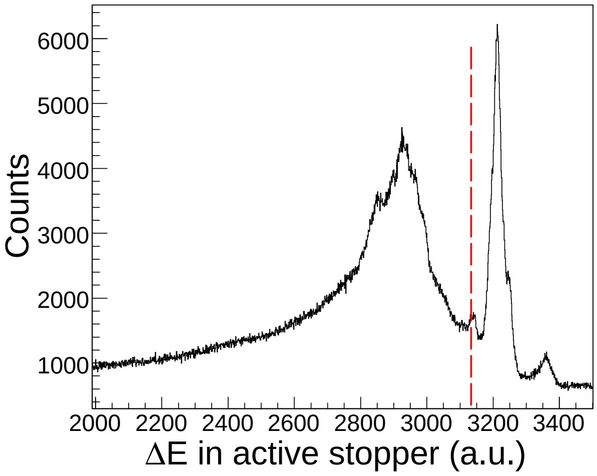

Figure 1.20: Corrected total energy spectrum of the active stopper for an FRS setting optimised to transmit ^{202}*Ir. All x and y strips are included. Implantation events are triggered when at least one strip detects an energy loss above the limit marked with a dashed red line.*

considered an electron event and triggered the acquisition, whereas energy values under the selected threshold were not recorded.

Implantation in the active stopper

Figure 1.21 shows the identification matrix corresponding to an FRS magnetic setting centred in ^{202}Ir. Whereas the left panel displays the neutron-rich nuclei transmitted to the final focal plane of the FRS, the right panel shows the corresponding fragments implanted in the Si catcher.

For this specific setting, nine of the selected nuclei along the FRS fall into the implantation range of the active stopper. Fragments with higher ranges traverse the slowing-down system and are detected in the veto scintillator SCI43. Fragments with shorter ranges, however, are stopped in the homogeneous degrader or in one of the previous layers of matter.

Table 1.3 summarises the different nuclear species implanted in the active stopper during the current experiment. The total number of ions at F4 and the number of corresponding implantations are shown.

The background of the γ-ray energy spectra induces a background in the β-decay curve. It can be directly evaluated and represents about a 10-20% of the total β-decays registered after the beam spill, depending on the energy of the selected γ-ray transition.

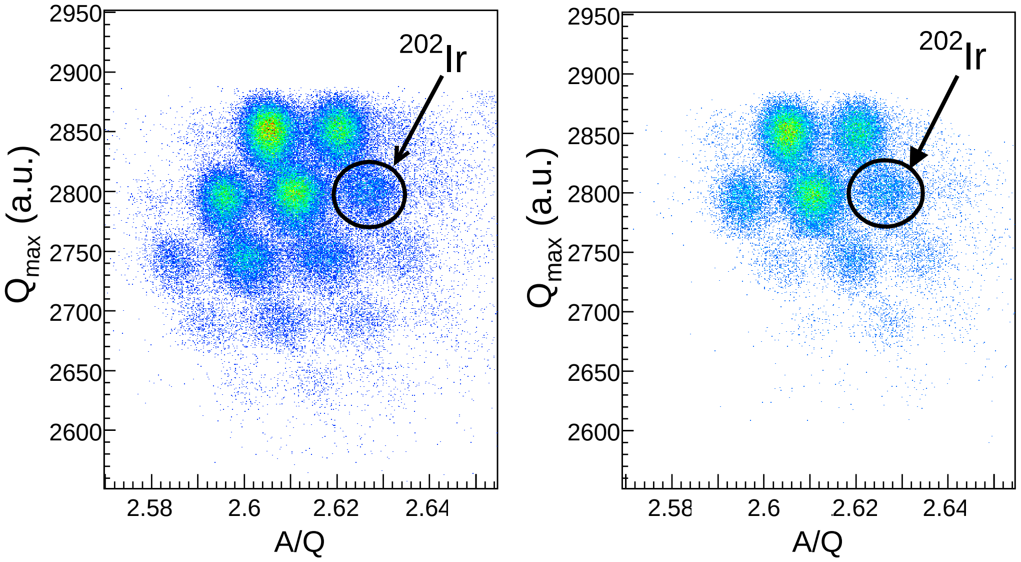

Figure 1.21: Two-dimensional cluster plots of identification for an FRS magnetic setting optimised to transmit ^{202}Ir. The left panel shows the total yield at the final focal plane of the FRS, whereas the right panel displays the corresponding heavy nuclei implanted in the active stopper.

1.6.3 The advanced RISING γ-ray spectrometer

The RISING γ-ray spectrometer consists of fifteen germanium cluster detectors from the decommissioned EUROBALL IV setup [84, 85], each of them housing seven hexagonal hyper pure n-type Ge crystals mounted in a common cryostat.

Hitherto, this spectrometer has been used to detect electromagnetic transitions depopulating isomeric states excited in fragmentation reactions [86–90]. The first results using β-decay delayed spectroscopy of fragmentation residues are reported in refs. [91, 92]. In this work, the RISING array is used to perform new β-delayed γ-ray spectroscopic measurements. The corresponding results are provided in chapters 3 and 4.

The principal parameters that specify the performance of a Ge array are the energy resolution, the photopeak detection efficiency and the peak-to-total ratio. The energy resolution of a detector is defined as the full width at half maximum (FWHM) of a peak distribution divided by the location of the peak centroid. The photopeak detection efficiency ϵ_γ is described as the

Nuclide	Produced fragments at F4	Implanted fragments
^{204}Au	12780	10628
^{204}Pt	27824	16168
^{203}Pt	32928	20678
^{202}Ir	7709	5189
^{201}Ir	23662	17245
^{200}Ir	15117	4792
^{200}Os	1552	968
^{199}Os	6541	2669
^{198}Os	10799	802
^{197}Re	1339	489

Table 1.3: Implanted nuclei in the present work. The production yields at F4 and the corresponding number of implanted fragments are shown.

number of γ-rays detected in the photopeak N_γ^{ph} divided by the number of γ-rays emitted by the source N_γ^s

$$\epsilon_\gamma = \frac{N_\gamma^{ph}}{N_\gamma^s} \tag{1.26}$$

Finally, the peak-to-total ratio PT is given by

$$PT = \frac{N_\gamma^{ph}}{N_\gamma^{tot}} \tag{1.27}$$

where N_γ^{tot} stands for the total number of γ-rays detected. During this specific experiment, the RISING γ-ray array performance was evaluated using radioactive sources before and after the measurements.

Along the subsequent sections we will describe the technical details and the performance of this high-granularity, high-efficiency spectrometer.

Technical details of the RISING γ-ray array

The Ge-cluster detectors of the RISING array are arranged in three angular rings of five detectors at angles of 51°, 90° and 129° with respect to

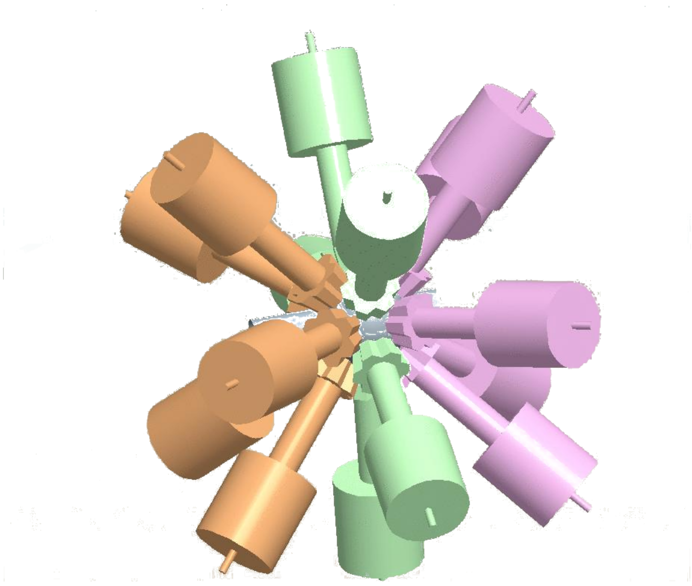

Figure 1.22: Technical drawing of the RISING stopped beam setup. See text for details.

the ion-optical axis of the FRS at distances from the centre of the active stopper of 20 cm for the ring at 90° and 22 cm for the other two rings. This configuration (shown in figure 1.22) enhances the maximum achievable γ-ray efficiency because, on the one hand, the close isotropic geometry surrounding the stopper increases the angular acceptance of the device and, on the other hand, the high granularity of the RISING γ-array minimises the loss of efficiency originated by the so-called "prompt flash" [93]. The prompt flash arises when heavy fragments with energies of several GeV are slowed down in the active stopper. In such cases, the *bremsstrahlung* or atomic radiation produced during the stopping process may induce to fire multiple Ge detectors with the arrival of the nucleus under study. Figure 1.23 shows a two dimensional cluster plot of the γ-ray energy registered in the Ge crystals related to the time sequences between γ-rays and implantations (Isomeric energy-time matrix). The red gate depicted denotes the prompt flash, whose time width profile is shown in the input figure. Notice that the prompt flash is wider at lower energies due to the time walk effect experienced by the low-energy γ-rays that interact in the most outer part of the crystal. The direct consequence is a significant reduction in the efficiency of the array for the measurement of γ-ray decays of isomeric states in a given event. Typical mean flash multiplicities for heavy ions (e.g., ^{204}Pt) are around 15 of the 105 individual Ge crystals [50].

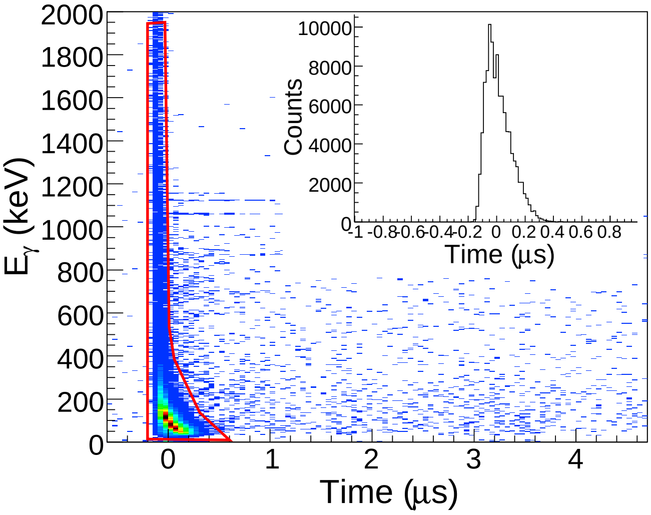

Figure 1.23: Isomeric energy-time matrix of the nuclide ^{204}*Pt. The red line illustrates the prompt flash, whose time width profile is shown in the input figure.*

In order to process the required information about time and energy, two types of electronics were implemented. Each Ge-cluster detector had two parallel pre-amplifier outputs. One was sent to the digital branch, consisting of 30 Digital Gamma Finders (DGF) [94] of 4 channels each that provided the 105 channels for the input signal of each crystal. The DGFs provided information on both time and energy of the γ-ray events. Each DGF channel trigger was validated by a GFLT (General First Level Trigger) provided by either, the plastic scintillator SCI41 for implantations of heavy ions or the active stopper for β-like particle events. The master trigger was sent to the DGFs in order to perform an internal check of the synchronisation of the DGF clocks. Furthermore, the time sequences between ions and γ-rays or β-decays and γ-rays were measured through the DGF γ-time signal. Thereby, it is possible to off-line correlate not only the implanted nuclei with their intrinsic isomeric γ-ray decays, but also the following β-decays with the characteristic γ-rays of the daughter nuclei. The DGF modules had a time resolution of 25 ns, and a maximum coincidence time window of 400 μs. Note that the correlation gate can be off-line adjusted according to the requirements of the spectroscopic measurements. Thus, typical values for isomeric decays range from a few hundred ns (constrained by the flight path of the ions along the FRS and the prompt flash of the RISING array) up to

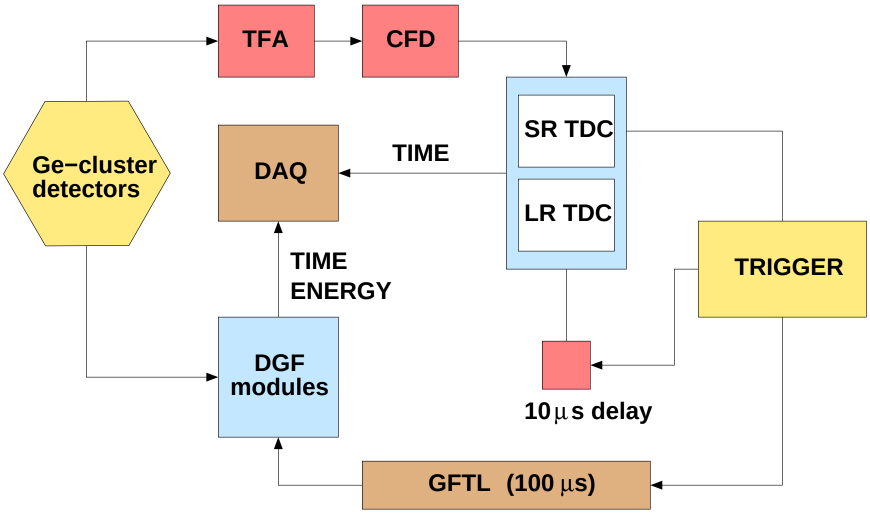

Figure 1.24: Schematic layout of the RISING γ-ray array electronics.

400 μs. Regarding the β-delayed γ-ray spectroscopy, the coincidence window comprises a few hundred ns, since the time elapsed between a β-decay and the subsequent γ-rays is of that order. The shape of the coincidence window is similar to that of the prompt flash for implantations.

The second output from the Ge-cluster pre-amplifier was sent to the analogue timing branch, consisting in an electronic circuit of the type TFA-CFD-TDC. The 105 individual time signals of each Ge crystal were sent to Timing-Filter-Amplifiers (TFA), whose outputs fed Constant-Fraction-Discriminators (CFD). The CFDs sent then the signals to two individual Time-to-Digital-Converter modules (TDC) [95] with 128 channels each. The first module, called the *Short Range* TDC, provided a coincidence gate up to 1 μs with a time resolution of 0.31 ns, thus allowing for precise lifetime measurements of short-lived isomeric states. The second module, called the *Long Range* TDC, had a maximum coincidence window of 800 μs with a time resolution of 0.73 ns, and provided a precise lifetime definition of long-lived isomers.

Both trigger signals (implantations and decays) were delayed 10 μs and sent to the TDCs in order to prevent recording non-sense data in the acquisition. Figure 1.24 shows a schematic layout of the electronics employed to process the γ-ray signals.

Energy calibration

The energy calibration is made with a ^{152}Eu source positioned in the middle of the RISING spectrometer. The nucleus ^{152}Eu has a significant number of well known γ-ray energy transitions [96]. Figure 1.25 shows an energy calibration spectrum for one of the Ge crystals. The nine labelled photopeaks were used to calibrate the array.

Every of the 105 Ge crystals provides an energy spectrum that should be properly calibrated. With this aim, the nine peaks of each spectrum are individually fitted to a Gaussian function. The calibration parameters are obtained from the linear regression between the centroids of the Gaussian fit and the corresponding energies.

The energy resolution is given by the addition of the 105 energy signals, and results in less than 3 keV at 1.3 MeV [50].

Efficiency calibration

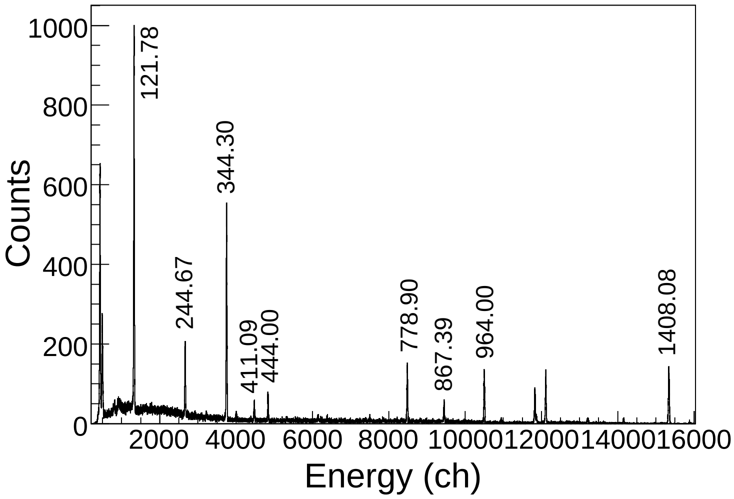

Figure 1.25: γ-ray energy spectrum of ^{152}Eu for one Ge crystal. The labelled photopeaks are used in the energy calibration of the RISING array.

The detection efficiency of γ-rays following either implantation or β-decay in the active stopper depends on the position and depth of the implantation and on the stopper composition, since thick materials may attenuate the emerging γ-rays. In the present work, the 1 mm thick Si catcher is surrounded by a Pertinax vessel 2 mm thick, corresponding to an Al equivalent for γ-ray transmission of 0.7 mm.

The efficiency calibration was performed at the beginning and the end of the experiment. In both cases we used two different low intensity calibrated γ-sources in order to measure the efficiency of the array at different energies. The first source was made up of ^{133}Ba, whereas the second one was a multi-γ source composed of ^{241}Am, ^{137}Cs and ^{60}Co. The implantation trigger was emulated with a 1 kHz clock, i.e., with a time interval between pulses long enough to avoid dead time problems in the acquisition (such as pile-up of subsequent pulses).

The photopeak efficiency ϵ_γ is given by

$$\epsilon_\gamma = \frac{N_\gamma^{ph}}{N_{event} \cdot A \cdot I_\gamma \cdot T_{DGF}} \tag{1.28}$$

where N_{event} refers to the number of pulse events registered by the acquisition, A stands for the activity of the source (the number of de-excitations per time unit), and I_γ corresponds to the source intensity at the photopeak energy. T_{DGF} is the maximum time width of the electronics, and it is provided by the plateau in the time signal of the DGFs, $T_{DGF} = 7.8 \times 10^{-5}$.

Table 1.4 summarises the different parameters involved in the efficiency calibration for the present experiment: the type of source employed, the photopeak energy, the source activity, the source intensity at the photopeak energy, the number of γ-rays detected in the photopeak and the resulting efficiency of the array.

Once the efficiency of the RISING γ-ray array has been measured at several energies, these points are fitted to a curve which describes the detector efficiency over the entire energy range. The fitting function used in the present work is the following [97]:

$$\epsilon_\gamma = exp\left\{\left[\left(A + Bx + Cx^2\right)^{-G} + \left(D + Ey + Cy^2\right)^{-G}\right]^{-1/G}\right\} \tag{1.29}$$

where

$$x = log\left(\frac{E_\gamma}{100}\right), y = log\left(\frac{E_\gamma}{1000}\right) \tag{1.30}$$

The fitting parameters of the calibration are labelled A through G. A, B and C describe the efficiency at low energies, whereas D, E and F describe it at high energies. G is an interaction parameter between the two regions. If G is large, the turnover between the two curves will be sharper. If the efficiency turns over with moderation, G will be small. E_γ is the γ-ray energy in keV.

Source	E_γ (keV)	A (s^{-1})	I_γ (%)	Photopeak events	ϵ_γ (%)
^{241}Am	59.5	3336.27	36	335670	31.3 ± 0.9
^{133}Ba	81	10485.96	34	1231975	38.7 ± 0.7
^{133}Ba	276.4	10485.96	7	182858	27.9 ± 1.1
^{133}Ba	303	10485.96	18	443241	26.3 ± 0.6
^{133}Ba	356	10485.96	62	1393205	24.0 ± 0.5
^{133}Ba	383.8	10485.96	9	195498	23.2 ± 0.8
^{137}Cs	661.66	2313.65	85	277445	15.8 ± 0.4
^{60}Co	1173.23	762.74	100	72873	10.7 ± 0.4
^{60}Co	1332.49	762.74	100	67424	9.9 ± 0.4

Table 1.4: Parameters involved in the efficiency calibration for the present experiment: photopeak energy, source activity, source intensity, number of γ-rays detected in the photopeak and efficiency of the array.

Figure 1.26 shows the corresponding fit for the efficiency calibration performed at the end of the current experiment. The maximum relative deviation from the measured values amounts to 4%. Note that the resulting curve has been obtained after adding back the energies of γ-rays registered simultaneously within the same Ge-cluster.

γ-ray addback corrections

The three interaction mechanisms that play an important role in radiation measurements at γ-ray energies below 10 MeV are photoelectric absorption, Compton scattering and pair production [73]. In these processes the photon either disappears or is scattered through a significant angle, inducing a reduction of the photopeak detection efficiency ϵ_γ.

The configuration of the RISING γ-ray spectrometer contemplates the efficiency losses due to the aforementioned interactions, since the compact geometry of each Ge-cluster (seven Ge crystals inside the same cryostat) allows to consider every cluster as one big Ge volume where it is possible to reconstruct the energy of the incident γ-ray by adding back the individual

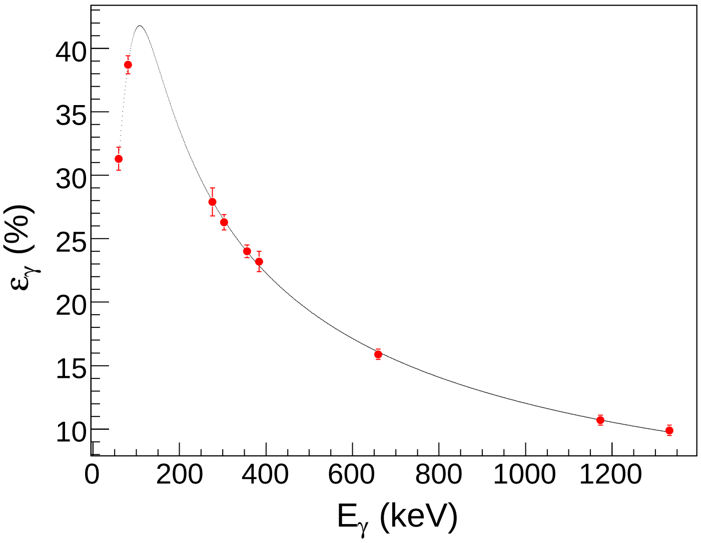

Figure 1.26: Efficiency calibration fit of the RISING spectrometer. The figure shows the range of energies of interest for the present work.

energy signals of the crystals fired within a time interval ranging from 200 ns to 400 ns. This is called the *intra-cluster addback routine*, since it is only performed for low multiplicity γ-rays occurred within the same Ge-cluster.

The addback correction increases the effective photopeak efficiency (see figure 1.26). Note that the high efficiency below 100 keV is due to the absence of absorbers in front of the Ge-cluster detectors.

As an example, figure 1.27 illustrates the γ-ray energy spectrum corresponding to the β-decay of ^{202}Ir to ^{202}Pt. The upper panel displays the spectrum without any addback correction, whereas the lower panel shows the addback-corrected spectrum. The improvement in the performance of the array (efficiency and energy resolution) after applying the intra-cluster addback routine is visible.

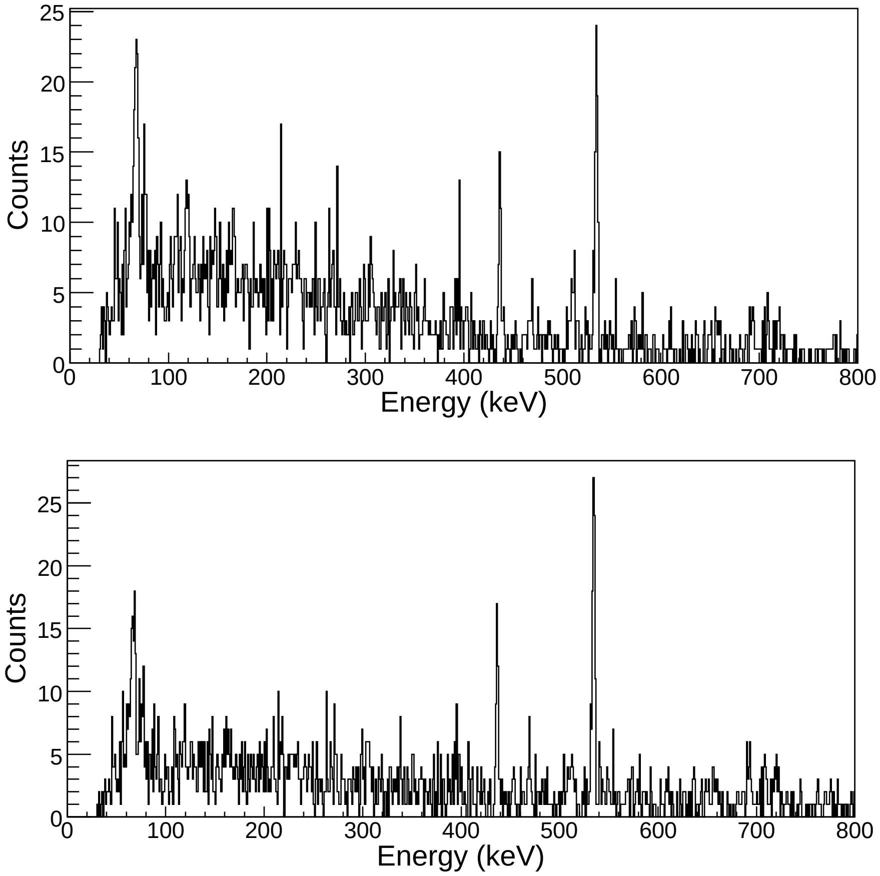

Figure 1.27: γ-ray energy spectra of the β-decay $^{202}Ir \to {}^{202}Pt$. Upper panel: Energy spectrum without addback correction. Lower panel: Energy spectrum with addback correction.

1.7 Trigger logic and Data ACquisition (DAC)

The VME Data ACquisition (DAQ) at the RISING project is based on a single "branch" within the GSI Multi-Branch System (MBS) framework [98]. The different duties are shared between two processors in order to improve the data recording time. The data sender is a RIO-3 processor included in the VME crate. The RIO-3 is in charge of the readout of ADCs, TDCs and other digitisers and eventually sends the data by means of TCP/IP to a data receiver (a PC), which formats the events and controls the disk storage.

In the present experiment, the FRS CAMAC crate and the USER VME crate included in the DAQ were triggered by a GSI Trigger Module [99] which controlled the timing cycle of the hardware readout. Two triggers were defined in order to start the DAQ. The first one (henceforth the *implantation trigger*) was provided by the scintillator SCI41 and allowed to read the experimental devices implicated in the detection of an implantation event (all the FRS detectors, the active stopper, the RISING γ-ray array, etc.). The second one (from now on the *β-decay trigger*) was given by an energy signal above β-threshold in any strip of the active stopper, and read only the Si catcher and the RISING γ-ray spectrometer.

The on-line visualisation of the data was performed with the CRACOW code [100]. It consists of two separate programs connected only by a shared disk: the on-line events analyser (SPY) and the on-line spectra viewer (CRACOW). The high quality on-line data analysis achieved with the CRACOW code allowed to create conditional spectra directly applied to the SPY program.

Chapter 2

Charge-exchange cross sections

The understanding of the single-particle structure in shell closures is of prime importance to study the limits of applicability of the shell model far from stability. Of particular interest is the study of the robustness of the 126-neutron shell closure at decreasing proton number Z due to its implications in the r-process of stellar nucleosynthesis [2, 101]. The β-decay of the N=127 isotones allows to tackle this topic, although their production yields from fragmentation of ^{238}U are very low because of their neutron rich nature. An optional way to synthesise these nuclei is opened up via charge-exchange reactions of a ^{208}Pb primary beam. Hitherto experimental knowledge on the charge-exchange mechanism has been focused on charge-pickup of intermediate [102, 103] and heavy mass isotopes [104, 105].

The measurement of charge-exchange cross sections of heavy neutron-rich nuclei represents a step forward towards the characterisation of this interaction mechanism, showing that it can be alternatively used to produce these nuclei.

In this chapter, we describe the charge-exchange reaction mechanism, we discuss the influence of charge states on the measured yields, and we provide the experimental cross sections, followed by a discussion of the results.

2.1 The charge-exchange process

The charge-exchange processes at relativistic energies may be conveniently described as very peripheral nuclear collisions between projectile and target, classified into a participant-spectator context. Within this picture, the reaction is divided in two separate stages [102]. In the first, faster step, the relativistic projectile collides very peripherally [104, 106] against the target nucleus, such that only the nucleons of projectile and target that overlap in the interaction volume participate in the reaction, whereas the other nucleons of projectile and target continue moving almost undisturbed as observers of the process. At the end of this stage, an excited pre-fragment is formed. In the second, slower stage, the excited pre-fragment decays by fission, evaporation of nucleons or emission of gammas. The mass and number of the resulting fragments will be a competition between the different decay modes.

The charge exchange is materialised within the time interval of the collision, where a sequence of independent two-body nucleon-nucleon interactions take place. It is worth noting that the nucleon-nucleon combinations $(n_p, n_{p'})$ that provide a charge exchange in the resulting pre-fragment are the charge-pickup ($\Delta Z = +1$) and the charge-stripping ($\Delta Z = -1$), henceforth referred to as (ν,π) and (π,ν), respectively.

There are two mechanisms responsible for the modification of the nuclear charge of the projectile [18]. The first one is a quasielastic isospin-exchange collision between a projectile nucleon n_p and a target nucleon n_t where n_p receives the total kinetic energy of n_t ending up in the phase volume of the projectile pre-fragment. We assume that the dominant quasielastic processes are

$$n_p + n_t \longrightarrow n_{p'} + n_t + \pi^{\pm} \tag{2.1}$$

$$n_p + n_t \longrightarrow n_{p'} + n_t + \rho^{\pm} \tag{2.2}$$

Where $n_{p'}$ is the corresponding projectile pre-fragment nucleon and $\pi^{\pm}$, $\rho^{\pm}$ are the virtual pion and rho mesons as a function of their charge. Notice that, at the energies relevant in this experiment, the exchange of a virtual pion is the most probable process. The second process responsible for the charge-exchange interaction is an inelastic isospin-exchange collision in which a nucleon from either the target or the projectile is excited into the $\Delta(1232)$-resonance state by the exchange of a virtual pion between both nuclei

$$n_p + n_t \longrightarrow n_{p',t'} + \Delta \tag{2.3}$$

Subsequently, the $\Delta(1232)$ resonance decays emitting a real pion

$$\Delta \longrightarrow n_{t',p'} + \pi^{\pm} \tag{2.4}$$

where the subscripts p', t' refer to the final projectile and target pre-fragments, respectively. The pion may escape from the nucleus or may be absorbed in the nuclear surface.

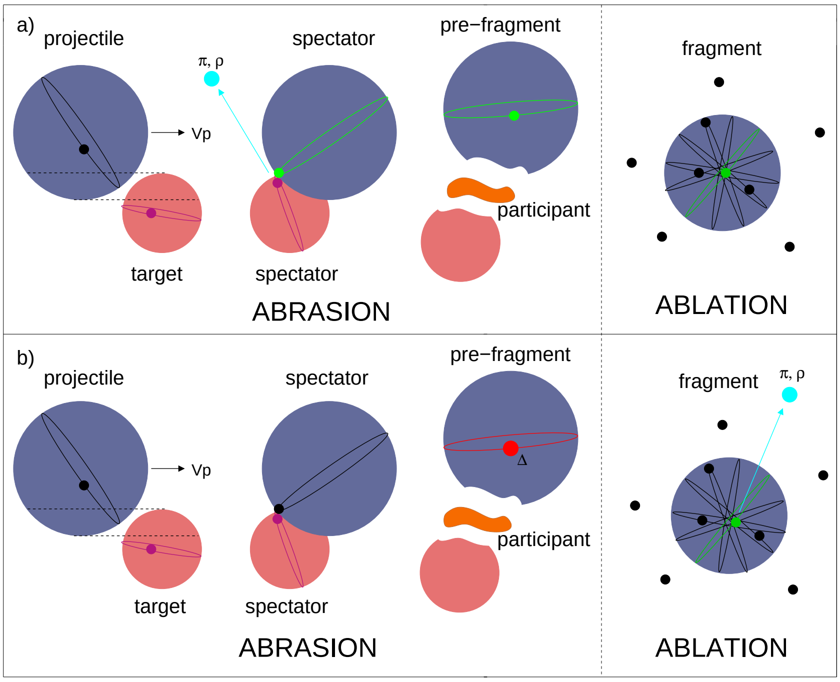
a)
projectile
π, ρ
Vp
spectator
pre−fragment
participant
target
spectator
ABRASION
fragment
ABLATION
b)
projectile
Vp
spectator
pre−fragment
Δ
participant
target
spectator
ABRASION
fragment
π, ρ
ABLATION

Figure 2.1: Schematic representation of the two charge-exchange reaction mechanisms. a) quasielastic isospin-exchange scattering. b) inelastic isospin-exchange scattering.

We have measured the cross sections of nuclei with one neutron more than the projectile nucleus. This allows to identify unambiguously the charge-exchange reaction. Indeed, the isospin-exchange is only observable if the pion generated after the Δ decay readily escapes from the nuclear surface, otherwise the net charge of the nucleus would not change. Moreover, if the pion were reabsorbed by the nucleus, the excitation energy of the pre-fragment would be high enough to exceed the neutron evaporation threshold and we would not be able to separate the fragments produced by charge-exchange from those produced by fragmentation reactions. Figure 2.1 shows an schematic view of the two charge-exchange reaction mechanisms described above.

2.2 Identification procedure

In this specific experiment, the observation of charge-exchange reactions becomes a difficult task due to the production of charge state contaminants as the ions cross thelayers of matter of the FRS. Let us define the fragment of interest by means of its mass and atomic number (A, Z). The hydrogen-like charge states that traverse the FRS with an A/Q ratio similar to that of the ion under study and cross the MUSIC chambers with an atomic charge Q equal to its atomic number Z collapse into the identification cluster of the studied fragment. Then, there are two contributions that contaminate the production rates. On the one hand, the ion $(A\text{-}3, Z)$ that traverses the FRS with $Q_{eff}=Z\text{-}1$ and losses the electron in one of the MUSIC chambers. On the other hand, the ion $(A, Z+1)$ that traverses the FRS with $Q_{eff}=Z$ and keeps the electron throughout the MUSIC detectors.

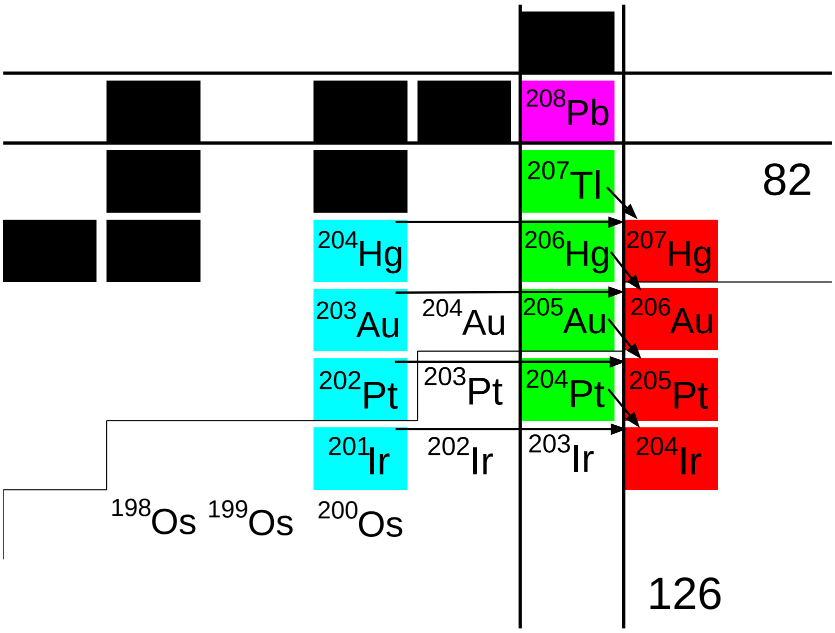

Figure 2.2: Region of the Segrè chart covered by the FRS setting optimised to transmit ^{206}*Au. The red boxes indicate the nuclei produced by a single* (π,ν) *charge-exchange reaction, whereas the blue and green boxes illustrate the corresponding charge state contaminants* $(A-3, Z)$ *and* $(A, Z+1)$*, respectively.*

To provide further insight into this question, we will show a practical example. In the current experiment we tuned a magnetic FRS setting optimised to transmit the heavy neutron-rich ion $^{206}\mathrm{Au}_{79}^{127}$. This nuclide has three proton holes out of the projectile nucleus $^{208}\mathrm{Pb}_{82}^{126}$, but one neutron over the magic number. Therefore, it can be only produced by a (π,ν) charge-exchange interaction ocurred in the first stage of the collision. The charge state contaminants of this nucleus are ^{203}Au (with an electron along the FRS lost subsequently in one of the MUSIC chambers) and ^{206}Hg (with an electron through the FRS kept in both MUSICs). The red boxes in figure 2.2 show the nuclei produced via the charge-exchange mechanism in the present experiment, with 2 → 5 proton holes relative to the ^{208}Pb core. Note that all of them are N=127 isotones. The blue boxes illustrate the charge state contaminants $(A\text{-}3, Z)$, whereas the green boxes denote the $(A, Z{+}1)$ contaminants.

The expected rates of each contaminant nucleus are calculated as the product between its fragmentation yields and the survival probability of the correspondent charge state configuration along the beam line. In this work, the code GLOBAL [107] has been used to calculate the production probabilities of the charge state contaminants after the target, the intermediate and final image planes, and the two MUSIC chambers. The percentage of contamination introduced by these hydrogen-like nuclei in the cross sections of the N=127 isotones is determined as the ratio between the expected production of contaminants and the yields of the N=127 nuclei. Table 2.1 summarises the probability of having those contaminants after the target, the central focal plane $F2$, the final focal plane $F4$ and both MUSIC chambers. P_{tot} denotes the survival probability of the charge state contaminants, and P. Cont. is the percentage of contamination in the measured cross sections. Looking at the table, one concludes that the production rates of N=127 isotones exceed by far the yields of hydrogen-like contaminants for proton numbers over 78, thus confirming unambiguously their production through (p,n) charge-exchange reactions.

Figure 2.3 shows the charge state distributions and mass identification matrices for the setting centred in ^{206}Au, exclusively performed to measure the single (π,ν) charge-exchange cross sections of nuclei with N=127. The procedure used to identify the nuclei of interest is described in detail in sections 1.4 and 1.5. The clear separation between the charge state distributions allows to disentangle the (1e-1e) charge state nuclei from the fully-stripped residues with an accuracy better than 8%.

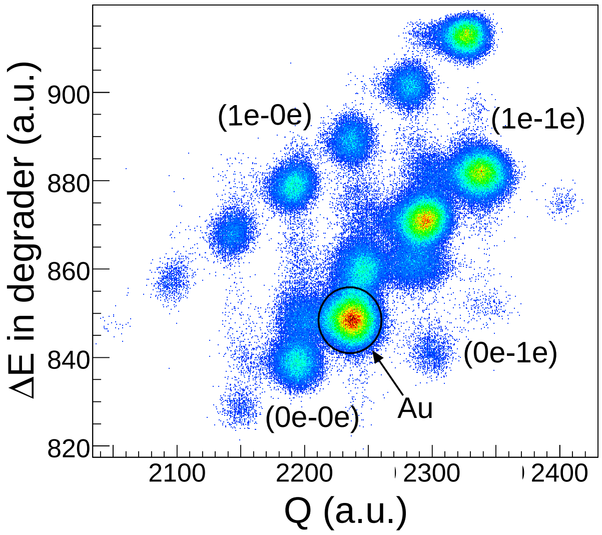

(a) *Charge state distributions matrix. Each labelled set of clusters corresponds to a different charge state configuration along the FRS.*

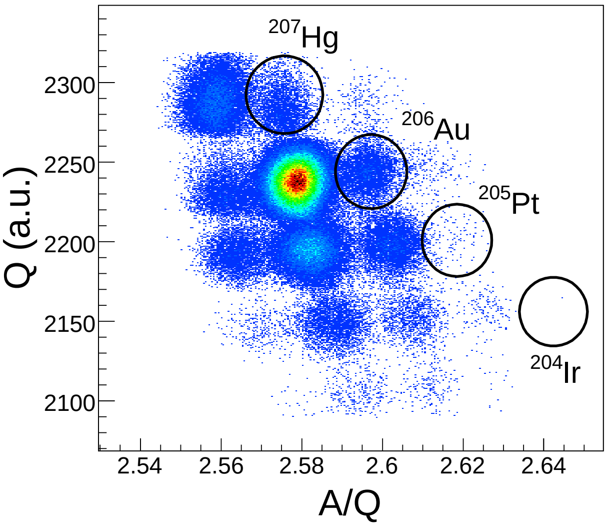

(b) *Mass identification matrix. The high isotopic resolution achieved is shown by the clear separation between clusters.*

Figure 2.3: Matrices of a) the charge state distributions along the FRS, and b) the mass identification. The corresponding magnetic setting is optimised to transmit ^{206}Au, and it has been specifically performed to measure the single (π,ν) charge-exchange cross sections of nuclei with $N = 127$.

(1e-1e-1e-1e)							
Cont.	P_t	P_{F2}	P_{F4}	P_{MUS41}	P_{MUS42}	P_{tot}	P. Cont.
^{207}Tl	0.08625	0.26192	0.06000	0.31686	0.34107	1.46e-4	3
^{206}Hg	0.08054	0.24079	0.05523	0.29505	0.31762	1.00e-4	3.5
^{205}Au	0.07509	0.22076	0.05083	0.27377	0.29462	6.81e-5	12
^{204}Pt	0.06992	0.20188	0.04678	0.25320	0.27228	4.55e-5	13
(1e-1e-0e-0e)							
Cont.	P_t	P_{F2}	P_{F4}	P_{MUS41}	P_{MUS42}	P_{tot}	P. Cont.
^{204}Hg	0.08070	0.24543	0.05634	0.66806	0.63750	4.76e-4	1
^{203}Au	0.07524	0.22498	0.05182	0.69536	0.66807	4.07e-4	2
^{202}Pt	0.07006	0.20570	0.04766	0.72103	0.69676	3.45e-4	5
^{201}Ir	0.06513	0.18761	0.04383	0.74508	0.72358	2.89e-4	26

Table 2.1: Charge state contaminants of the fragments produced by charge-exchange interactions. See text for details.

2.3 Measured cross sections

The charge-exchange production cross sections are given by

$$\sigma(A,Z) = \frac{N_F}{N_P \cdot N_T} \tag{2.5}$$

where N_F denotes the production rate of the selected isotope at the final focal plane $F4$, N_P refers to the total number of impinging projectiles, and N_T denotes the number of atoms in the target per unit area. N_T is determined from the relation

$$N_T = \frac{N_0 \cdot T}{A_T} \tag{2.6}$$

where N_0 is the Avogadro's number, T is the target thickness with dimensions of mg/cm^2, and A_T is the mass number of the target. At first sight, formula 2.5 seems to provide in a straightforward manner the charge-exchange production cross sections. Nevertheless, N_F must be corrected in order to deduce the real number of nuclei produced in the target, since both the analysis procedure and the experimental setup distort the measured yields. For instance, the restrictions in the isotopic identification reduce the number of measured events. Furthermore, the attenuation flux of the residues in each layer of matter of the separator, as well as the dead-time of the acquisition, the transmission through the FRS and the generation of ionic charge-states contribute to decrease the number of measured ions at $F4$.

The beam monitor SEETRAM is normally used to measure the yield of impinging projectiles N_p. During this experiment, the signal from the SEETRAM was off, thus preventing us from obtaining an experimental value of N_p. Fortunately, the fragmentation cross sections of several residues were previously measured in an experiment with analogous conditions [19], and the charge-exchange production cross sections have been normalised to the previously known cross section of ^{202}Ir, a nuclide that reaches the $S4$ region with a transmission of 100%.

2.3.1 Yield corrections

In order to obtain the real number of fragments produced in the target, the measured yields must be corrected by beam attenuation, dead-time, transmission, secondary reactions and ionic charge states.

Due to the particular circumstances of the current experiment, we considered the correction of dead-time included within the cross section taken as reference, $\sigma(^{202}Ir)$ [19]. The corrections due to beam attenuation, secondary nuclear reactions and charge state exchanges produced in the different materials placed along the beam line were calculated for each nucleus, using the program *Amadeus*. The error of the corrections of beam attenuation and secondary reactions amounts to 10% [108], whereas the uncertainty introduced by the correction of ionic charge states amounts to 5% [19].

The separator is limited in momentum and angular acceptance by ± 1.5 % and ± 15 mrad. The typical angular distribution of the forwarded ions is below 5 mrad. Thus, the transmission of the secondary products is near 100% except for those nuclides with positions close to the edges of the focal planes. In this cases, the position distributions of the fragments in the central and final focal planes are fitted to a gaussian function. The transmission correction factor f_t is obtained from the ratio between the number of measured events in the focal plane $N_{F2,F4}$ and the number of events encompassed within the area of the gaussian function N_{gauss}

$$f_t = \frac{N_{F2,F4}}{N_{gauss}} \tag{2.7}$$

The uncertainty for the transmission correction factor is below 20% [19].

The contribution to the measured yields from the charge state distributions of other nuclear species was given in the previous section, where table

Nuclide	σ (mb)	$\Delta\sigma$ (mb)
^{207}Hg	0.11×10^{-1}	0.05×10^{-1}
^{206}Au	0.36×10^{-3}	0.12×10^{-3}
^{205}Pt	0.57×10^{-5}	0.18×10^{-5}
^{204}Ir	0.19×10^{-6}	0.16×10^{-6}

Table 2.2: Single (π,ν) charge-exchange cross sections of the N=127 isotones synthesised for the first time in this experiment.

2.1 shows an associated uncertainty between $[1, 26]\%$, depending on the contaminant.

2.3.2 Experimental results

We have measured the charge-exchange production cross sections of ^{207}Hg, ^{206}Au, ^{205}Pt and ^{204}Ir, four isotones from the 127-neutron shell unambiguously produced by a single (π,ν) charge-exchange interaction. This is the first time that these nuclei are synthesized through this mechanism.

Table 2.2 summarises the charge-exchange cross sections of the N=127 isotones. The last column shows the corresponding absolute errors, which are calculated as the quadratic sum of the statistical and the systematic uncertainties. The statistical errors are determined by the width of the Poisson distribution $\sqrt{N}$ of the number of ions detected at $F4$, whereas the systematic uncertainties embody the errors related to the yield corrections and the cross section of reference.

2.3.3 Discussion of results

The production of nuclei beyond the current limits of experimental synthesis is a leading subject for nuclear physicists, providing unique opportunities to investigate the properties of exotic nuclei at extreme conditions of temperature and angular momentum, and also the nuclear reactions that occurr in the astrophysical processes that lead to the formation of the heaviest elements in the Universe [2].

The exploration of the nuclear chart in the neutron-rich region around N=126 will shed more light on the evolution of shell closures in heavy many-body systems. It has been shown that the robustness of the N=20, N=28 shell closures weakens towards the neutron-drip line [109, 110]. There are also indications of the weakening of the N=50 shell gap as the proton number decreases [111, 112]. In the case of the N=82 closed shell, the appearance of the shell quenching phenomenon for neutron-drip line nuclei is still a matter of debate [113–115]. The exploration of the neutron-rich N=126 isotones is also important for the r-process modeling in the region of the third peak of elemental abundance distribution. Indeed, the properties of nuclei at the waiting-point A≈195 determine the flow of matter to heavier fissioning r-process nuclei [101].

Hitherto, the attempts to synthesise the challenging N=126 neutron-rich nuclei were centred on the use of fragmentation reactions of ^{208}Pb and ^{238}U [19, 116]. As it has been shown, this work investigates an optional reaction mechanism to explore the interesting neutron-rich region around N=126, taking advantage of relativistic (π,ν) charge-exchange reactions of relativistic ^{208}Pb projectiles.

Figure 2.4 shows the evolution of the measured charge-exchange cross sections for the four N=127 isotones (dots) as a function of the number of protons removed from the primary beam, ^{208}Pb. The figure also shows the cross sections of the analogous N=126 isotones (triangles) synthesised by cold fragmentation of ^{208}Pb [19]. The cross sections of the N=127 nuclei produced by fragmentation of ^{238}U have been simulated with the code COFRA [17] (solid line) for comparison. We have also simulated the fragmentation cross sections of the N=126 isotones from ^{208}Pb beams (dashed line). In this last case, the perfect agreement with the measured data illustrates the predictive power of this code. The square refers to the only cross section measured from fragmentation of ^{238}U, corresponding to ^{205}Pt [116].

Perusal of figure 2.4 shows that the production yields of the N=127 isotones have the same slope than the cross sections of the N=126 isotones. This indicates that the proton removal channels dominate the trend followed by the measured charge-exchange cross sections. Indeed, the constant ratio

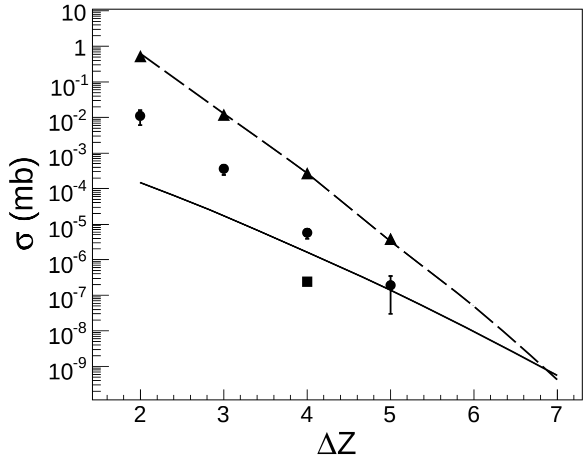

Figure 2.4: Production cross sections as a function of the number of protons removed from the projectile ^{208}*Pb. See text for details.*

between the measured charge-exchange yields and the fragmentation yields of the analogous proton removal channel is expected, since the charge-exchange mechanism takes place at very peripheral nuclear collisions between projectile and target and, in the case of the inelastic channel, the isospin-exchange can be only detected if the pion escapes from the nuclear surface, being less likely to occur than the abrasion of a proton.

We also learn from the figure that the (π,ν) charge exchange of lead beams is the optimal mechanism to synthesise the N=127 isotones with proton number larger or equal than 78, whereas for smaller Z the fragmentation of ^{238}U (solid line) is a more appropriate mechanism of production.

Chapter 3

γ-ray spectroscopy

Nuclei on the "south-west" part of Pb are of considerable interest because of their location in a transition region between spherical shape near the Z=82, N=126 shell closures to strong prolate deformation around the valence maximum nucleus ^{170}Dy. Different theoretical models have been developed to describe these nuclei [27, 117–120], although scarce experimental information on them is available. One of the purposes of this work is to determine the low-lying structure of some nuclei with a few neutron- and proton-holes relatives to ^{208}Pb through *β-delayed γ-ray spectroscopy*. In order to acquire a better understanding of the evolution of the single-particle states as nuclei move away from the Z=82, N=126 magic numbers, a systematic comparison with shell model calculations has been performed.

Figure 3.1 shows the nuclei produced in this experiment. Previous information on their structural properties can be found in data bases as ENSDF [121] and NUDAT [122]. The red-labelled nuclei correspond to the fragmentation residues implanted in the active stopper. Their internal structure can be investigated using isomeric spectroscopy. The green-labelled nuclei correspond to the β-decay products of the fragmentation residues, and their low-lying structure can be explored through β-delayed γ-ray spectroscopy. The blue and yellow boxes denote the grand-daughter and grand-grand-daughter nuclei of the implanted residues. Eventually, the ^{208}Pb projectile isotope is shown in a magenta box.

In this chapter we describe the spectroscopic analysis performed, and the corresponding results are shown. The interpretation of the experimental excited states in terms of the shell model is also discussed.

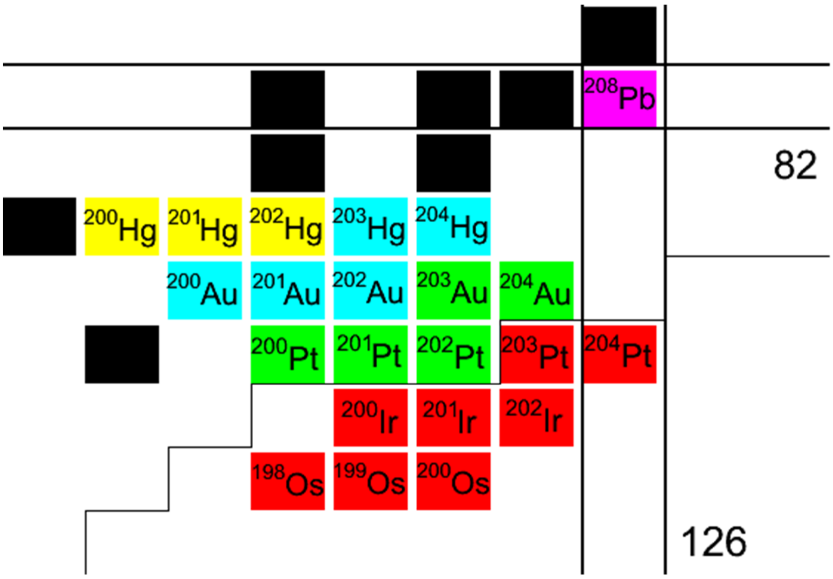

Figure 3.1: Region of the chart of nuclei analysed in the present work through both isomeric and β-delayed γ-ray spectroscopic studies.

3.1 Isomeric spectroscopy

An isomeric state is defined as that whose half life is long compared to the half life of the neighbour states. As the typical lifetime of a nuclear state is within the range of the *ps*, the states with longer decay times are considered isomeric states. Isomeric transitions take place when the wave functions of the initial and final states present a great difference between them.

3.1.1 Analysis technique

The isomeric decays are detected correlating the implantation of an identified nucleus with the γ-rays registered from 0 to 400 μs after the implantation. Since the fragment implantation rates in the active stopper are larger (of the order of a few seconds), we can unambiguously relate these transitions to a particular nuclear specie. Indeed, the isomeric spectra are free of the characteristic transitions of neighbouring nuclei due to the instantaneous character of the correlations between fragments and γ-ray decays.

The challenge of the isomeric analysis is the "prompt flash" - shown in figure 1.23- originated when heavy fragments with energies of several GeV are halted in the active stopper. Several issues minimise this effect, as the high granularity of the RISING γ-ray array or the enhancement of the detection efficiency with the *intra-cluster addback routine*. In addition to this, only the events registered after the prompt flash are selected. By this way, a high amount of background contamination is suppressed.

The time duration of the prompt flash (shown in figure 1.23), together with the typical flight time of the FRS ($\sim$ 300 ns) provide information on the minimum isomeric lifetime measurable with the present experimental setup. In addition to this, the maximum time interval recordable with the DGF electronics ($\sim$ 400 μs) makes the setup sensitive to γ-ray de-excitations from isomeric states with lifetimes encompassed between 300 ns → 1 ms [123]. Furthermore, decays with large internal conversion coefficients are hampered in flight since nuclei are typically fully stripped of electrons [89].

3.1.2 Verification of the isotopic identification

The observation of previously reported isomeric transitions in some of the nuclei under study serves as an internal check of the identification procedure, described in section 1.4. This is the case of the exotic nuclei ^{204,203}Pt. Figure 3.2(a) shows the delayed γ-ray energy spectrum of ^{204}Pt. The isomeric transitions at energies 1123 keV and 872 keV were interpreted as depopulating a (5^-) metastable state at 1995 keV [124, 125]. In the same manner, figure 3.2(b) displays the isomeric decay depopulating a tentative long-lived state at 1104 keV in ^{203}Pt [124]. Both spectra have been corrected in efficiency applying the intra-cluster addback routine to γ-rays with energies over 100 keV. The DGF coincidence time interval between the fragment implantations and the γ-ray decays is 55 μs for ^{204}Pt and 5 μs for ^{203}Pt.

The scarce statistics of the Ir isotopes prevents the identification of their characteristic isomeric transitions. Nevertheless, a wide study of the long-lived structure of these nuclei is reported in ref. [49].

3.2 β-delayed γ-ray spectroscopy

In this work, we have investigated the low-lying structure of the nuclei produced after the β-decay of the implanted fragmentation residues, using β-delayed γ-ray spectroscopy. The single-particle-like excitations of the nuclei of interest, with a few proton- and neutron-holes out of the doubly magic ^{208}Pb core, have been systematically compared with the calculations of the fast nuclear shell model code OXBASH [126], providing valuable information on the onset of collectivity in the transitional region between ^{208}Pb and ^{170}Dy.

In this section we describe the method employed to obtain the low energy level schemes, built from the β-delayed γ-ray energy spectra and the γ-γ

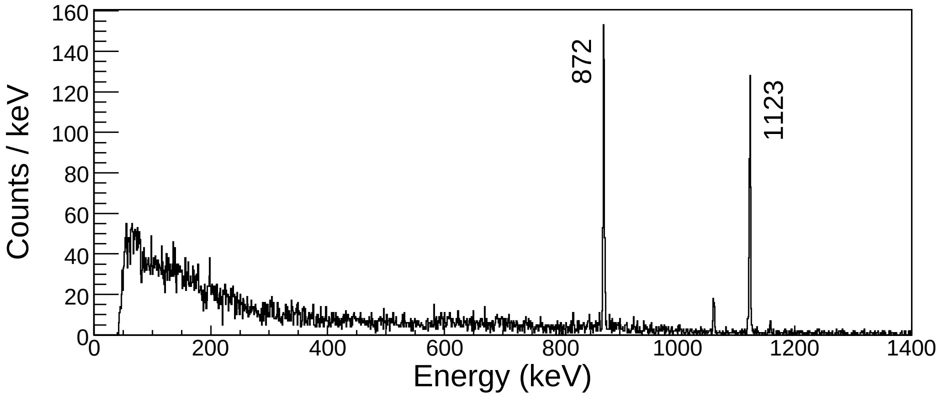

(a)

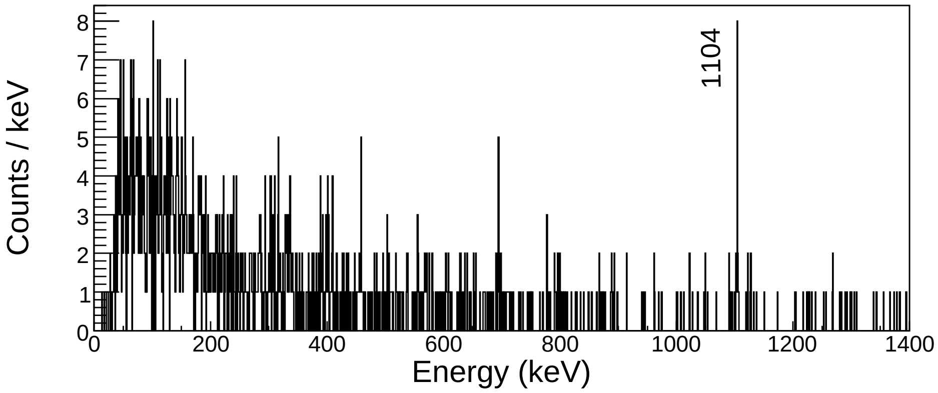

(b)

Figure 3.2: Delayed γ-ray spectra associated to the exotic nuclei ^{204}*Pt (figure 3.2(a)) and* ^{203}*Pt (figure 3.2(b)). The γ-ray de-excitations depopulate the isomeric states observed in refs. [124, 125], thus confirming the isotopic identification.*

coincidence analysis. Eventually, we provide a detailed discussion on the results obtained for each particular nuclide.

3.2.1 Analysis technique

The main goal of the β-delayed γ-ray spectroscopic technique consists in connecting as accurately as possible the electromagnetic transitions following a β-decay with the mother nucleus that originated the β process. In the region of interest, the levels populated in the daughter nuclide exhibit low spin differences with respect to the ground state of the mother nucleus, such that the de-excitation through γ-ray decays usually occurs in a time interval of a few hundred *ps* after the β-decay process. As the time interval of the β process is of the order of *s*, we can consider the emission of a β-electron and the emission of characteristic γ-rays from the daughter nuclide as simultaneous events. The analysis developed to connect the implantations with the proper β-delayed γ-rays, as well as other questions about the β-delayed γ-ray analysis procedure, will be discussed throughout this section.

Ion-β position correlations

The fragments identified at the end of the FRS may undergo secondary reactions with the matter of the devices that conform the β-delayed spectroscopy setup. The analyser should off-line suppress the events corresponding to residues destroyed in the slowing down process. With this aim, an energy signal above threshold was required in the SCI42 front-scintillator and no signal in the SC43 back one. As well, there was required a high-energy signal above ion threshold in an individual pixel (X,Y) of the active stopper, and a proper correlation between the position of the fragment in front of the active stopper (provided by the scintillator SCI42) and the pixel fired in the DSSSD detectors (see figure 3.3). After a particle implantation event (Z,A) and its implantation pixel (X,Y) were fixed by software, the electron emitted following its radioactive decay was identified requiring a low-energy signal above threshold (usually 150 keV) in either the implantation pixel (X,Y) or one of the neighbouring cells (x,y).

Some background events may be induced in the active stopper as a consequence of the multiplicity of the low-energy signals (see figure 3.4). In such a case, the β-decay event pixel (x,y) with maximum energy output compared to its neighbours would be the correlated one.

The technical complexity of the DSSSD detector lies in the wide energy range necessary to identify both, the implanted nucleus and the subsequent β-decay particle, in order to assign an individual pixel position to each. This

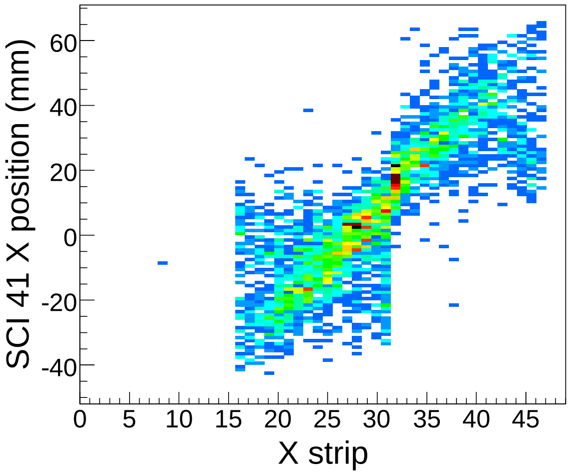

Figure 3.3: Position correlation between the x coordinate in the scintillator located in front of the active stopper and the x strip of the DSSSDs. The selected nuclide is ^{202}Ir.

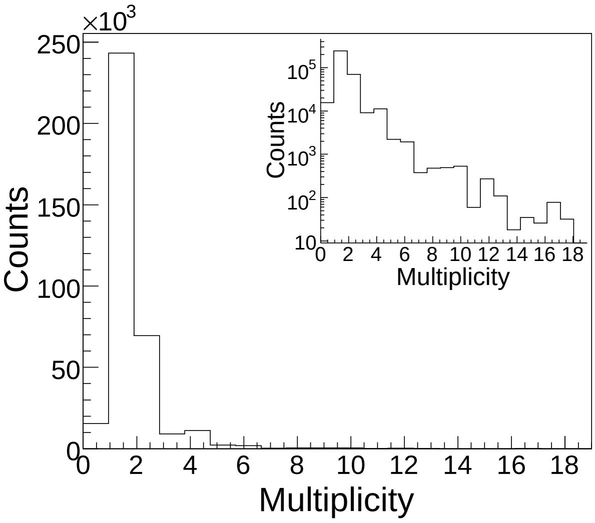

Figure 3.4: Multiplicity of the active stopper for β-like particle triggers in a setting centred in ^{205}Au. The inset shows the graphic in logarithmic scale. Multiplicity 1 indicates that only one pixel (x,y) has been fired with an energy above the β-particle detection threshold, and so on.

issue is overcome by the use of a semi-logarithmic preamplifier, which has a linear response for low-energy signals (β-decay particles) and provides logarithmic amplification for high-energy events (ions) [79]. Thus, the particle implantation data (Z,A) and their individual pixel position (X,Y), the β-decay particle pixel position (x,y), the implantation time and the β-decay particle time were recorded on an event by event basis to further correlate them by software.

Ion-β time correlations

The ^{208}Pb primary beam was delivered with a pulsed time structure consisting of cycles of about 10 s with a typical spill length of 2 s. During the spill time, a huge amount of δ-electrons were generated (see figure 3.5). The presence of such electrons introduces a significant number of background events in the β-delayed γ-ray energy spectrum. This question is addressed by selecting only the β-like particles registered during the beam pause.

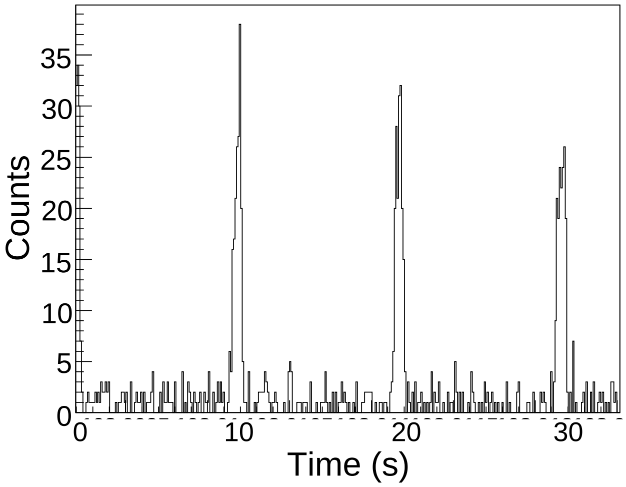

Figure 3.5: Time signal of the β-decay trigger detector. The modulated spill structure is shown up.

The time correlations between fragments and decays can be performed in two different ways. Firstly, one may correlate each fragment implantation with the first β-like particle detected during the beam pause in the same or adjacent pixels within a maximum time interval T. This method assumes that the first electron detected after the implantation belongs to the β-decay of the selected nuclide with a maximum probability. Secondly, one may correlate all the β-like particle events occurred during the beam pause in the same or adjacent pixels within a maximum time interval T. T is defined as the time period in which the probability of the β-decay process to occur is high. An appropriate estimation consists in assigning between 2 to 5 times the expected value of the half life of the nuclide [127].

Contamination in the energy spectrum

In the β-delayed γ-ray energy spectrum of a given nucleus, there are several sources of background contamination that may hamper a proper identification of the characteristic γ-ray decays. The best known is the Compton background, which constitutes a continuum of energies. As we pointed out, the intra-cluster addback routine decreases this effect, at the same time that increases the effective photopeak efficiency. In this work, all the β-delayed energy spectra were addback-corrected using this routine to γ-ray energies over 25 keV.

As we mentioned before, the β-decay of the nuclei under study generally takes place from the ground state to low-spin levels with lifetimes of a few hundred *ps*, such that the characteristic γ-rays of the daughter nucleus are contained in a “prompt coincidence” formed in the energy-time matrix of the β-delayed γ-rays. As the γ-ray events registered after the “prompt coincidence” do not normally contain spectral information, a time window similar to that shown in figure 1.23 is selected in the β-delayed energy-time matrix of each nuclear specie.

The most hazardous sources of contamination are those which may induce to an erroneous assignment of the γ-ray transitions. The time elapsed between a fragment implantation and the subsequent decay may be long if we consider the predictions of some theoretical models [128–131]. Indeed, the half lives measured in the present work, which will be shown in the following chapter, result longer than the time cycle of the primary beam. This means that the total implantation frequency[1] in a given cell is high enough to connect the fragments under study with β-decays from neighbouring nuclei or even from daughter nuclei if they are not stable, giving rise to false ion-β time correlations.

Determination of the β-delayed γ-ray energy spectrum

The β-delayed γ-ray energy spectra are strongly conditioned by the ion-β position and time correlations considered. Let us summarise the types of correlations that can be performed:

---

[1] Here we refer to the frequency between *all* the nuclei implanted in the silicon catcher, independently of their identification data (Z,A).

Position correlations

- ▷ Between fragments and β-decays detected in the same pixel.
- ▷ Between fragments and β-decays detected in the same or adjacent pixels.

Time correlations

- ▷ Between a fragment and the first β-decay detected during the beam pause in a maximum time interval T.
- ▷ Between a fragment and all β-decays detected during the beam pause in a maximum time interval T.

From a statistical point of view, the best selection would be connecting the nuclide under study with all the β-electrons detected during the beam pause in the same or adjacent pixels in a maximum time interval T, encompassing between 2 to 5 times the expected value of the half life of the nucleus. Nevertheless, such an spectrum would be strongly spoilt by the appearance of γ-ray decays of neighbouring nuclei, since the position distributions of the fragments cover the entire x-range of the active stopper, and their β-decay lifetimes are of the order of the time elapsed between implantations. Figure 3.6 shows the transversal x-position of the fragmentation residues in the final image plane and the active stopper for illustration.

In view of the operation conditions of the experiment, the energy spectra were obtained with the following requirements: firstly, the selected fragments were correlated with the first β-decay detected in the implantation pixel (X,Y) during the beam pause. These correlations were performed in the range of X-strips where the implantations of the studied nuclear specie accumulated the higher statistics, according to the position distribution of the ions in the active stopper. The background was then reproduced sorting a new energy spectrum with the reversed time sequence of ion-β correlations in the X-strips where the implantation of contaminants predominated over the rest. These strong limitations lead to a significant reduction of statistics, producing important losses of information on the weakest transitions.

To address this issue, new spectra were sorted correlating the selected fragment to all the β-decay electrons registered in the implantation pixel (X,Y) during the beam pause in a maximum time interval $T = 3T_{1/2}$, being $T_{1/2}$ the half life of each ion measured with the analysis technique described in chapter 4. By this way, the background induced by β-decays arisen in adjacent pixels was excluded, whereas the probability of recording the characteristic transitions of the fragment was enhanced.

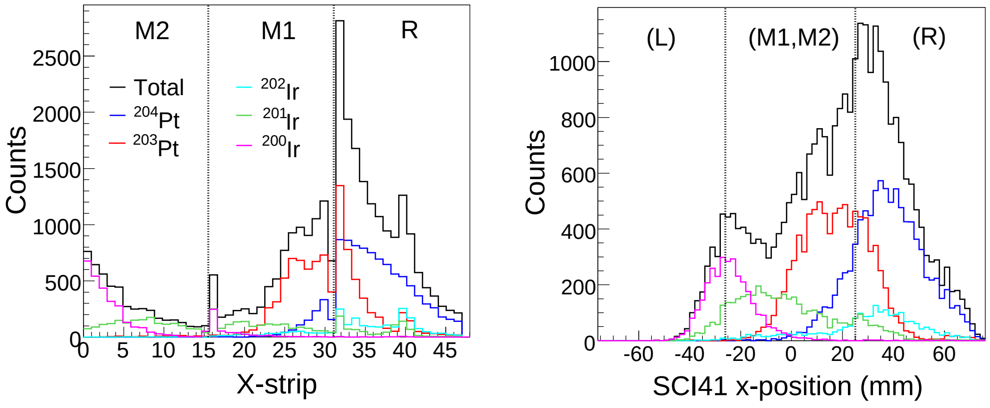

(a) (b)

Figure 3.6: (a) Transversal x-position distribution of the ions in the active stopper. (b) X-position distribution of the fragments in the scintillator SCI41.

Relative intensities and apparent β-feeding

The relative intensity I_γ is defined as the number of γ-rays N_γ^{ph} detected in the photopeak of a given transition divided by the number of γ-rays $N_\gamma^{ph}(ref)$ detected in the photopeak of the transition of reference. Both of them are normalised to the corresponding photopeak efficiency:

$$I_\gamma = \frac{N_\gamma^{ph}/\epsilon_\gamma^{ph}}{N_\gamma^{ph}(ref)/\epsilon_\gamma^{ph}(ref)} \tag{3.1}$$

For each nucleus, the γ-peak with a higher number of counts is taken as the transition of reference. The uncertainty in the relative intensity is determined by the width of the Poisson distribution of the number of counts $\sqrt{N}$ in the photopeaks and the maximum relative deviation of the efficiency calibration fit, which amounts to 4%.

If we observe n states in the configuration of a given nucleus, the apparent β-feeding $I_{\beta,i}$ of the ith state is given by:

$$I_{\beta,i} = \frac{N_i}{\sum_{i=1}^{n} N_i} \tag{3.2}$$

Where N_i is the number of γ-rays depopulating the ith state minus the number of γ-rays feeding it, each of them normalised to its particular photopeak efficiency. The corresponding error is given by the width of the Poisson distribution of the number of counts N_i. Note that the definition of $I_{\beta,i}$ is similar to that of the β-decay branching ratio, so it may provide a qualitative estimation of the β-feeding of each state. Nevertheless, not the ground state or other unobserved states are considered in the calculation of $I_{\beta,i}$.

3.2.2 γ-γ coincidences

The γ-γ coincidence analysis represents an important tool in the investigation of the internal structure of the selected nuclei. This technique is decisive to assign unambiguously the low-intensity γ-ray transitions to a particular nucleus, as well as to determine the ordering of the excited states in the decay diagram.

The off-line γ-γ coincidence analysis performed in the current work does not require the strong restrictions needed to obtain the β-delayed γ-ray energy spectra, since the goal does not lie in relating the observed transitions to a given nucleus, but in finding cascades of coincident γ-rays. With this aim we created a γ-ray energy spectrum corresponding to all the β-decay events detected during the beam pause with an energy signal over 150 keV. The position and time correlations between fragments and decays were suppressed. Appendix D shows this spectrum (henceforth referred to as *total energy spectrum*), which has been "prompt-flash" and addback corrected.

The γ-γ coincidence spectra were obtained gating each γ-ray peak on the total energy spectrum and establishing a coincidence time window of 200 ns between the selected transition and the energy signals detected in the RISING array.

3.3 Results

The low energy structure of the heavy neutron-rich nuclei ^{204,203}Au and ^{202,201,200}Pt has been investigated for the first time following β-decay of ^{204,203}Pt and ^{202,201,200}Ir, respectively. Subsequently, shell model calculations have been used to test the single-particle purity of the observed nuclear states. Along this section, we show and discuss the new results.

3.3.1 β-decay of ^{204}Pt to ^{204}Au

So far, the information on ^{204}Au has been scarce. The Q_{β^-} value and the half life ($T_{1/2}$ = 39.8 ± 0.9 s) have been measured via the reaction ^{204}Hg(n,p)^{204}Au [132, 133] and β-delayed γ-ray spectroscopic measurements

[134, 135], respectively. Additionally, isomeric spectroscopy of this nucleus has been performed [49], finding a metastable state of 2.1 μs.

The γ-ray transitions associated to the internal decay of ^{204}Au are shown in red in figures 3.7 and 3.8. The first graphic displays the energy spectrum with all the ion-β correlations of ^{204}Pt found in the active stopper, within a time interval of $3T_{1/2}$. Black-labelled decays denote background γ-ray transitions. The characteristic decays of the grand-daughter ^{204}Hg [135] appear because the addition of the half lives of ^{204}Pt and ^{204}Au is of the order of the time elapsed between implantations of ^{204}Pt, with $T_{1/2}^{^{204}Pt} + T_{1/2}^{^{204}Au}$=53 s and T_F=42 s (the measurement of $T_{1/2}$ and T_F will be discussed in chapter 4). The peaks at 67, 69 and 77 keV correspond to the kα_1, kα_2 and kβ_1 x-rays of Au, respectively. They appear as a consequence of the internal conversion process undergone by the most inner atomic electrons. The line at 511 keV results from the e^-e^+ annihilation in the Ge-clusters of the RISING array, whereas the other γ-ray transitions belong to the decay of neighbouring implanted nuclei.

Figure 3.8 shows the background-subtracted spectrum, obtained to identify the most intense γ-rays of this nucleus. It corresponds to the ion-β correlations registered in the x-strips placed in the right of the fifth strip of the right DSSSD detector, since in this region of the active stopper the implantation of ^{204}Pt predominates over the other residues (see the position distribution of the ions in figure 3.6). The background has been reproduced correlating each ion to the previous β-decay registered during the pause in the pixel of implantation. Notice that this background is normalised to the number of fragmentation residues implanted in the active stopper instead of to the number of false ion-β correlations. Even so, the good quality of the spectrum shown in figure 3.8 allows to identify unambiguously the peaks at 165, 197, 305, 379, 602 and 694 keV as characteristic γ-rays of ^{204}Au.

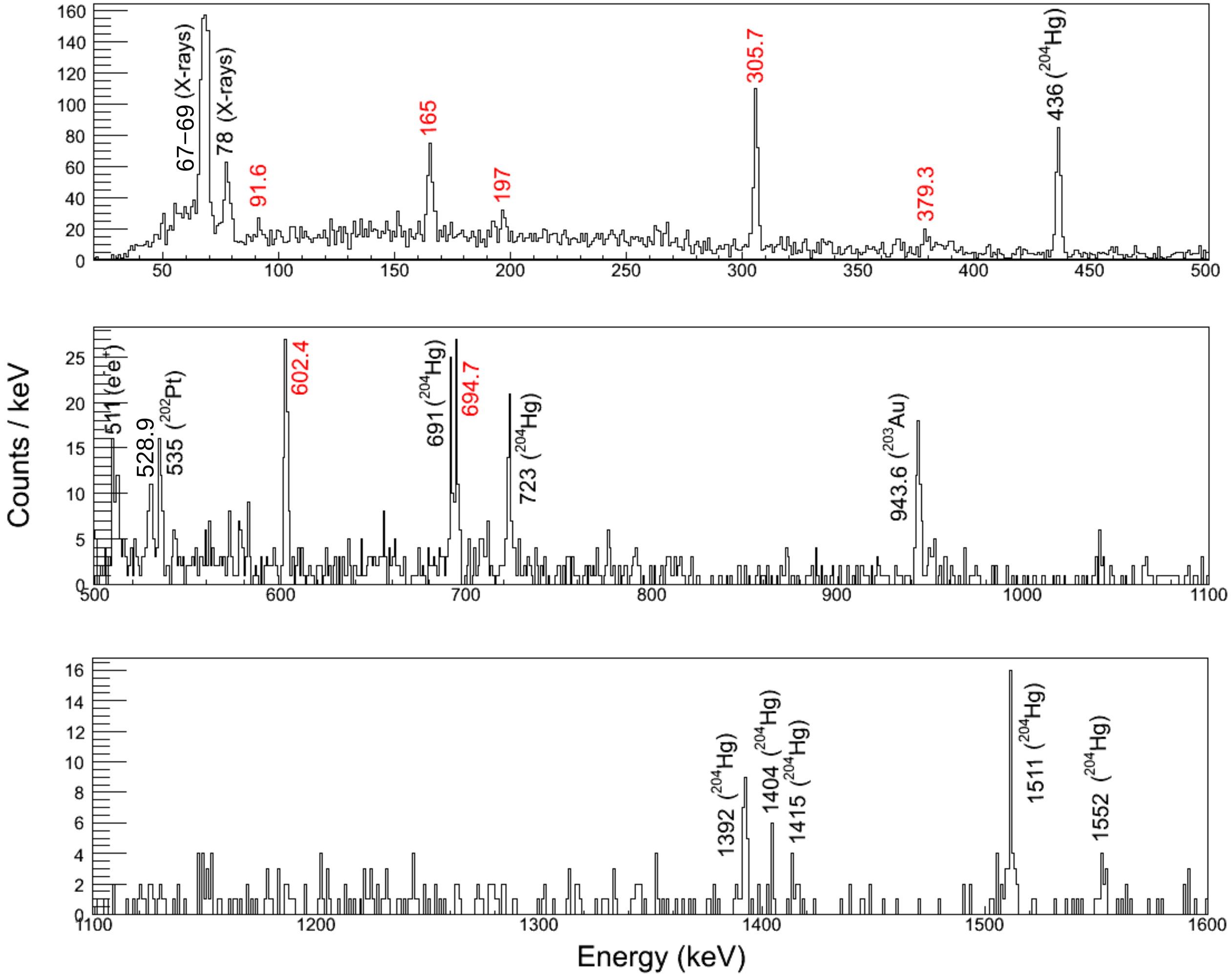

Figure 3.7: β-delayed γ-ray energy spectrum of the decay ^{204}Pt to ^{204}Au. The red-labelled γ-ray transitions are tentatively assigned to the internal decay of ^{204}Au. The black-labelled transitions belong to background contamination. See text for details.

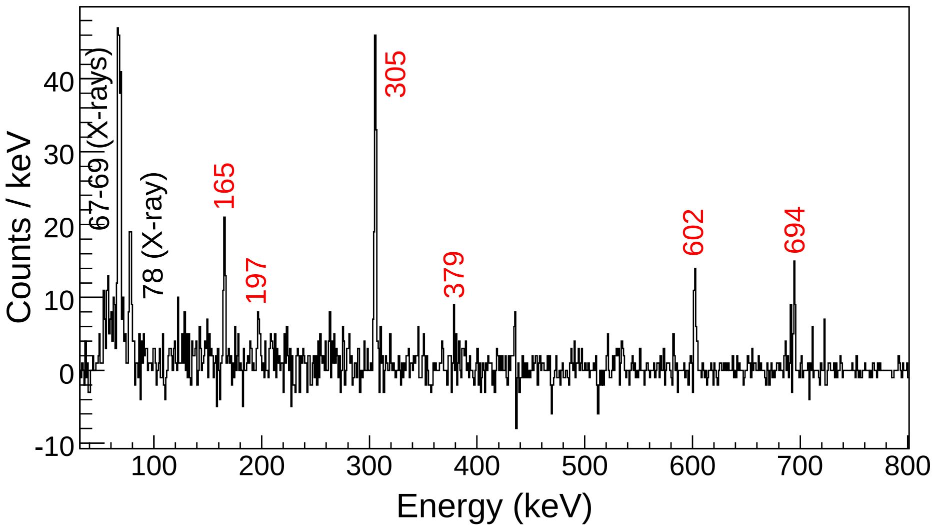

Figure 3.8: Background-subtracted β-delayed γ-ray energy spectrum of the decay ^{204}Pt to ^{204}Au. The red-labelled γ-ray transitions correspond to the internal decay of ^{204}Au. See text for details on the subtraction of background.

The γ-γ coincidence analysis (see figure 3.9) displays three cascades of γ-rays: 165 keV → 305.7 keV, 197 keV → 305.7 keV, and 91.6 keV → 602.4 keV. From the experimental information acquired, the proposed level scheme is shown in the left side of figure 3.10. The seven transitions de-exciting the six proposed low-energy states represent the first spectroscopic information on this N=125 isotone. On the right side of the figure the shell model calculation is shown for comparison, and will be discussed in section 3.4.4. Table 3.1 summarises the parameters associated to the internal decay of ^{204}Au: tentative low-lying states E_s, γ-ray transitions E_γ, relative intensities I_γ and apparent β-feeding of each state I_β with their corresponding uncertainties. Note that the internal conversion coefficient of the tentative M1 decay $(1^-)_4 \rightarrow (2^-)_3$ ($\alpha_{tot} = 9.5(4)$) [136]) has been included in the calculation of the relative intensities and apparent β-feedings.

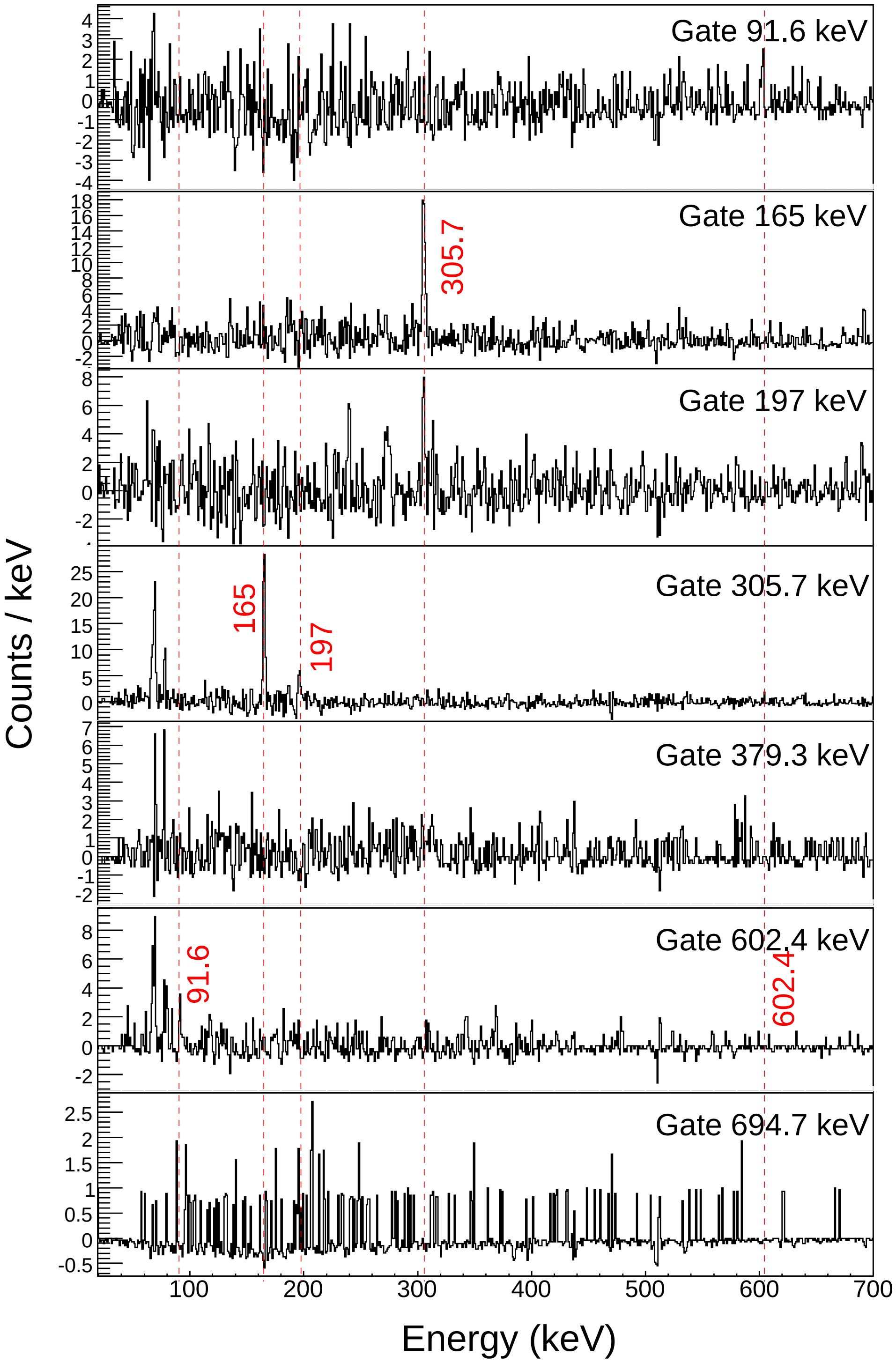

Figure 3.9: γ-γ coincident spectra of the transitions tentatively assigned to the decay of ^{204}Au.

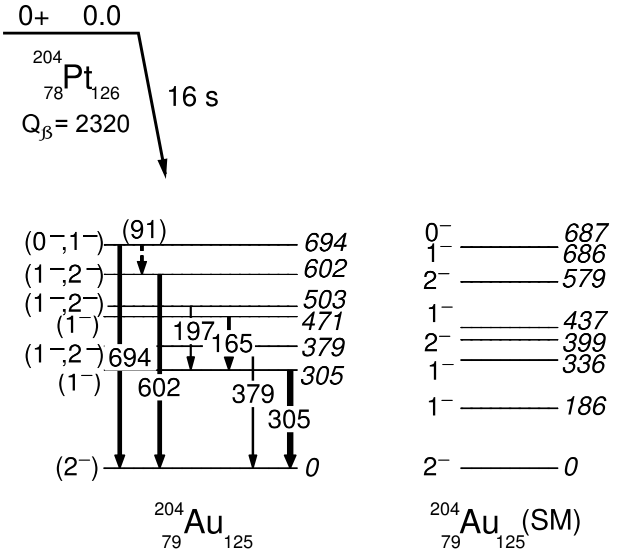
0+ 0.0
204Pt 78 126
Qβ= 2320
16 s
(0⁻,1⁻)
(91)
694
(1⁻,2⁻)
602
(1⁻,2⁻)
503
(1⁻)
471
197
165
(1⁻,2⁻)
694
379
(1⁻)
602
379
305
305
(2⁻)
0
204Au 79 125
0⁻ 687
1⁻ 686
2⁻ 579
1⁻ 437
2⁻ 399
1⁻ 336
1⁻ 186
2⁻ 0
204Au 79 125 (SM)

Figure 3.10: Experimental level scheme of ^{204}Au. For comparison, the shell model approach is also shown. Q_β value taken from [137].

Nuclide	**E$_s$ (keV)**	**E$_\gamma$ (keV)**	**I$_\gamma$(%)**	**I$_\beta$(%)**
^{204}Au	305.7(1.1)	305.7(1.1)	100(8)	17(6)
	379.3(1.9)	379.3(1.9)	18(2)	7.2(1.9)
	471(2)	165(2)	46(4)	19(5)
	503(2)	197.0(1.7)	11.7(1.3)	4.7(1.2)
	602.4(1.9)	602.4(1.9)	65(6)	7(9)
	694(2)	91.6(1.0) 694.7(0.9)	47(18) 63(6)	45(11)

Table 3.1: Energy levels, γ-ray energy transitions, relative intensities and apparent β-feeding associated to the decay ^{204}Pt → ^{204}Au. The parameters related to the 91.6 keV peak have been calculated assuming an M1 character for this low-energy transition (α_{tot} = 9.5(4)).

3.3.2 β-decay of ^{203}Pt to ^{203}Au

Prior to this work, the Q_{β^-} value ($Q_{\beta^-} = 2040 \pm 60$ keV) and half life ($T_{1/2} = 60 \pm 6$ s) of ^{203}Au were measured using deep inelastic transfer reactions between a ^{208}Pb projectile beam and a natural tungsten target [138]. The low-lying structure of this nucleus was also investigated using the proton-removal reactions ^{204}Hg(t,α)^{203}Au [139] and ^{204}Hg(d,^{3}He)^{203}Au [140]. Isomeric spectroscopic studies were also performed [89], confirming the existence of a high spin state at approximately 640 keV already cited in refs. [139, 140].

The current work shows, for the first time, γ-ray energy transitions following the decay ^{203}Pt → ^{203}Au. Figure 3.11 displays the energy spectrum corresponding to all the ion-β correlations of ^{203}Pt found in the active stopper, within a time interval of $3T_{1/2}$. The cocktail of accidental correlations included in the spectrum is manifested through the appearance of decays associated to neighbouring nuclei. The transitions related to the decay of ^{203}Au to ^{203}Hg do not appear in the figure owing to the high branching ratio to the ground state [138].

The identification of the characteristic decays in the forward-time spectrum 3.11 is therefore rather difficult. Furthermore, because of the long half life and high implantation rates of the selected residue, an important amount of backward-time correlations performed in the pixel of implantation accidentally belong to the selected decay, and the usual background-subtracted spectrum is spoilt. To address this challenge, the background has been qualitatively reproduced in the X-strips of the active stopper where the implantation of the contaminants prevailed over the rest. According to the position distributions shown in figure 3.6, if the ion was detected in a pixel of the front central DSSSD, the corresponding background event was selected performing a correlation with the previous β-decay registered in the same pixel of the rear central DSSSD; if the fragment was found in the right DSSSD, the analogous backward-time correlation was performed in the same detector. Figure 3.12 shows the resulting background-subtracted spectrum. Note that the transitions of neighbouring nuclei included in figure 3.11 have been suppressed without losing spectral information on ^{203}Au.

From the γ-γ coincidence spectra, shown in figures 3.13 and 3.14, a new γ-ray decay at 776 keV can be related to the selected nuclei according to the mutual coincidence shown with the 385 keV transition. As well, two weak cascades can be distinguished: 943.6 keV→39 keV and 311 keV→563 keV. The 311 keV decay cannot even be observed in the singles γ-ray spectra. Its role in the single-particle interpretation of ^{203}Au, however, will be discussed in section 3.4.4. The transition at 65 keV, in mutual coincidence with the

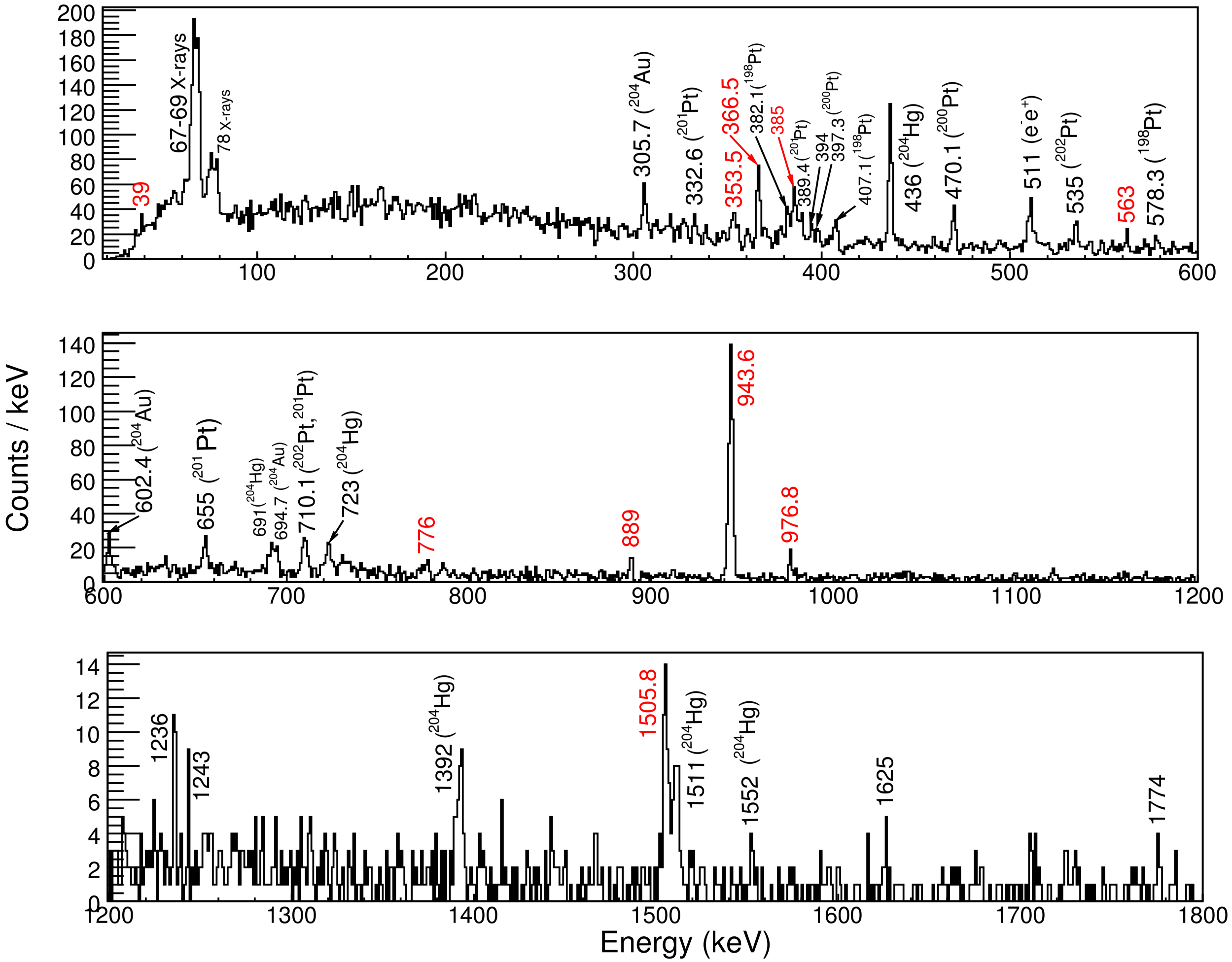

Figure 3.11: β-delayed γ-ray energy spectrum of the decay ^{203}Pt to ^{203}Au. The red-labelled γ-ray transitions are tentatively assigned to the internal decay of ^{203}Au. The black-labelled transitions belong to background contamination. See text for details.

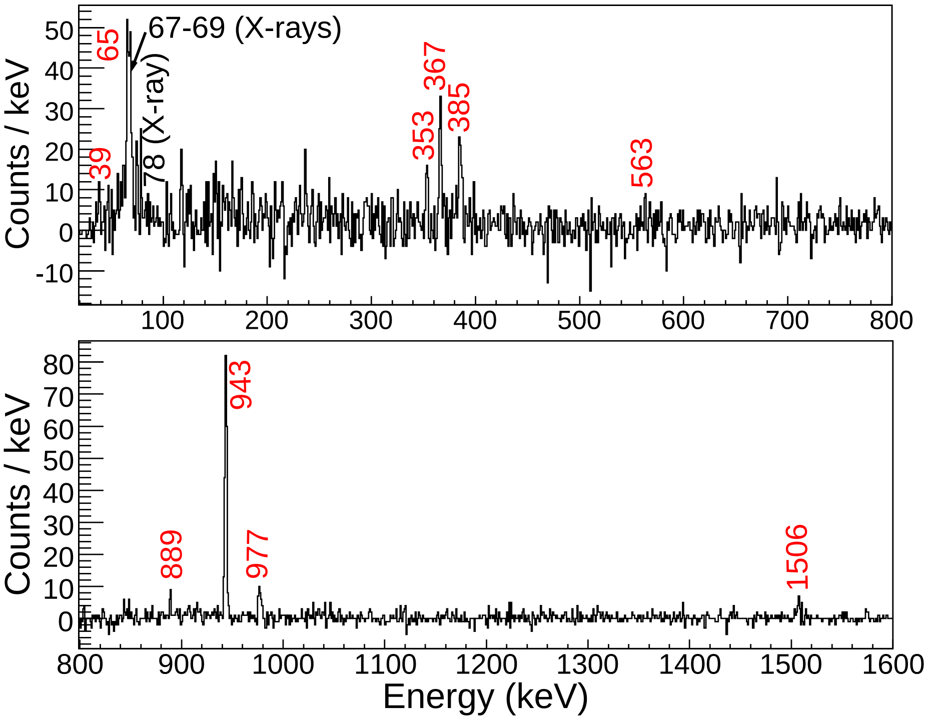

Figure 3.12: Background-subtracted β-delayed γ-ray energy spectrum of the decay ^{203}Pt to ^{203}Au. The red-labelled γ-ray transitions are tentatively assigned to the internal decay of ^{203}Au. See text for details on the subtraction of background.

366.5 keV peak, may be interpreted as an x-ray if one considers its proximity to the kα_1 and kα_2 peaks of Au. This argument is rejected on the basis that, in such a case, all the γ-coincident spectra of ^{203}Au would display this transition.

The experimental level scheme of ^{203}Au is shown in figure 3.15, together with the experimental nuclear states detailed in refs. [139, 140] and the single-particle structure obtained with shell model calculations. The states labelled with an asterisk were previously reported, insofar as ref. [140] provides an overall energy resolution of 30 keV. The reader can observe in the singles energy spectrum 3.11 the high inhibition of the 39 keV peak. Assuming an M1 charcater for this low energy transition, its decay by internal conversion must play an important role, as shown by the calculated conversion coefficient ($\alpha_{tot} = 20.5(3)$ [136]).

Summarising, nine γ-ray transitions have been associated to the decay

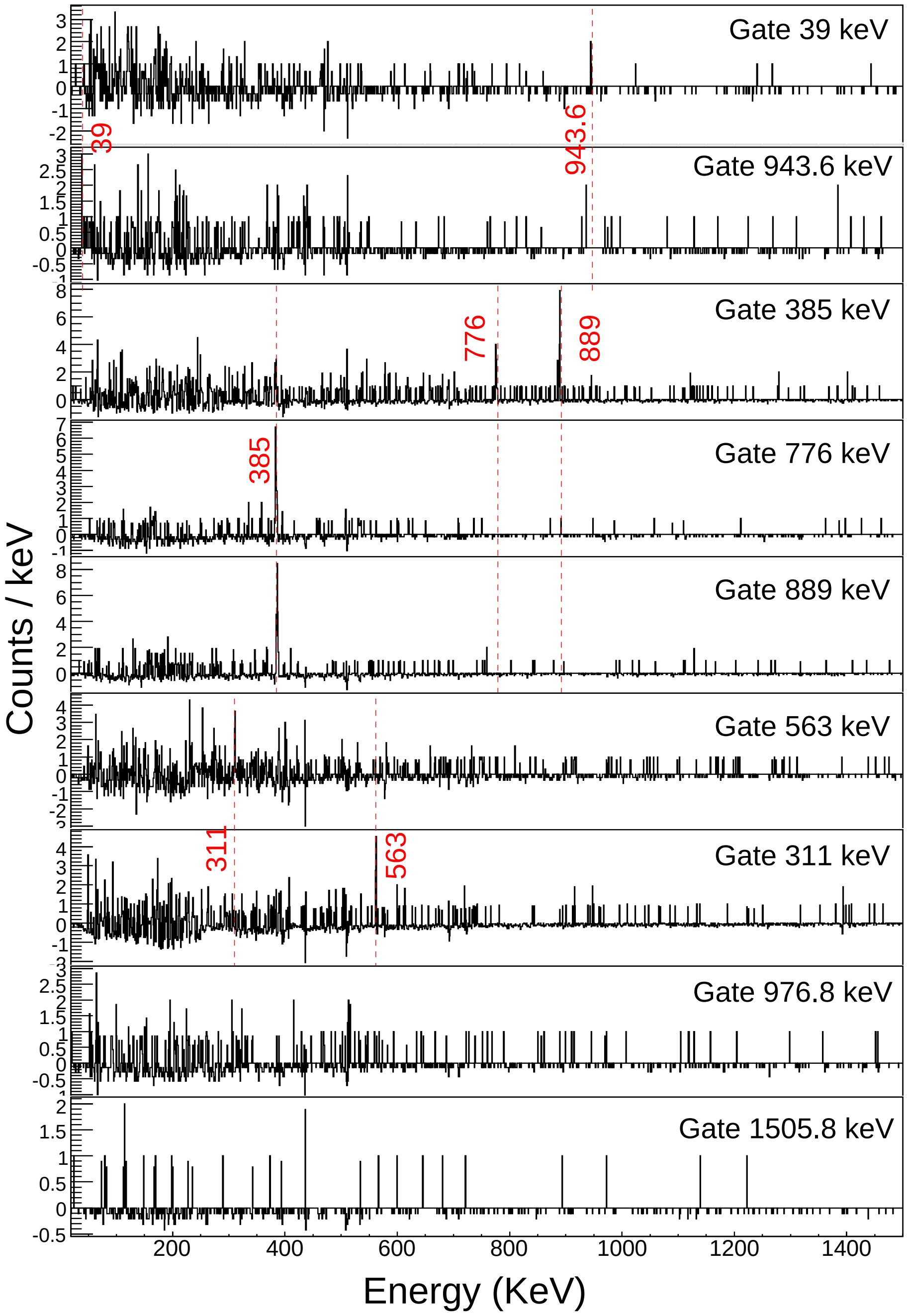

Figure 3.13: γ-γ coincident spectra of the transitions tentatively assigned to the decay of ^{203}*Au. A discussion on these spectra is developed in the text.*

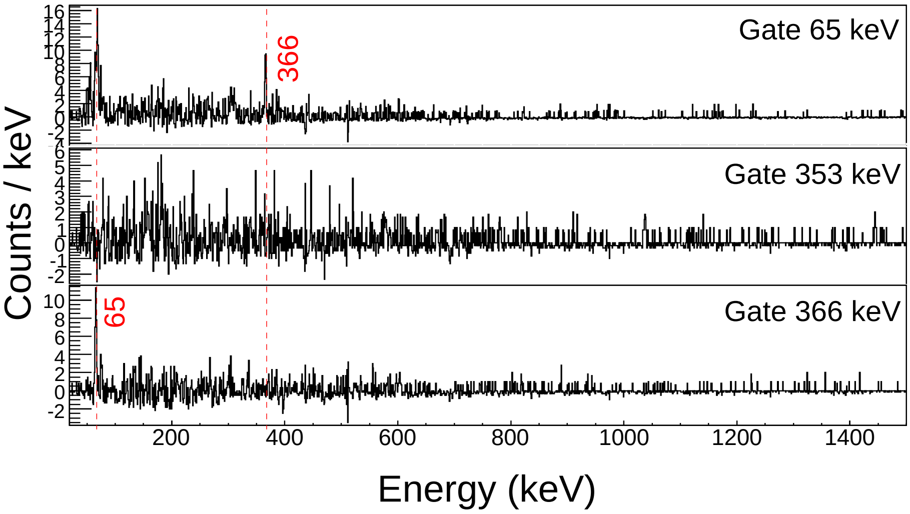

Figure 3.14: γ-γ coincident spectra of the transitions tentatively assigned to the decay of ^{203}Au. A discussion on these spectra is developed in the text.

^{203}Pt to ^{203}Au, de-exciting the nine low-energy states suggested by this work. The proposed level scheme is supported by the γ-ray cascade 889 keV$\rightarrow$385 keV, interpreted as connecting the $(1/2^+) \rightarrow 3/2^+ \rightarrow 3/2^+$ states at 1275 keV and 385 keV previously reported in refs. [139, 140].

Table 3.2 shows the parameters associated to the internal decay of ^{203}Au: tentative low-lying states E_s, γ-ray energy transitions E_γ, relative intensities I_γ, and apparent β-feeding of each state I_β with their corresponding uncertainties. Note that the decays at 65, 353 and 367 keV are not included in the list. Despite there are experimental reasons to connect them to the β-decay of ^{203}Pt, other arguments suggest an unknown origin. For instance, they show a shorter lifetime than the γ-rays firmly assigned to ^{203}Au ($T_{1/2}$ = 12(5)s vs $T_{1/2}^{{}^{203}Pt}$ = 22(4)s), and the shell model approach does not predict their appearance in the internal de-excitation of ^{203}Au.

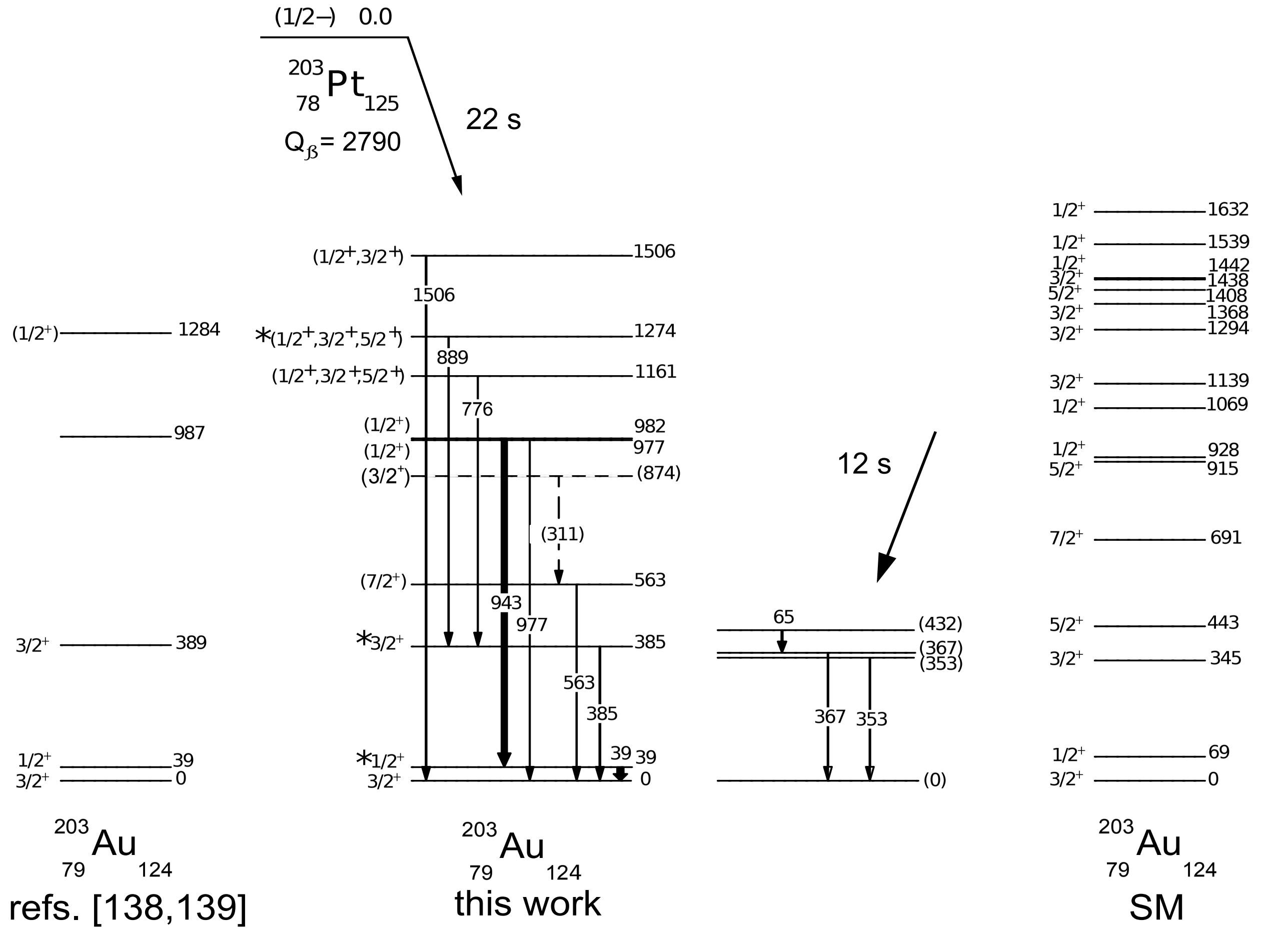
(1/2−) 0.0
203 Pt 78 125
Qβ= 2790
22 s
12 s
(1/2+) 1284
987
3/2+ 389
1/2+ 39
3/2+ 0
203 Au 79 124
refs. [138,139]
(1/2+,3/2+) 1506
*(1/2+,3/2+,5/2+) 1274
(1/2+,3/2+,5/2+) 1161
(1/2+) 982
(1/2+) 977
(3/2+) (874)
(7/2+) 563
*3/2+ 385
*1/2+ 39
3/2+ 0
1506
889
776
943
977
(311)
563
385
39
203 Au 79 124
this work
65
367
353
(432)
(367)
(353)
(0)
1/2+ 1632
1/2+ 1539
1/2+ 1442
3/2+ 1438
5/2+ 1408
3/2+ 1368
3/2+ 1294
3/2+ 1139
1/2+ 1069
1/2+ 928
5/2+ 915
7/2+ 691
5/2+ 443
3/2+ 345
1/2+ 69
3/2+ 0
203 Au 79 124
SM

Figure 3.15: Left: experimental level scheme of ^{203}Au determined by refs. [139, 140]. Centre: level scheme deduced in our β-decay studies. The states marked with an asterisk were previously identified in refs. [139, 140]. Right: Shell model approach shown for comparison. Q_β value taken from [137].

Nuclide	**E$_s$ (keV)**	**E$_\gamma$ (keV)**	**I$_\gamma$(%)**	**I$_\beta$(%)**
^{203}Au	39.0(0.9)	39.0(0.9)	117(17)	10(13)
	385(2)	385(2)	17.4(1.4)	4.0(1.7)
	563(2)	563(2)	8.5(0.9)	1.5(0.6)
	874(5)	311(5)	6.0(0.6)	3.7(0.8)
	976.8(1.6)	976.8(1.6)	6.1(0.8)	3.7(0.9)
	982.6(1.5)	943.6(1.2)	100(7)	61(13)
	1161(4)	776(4)	4.1(0.6)	2.5(0.6)
	1275(3)	889.0(1.5)	6.7(0.9)	4.1(1.0)
	1505.8(1.3)	1505.8(1.3)	15.7(1.7)	10(2)

Table 3.2: Energy levels, γ-ray energy transitions, relative intensities and apparent β-feeding associated to the decay $^{203}Pt \rightarrow {}^{203}Au$. The measured parameters of the tentative M1 transition of 39 keV include the calculated internal conversion coefficient (α_{tot} = 20.5(3)).

3.3.3 β-decay of ^{202}Ir to ^{202}Pt

Some properties of ^{202}Pt were previously reported, as the half life ($T_{1/2}$ = 44 h [141]), the Q_β value ($Q_\beta = 1802 \pm 340$ keV [142]), and the isomeric decay scheme [89], confirming the existence of a (7-) metastable state at 1789 keV.

The γ-ray energy spectrum of the decay ^{202}Ir → ^{202}Pt with all the ion-β correlations registered in a time interval t=3$T_{1/2}$ is shown in figure 3.16. Red-labelled γ-lines are characteristic transitions of ^{202}Pt. They represent the first spectroscopic information obtained from the β-decay of ^{202}Ir, though the 535 keV γ-peak was already observed and interpreted as the $2_1^+ \rightarrow 0_{g.s.}^+$ decay [89]. Figure 3.17 shows the background-subtracted spectrum. In this case, the combination of the short half life ($T_{1/2}$(^{202}Ir)=15(3) s) and the long time elapsed between implantations (T_F(^{202}Ir)=182 s) allows to reproduce the γ-lines related to neighbouring and grand-daughter nuclei by performing the backward-time ion-β correlations -described in section 3.3.1- in the pixels of implantation of ^{202}Ir.

Figure 3.18 displays the coincident γ-ray spectra of ^{202}Pt. The γ-ray decays at 710.1, 514, 1224 and 2165 keV feed the first excited state at 535 keV. Note that, although the γ-rays at 1048 and 718 keV cannot be observed in the energy spectra, they are characteristic of ^{202}Pt because of the mutual coincidence shown with the 535 keV γ-peak. Particularly, the appearance of the 718 keV γ-line, previously reported and interpreted as the $4^+ \rightarrow 2_1^+$

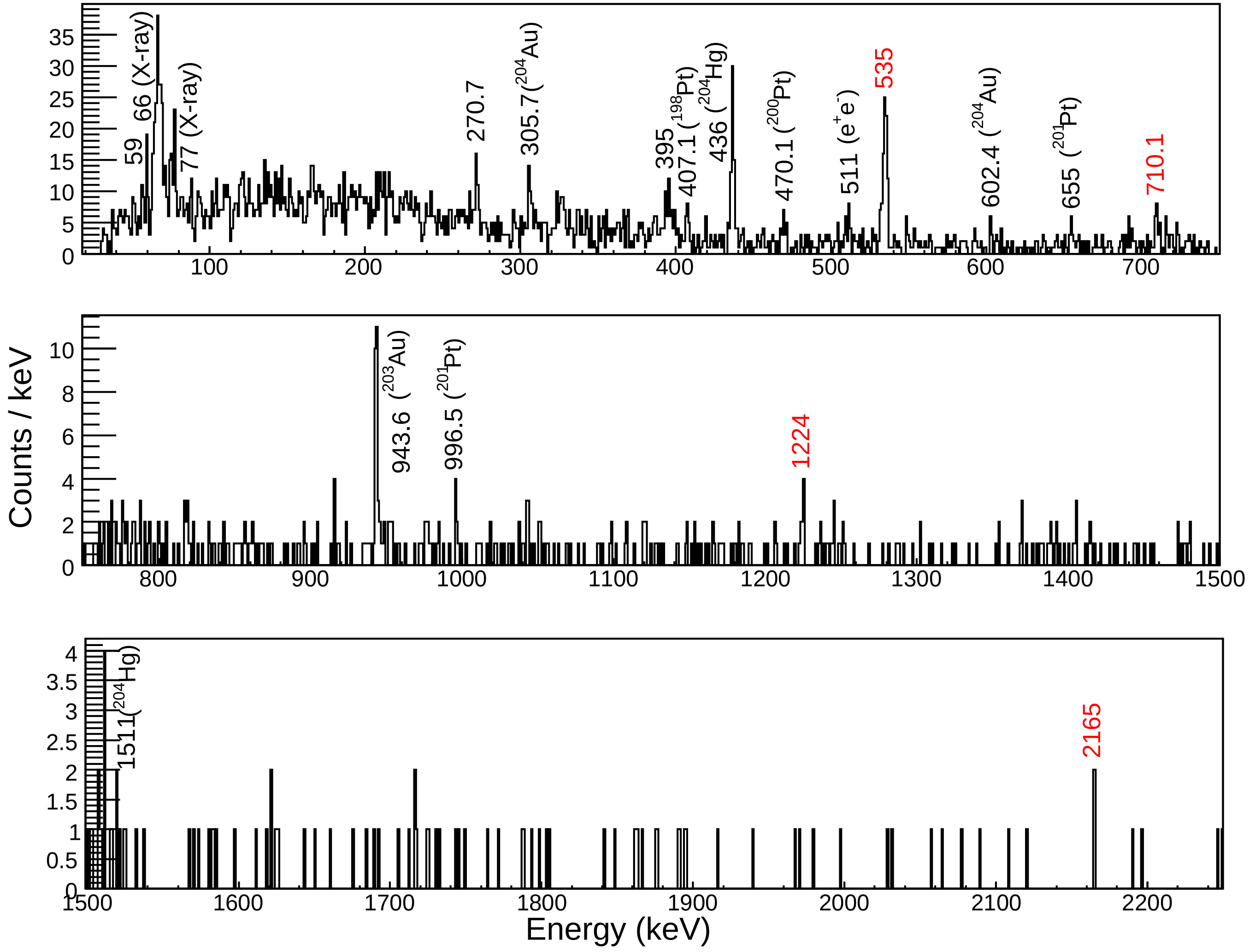

Figure 3.16: β-delayed γ-ray energy spectrum of the decay ^{202}Ir to ^{202}Pt. The red-labelled γ-ray transitions are tentatively assigned to the internal decay of ^{202}Pt. The black-labelled transitions belong to background contamination. See text for details.

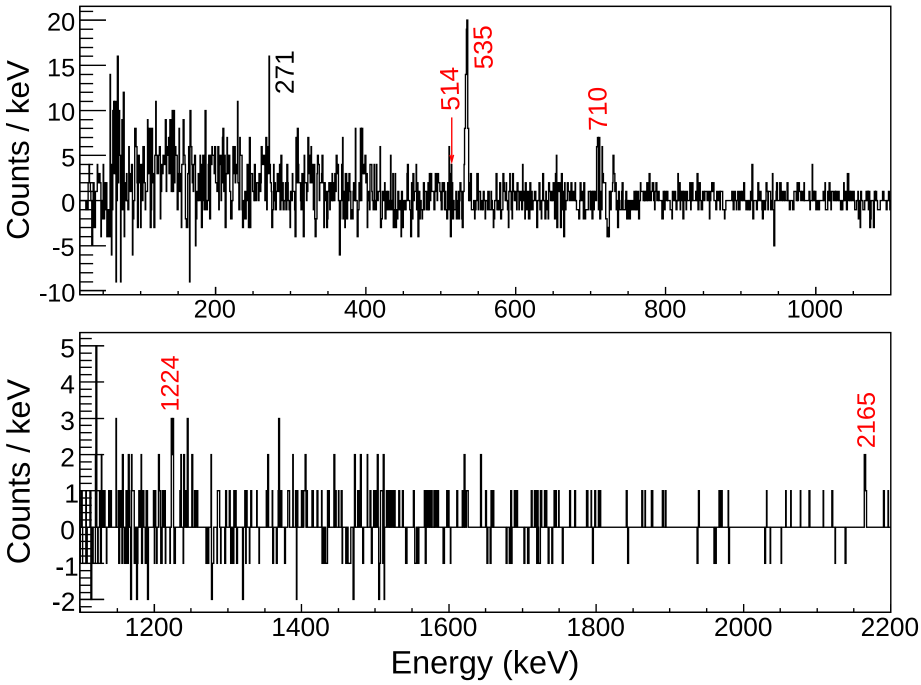

Figure 3.17: Background-subtracted γ-ray energy spectrum of the decay ^{202}Ir to ^{202}Pt. The red-labelled γ-ray transitions are tentatively assigned to the internal decay of ^{202}Pt. See text for details on the subtraction of background.

transition [89], confirms the quality of the γ-γ correlations presented in the current work. The γ-coincident spectrum gated on the 710.1 keV γ-peak shows mutual coincidence with a 732 keV γ-line that is not emitted simultaneously with the 535 keV decay. The 710.1 keV γ-peak must contain, then, the contributions of two γ-ray decays related to two independent nuclei. From this analysis, the 710.1 keV → 535 keV cascade is unambiguously related to ^{202}Pt. The origin of the 732 keV → 710.1 keV cascade will be discussed in the next section. Note that the strong contamination of the singles γ-ray energy spectrum prevent us from identifying any γ-ray decay to the ground state. The nuclear levels, thus, are deduced from the γ-γ coincident analysis. The proposed experimental level scheme of ^{202}Pt is shown in figure 3.19, together with two shell model calculations for comparison. The states previously reported [89] support the plausibility of the proposed nuclear scheme. Table 3.3 summarises the parameters associated to the internal decay of ^{202}Pt: tentative low-lying states E_s, γ-ray energy transitions E_γ, relative intensities I_γ, and apparent β-feeding of each state I_β with their corresponding uncertainties.

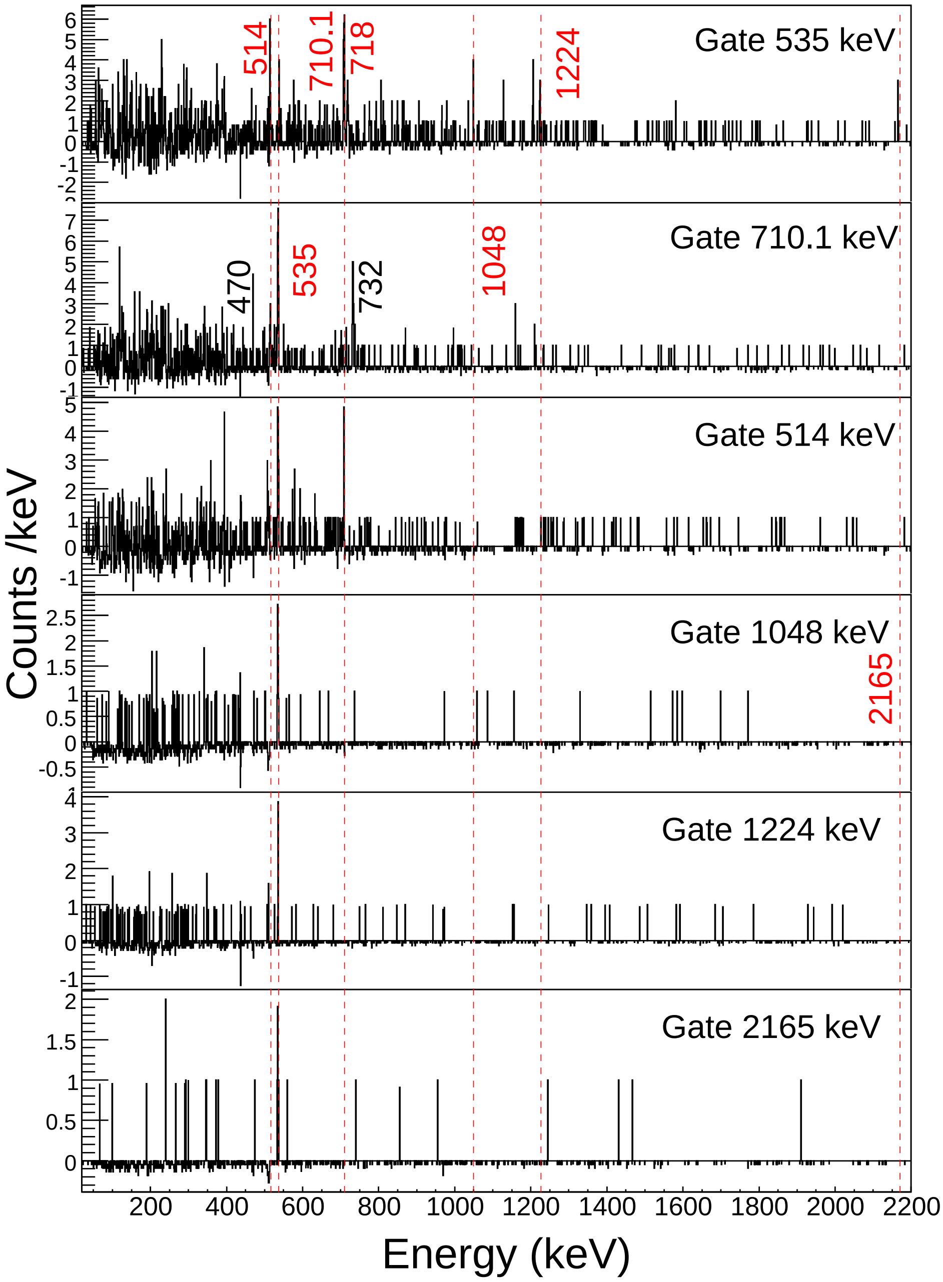

Figure 3.18: γ-γ coincident spectra of the transitions tentatively assigned to the decay of ^{202}Pt. Red-labelled decays are thought to belong to the internal de-excitation of ^{202}Pt, whereas black-labelled transitions correspond to background contamination. A discussion on these spectra is developed in the text.

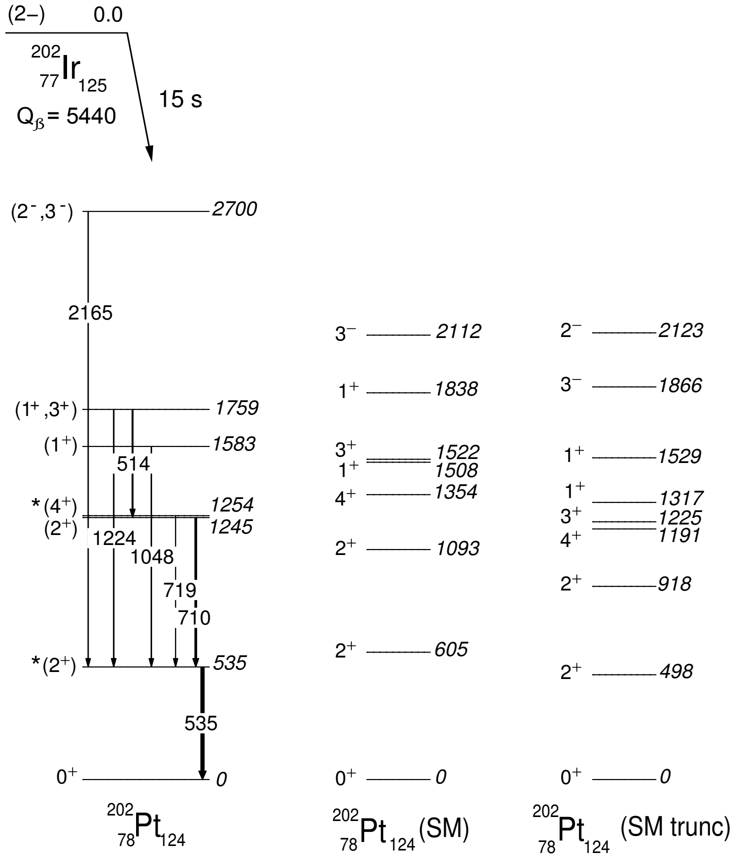
(2–) 0.0
202 77 Ir 125
Qβ= 5440
15 s
(2⁻,3⁻) 2700
2165
(1⁺,3⁺) 1759
(1⁺) 1583
514
*(4⁺) 1254
(2⁺) 1245
1224
1048
719
710
*(2⁺) 535
535
0⁺ 0
202 78 Pt 124
3⁻ 2112
1⁺ 1838
3⁺ 1522
1⁺ 1508
4⁺ 1354
2⁺ 1093
2⁺ 605
0⁺ 0
202 78 Pt 124 (SM)
2⁻ 2123
3⁻ 1866
1⁺ 1529
1⁺ 1317
3⁺ 1225
4⁺ 1191
2⁺ 918
2⁺ 498
0⁺ 0
202 78 Pt 124 (SM trunc)

Figure 3.19: Left: Proposed level scheme of ^{202}Pt. The states marked with an asterisk were previously reported [89]. Centre: shell model approach calculated with the OXBASH code. Right: shell model approach calculated with a truncation of the OXBASH code. Q_β value taken from [137].

Nuclide	**E$_s$ (keV)**	**E$_\gamma$ (keV)**	**I$_\gamma$(%)**	**I$_\beta$(%)**
^{202}Pt	535.0(1.3)	535.0(1.3)	100(8)	8(18)
	1245(2)	710.1(1.5)	52(5)	24(35)
	1253.7(1.9)	718.7(1.4)	3.8(1.0)	4(2)
	1583.0(1.8)	1048.0(1.2)	10.0(1.9)	10(6)
	1759(4)	514(3) 1224.0(1.9)	28(3) 15(2)	43(26)
	2700.0(1.7)	2165.0(1.1)	11(2)	11(7)

Table 3.3: Energy levels, γ-ray energy transitions, relative intensities, and apparent β-feeding of each state associated to the decay $^{202}Ir \rightarrow {}^{202}Pt$.

3.3.4 β-decay of ^{201}Ir to ^{201}Pt

Hitherto, the studies on the nuclear properties of ^{201}Pt have been focused on the determination of the Q_β value ($Q_\beta = 2660 \pm 50$ keV [142]), the half life ($T_{1/2} = 2.3 \pm 0.2$ min [143], $T_{1/2} = 2.5$ min [144]) and the isomeric excited states [88, 89]. In this work, γ-ray energy transitions following the β-decay of ^{201}Ir have been observed for the first time. Figure 3.20 shows the spectrum related to all the ion-β time correlations found in the pixel of implantation during a time period t=3$T_{1/2}$. The determination of the characteristic decays of ^{201}Pt becomes a challenge due to the implantation distribution of the mother nucleus in the active stopper. As can be seen in figure 3.6, neighbouring residues hit the X-strips where the selected ion is implanted. Because of the high implantation rates and long half life of this nucleus a significant fraction of the accidental backward-time correlations correspond to ^{201}Ir. The background-subtracted spectrum associated to the pixels of implantation is thus spoilt. However, qualitative background spectra can be sorted with the backward-time correlations performed in the X-strips of the active stopper where the contaminant nuclei accumulate the maximum statistics. Such spectra are shown in figure 3.21. The black spectrum displays the forward ion-β time correlations registered in the pixel of implantation of the front middle DSSSD. The green-labelled spectrum corresponds to the backward-time correlations detected in the X-strips ≥ 7 of the same DSSSD, where the nuclei ^{203,204}Pt and ^{202}Ir are mostly implanted. The characteristic transitions following β-decay of ^{200}Ir are reproduced in the red-labelled spectrum, corresponding to the backward-time correlations registered in the X-strips ≤ 6 of the rear middle DSSSD detector. One can observe how the tentative γ-ray transitions of ^{201}Pt emerge from the qualitative background in figure 3.21.

Figure 3.22 shows the γ-γ coincident spectra of ^{201}Pt. Three cascades of γ-rays can be distinguished: 1317 keV→389.4 keV, 732 keV→710.1 keV and 996.5 keV→710.1 keV. Note that the 1706 keV γ-line is strongly contaminated by the 1705 keV γ-decay of ^{204}Au [135]. Its connection to ^{201}Pt, however, is firmly established. Firstly, because its relative intensity in the total energy spectrum exceeds that given in the decay of ^{204}Au. Secondly, because it de-excites the same nuclear state than the cascades 1317 keV→389.4 keV and 996.5 keV→710.1 keV.

The left side of figure 3.23 shows the level scheme of ^{201}Pt deduced from this work. The right side displays the single-particle structure calculated with the truncated shell model approach. Note that none of the states reported in the isomeric decay of this nucleus [89] are observed following β-decay of ^{201}Ir, probably because of the high spin difference with respect to the ground state of the mother nucleus.

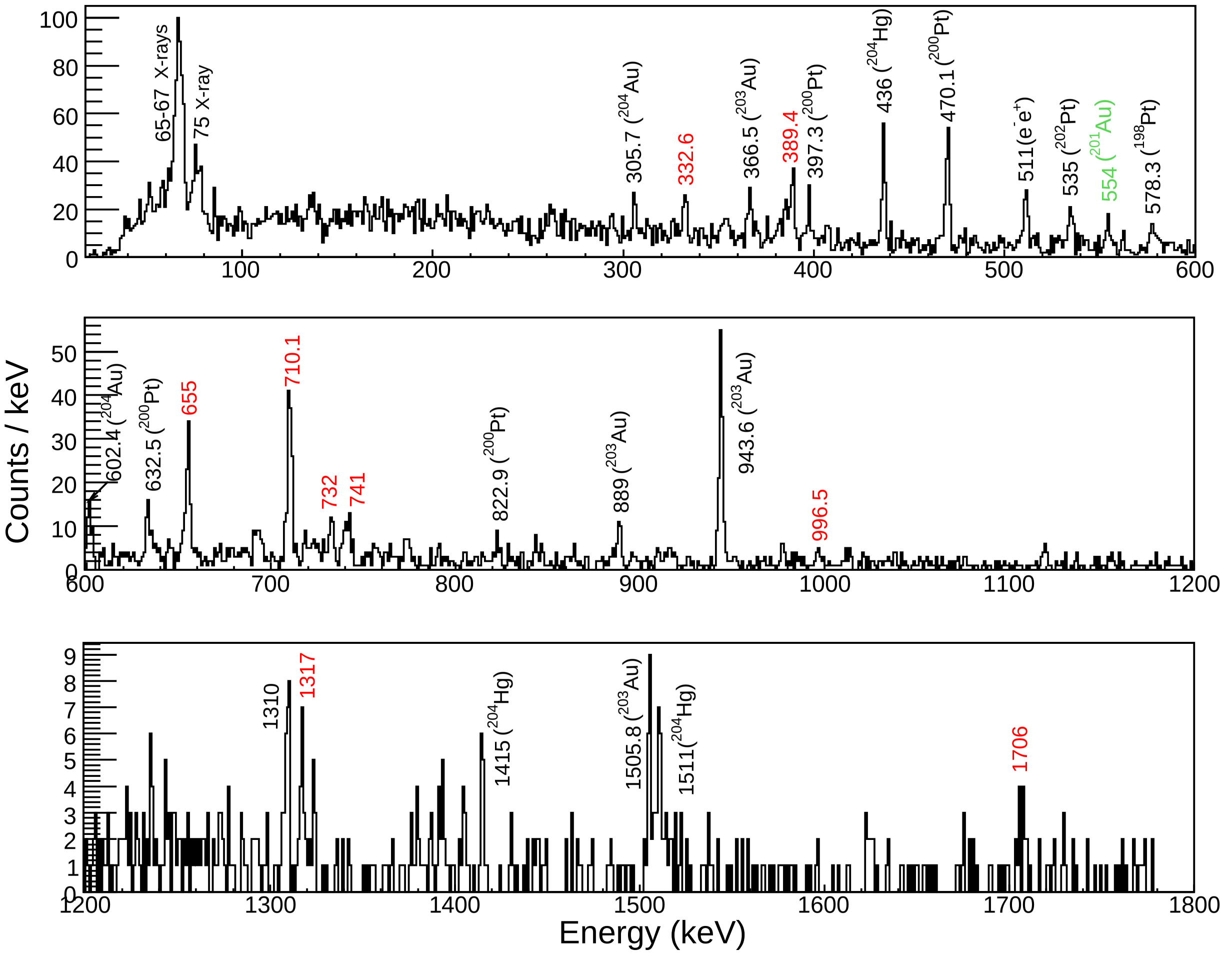

Figure 3.20: β-delayed γ-ray energy spectrum of the decay ^{201}Ir to ^{201}Pt. The red-labelled γ-ray transitions are tentatively assigned to the internal decay of this nucleus, whereas the green-labelled γ-ray peak was previously observed in the internal decay of ^{201}Au [145]. The black-labelled transitions belong to background contamination.

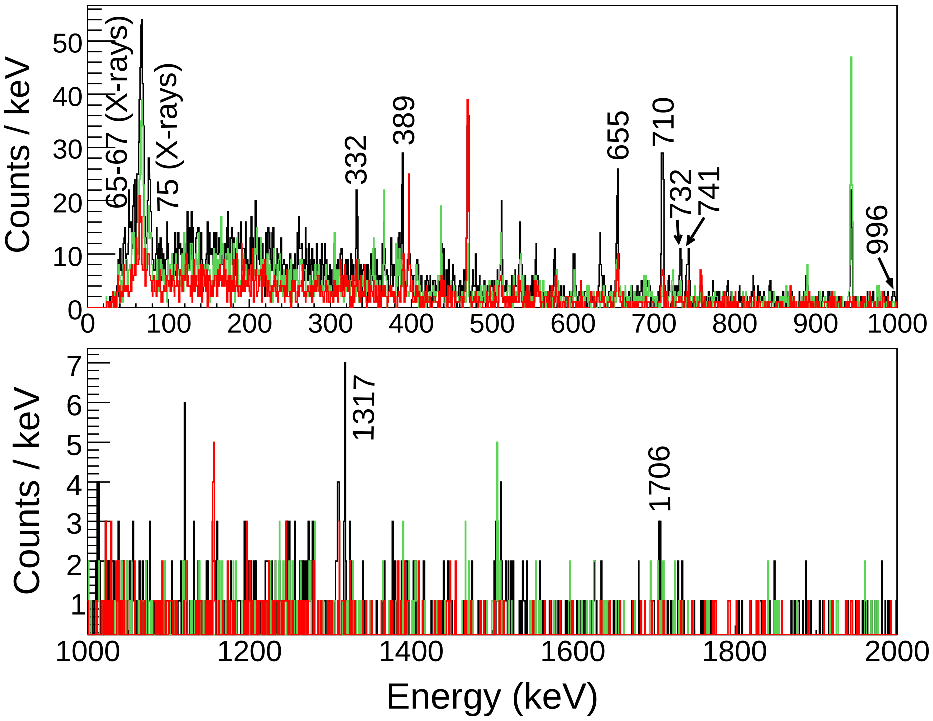

Figure 3.21: Black: γ-ray energy spectrum of the decay ^{201}Ir to ^{201}Pt. Green: Qualitative contribution of background related to ^{204,203}Au and ^{202}Pt. Red: Qualitative contribution of background related to ^{200}Pt. See text for details.

Nuclide	**E$_s$ (keV)**	**E$_\gamma$ (keV)**	**I$_\gamma$(%)**	**I$_\beta$(%)**
^{201}Pt	332.6(1.7)	332.6(1.7)	31(3)	13.1(1.9)
	389.4(1.5)	389.4(1.5)	26(3)	6.2(1.9)
	655(2)	655(2)	100(8)	42(6)
	710.1(1.5)	710.1(1.5)	46(4)	5(3)
	741(2)	741(2)	22(3)	9.2(1.5)
	1442(3)	732(2)	28(3)	12.0(1.9)
	1706(2)	996.5(1.6) 1317(2) 1706(2)	5.0(1.2) 11(2) 12(2)	12.0(1.6)

Table 3.4: Energy levels, γ-ray energy transitions, relative intensities and apparent β-feeding of each state associated to the decay ^{201}Ir → ^{201}Pt.

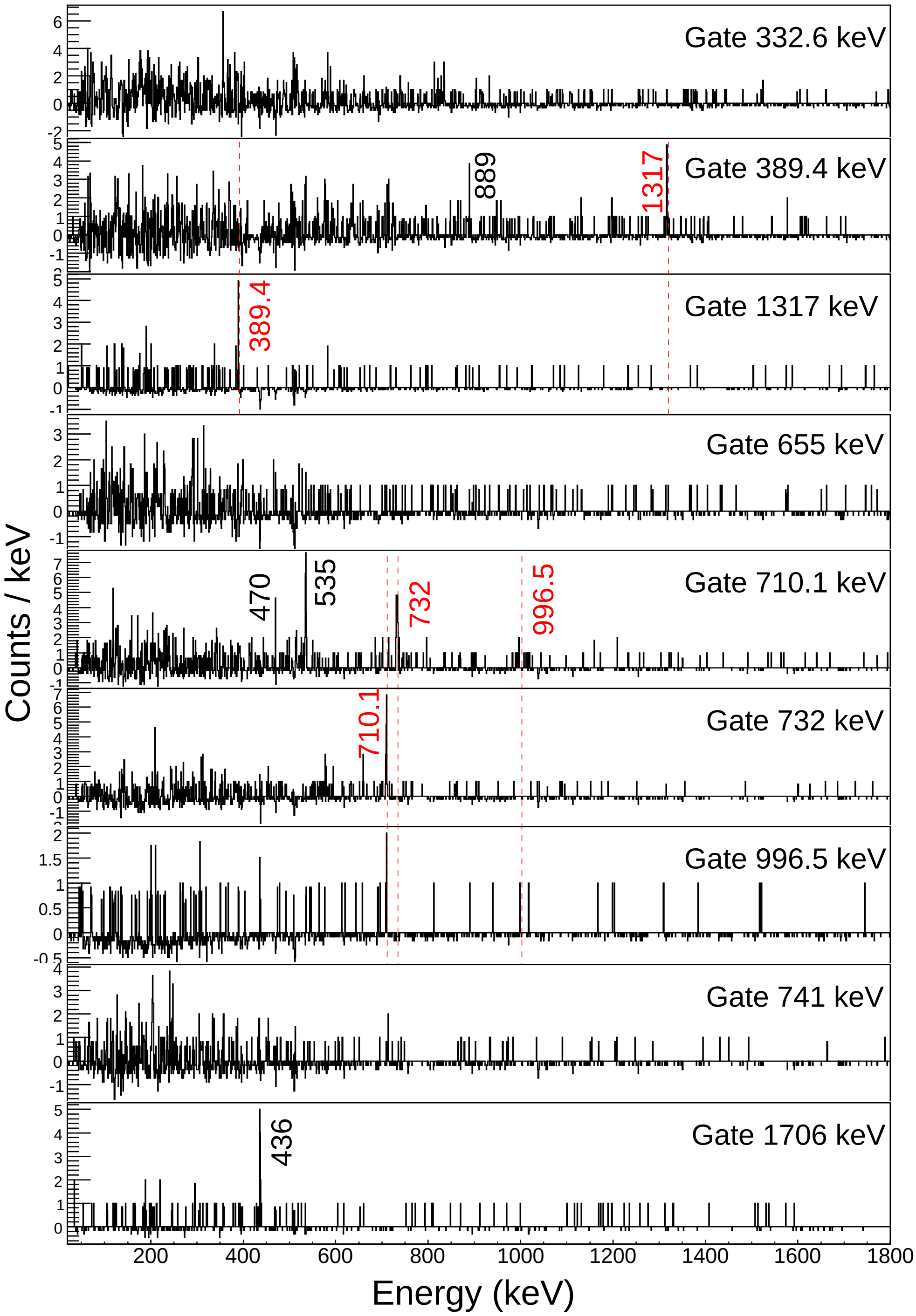

Figure 3.22: γ-γ coincident spectra of ^{201}Pt. Red-labelled decays are tentatively assigned to the internal de-excitation of ^{201}Pt. Black-labelled transitions correspond to background contamination, appeared due to the overlapping of the selected γ-peaks with other γ-ray decays of similar energy.

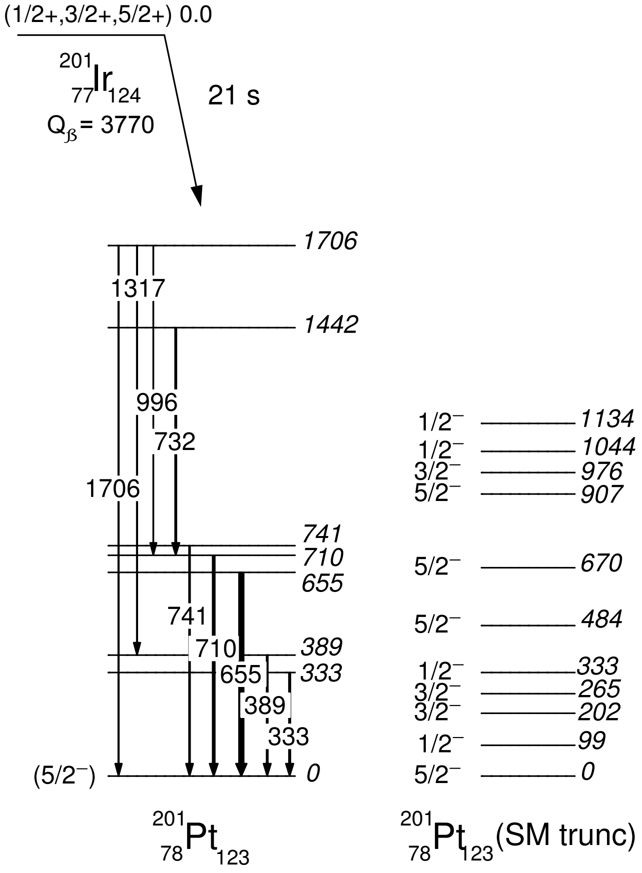
(1/2+,3/2+,5/2+) 0.0
201Ir77 124
Qβ= 3770
21 s
1706
1317
1442
996
732
1706
741
710
655
741
710
655
389
333
389
333
(5/2−)
0
201Pt78 123
1/2− 1134
1/2− 1044
3/2− 976
5/2− 907
5/2− 670
5/2− 484
1/2− 333
3/2− 265
3/2− 202
1/2− 99
5/2− 0
201Pt78 123(SM trunc)

Figure 3.23: Right: Level scheme of ^{201}Pt proposed from this work. Right: structure of ^{201}Pt predicted with a truncation of the OXBASH code. Q_β value taken from [137].

The transitions tentatively related to the decay of ^{201}Ir show a shorter lifetime than the nucleus ^{201}Pt ($T_{1/2}^{201Ir}$=21 s vs $T_{1/2}^{201Pt}$=2.3 min). Furthermore, any of the γ-rays reported in the decay ^{201}Pt → ^{201}Au [144] has been observed in the current data. These arguments strongly support the plausibility of the proposed level scheme. Table 3.4 summarises the parameters associated to the internal decay of ^{201}Pt.

3.3.5 β-decay of ^{200}Ir to ^{200}Pt

So far, the low-lying structure of ^{200}Pt has been investigated via the reactions ^{198}Pt(t,p)^{200}Pt [44], ^{198}Pt(t,pγ)^{200}Pt [46], and $^{208}Pb+^{9}Be$ at 1A·GeV [89]. The partial decay diagram can be seen in ref. [146]. Information on its Q_β value (Q_β = 670 ± 50 keV) and half life ($T_{1/2}$ = 12.6 ± 0.3 h) is also provided in refs. [142] and [147], respectively.

New γ-ray peaks, decaying in coincidence with already reported transitions, have been observed from the β-decay of ^{200}Ir. Figure 3.24 shows all the ion-β correlations registered in the pixel of implantation during a time t=3$T_{1/2}$. Red-labelled transitions belong to the internal decay of ^{200}Pt, whereas black-labelled transitions arise from other nuclear species present in the Si catcher. According to the position distribution of the residues shown in figure 3.6, the implantation rate in the rear DSSSD is low, and it is governed by the nucleus of interest. Consequently, the energy spectrum displayed in figure 3.25, gated on the first β-electron registered after an implantation of ^{200}Ir in the rear DSSSD, is free of contaminant γ-rays. According to the γ-γ coincident spectra shown in figure 3.26, all the γ-decays observed in the singles energy spectrum are related unambiguously to ^{200}Pt, since they show mutual coincidence with at least one of the previously reported transitions (470.1, 397.3, 313.7, 632.5 and 711 keV [46]).

Figure 3.27 shows the experimental level scheme of ^{200}Pt. Six of the eleven transitions observed after the β-decay of ^{200}Ir have been identified for the first time in this work. The placement of the energy levels is based on either observed γ-γ coincidences or former spectral information [146]. Except for the state at 1833 keV, the levels were previously observed via two-neutron transfer reactions [44, 46]. Note that the isomeric states detected in the reaction $^{208}Pb+^{9}Be$ [89] are not populated following β-decay, as it is expected from J^π considerations.

Table 3.5 summarises the parameters related to the internal structure of ^{200}Pt: tentative low-lying states E_s, γ-ray energy transitions E_γ, relative intensities I_γ, and apparent β-feeding of each state I_β with their corresponding uncertainties.

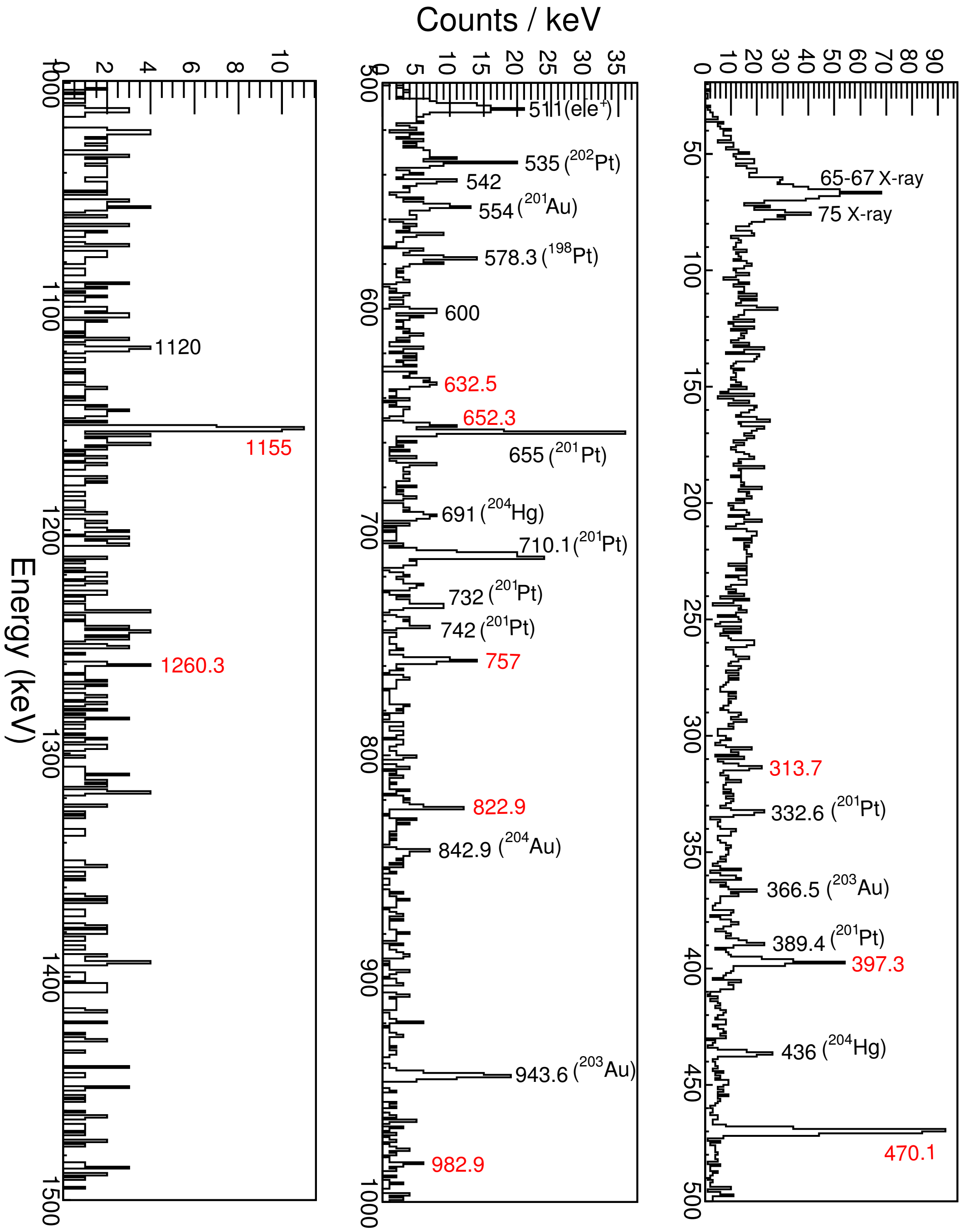

Figure 3.24: β-delayed γ-ray energy spectrum of the decay ^{200}Ir to ^{200}Pt for all the ion-β time correlations registered in the active stopper.

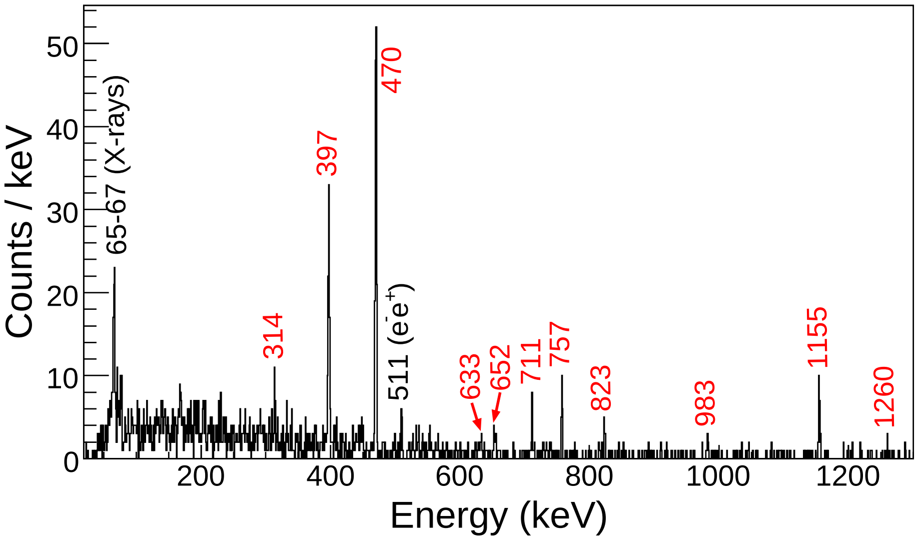

Figure 3.25: β-delayed γ-ray energy spectrum of the decay ^{200}Ir to ^{200}Pt showing the forward ion-β time correlations registered in the pixel of implantation of the rear middle DSSSD.

Nuclide	**E$_s$ (keV)**	**E$_\gamma$ (keV)**	**I$_\gamma$(%)**	**I$_\beta$(%)**
^{200}Pt	470.1(1.2)	470.1(1.2)	100(7)	24(14)
	867(2)	397.3(1.6)	42(3)	0(8)
	1103(2)	632.5(1.9)	13.0(1.5)	13(4)
	1181(2)	313.7(1.4) 711	7.5(0.9) 2.5(0.6)	8(2)
	1625(3)	757(2) 1155.0(1.6)	12.4(1.6) 16(2)	29(6)
	1690(3)	822.9(1.7)	8.6(1.3)	9(3)
	1730.4(1.4)	1260.3(0.7)	2.3(0.7)	2.3(1.0)
	1833(3)	652.3(1.1)	2.2(0.6)	2.2(0.9)
	1850(3)	982.9(1.5)	13.3(1.8)	13(4)

Table 3.5: Energy levels, γ-ray energy transitions, relative intensities, and apparent β-feeding of each state associated to the decay ^{200}Ir $\rightarrow$ ^{200}Pt.

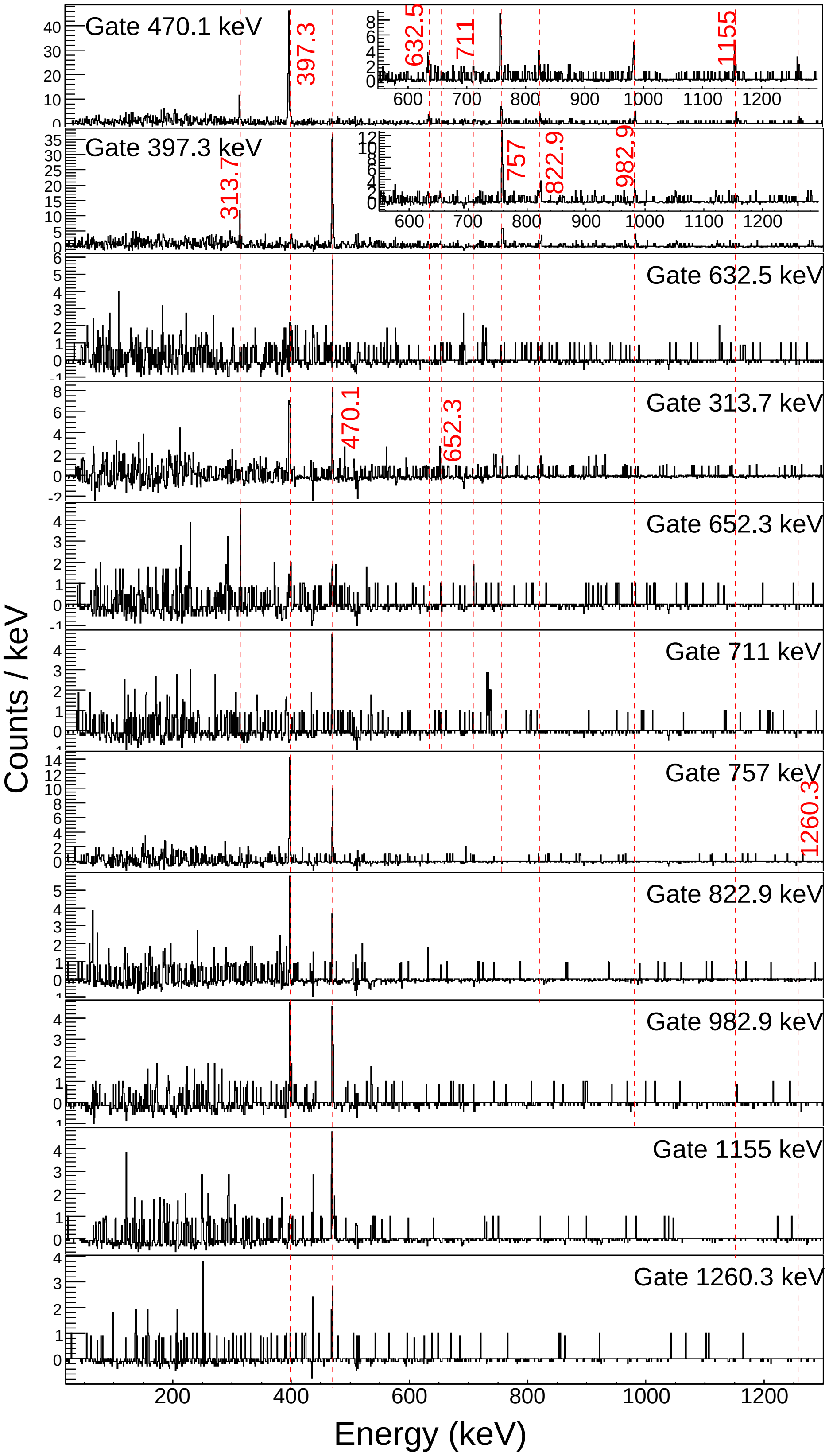

Figure 3.26: γ-γ coincident spectra of ^{200}Pt.

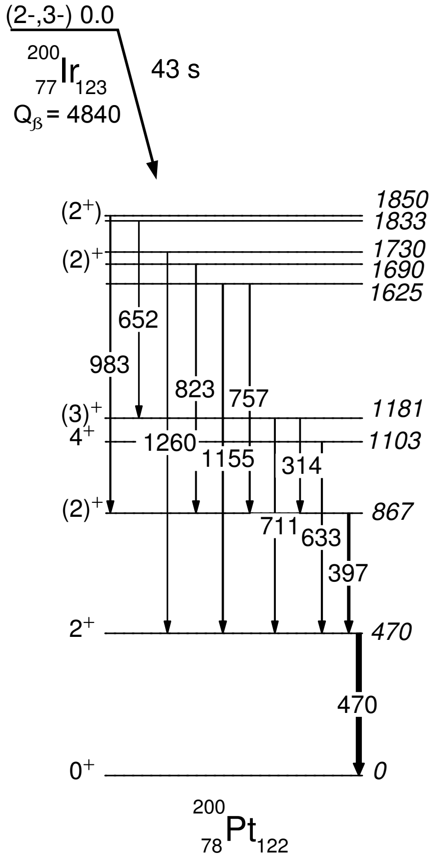
(2-,3-) 0.0
200 77 Ir 123
Qβ = 4840
43 s
(2+)
(2)+
(3)+
4+
(2)+
2+
0+
1850
1833
1730
1690
1625
1181
1103
867
470
0
652
983
823
757
1260
1155
314
711
633
397
470
200 78 Pt 122

Figure 3.27: Experimental level scheme of ${}^{200}Pt$ *measured in the present work. Note that all the energy levels were previously reported [44], excluding the excited state at 1833 keV.* Q_β *value taken from [137].*

3.4 Discussion

3.4.1 Nuclear β decay

The physic phenomenon exploited in this work is the nuclear β decay. The nuclei with an excess of protons or neutrons undergo this process spontaneously to acquire a more stable composition. There are three types of β decay: β^-, β^+ and electron capture. Due to the neutron-rich nature of the isotopes studied in this work we will concentrate in the β^- decay:

$$ {}^{A}_{N}X_Z \rightarrow {}^{A}_{N-1} X_{Z+1} + e^- + \bar{\nu}_e \tag{3.3} $$

A theory on the β decay mechanism was elaborated by Fermi in 1934 [148]. The transition rate $\lambda = ln2/T_{1/2}$ between the initial and final states is given by the Fermi's golden rule:

$$\lambda = \frac{2\pi}{\hbar} \mid V_{fi} \mid^2 \rho_f \tag{3.4}$$

Where ρ_f is the density of final states that determines the shape of the β spectrum and V_{fi} is the matrix element that reflects the strength of the coupling between the initial and final states of the system. ρ_f can be expressed in terms of an angular momentum expansion. If the change in total angular momentum between the initial and final states is ΔJ=0 or 1, the expansion can be approximated only by the term l=0. These transition are referred to as *allowed transitions*, and are characterised by the condition $\Delta\pi$=(-1)^l=+1, where π is the parity of the system. Allowed transitions can be of Fermi (F) or Gamow-Teller (GT) type. A Fermi decay occurs when the spins of the electron and the neutrino are anti-parallel (s=0 and so ΔJ=0). A Gamow-Teller transition, however, takes place when the spins of the electron and the neutrino are aligned in parallel (s=1 and so ΔJ=0 or 1).

When the transition between the initial and final states can only occur with the transfer of angular momentum, higher order terms of the angular momentum expansion are required. These are known as *forbidden transitions* due to their low probability. First-forbidden (FF) decays are characterised by the selection rules ΔJ=0 or 1, $\Delta\pi$=-1 in the case of Fermi transitions, and ΔJ=0,1 or 2, $\Delta\pi$=-1 for GT decays.

The existence of very fast, first-forbidden transitions in nuclei with low Q_β energies close to the doubly magic ^{208}Pb is well known. They prevail over the allowed decays because they are not hindered by any selection rules and are, indeed, the strongest in the whole periodic table. The β interaction for FF decays can be evaluated in moments of multipole order of λ=0,1 and 2. Since these transitions are very strong, moments of multipolarity λ=2 contribute less than a 1% to the transition rates and can be neglected [149].

3.4.2 The nuclear shell model

In nature, some nuclei are bound stronger than others. They are called *magic* because they have a particular number of protons and/or neutrons. They are characterised by an spherical shape and higher-lying first excited states as compared to neighbouring nuclei. This suggests the existence of nuclear shells analogous to those in the atom, in such a way that the magic numbers correspond to closed shells of nucleons.

The nuclear shell model (SM) [27–29] describes appropriately many properties of nuclei with a magic (or nearly magic) number of protons and neutrons, such as the energy, spin and parity of the single-particle states. It also provides reasonable agreement with the electromagnetic moments, occupation number, transition rates, and Gamow-Teller β-decay of nuclear systems close to doubly magic nuclei.

The total nuclear Hamiltonian is defined as:

$$H = \sum_{i=1}^{A} T_i + \sum_{i=1}^{A} \sum_{k>i}^{A} W(\vec{r_i}, \vec{r_k}) \tag{3.5}$$

Where T_i is the kinetic energy operator of the i-th nucleon and $W(\vec{r_i}, \vec{r_k})$ is the two-body interaction between pairs of nucleons. A refers to the total number of nucleons in the nucleus. This Hamiltonian does not have an analytical solution in the many-body Schrödinger equation. To solve this problem, the nuclear shell model assumes independent motion of nucleons in a spherically symmetric potential. With the introduction of the central potential the Hamiltonian can be split into two parts:

$$H = \sum_{i=1}^{A} [T_i + U(r_i)] + \left[\sum_{i=1}^{A} \sum_{k>i}^{A} W(\vec{r_i}, \vec{r_k}) - \sum_{i=1}^{A} U(r_i) \right] = H^{(0)} + H^{(1)} \tag{3.6}$$

Where $H^{(0)}$ defines the motion of an independent particle and $H^{(1)}$ denotes the residual interaction. The average potential U can be chosen so that the residual interaction $H^{(1)}$ can be treated as a perturbation, and the solutions to $H^{(0)}$ are good to a first approximation.

The potential $U(r_i)$ is typically approximated by a harmonic oscillator well. The solutions to the single-particle Schrödinger equation are then given by $N\hbar\omega$, where N is the quantum number describing a *major shell.* For each N, the allowed orbital momentum quantum numbers are l=N,N-2,N-4...1 or 0. As the orbital angular momentum of a nucleon l is coupled to its intrinsic spin (s=1/2), the total angular momentum quantum number of a nucleon takes the values $j = l \pm s$. The spin-orbit coupling splits the states with different total angular momenta such that the orbital with the highest j in the N-th shell can be lowered in energy enough to lay among the states of the N-1 shell. According to the Pauli principle, each orbital can accommodate $2j$+1 nucleons, and by adding the number of nucleons in the orbitals between shell gaps, the magic numbers are reproduced. The single-particle orbitals of the shell model are schematically shown in figure 3.28.

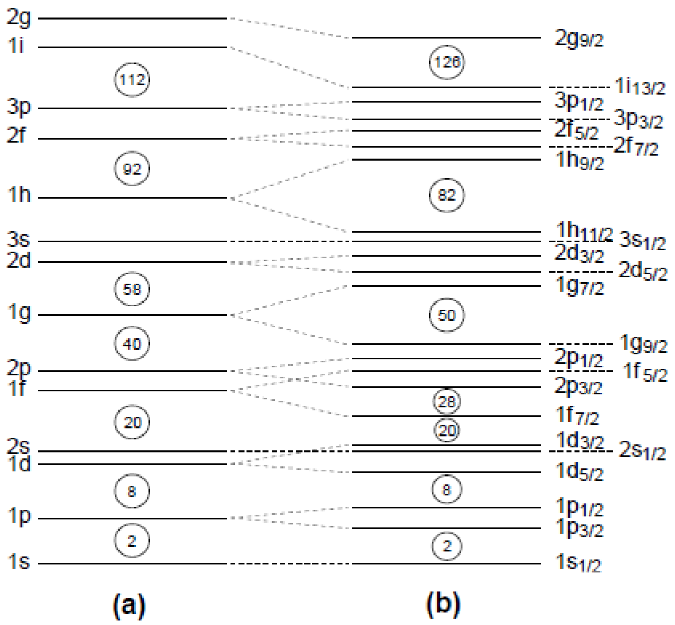
2g
1i
112
3p
2f
92
1h
3s
2d
58
1g
40
2p
1f
20
2s
1d
8
1p
2
1s
(a)
$2g_{9/2}$
126
$1i_{13/2}$
$3p_{1/2}$
$3p_{3/2}$
$2f_{5/2}$
$2f_{7/2}$
$1h_{9/2}$
82
$1h_{11/2}$
$3s_{1/2}$
$2d_{3/2}$
$2d_{5/2}$
$1g_{7/2}$
50
$1g_{9/2}$
$2p_{1/2}$
$1f_{5/2}$
$2p_{3/2}$
28
$1f_{7/2}$
20
$1d_{3/2}$
$2s_{1/2}$
$1d_{5/2}$
8
$1p_{1/2}$
$1p_{3/2}$
2
$1s_{1/2}$
(b)

Figure 3.28: Single-particle energies obtained using (a) the harmonic oscillator and (b) the harmonic oscillator and the spin-orbit interaction. The numbers in the circles are the magic numbers.

3.4.3 Shell model calculations

The shell model calculations solve the Schrödinger equation for the Hamiltonian shown in eq. 3.6. The unperturbed single-particle basis $\mid \Phi_i >$ is constructed from Slater determinants of harmonic oscillator wave functions. The dimensions of the single-particle basis increase rapidly with the number of nucleons(holes), and the equations should be solved in a subspace called the *model space*. A hard core consisting of inactive nucleons is considered, such that only the nuclear configurations of the valence nucleons(holes) outside the core are included in the model space.

In this specific work, the shell model calculations have been performed using the code OXBASH [126]. The program generates an m-scheme Slater determinant basis for a given number of particles, parity, J_z, and T_z. Subsequently, the basis states with good spin ($J \geq J_z$) and isospin ($T \geq T_z$) are constructed, and the Hamiltonian matrix is built for the nucleus of interest. An operator file is required as an input containing the single-particle energies and the two-body m-scheme matrix elements. It is possible then to calculate parentage amplitudes and one- and two-body transition densities.

As well, the electromagnetic moments, occupation numbers, transition rates and Gamow-Teller β-decay can be calculated from the one-body transition densities and the harmonic oscillator radial wave functions.

A ^{208}Pb core has been used in the current calculations. The model space for neutrons consists of the $1\mathrm{h}_{9/2}$, $2\mathrm{f}_{7/2}$, $2\mathrm{f}_{5/2}$, $3\mathrm{p}_{3/2}$, $3\mathrm{p}_{1/2}$ and $1\mathrm{i}_{13/2}$ orbitals, whereas for protons the $1\mathrm{g}_{7/2}$, $2\mathrm{d}_{5/2}$, $2\mathrm{d}_{3/2}$, $3\mathrm{s}_{1/2}$ and $1\mathrm{h}_{11/2}$ orbitals are considered. The single-particle energies and effective residual interaction are fairly well established [150]. Prior to this work, SM calculations using these parameters as input reproduced satisfactorily the experimental decay schemes of nuclei close to the doubly magic ^{208}Pb [25, 125, 151]. For the Pt isotopes discussed in this work, shell model calculations pose a computationally challenging problem due to the high number of holes out of the shell closures. Particularly, the high-spin orbitals $\nu 1\mathrm{i}_{13/2}$, $\nu 1\mathrm{h}_{9/2}$ and $\pi 1\mathrm{g}_{7/2}$ have been removed from the calculations of ^{202,201}Pt. The effect of the model space truncation in the predicted single-particle levels will be discussed in the next sections.

In general, the shell model approach of nuclei with several valence orbitals implies nuclear states with a strong configuration mixing because of the high density of states in these systems. Performing a reasonable assignment of spins and parities based on the single-particle wave functions is thus too challenging. In some nuclei, however, the consistency between the β-decay selection rules and the shell model predictions led us to propose logical J^{π} values, though they could not be firmly determined.

3.4.4 Nuclear structure of Au isotopes

As figure 3.10 shows, the shell model approach reproduces well the level scheme of the four-hole nucleus ^{204}Au. The first nuclear state is considerably lowered in energy in the calculations, probably due to a deficiency in the interaction. The spin-parity of each level has been tentatively assigned according to a combination of the FF transition selection rules that govern nuclei in the nearby of ^{208}Pb and the nuclear states expected by the SM calculations. Since the ground state spin-parity of the mother nucleus ^{204}Pt is 0^{+}, the strongest transitions are expected to decay to nuclear states in ^{204}Au with J^{π}=(0^{-}) or (1^{-}). (2^{-}) levels are expected to appear with a transition rate bellow 1% [149]. Shell model calculations locate two (2^{-}) states in the energy range of the experimental level scheme. From the I_{β} values given in table 3.1, the states at 379, 503 and 602 keV are proposed to have spin-parity (1^{-}) or (2^{-}), though their apparent β-feedings are quite above the expected rates for (2^{-}) states. This excess of feeding could be justified if these levels were populated from higher energy states that are not observed in the current data. The rest of states show a strong feeding, for that a tentative J^{π}=(0^-) or (1^-) assignment has been proposed according to the predictions of the shell model calculations. The consistency in J^{π} and energy with the calculated nuclear levels shows the underlying single-particle structure of this A=204 isotone.

The interpretation of the structure of ^{203}Au in terms of the shell model is quite challenging. As it was mentioned before, the states de-excited by the 65, 367 and 353 keV γ-decays do not characterise this isotope. The strongest argument for this conclusion is the short lifetime shown in comparison with the γ-lines firmly related to the decay ^{203}Pt $\rightarrow$ ^{203}Au. The different lifetime can be justified if the mother nucleus is produced in an isomeric state that undergoes β-decay. Shell model calculations predict the existence in ^{203}Pt of a $13/2^+$ metastable state at 1484 keV. Assuming that it can decay through an E3 transition to the first $7/2^-$ at 1210 keV, its expected half life is of the order of several hundred μs. The β-decay process of several seconds from this state cannot then compete with the γ-ray de-excitation of the isomer. In recent isomeric studies of this isotope only one transition of 1104 keV with a half life of $T_{1/2}$=641(55)ns has been observed [49]. The possibility of following the decay of the $13/2^+$ metastable state is thus rejected.

The connection of the three γ-rays to the $13/2^+$ isomeric state in ^{203}Pt is further excluded from β-decay arguments. According to the β-decay selection rules that govern these nuclei, the $13/2^+$ isomer can decay only through allowed or FF transitions to states that subsequently feed an $11/2^-$ isomeric state in ^{203}Au, already observed at 641 keV [139, 140]. Nevertheless, this possibility is excluded on the basis that a 563 keV γ-transition with a half life of $T_{1/2}$=140(44) μs must arise from the $11/2^-$ state through an unobserved M2 decay of 78 keV, as shown by recent isomeric studies on this nucleus [49]. Though the 563 γ-ray is observed in this work, its half life is of the order of ns. Following this argument, the $11/2^-$ metastable state in ^{203}Au cannot be directly fed by the isomer in ^{203}Pt. The shell model approach cannot either justify the presence of the 65, 367 and 353 keV γ-peaks in the energy spectrum. Shell model calculations only predict the second $(3/2)^+$ state beneath 400 keV, and previous studies locate it between 386-389 keV [139, 140]. According to this, the 385 keV γ-line has been proposed as the second $(3/2)^+$, whereas the nuclear states related to the 353, 367 and 65 keV γ-decays have been excluded from the level scheme of this nucleus. Their origin is, however, unambiguously related to the implantation of ^{203}Pt. Firstly, because their position distribution covers the range of implantation of the selected ion. Secondly, because if they were related to other nucleus present in the active stopper, the backward-time energy spectrum of accidental correlations would reproduce them, and their appearance in the background-subtracted spectrum 3.12 would be prevented. Their connection to the implantation of ^{203}Pt is, unfortunately, beyond our comprehension.

The spin-parity assignment of the proposed excited states in ^{203}Au has been made according to the previous spectral information and the FF transition selection rules. The values of spin given in brackets are consistent with shell model calculations, but cannot be firmly determined. We have kept the $(7/2^+)$ spin assignment given in ref. [49] for the state at 563 keV. Due to the prompt-time character of this γ-ray in our β-delayed γ-ray studies, it is interpreted as arising from a FF transition connecting the $(1/2^-)$ g.s in ^{203}Pt to a higher energy $(3/2^+, 5/2^+)$ state in ^{203}Au, that subsequently feeds the 563 keV level. This higher energy state can be drawn from the γ-γ coincidence spectra of figure 3.13. Looking in detail, a 311 keV transition is observed in coincidence with the 563 keV γ-peak. The corresponding 874 keV level has a apparent β-feeding I_β=3.7(0.8), consistent with the feeding of the $(7/2^+)$ state (I_β=1.5(0.6)%) and the β transition rules within two standard deviations. To conclude the discussion on the 874 keV level, the spin-parity assignment $(5/2^+)$ is rejected on the basis that the first $(5/2^+)$ state, expected to lay at 443 keV by SM calculations, is not observed after the β-decay of ^{203}Pt. As a consequence, the only J^π value in agreement with our observations is $(3/2^+)$.

3.4.5 Nuclear structure of Pt isotopes

The most striking feature of the level scheme of ^{202}Pt, shown in figure 3.19, is the appearance of the high energy state at 2700 keV. It is reasonable to propose the existence of an allowed transition from the $(1^-,2^-)$ g.s. of ^{202}Ir, particularly if one observes the significant apparent β-feeding of this level (see table 3.3) and the large energy gap to the subsequent states. Based on these arguments, its proposed spin-parity is $(2^-,3^-)$. The appearance of the weak (4^+) state suggests, from the β-decay selection rules of these nuclei, that the spin of the g.s. of ^{202}Ir is (2^-).

In spite of having two neutron and four proton holes out of the doubly magic ^{208}Pb core, shell model calculations comprising the full model space have been performed. The margin of error of the calculated low-lying states is typically bellow 160 keV; this is not the case of the first (3^-), which is expected to lay 600 keV under the experimental energy. Due to the large energy interval between model predictions and experimental results, the assignment of spin-parities is only tentative. For the higher energy levels, in which the energy window increases, several spins can be proposed.

As it was mentioned before, the truncated SM calculations exclude the contribution of the highest j-orbitals. Figure 3.29 shows the residual inter-

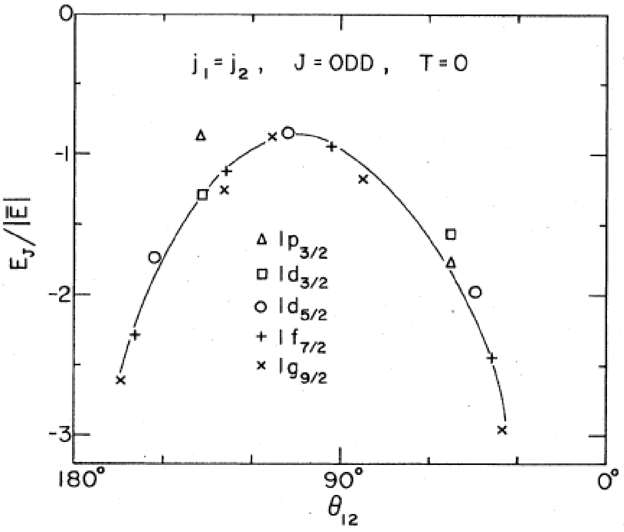

Figure 3.29: Angular dependence of the residual interaction strength for two particles in identical orbits and J=ODD. The E_J values are divided by the (2J+1)-weighted average matrix elements $\mid \bar{E} \mid$ to display the similarity in the J dependence (or θ dependence) of the various orbits.

action strength of several two-particle(hole) configurations in identical orbits as a function of the angle θ between the orbital planes j_1 and j_2, where the subindexes 1 and 2 refer to the first and second particle(hole), respectively. The residual interaction is maximum for $\theta \rightarrow 0^o$, 180^o (or for J_{max}, J_{min}, respectively), whereas for medium angles (or J values) it decreases. This trend is emphasised for high j-orbitals. Consequently, when they are removed from the calculation, the J_{max}, J_{min} states lay at higher energies compared to the full SM calculations, and the overall decay diagram is comprised in energy. This effect is shown in figure 3.19, where the truncated SM calculation for ^{202}Pt predicts the 0^+ ground state at higher energy than the full SM calculations, and the medium-J states lay at closer energies. The compression of the overall decay diagram is also evident in the truncated SM calculation of ^{201}Pt, as figure 3.23 reflects. Due to the high energy differences between the measured and calculated levels for this isotope (ΔE >200 keV), the spin-parity assignment of the observed nuclear states has not been done. However, from the SM calculations, it is expected that all the low-lying states of this nucleus have spins $(1/2^-)$, $(3/2^-)$ or $(5/2^-)$. Only the tentative $(5/2^-)$ spin has been kept for the ground state according to the systematics of neighbouring N=123 nuclei, although spins $(1/2^-)$ and $(3/2^-)$ cannot be unambiguously excluded. Also based in the systematics of neighbouring N=124 isotones, the spins $(1/2^+)$, $(3/2^+)$ are proposed for the ground state of the mother ^{201}Ir, albeit from the β-decay picture a $(5/2^+)$ spin can also be possible.

The large number of proton and neutron holes in ^{200}Pt computationally prevents to perform shell model calculations, even using the truncated model space. However, refs. [44, 46] report spectral information on this isotope, as the J^π values given in the level scheme 3.27. According to the systematics of the neighbouring N=122 isotones, one can expect a spin (1^-) or (2^-) for the g.s. of the mother ^{200}Ir, although higher spins of negative parity cannot be unambiguously excluded. Combining the information of this work with the previous investigations, the number of possible spins can be reduced. In two neutron transfer reactions studies [44, 46], a 4^+ state at 1103 keV and a 0^+ state at 1583 keV were reported, whereas in the β-decay of ^{200}Ir only the 4^+ state is populated. This excludes the $(0^-_{g.s.})$, $(1^-_{g.s.})$ possibilities. A $(4^-_{g.s.})^{200Ir}$ can also be excluded due the absence in the β-decay studies of the tentative $(5)^-$ state at 1567 keV observed in the isomeric spectroscopy of ^{200}Pt [89]. Higher $J^-_{g.s.}$ values are automatically excluded because of the population of several 2^+ states with non-zero apparent β-feeding in the β-decay studies (see table 3.5). These arguments lead to the conclusion for the spin of the g.s. of ^{200}Ir being (2^-) or (3^-).

3.4.6 Summary

As we mentioned before, the interpretation of the observed nuclear states has been performed according to a combination of the β-decay selection rules that govern the nuclei under study [149] and the predictions of SM calculations. The difficulty to perform the single-particle interpretation of these nuclei scales with the number of valence holes out of the ^{208}Pb core, since the configuration mixing of the calculated nuclear levels increases with the density of nuclear states. The γ-ray transition selection rules of such systems cannot be explained from the shell model approach for the same reason. In spite of this, the good agreement between the calculated and measured nuclear states for the Au isotopes confirms their underlying single-particle structure, and consequently, their spherical-like shape. This is not the case of the lighter Pt isotopes, whose large number of valence holes hampers their interpretation from the shell model framework. However, some characteristics typical of the O(6) limiting symmetry of the IBA model [45] are observed in the even-even ^{200,202}Pt isotopes, as the repeating 0^+-2^+-2^+ cascade with strong E2 transitions. Such cascade is not normally expected because relative high-lying 2^+ states decay to the ground state rather than decaying only to another 2^+ level. Furthermore, the quantum number selection rules of the IBA theory could justify some transition sequences and relative intensities that cannot be explained from a shell model framework where the nuclear configurations of the excited states are strongly mixed. The treatment of these nuclei as collective systems is, unfortunately, out of the scope of this work. Further investigations on how pairing vibrational excitations evolve towards spherical shapes in even-even nuclei approaching the doubly magic ^{208}Pb will be necessary to understand completely the structure of these transitional many-body systems.

The existence of very fast, first-forbidden transitions in spherical-like nuclei with low Q_β values close to the doubly magic ^{208}Pb is well known [149]. Based on this, some nuclear models used in r-process calculations consider decisive the role of FF decays in medium- and high-Q_β nuclei near the shell gap N=126 [152]. They predict the existence of high energy FF decays, mostly due to the $\nu 3p_{1/2} \rightarrow \pi 3d_{3/2}$ and $\nu 1i_{13/2} \rightarrow \pi 1h_{11/2}$ configurations. The contribution of the allowed GT decays, related to the $\nu 1h_{9/2} \rightarrow \pi 1h_{11/2}$ transition, is expected to be hindered because of the low transition energy and the partial blocking of the $1h_{11/2}$ proton orbital.

In general, the SM calculations predict transfers of angular momentum beetween the initial and final states ranging from 0 to 2 units, along with a change in parity. The agreement between the SM predictions and the observed apparent β-feedings in the final states represents the first experimental sign on the importance of the FF decays in the "south-west" region of lead. Indeed, the fragmentation residues investigated in this work are the closest nuclear systems to the r-process waiting-point A=195 that have ever been produced in experiment. Particularly, in the β-decay of ^{204}Pt, only FF tansitions feed the low energy states of the spherical-like daughter nucleus ^{204}Au. This result is expectable due to the low Q_β window of the mother ^{204}Pt. For nuclei with higher Q_β values, as the Pt isotopes, our studies point out the strong competition of low energy GT decays and high energy FF transitions expected by some nuclear theorists [152].

In spite of the important hints found out in these data, further experiments will be necessary to confirm the role of the FF decays in this region approaching the r-process path near the shell closure N=126. Such verification will lead to a revision of the nuclear models that predict the properties of the r-process nuclei in the third peak of elemental abundance distribution, which in turn will modify the current picture of the astrophysical r-process of stellar nucleosynthesis.

Chapter 4

γ-labelled β half life measurements

The local maxima in the solar r-process abundances reveal three waiting-points around A=80,130 and 195. The predictions of half lives in these regions are of interest in order to reproduce the relative yields and isotopic composition of the peak abundances. Particularly important is the third peak of elemental abundance distribution, since most of the nuclei with N$\approx$126 and Z>70 have been out of experimental reach until recently. Most of the information on their structural properties has been obtained from the nuclear models used in r-process calculations [129, 130], being their predictions significantly discordant between them. The measurement of half lives in this neutron-rich region is eagerly demanded, since they will put an important constraint on the models required to calculate the properties of the r-process nuclei.

One of the purposes of our work is measuring the lifetimes of some nuclei nearby the shell closure N=126. This aim becomes challenging due to the operation conditions of the experiment, using a pulsed primary beam that provides modulated rates of implantations and decays. The combination of long lifetimes and high implantation frequencies prevents the use of conventional methods to measure the half lives. Alternatively, a novel very efficient numerical technique is employed. The fitting procedure will be described in detail throughout this chapter.

4.1 Ion-β correlations

In order to obtain reliable measurements of the half lives, a proper connection between the fragments implated in the active stopper and the electrons emitted in their β-decay is essential. The correlations performed to measure the half lives are practically identical to those described in chapter 3 to obtain the β-delayed γ-ray energy spectra. In the following sections we will point out the main differences of the correlation procedure.

4.1.1 Position correlations

The high pixelation of the active stopper allows to perform position correlations between the fragmentation residues and the subsequent β-like electrons following the technique described in section 3.2.1. Let us denote (X,Y) as the individual x- and y-strips of implantation, and (x,y) as the x- and y-strips of the β-decay particle. In order to measure the β-decay half lives of the selected ions (Z,A), the position correlation is established requiring a β-like signal in either, the pixel of implantation or in the contiguous pixels:

$$\begin{gathered}(x,y) = (X,Y) \\ or \\ (x,y) = (X \pm 1, Y \pm 1)\end{gathered} \tag{4.1}$$

Henceforth, let us define a "cell" as the individual pixel or group of adjacent pixels where the ion-β position correlations are performed, it doesn't matter which.

4.1.2 Time correlations

Let us recall that the ^{208}Pb primary beam was delivered with a pulsed time structure consisting of cycles with a spill of 2 s followed by a pause of 8 s. The ion-β time correlated spectra are modulated by the spill cycle, due to the presence of δ-electrons generated by the implantation of fragments during the beam pulses (see figure 3.5). Furthermore, the measurement of the half lives may be limited by the ion implantation frequency, since multiple implantation events occur when the lifetime of the selected ion is of the order of the time elapsed between implantations.

4.1.3 β-prompt γ-ray time correlations

The path of a β-particle inside the active stopper can be longer than the width of a pixel. Consequently, the position correlations should be extended to the neighbouring pixels, and the probability of correlating an implantation to the β-electron of a neighbour fragment or a daughter nucleus increases.

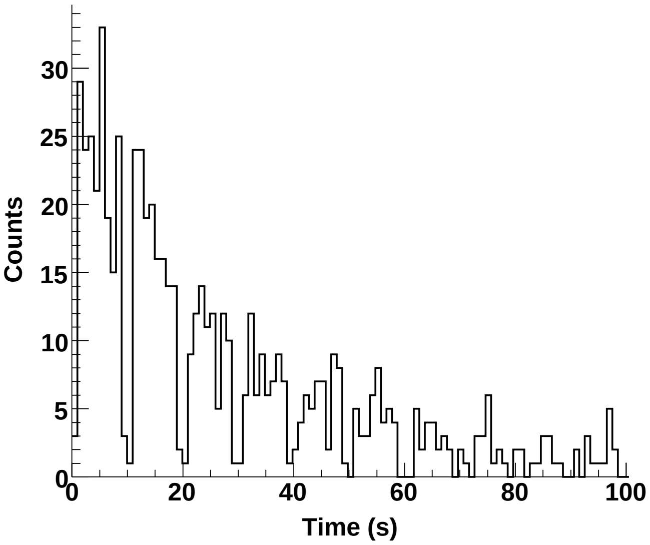

Figure 4.1: Experimental β-decay curve of the nuclide ^{204}Pt. The figure reveals the suppression of time correlations between fragments and β-like particles during the spill time.

These β-decays are off-line suppressed by connecting the β-decay electrons registered after the implantation with the characteristic γ-ray decays of the daughter nuclei. In spite of this, a contamination originated by the own γ-ray background is present in the ion-β time correlated spectrum.

Summarising, each implanted fragment is correlated to the first β-decay event recorded in the same or adjacent pixels during the beam pause in coincidence with the most intense γ-ray transition of the daughter nucleus. Only these time differences are included in the β-decay curve, as figure 4.1 shows.

4.2 Feasibility of a direct measurement

If the lifetime of the selected ion is much shorter than the implantation rates, the decay spectra can be obtained correlating every γ-tagged electron with the first previous implantation, which is, with a maximum probability, that which underwent the β-decay. In this case the half life can be measured from conventional techniques, as fitting the radioactive data to an exponential function.

If, on the contrary, the lifetime of the ion under study is of the order of

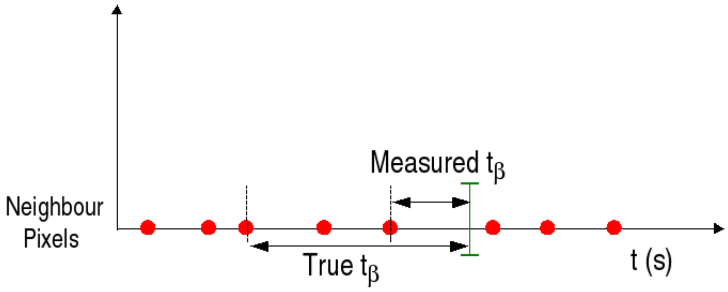

Figure 4.2: Contributions of background contamination events originated by the selection of a "false" fragment implantation.

its implantation rates, the measured β-decay curve can be spoilt with false correlations originated by the periodic time structure of the implantation data. These are called Multiple Implantation Events (MIE), since the β-electron produced by a particular ion is correlated to a subsequent fragment implanted in the same cell. As a result, the measured ion-β time differences are shorter than the "real" time differences (see figure 4.2) and the measured β-decay curve is compressed. Observe that these false correlations are originated by a "false" implantation event. Along with this noise contribution are the uncorrelated events introduced by a "false" β-electron. False β-decays appear connected to either a background γ-ray energy transition or a false pixel identification (x,y).

The feasibility of determining the β-decay half life of a given nucleus from the measured β-decay curve depends on the signal-to-noise ratio of the time-correlated spectrum. In our particular analysis, the impossibility of experimentally disentangle the "true" time sequences from the false correlations aforementioned requires the use of a different procedure, which will be discussed in the next section.

4.3 Evaluation technique of β-decay half lives

The technique used in this work to evaluate the β-decay half lives was initially proposed by T. Kurtukian et al [19]. It consists in performing a χ^2 fit between the experimental data and a numerical function, obtained from Monte-Carlo simulations of ion-β time correlations. The shape of the background distribution is procured by sorting a new spectrum with the reversed time sequence of ion-β correlations. The ratio between the forward-

and backward-time spectra contains the information on the genuine β-decay curve. The new technique will be described in detail throughout this section.

4.3.1 Monte-Carlo simulation

The Monte-Carlo code simulates the ion-β time sequences of the measured data, reproducing as faithfully as possible the operation conditions of the experiment. Indeed, the input parameters introduced in the code, i.e., the spill sequence, the fragment implantation rate during the spill, the γ-labelled β-particle rate during the pause, the detection probability of a given γ-ray transition, and the detection efficiency ϵ, are extracted from the recorded data, whereas the β-decay lifetime τ is set up as a free parameter. By this way, the value τ responsible of the minimisation of the χ^2 fit procedure is that one most compatible with the experimental β-decay curve. For the specific cases in which no γ-ray energy transitions can be related to the implanted nucleus, the detection efficiency is also set up as free parameter, being the pair (ϵ,τ) responsible of the minimisation of the χ^2 fit procedure the one which best fits the experimental β-decay curve.
When N_F nuclei are implanted in the active stopper, the expected number of β-decay events in the ion-β time correlated spectrum, recorded in a time interval $[t, t+\Delta t]$, is

$$\Delta N(t) = N_F \cdot \rho(\tau, \epsilon_\beta, t) \cdot \Delta t \tag{4.2}$$

Where $\rho(\tau, \epsilon_\beta, t)$ is the probability density of detecting a β-decay event in a time t after the implantation of the selected fragment. τ and ϵ_β refer to the lifetime of the nucleus of interest and the β detection efficiency of the active stopper, respectively.

The expected number of γ-labelled β-decay events N_β^γ integrated over the whole time range is

$$N_\beta^\gamma = N_F \cdot \epsilon_\beta \cdot \epsilon_\gamma \cdot I_\gamma(keV) \tag{4.3}$$

Where the product of the DSSSDs detection efficiency ϵ_β, the RISING γ-ray detection efficiency ϵ_γ and the γ-ray transition intensity $I_\gamma(keV)$ corresponds to the total probability ε of detecting a γ-labelled β-decay

$$\varepsilon = \epsilon_\beta \cdot \epsilon_\gamma \cdot I_\gamma(keV) \tag{4.4}$$

In this particular experiment, not ϵ_β nor $I_\gamma(keV)$ could be extracted from the recorded data. As a solution, the product ϵ=$\epsilon_\beta I_\gamma$ -previously referred to as the detection efficiency- is obtained from expression 4.3 and used as input parameter of the Monte-Carlo code.

Nuclide	N_F	Energy (keV)	N_γ	ϵ_γ (%)	ϵ (%)
^{204}Au	10628	436	1285	21.11	57(3)
^{204}Pt	16168	305	943	26.35	22(1)
^{203}Pt	20678	943	1175	12.55	45(2)
^{202}Ir	5189	535	530	18.49	55(3)
^{201}Ir	17245	655	560	16.15	20(1)
^{200}Ir	4792	470	816	20.12	85(5)

Table 4.1: Measured parameters associated with the experiment: number of fragments N_F, γ-ray energy transition of the first excited state of the daughter nucleus, number of γ-ray de-excitations N_γ, γ-ray detection efficiency ϵ_γ, and the corresponding value of the detection efficiency ϵ.

Table 4.1 shows the parameters associated to the measurement of the detection efficiency ϵ for the ions whose daughter nuclei are unambiguously characterised by a γ-ray decay.

Reliability of the input parameters

The reliability of the fitting procedure lies in an appropriate reproduction of the experimental conditions in the Monte-Carlo simulation. For this reason the accuracy of the input parameters is of great importance, even though obtaining the "real" values is not feasible for some of them. For instance, the fragment implantation rates -and consequently, the β-decay rates- depend on any variation in the intensity of the primary beam, as well as on the spatial distribution of the implanted residues. To illustrate this situation, figure 4.3 displays the transversal distribution of the ions of ^{203}Pt implanted in the active stopper. As a consequence, an individual implantation -or β-decay-frequency per cell can be obtained from the experimental data. Nevertheless, to simplify the calculations, the Monte-Carlo code developed in this work considers these frequencies averaged over the total number of pixels in the active stopper.

The measurement of the detection efficiency ϵ depends on two parameters: the γ-ray energy transition intensity $I_\gamma(keV)$ and the detection efficiency of the active stopper ϵ_β. As far as $I_\gamma(keV)$ is concerning, the background con-

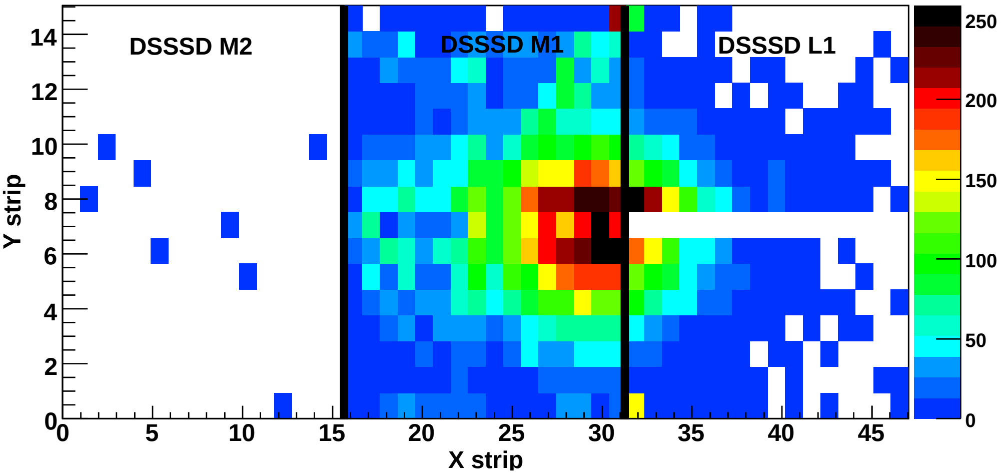

Figure 4.3: Spatial distribution of the secondary nuclide ^{203}Pt as seen by the active stopper. The colour scale indicates the number of ions hit in a given pixel (X,Y).

tribution to the selected γ-ray peak should be carefully determined. As we discussed in section 1.6.3, addback corrections are applied to the β-delayed γ-ray spectra to minimise the error in the peak-to-noise ratio. The detection efficiency of β-electrons ϵ_β depends on their emission direction and on the implantation depth z in the DSSSD detectors, since the β detection probability is subject to the quantity of energy deposited by the electrons in their path through the silicon catcher. Thus, the β detection efficiency increases from a minimum value in the edges of the active stopper towards a maximum value in the centre of the DSSSD detectors.

The implantation width profiles of ^{203}Pt and ^{202}Ir are distributed throughout the rear and front edges of the two central DSSSD detectors -the arrangement of the DSSSDs is shown in figure 1.15-. In such cases, two equivalent configurations of the active stopper can be considered to determine the γ-labelled ion-β time correlations:

- Two independent DSSSD detectors of 1 mm thickness each one.
- One unique DSSSD detector of 2 mm thickness.

ϵ_β also depends on the β detection threshold established to discriminate electron radioactive decays from noise events. As the β threshold increases, the number of registered γ-tagged β-like particles, the γ-labelled β-decay frequency f_β^γ and, consequently, the detection efficiency ϵ_β decrease. Along this chapter, the values provided for N_γ, f_β^γ and ϵ correspond to the experimental β detection threshold ($\sim$ 150 keV), except for those associated to the nucleus ^{200}Ir, which are obtained for a β threshold of 300 keV because of the observation of background electrons at 150 keV.

In appendix E the reader can peruse the complete list of parameters associated to the different DSSSD configurations and β thresholds studied in the present analysis, together with the resulting half lives.

4.3.2 The χ^2 test

When we have two sets of data, $g(x_i)$ and $h(x_i)$, drawn from the same parent population, the χ^2 is given by [153]

$$\chi^2 = \sum_{i=1}^{n} \frac{[g(x_i) - h(x_i)]^2}{\sigma^2(g) + \sigma^2(h)} \tag{4.5}$$

The denominator $\sigma^2(g) + \sigma^2(h)$ is just the variance of the difference $g(x_i) - h(x_i)$. The expectation value χ^2 depends on the similitude between the distributions of the two data sets $g(x_i)$ and $h(x_i)$, and is $\langle\chi^2\rangle = \nu$, where ν is the number of degrees of freedom and is equal to the number n of sample frequencies minus the number of parameters that have been fitted from the data. It is convenient to define the reduced chi-squared as $\chi^2_\nu = \chi^2/\nu$, with expectation value $\langle\chi^2_\nu\rangle = 1$. A value of χ^2_ν much larger than 1 results from a large deviation between the two distributions and may indicate poor measurements or an incorrect assignment of uncertainties. Values of χ^2_ν much smaller are equally unacceptable and may indicate some misunderstanding of the experiment. On the contrary, if the $\chi^2_\nu \simeq 1$, the assumed distributions describe the spread of the data points reasonably well. It is worthwhile mentioning that we assume Gaussian statistics in the χ^2 calculation, since the standard deviation σ is obtained from the Gaussian probability density function, in which approximately 68.3 % of the events of the Gaussian distribution are comprised within $\pm\sigma$ of the mean and approximately 95.4 % are comprised within $\pm 2\sigma$.
If we want to extract certain parameters a_i from a χ^2 fit procedure, it is appropriate to apply the least-squares fit method, consisting in minimising χ^2 simultaneously for each parameter in order to obtain the optimal values. For a given probability distribution, the χ^2 is minimum when the first partial derivative with respect to each parameter vanishes ($\partial\chi^2/\partial a_i = 0$). Hence, it is expected that the vicinity of a local minimum in any parameter a_i will be a quadratic function of that parameter. The errors in the fitting parameters

a_i can be estimated by varying each parameter about the local minimum to increase χ^2 in one unit from the minimum value.
In order to evaluate the goodness of the fitting procedure, the confidence level (CL) is defined [154]. It represents the probability of obtaining in a new set of measurements a value greater than the one we have on hand, this is, a worse value of χ^2. Although when two or more variables have been determined from the fit and exhibit some correlation, the definition of CL becomes more difficult. Indeed, the degree of correlation between two parameters a_1 and a_2 in a contour plot of χ^2 as a function of both of them is indicated by the tilt of the ellipse shaped by the parameters. As we are interested in determining a confidence interval of the fit, we have to consider the full range of the $\Delta\chi^2 = 1$ contour, so that approximately a 68% probability of finding the true values of the parameters is kept.

The number of counts in the histogram bins is subject to statistical fluctuations according to the Poisson distribution. Furthermore, the measured time correlated spectra handled in this work correspond to a limited number of events. To ensure a correct statistical application of the χ^2 test, the Gaussian statistics requirements must be also satisfied, for that the number of counts per bin must be larger or equal than 10 [153].

The lifetimes τ of interest are obtained from χ^2 fits between the simulated and measured ratios of the forward- and backward-time spectra, by applying the least-squares method to the free parameter τ. In some cases, when the detection efficiency ϵ is not experimentally measurable, the pair of free parameters (ϵ,τ) is determined from χ^2 bi-dimensional fits. Since the Monte-Carlo calculation produces data sets comparable to the measured data, this method only depends on the assumptions made in the Monte-Carlo code (i.e., the input parameters considered), and not on any statistical expectations about the shape of the probability function.

4.3.3 The fitting procedure

To estimate the shape of the modulated background, new spectra with the reversed time sequence of ion-β correlations were sorted. Any correlation between a given implantation and the previous β-decay represents, in principle, an accidental event. Nevertheless, the backward-time correlations are conditioned to the same operation parameters than the forward-time sequence, being constrained by the modulated time structure of implantations and decays. As a result, when the frequency of implantation and the decay constant of a given nuclear specie are of the same order, the backward-time correlations cannot be considered fully random, and the background is directly reproduced in the simulated forward-time spectrum. The aim of examining the inverse time correlation lies in applying the χ^2 fit procedure to the ratios between the forward- and backward-time spectra rather than estimate it directly from the forward-time sequence. The goal is straightforward: the time distributions are subject to statistical fluctuations in the histogram bins when they are treated independently. The forward-backward ratio, however, is less sensitive to the fluctuations and the chi-squared fit is improved. The fitting procedure consists in performing sets of simulations with a given value of τ and calculating the χ^2 of the measured and simulated ratios of time correlations in forward- and backward-time directions.

As an illustration, figure 4.4(a) shows the experimental ion-β time correlated spectra in forward- (solid line) and backward-time (dashed red line) directions for the nucleus ^{204}Pt. Recall that, in order to avoid background contributions, the time correlations are made only for γ-labelled β-decays during the spill pause. Comparatively, figure 4.4(b) shows the same correlations simulated with the Monte-Carlo code for the lifetime τ responsible of the minimisation of the χ^2 fit. Notice that we have applied high statistics to the simulated spectra in order to minimise the statistical fluctuations. The inset panel of this figure displays the measured forward-backward ratio with the experimental error bars, together with the simulated ratio that minimises the χ^2 function. Figures 4.4(c) and 4.4(d) show the same spectra for ^{202}Ir.

The β-decay curves of the nuclei under study present low statistics due to the restrictive conditions of the analysis. In some cases, one can increase the bin size in order to satisfy the Gaussian statistics requirements. Indeed, the number of samples selected for the χ^2 fitting procedure is subject to this constraint.

For the most general case of the analysis, χ^2 is a continuous function of the parameters (ϵ,τ) that describes a hypersurface for the appropriate minimum value of χ^2. Figure 4.5 shows such a hypersurface for ^{202}Ir. The data corresponds to a β detection threshold of 300 keV. The detection efficiency of the active stopper and the half life of the selected nucleus can be determined fitting the region near the local minimum to a quadratic function of the pair (ϵ,τ).

Figure 4.6 shows the projection of χ^2 as a function of the detection efficiency ϵ and the lifetime τ, respectively, for the same nucleus. The detection efficiency calculated from the simulation corresponds to ϵ=(37±6)%, whereas the value extracted from the data is ϵ=40%. The half life of this ion was previously reported as 11 ± 3 s [155]. The present χ^2 fitting procedure returns a half life of 15 ± 3 s. The agreement of the values provided for ϵ and τ confirms the success of the numerical procedure even when the parameter ϵ is also set up as free parameter in the Monte-Carlo simulation.

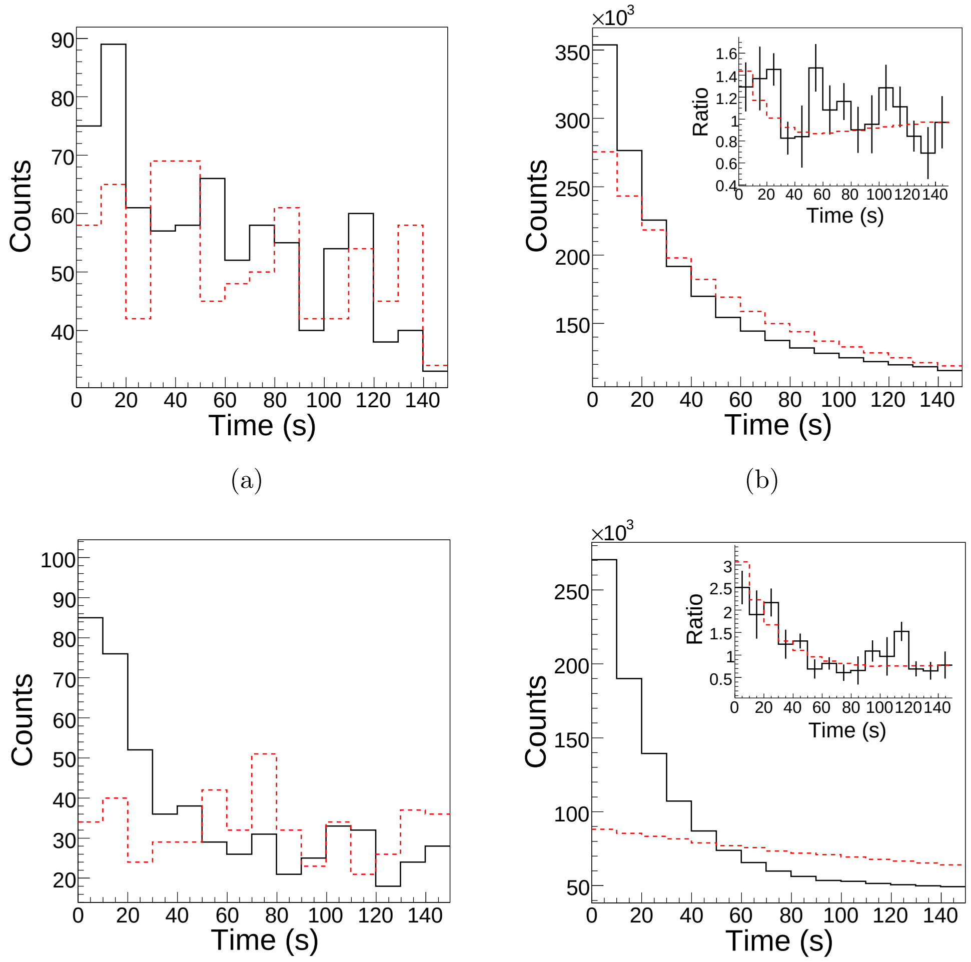

(a) (b)

(c) (d)

Figure 4.4: (a) Measured ion-β time correlations in forward- (solid line) and backward-time (dashed red line) directions for the nucleus ^{204}Pt. (b) Simulated time distributions of the same fragment in forward- and backward-time directions for the value of τ (23 s) responsible of the χ^2 minimisation. The inset panel shows the measured ratios of the forward- and backward-time correlations (black line) with their error bars, as well as the Monte-Carlo simulated ratios for the lifetime that minimises the χ^2 fit (dashed red line). (c) and (d) Same figures for the nucleus ^{202}Ir, corresponding to a value of $\tau = 22$ s.

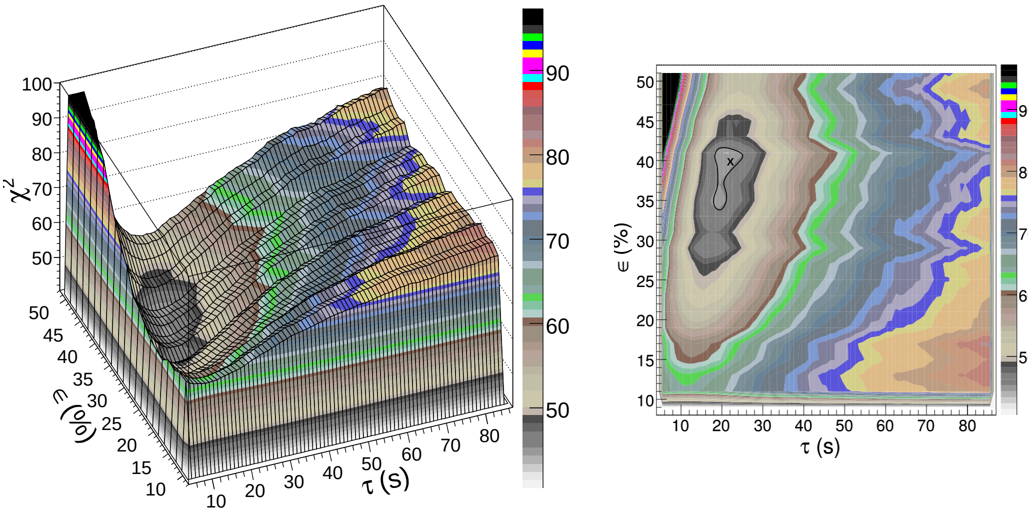

Figure 4.5: Left: hypersurface of χ^2 as a function of the detection efficiency ϵ and the lifetime τ. Right: contour plot of χ^2 as a function of the detection efficiency ϵ and the lifetime τ. The black solid line indicates the $\Delta\chi^2 = 1$ contour, whereas the cross points out the pair (ϵ,τ) = (40,22) responsible of the χ^2 minimisation. Data corresponding to ^{202}Ir.

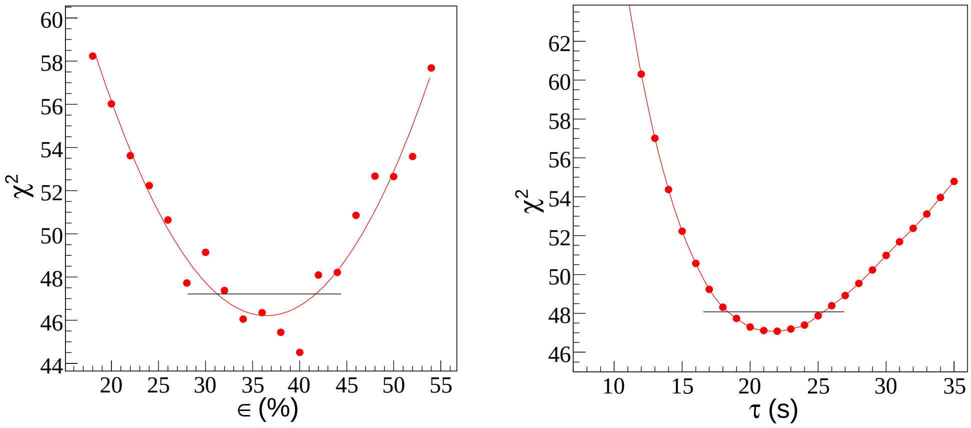

Figure 4.6: Left: Projection of χ^2 into the detection efficiency coordinate for a lifetime of 22 s. Right. Projection of χ^2 into the lifetime coordinate for a detection efficiency of 40%. Data corresponding to ^{202}Ir.

4.3.4 Limits of the procedure

The MIE background contamination events determine the minimum correlation time T_{min}, which is defined as the minimum time interval between two successive implantation events. Shorter times would imply the correlation of a β-like event to the next implanted fragment. On the contrary, the time T_{max} is defined as the longest time interval in which a β-decay electron can be correlated with an implanted nucleus. Since β-decays are random events, an appropriate estimation for T_{max} encompasses between 2 to 5 times the expected value of the half life of the selected nucleus [127]. Longer T_{max} times would increase the possibility of correlating the γ-labelled β-decay event with a false implantation.

In order to evaluate the quality of our data, it is worth determining the signal-to-noise ratio of our spectra. With this aim, we define a *figure of merit* F [156], as the ratio between the number of "true" correlations N_{true} and the random fluctuations of background events $\sqrt{N_{back}}$, characterising the statistical significance of the experimental conditions:

$$F = \frac{N_{true}}{\sqrt{N_{back}}} \tag{4.6}$$

A value of $F = 1$ means that the experimental β-decay curve can very likely be interpreted as a statistical fluctuation of the background contamination. For larger values of F, this probability becomes smaller.

A straightforward calculation of F consists in considering all the correlations within a time interval $t = T_{1/2}$ and determining the number of "true" correlations. The number of false β-like events detected within a given cell in a time period t depends on the β-background probability, which follows a Poisson distribution:

$$P_{\beta}^{back}(t) = \frac{(\nu_{\gamma,\beta}^{back} t)^n}{n!} e^{-\nu_{\gamma,\beta}^{back} t} \tag{4.7}$$

where $\nu_{\gamma,\beta}^{back}$ is the frequency of γ-labelled β-background events, and can be determined from the slope of the correlation spectra in backward-time direction. Note that, identically, the implantation probability follows a Poisson distribution. Let N_F be the total number of implanted nuclei from which the half life $T_{1/2}$ can be measured. The number of genuine β-decays detected in a time interval $t = T_{1/2}$ after the implantation of the nuclide is then $N_F \varepsilon/2$, and the number of true correlations is given by

$$N_{true} = \frac{N_F}{2} \cdot \varepsilon \cdot P_{0,\beta}^{back}(T_{1/2}) \tag{4.8}$$

Nuclide	N_F	ν_F (s^{-1})	$\nu_{\gamma,\beta}^{back}$ (s^{-1})	ε (%)
^{204}Au	10628	0.018	0.0031	0.12
^{204}Pt	16168	0.024	0.0034	0.058
^{203}Pt	20678	0.038	0.0033	0.056
^{202}Ir	5189	0.0055	0.0010	0.103
^{201}Ir	17245	0.033	0.0017	0.032
^{200}Ir	4792	0.012	0.0031	0.17

Table 4.2: Parameters associated with each nucleus: number of fragments N_F, average fragment implantation rate ν_F, γ-labelled β-background frequency $\nu_{\gamma,\beta}^{back}$, and total detection efficiency ε. Recall that the β detection thresholds correspond to those pointed out in section 4.3.1.

where $P_{0,\beta}^{back}(T_{1/2})$ is the probability of detection of no one background electron in a time $T_{1/2}$.

Following the discussion, the number of background events detected in a time interval $t = T_{1/2}$ is given by the probability of having either one or more background electrons in this period:

$$N_{back} = N_F \cdot [1 - P_{0,\beta}^{back}(T_{1/2})] \tag{4.9}$$

Note that we have considered false all the correlations registered in the same time period than a background electron. From equations 4.6, 4.8 and 4.9, we learn that the figure of merit depends on the half life of the nucleus of interest:

$$F = \frac{\varepsilon\sqrt{N_F}}{2} \cdot \frac{e^{-\nu_{\gamma,\beta}^{back} \cdot T_{1/2}}}{\sqrt{1 - e^{-\nu_{\gamma,\beta}^{back} \cdot T_{1/2}}}} \tag{4.10}$$

A value of F=3 means that the probability of having a significant background is 2×10^{-5} [156], thus ensuring reliable results. If we take this value as reference, the maximum half life $T_{1/2}^{max}$ experimentally measurable can be extracted from eq. 4.10. Note that this criterion is only an approximate estimation of the signal-to-noise ratio in the time distributions, since the β-decays occurred during the spill time are omitted, and the real data present a single fragment implantation rate $\nu_F^{(x,y)}$ per pixel instead of an averaged value for all the pixels in the active stopper.

Table 4.2 summarises the parameters associated to each nucleus: number of fragments N_F, average fragment implantation rate ν_F, γ-labelled β-background frequency $\nu_{\gamma,\beta}^{back}$, and total detection efficiency ε. The correspondent values of F and $T_{1/2}^{max}$ are shown in table 4.3 and will be discussed in the next section.

4.3.5 Results

The β-decay half lives of six nuclei have been measured using the novel numerical procedure, two of which were previously reported. Prior measurements on the half life of ^{204}Au provide a value of $T_{1/2}$=39.8 ± 0.9 s [135]. The method used consisted in fitting the experimental data to exponential time distribution functions. The half life measured from this experiment is $T_{1/2}$=37.2 ± 0.8 s, which is in agreement with the reported result within two standard deviations, despite the presence of MIE background events in the ion-β time correlated spectrum. Concerning ^{202}Ir, the reported half life was $T_{1/2}$=11 ± 3 s [156], in perfect agreement with the result obtained in the present work, $T_{1/2}(^{202}Ir)$=15 ± 3 s.

The half lives of the other four heavy neutron-rich nuclei, ^{204,203}Pt and ^{201,200}Ir, have been measured for the first time from the data of this experiment. Note that the input parameters of the Monte-Carlo code depend on the configuration of the middle DSSSD detectors and on the β-decay threshold established. Thus, the fitting procedure can be performed for several configuration settings of the same nucleus, providing analogous measurements of its half life. These values, provided in appendix E, correspond to the minimum χ^2 obtained from the measured and simulated ratios between the forward- and backward-time distributions as a function of the lifetime τ.

Table 4.3 summarises the properties of the nuclei under study: γ-ray decays used to label the β-electrons, experimental half lives with their uncertainties, time T_F elapsed between two consecutive implantations, figures of merit F and maximum half lives measurable considering a figure of merit of 3. The half lives have been calculated as the average of the values measured in every configuration setting for each nucleus. The excellent quality of the data analysis is manifested in the table, where the smaller figure of merit, $F^{^{201}Ir}$=10.7, triplicates the value F=3 from which the numerical analysis is considered reliable. Furthermore, the broad time interval between the measured values and the maximum lifetimes experimentally measurable -above 2 min- ensures that the observed γ-ray decays characterise the daughter nuclei, instead of the grand-daughter nuclei.

Nucleus	E_γ	$T_{1/2}$ (s)	T_F	F	$T_{1/2}^{max}$ (s) (F=3)
^{204}Au (*)	436	$37.2^{+0.8}_{-0.8}$	56	16.8	311
^{204}Pt	305	16^{+6}_{-5}	42	13.3	153
^{203}Pt	943	22^{+4}_{-4}	26	13.2	193
^{202}Ir (*)	535	15^{+3}_{-3}	182	30.0	607
^{201}Ir	655	21^{+5}_{-5}	30	10.7	178
^{200}Ir	470	43^{+6}_{-6}	83	16.9	335

Table 4.3: Nuclei studied in the current work. The γ-ray transitions used to label the β-electrons are shown in the table, as well as the measured β-decay half lives, the time elapsed between two consecutive implantations, the figures of merit and the maximum half life experimentally measurable considering F=3. The half lives of the nuclei marked with an asterisk were previously reported (see text for details).

4.4 Validation of the analysis procedure

4.4.1 Comparison with analytical techniques

The novel technique used in this dissertation represents a powerful analysis tool to determine β-decay half lives, since it can be employed under the most extreme conditions, either if they are low statistics or complex background contamination. To verify its success, it is worth evaluating the half lives using a conventional method. The most well known consists in fitting the experimental data to an exponential time-distribution function.

As we discussed somewhere else, the forward-time spectra show a convoluted background originated by the combination of high implantation rates and long lifetimes, as well as by other β-like events that do not come from the selected nucleus. The shape of the background distribution must be well established in order to disentangle the real events from the uncorrelated ones. With this aim, the backward-time spectra are fitted to an exponential function, in such a way that the genuine decay constant λ of the radioactive-decay data is extracted by using the fitting function

$$N_0 e^{-\lambda t} = N_0^{forw} e^{-\lambda^{forw} t} - N_0^{back} e^{-\lambda^{back} t} \tag{4.11}$$

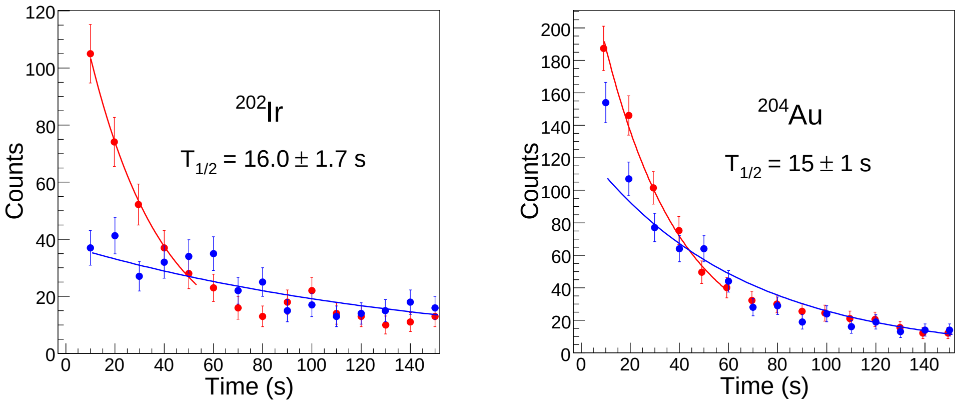

Figure 4.7: Forward- (red line) and backward-time (blue line) exponential fits of the time correlated distributions for ^{202}Ir (left) and ^{204}Au (right). See text for details.

where N_0^{forw}, N_0^{back} refer to the fitting constants and λ^{forw}, λ^{back} to the decay constants of the forward- and backward-time distributions, respectively.

As an example, figure 4.7 shows the exponential fits of the forward- (red line) and backward-time (blue line) distributions for ^{202}Ir and ^{204}Au. These spectra have been obtained for a β-decay detection threshold of 150 keV and a time binning of 10 s/bin. The considered DSSSDs configuration corresponds to two individual DSSSD middle detectors each of 1mm Si thickness, and the β events are labelled by the 535 keV and 436 keV transitions of the first excited state in the daughter nuclei ^{202}Pt and ^{204}Hg, respectively.

The β-decay half lives evaluated with this method are $T_{1/2}(^{202}Ir) = 16.0 \pm 1.7$ s and $T_{1/2}(^{204}Au) = 15 \pm 1$ s. In the first case, the good agreement with the value provided in section 4.3.5 ($T_{1/2}(^{202}Ir) = 15 \pm 3$ s) confirms the validity of the novel technique. In the second case, the half life measured with the analytical technique is much shorter than the values provided by the numerical procedure and ref. [135]. As table 4.3 illustrates, the half life of ^{204}Au is of the order of the time elapsed between implantations. This produces a significant amount of MIE events in the time correlated spectra that spoil the measurement of the half life from analytical fits. In the case of ^{202}Ir, the half life is much shorter than the time elapsed between implantations, and the MIE background in the decay-time spectrum is negligible. The numerical procedure, thus, provides reasonable $T_{1/2}$ values when the frequency of implantation is of the order of the decay constant, since the technique evaluates and disentangles properly the false correlations. The experimental conditions of the other nuclei of interest -shown in table 4.3- justify the necessity of employing this novel method to determine their half lives.

4.4.2 Comparison with former data

The data analysed in previous works using the numerical procedure [19] were extremely complex due to the absence of the γ-ray spectrometer in the experimental setup. Thus, implantations and decays were only correlated in position and time using the active stopper, and the authors ignored if the selected β-like event was the β-decay of the nuclide under study or a β-background event. Two versions of the method were developed. Firstly, one that accumulated all β-like events observed after the fragment implantation up to a given maximum time T_{max} and, secondly, a version which accumulated only the first β-like event detected after implantation, making the time correlations in both, spill and pause and only during the pause for each of them. From the study of the resulting β-decay half lives, they observed that finding the first β-like event during the pause after fragment implantation gave a clearer sign of the β-decay and reduced the influence of the β-background.

In spite of the different experimental conditions present in both experiments, it is worthwhile pointing out the good agreement between the measured half lives of the neutron-rich nuclide ^{202}Ir (see section 4.3.5). The consistency of both results allows us to verify the described analysis procedure, whether we take advantage of the β-prompt γ-ray time coincidences or we approach the analysis only with position-time correlations between implantations and decays.

4.4.3 Comparison with theoretical predictions

Hitherto several models have been developed to calculate the half lives of nuclei approaching the r-process path. We will concentrate in two of them. The first is a macroscopic phenomenological approximation known as the Gross Theory [128]. The second, the Quasi-particle Random-Phase Approximation (QRPA), is a microscopic model. In this work we will concentrate on the two QRPA calculations performed in the $N \approx 126$, $Z > 70$ region, developed by P. Möller et al. [129] and by I.N. Borzov et al. [130], respectively. The first calculation is a macroscopic-microscopic approach based on the Finite-Range Droplet Mass model (FRDM) [137], which includes the Gamow-Teller (GT) transitions within the Quasi-particle Random-Phase Approximation (QRPA) and the first-forbidden (FF) transitions within the Gross Theory framework. The second calculation is based on a self-consistent

Nuclide	$T_{1/2}$ (s)	$T^{th}_{1/2}$ (s) Gr. Th.	$T^{th}_{1/2}$ (s) FRDM+QRPA	$T^{th}_{1/2}$ (s) DF3+cQRPA
^{204}Au	$37.2^{+0.8}_{-0.8}$			
^{204}Pt	16^{+6}_{-5}	6.8	321.8	7.4
^{203}Pt	22^{+4}_{-4}	41.1	564.0	12.7
^{202}Ir	15^{+3}_{-3}	8.5	68.4	9.8
^{201}Ir	21^{+5}_{-5}	18.5	130.0	28.4
^{200}Ir	43^{+6}_{-6}	13.3	124.1	25

Table 4.4: β-decay half lives measured in this work. For comparison, the half lives predicted by some theoretical models are also indicated. See text for details.

DF3 energy density functional+continuum QRPA (cQRPA), which includes the contributions of GT and FF decays on an equal microscopic footing.

Table 4.4 shows the half lives measured in this work. For comparison, the predictions of the astrophysical models aforementioned are also displayed.

Figure 4.8 shows a comparison between the half lives measured in this work and the theoretical predictions discussed above. Regarding the FRDM-hybrid QRPA(GT)+FF(Gr.Th.) calculations, the experimental half lives are overestimated typically by one order of magnitude, getting this effect stronger as the closed proton shell Z=82 is approached. The Gross Theory and the DF3+cQRPA models reproduce better the experimental data. Generally, the half lives calculated by Borzov et al. differ from the experimental values by a factor of two. These results are consistent with the systematic comparison performed in ref. [19].

From the β-delayed spectroscopic analysis of chapter 3 two conclusions were drawn: the spherical-like shape of the investigated nuclei, and the major role of FF transitions in the β-decay of nuclei with low and medium Q_β values approaching the N=126 shell closure. The microscopic treatment of FF decays in near spherical nuclei close to the 126-neutron shell is well described in the DF3+cQRPA approach. As a consequence, this model provides unexpected shorter half lives that are in good agreement with our data. As well, it supports the conclusions on the β-decay process picture in this region of the Segrè chart [149], pointing out the importance of including GT and FF transitions from an equal microscopic footing in the calculation of the total

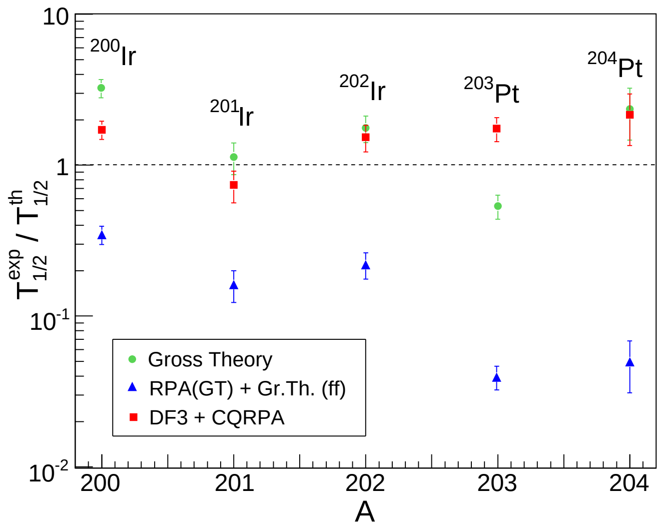

Figure 4.8: Ratios between the experimental half lives and the theoretical calculations mentioned in the text.

half lives. Following this argument, the macroscopic statistical treatment of the FF transitions in the astrophysical model of P. Möller et al. may be the cause of the orders-of-magnitude deviation from the measured half lives.

Although these conclusion cannot be firmly established from this work, they indicate that the r-process matter flow through the A=195 waiting-point is faster than expected by the QRPA(GT)+FF(Gr.Th.) model, used in standard r-process calculations. As well, the velocity of synthesis of the heaviest r-process nuclei would be faster than expected, thus modifying the existing picture of the r-process nucleosynthesis. Their confirmation, hence, would shed light on one of the most relevant unanswered questions of the current physics: which is the origin of heavy elements in the Universe [1].

Summary and conclusions

This work is devoted to the study of the β-decay of nuclei approaching the r-process path near the magic 126-neutron shell, of main importance to understand the evolution of shell structure in heavy nuclear systems and the matter flow through the third r-process peak of elemental abundance distribution. These investigations require the use of an experimental set up where heavy neutron-rich nuclei can be produced, identified and analysed. Such expectations are fulfilled in the worldwide unique facility GSI, where the nuclei of interest can be produced using in-flight fragmentation of relativistic lead projectiles in inverse kinematics. The most neutron-rich fragments, synthesised in cold fragmentation reactions, are selected and identified in the FRagment Separator, and finally are stopped in a β-delayed spectroscopy system set up to carry out the β-decay studies. These residues are some of the most exotic nuclei synthesised up to date.

Under this experimental landscape, we have approached the study of the β-decay phenomenon in nuclei "south-west" of ^{208}Pb through three different areas in nuclear physics. The first of them encompasses the investigation of the (p,n) charge-exchange as an optional reaction mechanism to produce new nuclei approaching the waiting-point A=195. In this work, the N=127 isotones ^{207}Hg, ^{206}Au, ^{205}Pt and ^{204}Ir have been produced for the first time from (p,n) charge-exchange reactions, induced in the collision $^{208}Pb+^{9}Be$ at 1 A·GeV. Their production cross sections have been measured and compared to their fragmentation cross sections using ^{238}U projectiles, simulated with the code COFRA. As a result, the (p,n) charge exchange of lead beams has been proved to be an optimum reaction mechanism to synthesise N=127 isotones with proton number larger or equal than 78, whereas for smaller masses the fragmentation of ^{238}U is a more appropriate mechanism of production.

The second topic approached in this dissertation is the study of the low energy structure of several nuclei following β-decay of the residues produced in fragmentation reactions. Particularly, we have measured the low-lying excited states of ^{204,203}Au and ^{202,201,200}Pt using β-delayed γ-ray spectroscopy. The observed nuclear states have been compared to shell model calculations to test their single-particle purity, using the code OXBASH. The difficulty to perform the single-particle interpretation of these nuclei scales with the number of valence holes out of the ^{208}Pb core, since the configuration mixing of the calculated nuclear levels increases with the density of nuclear states. In spite of this, the spherical-like shape of these systems has been proved. In the case of the even-even Pt isotopes, we have observed some features typical of the O(6) limit of the IBM theory, pointing out an incipient collective behaviour beyond the scope of the shell model. These are the repeating 0^+-2^+-2^+ cascade with strong E2 transitions, and some transition sequences or relative intensities that cannot be explained from a shell model framework where the configurations of the nuclear states are strongly mixed. The treatment of these nuclei as collective systems is, unfortunately, beyond the scope of this thesis.

The SM calculations performed in this work generally predict transfers of angular momentum between the initial and final states ranging from 0 to 2 units, along with a change in parity. On the contrary, the allowed GT transitions appear only in nuclei with medium Q_β values, feeding high-lying states in the daughter nuclei. All these features point out the strong competition of high energy FF decays and low energy GT transitions in the β-decay near the 126-neutron shell gap. These expectations are supported by the observed apparent β-feeding to the final states, which represent the first structural evidence on the main role of the FF transitions in this region of the Segrè chart. The best example for this conclusion is the β-decay of ^{204}Pt, where only FF transitions feed the low energy states of the spherical-like daughter ^{204}Au, being the GT decays expected to lay far above the Q_β window by the SM calculations.

The third area covered in this experiment is the measurement of β-decay half lives, relevant to fix the r-process abundance pattern in the N≈126 bottleneck. The experimental lifetimes serve to constraint the nuclear models used in r-process calculations, whose predictions are particularly discordant near the waiting-point A=195. In this work, the β-decay half lives of ^{204}Au, ^{204,203}Pt and ^{202,201,200}Ir have been measured using the delayed-coincidence technique. Due to the specific operation conditions of the experiment, conventional analysis tools could not be applied to most of the nuclei. As a consequence, the numerical procedure proposed by T. Kurtukián et al. was adapted to the new data to measure the half lives of the exotic nuclei. The novel technique deals with complex background structures in the time-correlated spectra, as those induced when the lifetimes of the nuclei of interest are of the order of the time elapsed between implantations. The efficiency of the new analysis tool has been demonstrated with the exotic ^{202}Ir, whose half life has been measured using analytical functions and the two versions of the numerical procedure. The consistency of the three results guarantees the robustness of the method. We have also performed a systematic comparison of the measured half lives with the values predicted by two state-of-the-art nuclear models used in r-process calculations. The first, the FRDM+QRPA model, includes GT decays within the microscopic QRPA approximation and FF transitions within the macroscopic Gross Theory framework. The second, the new DF3+cQRPA model, assumes a strong competition of high energy FF decays and low energy GT transitions in the β-decay of nuclei near the waiting-point A=195, describing GT and FF transitions from an equal microscopic footing. Whilst the standard FRDM+QRPA approach overestimates the experimental half lives by one order of magnitude, the successful description of our measurements with the DF3+QRPA model indicates the important role of the FF decays in the calculation of the total half lives, confirming the conclusions drawn from our spectroscopic studies. Consequently, if this tendency is kept towards the third r-process abundance peak, the matter flow to heavier fissioning nuclei will be faster than expected by the current standard r-process calculations.

In spite of the significant indications found out in this work, further experiments will be necessary to confirm the role of the FF decays in N$\sim$126 nuclei approaching the neutron drip-line. Such verification would lead to a revision of the current β-decay models used to predict the properties of the r-process nuclei in the third peak of elemental abundance distribution, which in turn would modify the global picture of the r-process nucleosynthesis.

In summary, this work provides a step forward in the attempts to explore the challenging region “south-west” of lead. Further expectations to investigate the nuclear reactions occurred in the astrophysical processes that lead to the formation of the heaviest elements in the Universe will be approached in the new-generation of in-flight radioactive-beam facilities, like RIKEN or FAIR, where many of the remote exotic nuclei will be accessible for the first time.

Appendix A

Beam-line setup at S2

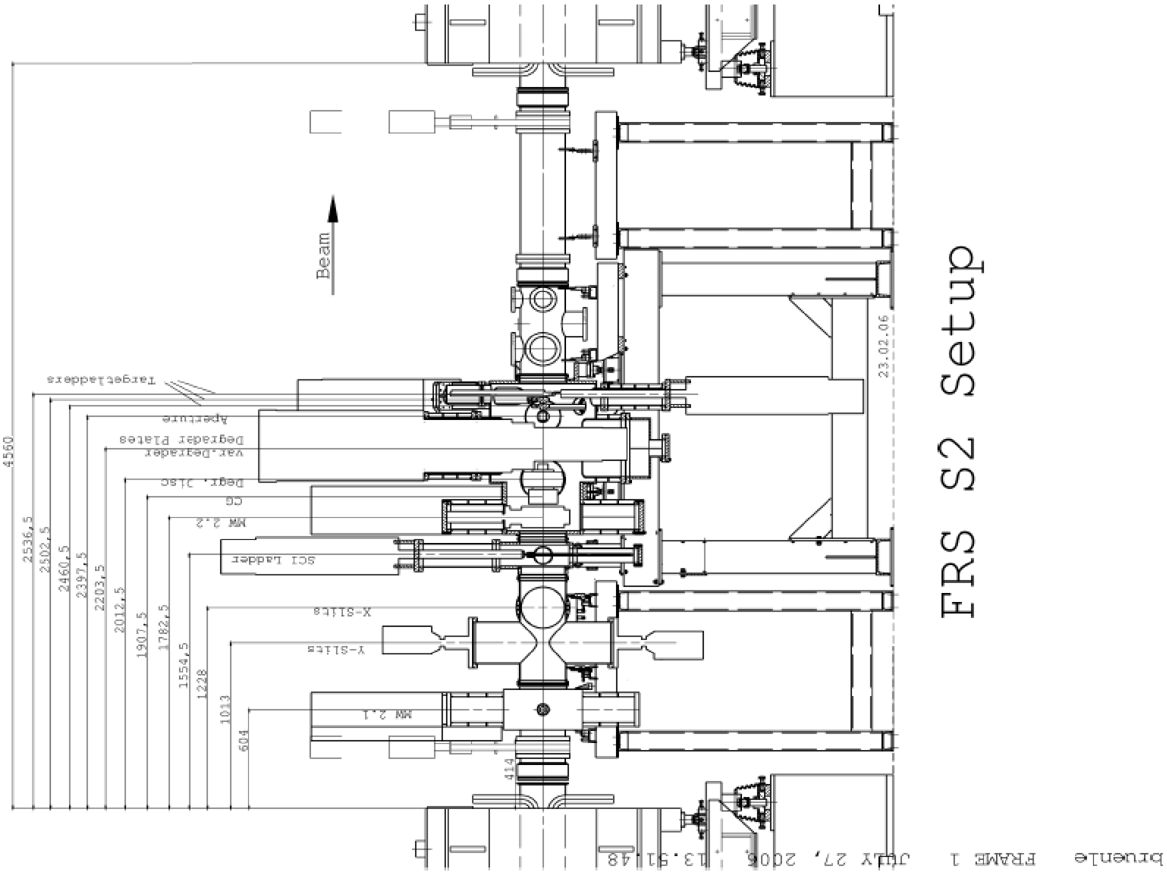
FRS S2 Setup
Beam
23.02.06
Targetladders
Aperture
Degrader Plates
var.Degrader
Degr. Disc
CG
MW 2.2
SCI Ladder
X-Slits
Y-Slits
MW 2.1
4560
2536,5
2502,5
2460,5
2397,5
2203,5
2012,5
1907,5
1782,5
1554,5
1228
1013
604
414
bruenle FRAME 1 July 27, 2006 13:51:48

Figure A.1: Technical drawing of the FRS beam-line setup at the S2 region. The arrows indicate the distance in mm from the beginning of S2 to the corresponding device.

Appendix B

Beam-line setup at S4

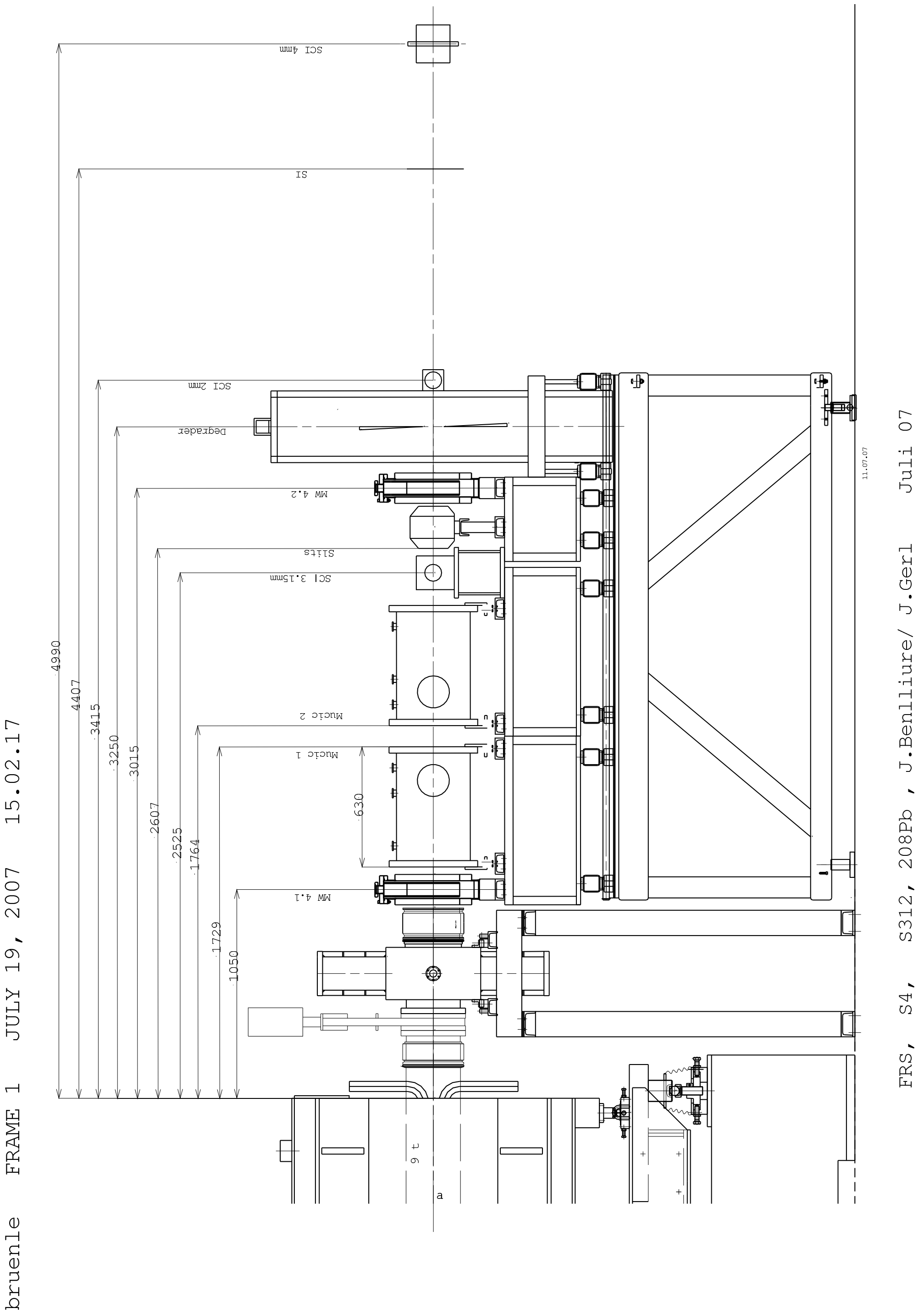
SCI 4mm
SI
SCI 2mm
Degrader
MW 4.2
Slits
SCI 3.15mm
Music 2
Music 1
MW 4.1
4990
4407
3415
3250
3015
2607
2525
1764
1729
1050
630
11.07.07
bruenle FRAME 1 JULY 19, 2007 15.02.17
FRS, S4, S312, 208Pb , J.Benlliure/ J.Gerl Juli 07

Figure B.1: Technical drawing of the FRS beam-line setup at the S4 region. The arrows indicate the distance in mm from the beginning of S4 to the corresponding device.

Appendix C

List of layers in the beam line

Area	Layer	Material	Thickness (mg/cm^2)	Eq. Al thickness (mg/cm^2)
TA	SIS window	C	0.035	0.05
	SEETRAM	Ti	13.5567	12.08
	Target 1	Be	1624	1638.15
	Target 2	Be	2513	2537.04
	Stripper	Nb	221	183.01
S2	SCI21		-	379.92
	Degrader	Al	variable	variable
	Stripper	Nb	106.88	88.38
S4	Vacuum window	Ti	90	81.43
	Air		-	140
	MW41		-	116.71
	Air		-	10
	MUSIC41		-	274.98
	Air		-	14.85
	Stripper	Nb	222.82	177.95

Continue in the next page.

Area	**Layer**	**Material**	**Thickness** (mg/cm^2)	**Eq.Al thickness** (mg/cm^2)
	MUSIC42		-	274.98
S4	Air		-	54.48
	SCI41		-	505.8
	Air		-	46.54
	MW42		-	116.71
	Degrader	Al	variable	variable
	Air		-	15.39
	SCI42		-	252.94
	Air		-	158.75
	Active stopper	N	-	1.92
	(DSSSD 1)	Si	-	238.36
		N	-	0.465
	(DSSSD 2)	Si	-	238.36
		N	-	1.92
	Air		-	78
	SCI43		-	505.86

Table C.1: List of layers of matter placed along the set-up line during the experiment. The degrader thicknesses of every setting can be perused in ref. [67].

- Total equivalent Al thickness of S4 (without degrader) ⇒ 3727.44 mg/cm^2
- Equivalent Al thickness from the beginning of the S4 area till the end of the active stopper ⇒ 3141.64 mg/cm^2
- Equivalent Al thickness of 1 mm of Si ⇒ 238.36 mg/cm^2
- Equivalent Al thickness from 0.5 mm of DSSSD 1 to the surface of SCI43 ⇒ 440 mg/cm^2

Appendix D

Total β-delayed γ-ray energy spectrum

The experimental conditions of the present work make the β-delayed γ-ray spectroscopic analysis substantially delicate. Indeed, the information available in our data is significantly reduced by the strong restrictions imposed over the already scarce statistics.

We stated previously that the γ-γ coincidence analysis represents an extraordinary efficient tool to find out explicit information on the low-energy structure of the isotopes of interest. The reason is straightforward: due to the high precision of the coincidence technique, most of the conditions established in the β-delayed γ-ray spectroscopic analysis could be avoided. By this way, we obtained a *total energy spectrum* containing all the electromagnetic decays detected after the implantation of the fragmentation residues. Recall that the collected data correspond to an FRS magnetic setting optimised to transmit the neutron-rich nuclide ^{202}Ir. The spectrum, shown in figure D.1, was sorted under the following conditions: firstly, all the β-decay triggers detected during the beam pause were considered. Secondly, no time or position correlations between implantations and decays were established. Thirdly, only the γ-ray transitions observed within the prompt-flash (see figure 1.23) were included. Finally, the spectrum was addback-corrected applying the intra-cluster addback-routine described in section 1.6.3 to γ-ray energy signals above 25 keV.

One last point worth mentioning is that figure D.1 displays characteristic γ-rays of all the nuclides formed after subsequent β-decays of the species implanted in the active stopper. Whilst the nuclide to which every transition belongs (if known) is labelled in parenthesis after the energy of the photopeak, the γ-rays marked with an asterisk have not been located in any decay diagram.

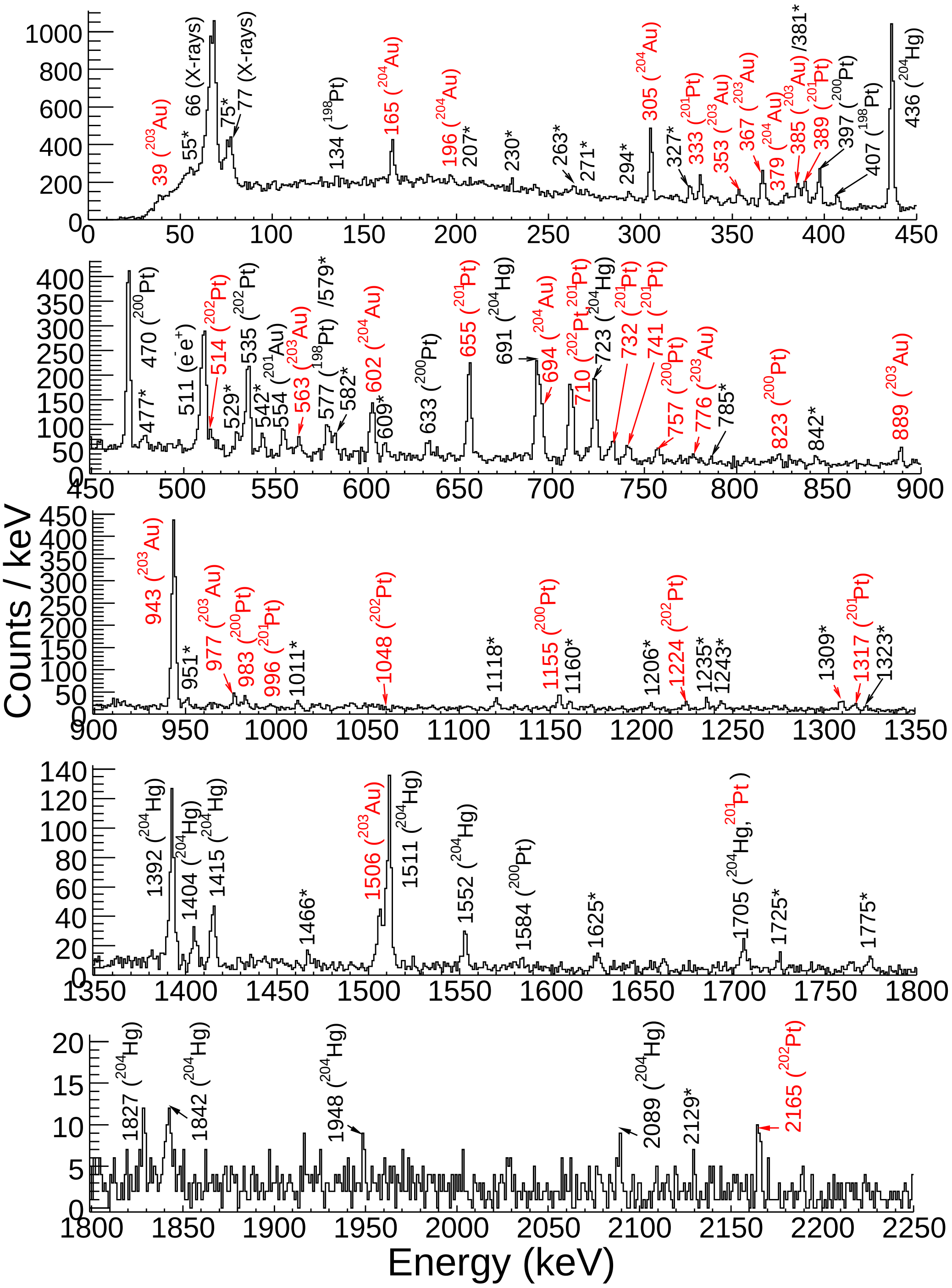

Figure D.1: Total β-delayed γ-ray energy spectrum for an FRS magnetic setting centred in ^{202}Ir. The nuclide to which every transition belongs, if known, is attached within parenthesis beside the energy of the photopeak, whereas an asterisk indicates that the origin of the γ-ray decay is uncertain. The transitions characterised for the first time in the present work are labelled in red in order to provide a general view of the spectroscopic results.
]]>

Appendix E

γ-labelled β-decay half lives

As we mentioned in chapter 4, the β-decay half lives of the heavy neutron-rich nuclei ^{204}Au, ^{204,203}Pt and ^{202,201,200}Ir have been measured from a χ^2 fit between the simulated and experimental ratios of the γ labelled ion-β time correlations in forward- and backward-time directions. The simulated spectra were generated using a Monte-Carlo code, whereas the experimental curves were obtained from event by event position and time correlations between the implanted ions and the γ-labelled electrons emitted in their decay.

The shape of every β-decay spectrum depends on two factors. The first is related to the two central DSSSD detectors, that can be considered as two independent catchers or a unique device depending on the implantation width profile of the exotic nuclides. The second is related to the energy threshold considered to select a β-decay electron, since higher β-decay thresholds imply lower number of β-like particles detected. Nevertheless, the "true" β-decay half life is constant, and thus independent of any variation in the γ-labelled β-decay spectrum. This fact can be used as a benchmark of the analysis procedure, since the Monte-Carlo simulation must reproduce faithfully the experimental conditions. Indeed, the parameters f_β^γ and ϵ introduced in the Monte-Carlo code (see section 4.3.1) take different values according to the conditions considered, thus modifying the simulated β-decay curve and keeping constant the experimental half life.

Table E.1 summarises the γ-labelled β-decay half lives measured in the present work for every DSSSD configuration and every β-decay threshold, together with all the associated parameters: implantation frequency f_I, γ-labelled β-decay frequency f_β^γ, number of counts of the most intense γ-ray peak of the daughter nuclide N_γ, detection efficiency ϵ and reduced chi-squared χ^2_ν. Note that both the half lives and uncertainties presented in table 4.3 result from calculating the average value of the different half lives measured for each nuclide.

Ion	**DSSSD config.**	**β thrs. (keV)**	**f_I (s^{-1})**	**f_β^γ (s^{-1})**	**N_γ**	**ϵ (%)**	**χ^2_ν**	**$T_{1/2}$ (s)**
^{204}Au	A	150	0.018	0.00175	1279	57	1.30	37.6 ± 0.5
		300		0.00143	1007	45	1.59	37 ± 1
		400		0.00111	797	36	1.47	37 ± 1
^{204}Pt	A	150	0.024	0.00264	943	22	1.20	16^{+5}_{-4}
		300		0.00219	715	17	0.86	15^{+7}_{-5}
^{203}Pt	A	150	0.038	0.00331	1164	45	1.22	23 ± 3
		300		0.00275	873	34	1.17	22 ± 4
		400		0.00207	661	25	1.31	22 ± 4
	B	150		0.00372	1164	45	1.15	22 ± 3
		300		0.00317	873	34	1.26	21 ± 4
		400		0.00247	661	25	1.25	21^{+6}_{-3}
^{202}Ir	A	150	0.0055	0.00086	533	55	1.12	17 ± 2
		300		0.00067	383	40	0.97	15 ± 3
		400		0.00049	309	32	1.15	13 ± 3
	B	150		0.00103	533	55	1.01	18 ± 3
		300		0.00078	383	40	0.98	15 ± 2
		400		0.00064	309	32	1.07	12 ± 2
^{201}Ir	B	150	0.033	0.00166	558	20	0.67	20 ± 4
		300		0.00133	446	16	0.68	20^{+5}_{-4}
		400		0.00099	335	12	0.84	23^{+7}_{-6}
^{200}Ir	B	300	0.012	0.00264	816	85	1.10	44 ± 5
		400		0.00231	651	68	1.24	42 ± 6

Table E.1: Parameters associated to the measurement of the β-decay half life of each nuclide. The DSSSD configuration A refers to two independent central DSSSD, whereas B refers to a unique central DSSSD of double the thickness.

Resumen en castellano

Introducción

Este trabajo se centra en el estudio estructural de varios isótopos exóticos cercanos a la capa cerrada de neutrones N=126. A través de la espectroscopía γ β-retrasada, trata dos de los asuntos más relevantes en la física nuclear moderna. El primero consiste en conocer los procesos que conducen a la formación de los elementos pesados en el Universo, ya que constituye uno de los mayores retos de la astrofísica nuclear moderna. Es bien sabido que la teoría de nucleosíntesis estelar predice la formación de aproximadamente la mitad de los elementos más pesados que el hierro como consecuencia del proceso de captura rápida de neutrones, también llamado *proceso r* [2–4]. El segundo tema consiste en comprender la evolución de la estructura interna de los núcleos a medida que éstos se hacen más ricos en neutrones. De este modo es posible comprobar la validez del formalismo teórico ya existente y modificarlo en su caso.

La formación de elementos pesados como el hierro tiene lugar en estrellas con temperaturas extremadamente elevadas, ya que se requiere la fusión del carbono, oxígeno y silicio. Los elementos aún más pesados se crean por la sucesión de capturas neutrónicas y desintegraciones β, de modo que el núcleo inicial adquiere neutrones que posteriormente se convierten en protones sin necesidad de suministrar energía. Dadas las condiciones astrofísicas requeridas, se cree que los escenarios estelares más propicios para la formación de los elementos pesados son las explosiones de Supernova tipo II y las estrellas de neutrones.

La vida media de la desintegración β es muy sensible al espaciado de los niveles energéticos altamente excitados en el núcleo hijo, como han demostrado recientes estudios teóricos [131]. Por ello representa un elemento crucial no sólo para comprobar la validez de los modelos nucleares lejos de la estabilidad, sino también para calcular la producción de elementos pesados en supernovas y estrellas de neutrones.

La región de la carta de núcleos con $N < 126$ y $Z < 82$ ha permanecido prácticamente inexplorada hasta hace pocos años, debido a la incapacidad de producir fragmentos tan exóticos en el laboratorio. Afortunadamente, la aceleración de proyectiles pesados a energías relativistas ha abierto la posibilidad de producir los núcleos pesados ricos en neutrones a través de mecanismos de reacción como la fragmentación fría [17] o las reacciones de intercambio de carga [18]. Cabe destacar el trabajo pionero realizado por T. Kurtukián et al. [19], consistente en el cálculo de la vidas medias de núcleos en torno al "punto de espera" $A = 195$.

A parte del cálculo de vidas medias, el trabajo tiene como principal propósito verificar la robustez de la cerradura de capas N=126 a medida que disminuye el número de neutrones y protones respecto al núcleo doblemente mágico ^{208}Pb. Las propiedades de los núcleos con forma esférica, esto es, con un número mágico o casi mágico de nucleones, son bien descritas por el modelo de capas [27–29]. En la región de interés, se espera observar el desarrollo de excitaciones colectivas y, en consecuencia, la aparición de deformaciones cuadrupolares β_2 del estado base a medida que el número de vacantes de neutrones aumenta[20, 21]. A lo largo de las últimas décadas se han desarrollado diferentes modelos nucleares para reproducir las estructura de los isótopos alejados de la estabilidad, el más importante de los cuales es el *Interacting Boson Model* (IBM) [30–35].

Los estudios elaborados en esta región de la carta de núcleos indican que el isótopo ^{196}Pt [43, 44] representa un ejemplo excelente de la simetría O(6) [45] del IBM. De hecho, estudios recientes [92] apoyan la idea de considerar la capa N=116 como la intersección entre formas proladas y obladas para núcleos más ligeros y más pesados, respectivamente. También se cree que los isótopos de Pt evolucionan hacia un carácter más vibracional a medida que se acercan a la capa N=126 [44, 46].

Esta tesis doctoral estudia la desintegración β de algunos núcleos pesados con N$\approx$126 próximos al proceso r de nucleosíntesis estelar. En particular, se propone la medida experimental de la vida media de los isótopos madre (^{204,203}Pt y ^{202,201,200}Ir), así como el estudio de la estructura a baja energía de los núcleos hijo (^{204,203}Au y ^{202,201,200}Pt) por medio de espectroscopía γ β-retrasada. Algunas propiedades de los isótopos de interés, como vidas medias, valores Q_β, estados isoméricos o niveles de baja energía, han sido estudiadas previamente via espectroscopía γ β-retrasada [134, 135, 141, 143, 144, 147], espectroscopía de isómeros [89], reacciones de transferencia de dos neutrones [44, 46] y extracción de protones [139, 140].

La técnica experimental requerida para realizar estos estudios debe ser capaz de producir e identificar los fragmentos en vuelo, así como de estudiar su desintegración β. Gracias al uso de detectores de última generación y a la colaboración de un gran equipo de científicos, la colaboración RISING de

GSI, la elaboración del presente trabajo ha sido posible.

Técnica experimental

El presente experimento se llevó a cabo en las instalaciones del *Gesellschaft für Schwerionenforschung* (GSI, Alemania) [51], donde es posible acelerar haces de Pb a energías relativistas utilizando el sincrotrón SIS-18 [47]. La figura 1 muestra un esquema del dispositivo experimental empleado.

Para producir los fragmentos pesados ricos en neutrones se inducen reacciones de fragmentación fría [17] haciendo colisionar un haz de ^{208}Pb a 1 A·GeV contra un blanco de Be de unos 2.5 g/cm^2 de espesor. Las reacciones de fragmentación son reacciones nucleares muy periféricas, en las que los nucleones del volumen de interacción son arrancados, dando lugar a un nuevo fragmento excitado. Posteriormente, el fragmento se desexcita mediante la emisión de partículas γ o nucleones. Cuando la energía de excitación está por debajo de la energía de separación neutrónica (es fría), únicamente se emiten protones, de forma que el núcleo resultante es rico en neutrones.

La separación e identificación de los fragmentos secundarios se realiza en vuelo, con la ayuda del separador magnético *FRagment Separator* (FRS) [68]. El FRS es un espectrómetro de alta resolución capaz de identificar en vuelo el cociente A/Q de cada núcleo, donde A representa el número másico y Q la carga iónica efectiva. Cuando un núcleo cargado atraviesa un campo magnético es deflectado de acuerdo con:

$$B\rho = \left(\frac{A}{Q}\right) \cdot \frac{m_0 c}{e} \cdot \beta\gamma \tag{1}$$

donde m_0 representa la unidad de masa, c la velocidad de la luz, e la carga del electrón y $\beta\gamma$ el momento relativista reducido, siendo $\beta = v/c$ y v la velocidad del fragmento de interés.

El método empleado para separar las diferentes especies nucleares en el FRS es el llamado $B\rho - \Delta E - B\rho$, que consiste en realizar dos selecciones magnéticas de los iones. La primera de ellas tiene lugar en los dos primeros dipolos y separa los fragmentos de acuerdo con su rigidez magnética $B\rho$, o lo que es lo mismo, con su cociente A/Q, ya que la velocidad de los fragmentos producidos en fragmentación fría apenas varía. La precisión en la medida de A/Q viene determinada por la resolución de las rigideces magnéticas y por la aceptancia del espectrómetro (±1.5%), por lo que una cantidad considerable de iones con un cociente A/Q similar al del fragmento estudiado se transmite a lo largo del FRS. Este problema se resuelve colocando un *degrader* de aluminio en el plano dispersivo del espectrómetro, de manera que los fragmentos

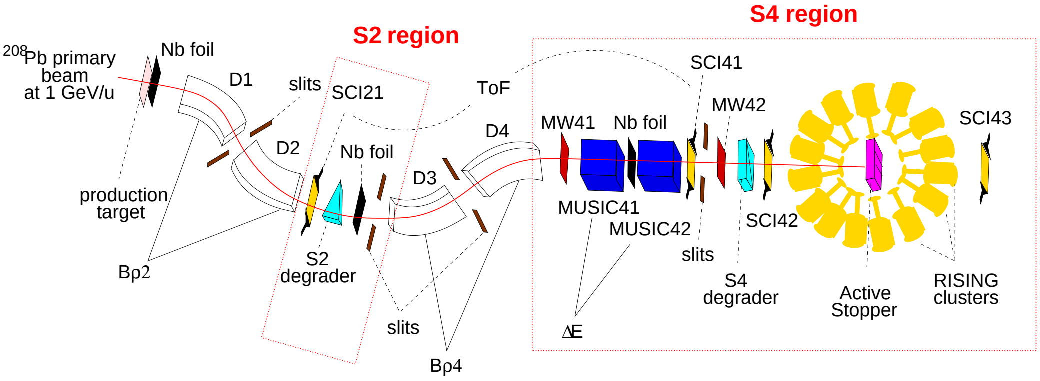
S2 region
S4 region
^{208}Pb primary beam at 1 GeV/u
Nb foil
D1
slits
SCI21
ToF
SCI41
MW42
SCI43
D2
Nb foil
D4
MW41
Nb foil
D3
production target
MUSIC41
MUSIC42
SCI42
slits
Bρ2
S2 degrader
S4 degrader
Active Stopper
RISING clusters
ΔE
slits
Bρ4

Figure 1: Vista esquemática del FRS y el equipo de detección utilizado para producir, identificar y estudiar la desintegración β de los núcleos pesados ricos en neutrones.

que lo atraviesan experimentan diferentes pérdidas de energía en función de su posición y salen con diferentes momentos del degrader. Los fragmentos pueden ser separados tras el degrader en una segunda selección magnética, en la que el cociente p/p' entre los momentos en la primera y la segunda etapa del FRS debe ser igual al cociente $B\rho/B\rho'$ entre las respectivas rigideces magnéticas.

De acuerdo con la ecuación 2, la masa de un isótopo puede ser calculada si se conocen su velocidad, su carga y su rigidez magnética. Esta última magnitud puede calcularse para cada etapa del FRS a partir de la medida de la dispersión y de la posición de los fragmentos, mientras que la velocidad se obtiene a partir de la medida del tiempo de vuelo de los iones en la segunda parte del FRS. Los detectores empleados para determinar la posición y velocidad de los fragmentos son centelleadores plásticos, mientras que las cámaras de ionización gaseosa (MUSICs [74]) miden la pérdida de energía de los fragmentos, proporcional a la carga iónica de acuerdo con la fórmula de Bethe-Bloch.

Uno de los principales obstáculos a la hora de trabajar con núcleos pesados son los estados de carga, i.e., estados de núcleos con uno o más electrones que se forman cuando un ion atraviesa un material. Si la determinación de los estados de carga no se realiza correctamente, la identificación de los fragmentos secundarios es confusa. Afortunadamente, el uso del degrader de Al en el plano dispersivo permite identificar sin ambigüedad cada núcleo. La selección en rigidez magnética que introduce, unida a la medida adicional de la pérdida de energía de los fragmentos al atravesarlo permiten identificar las distribuciones de estados de carga en el espectrómetro.

Para resolver este problema en las cámaras de ionización se combinan las medidas de dos MUSICs independientes separadas por una hoja de Nb, de manera que las variaciones de estados de carga son detectadas al comparar las pérdidas de energía en ambas cámaras.

La técnica experimental permite determinar las secciones eficaces de producción de cada núcleo mediante la medida de sus tasas de producción N_F, normalizadas al número total de proyectiles N_P y al número de átomos por unidad de área en el blanco N_T

$$\sigma(A, Z) = \frac{N_F}{N_P \cdot N_T} \tag{2}$$

Dado que la intensidad del haz incidente no fue monitorizada durante el presente experimento, el número total de proyectiles se extrapoló a partir de la ya conocida sección eficaz de fragmentación de ^{202}Ir [19], siendo considerado constante durante la toma de datos.

Después de la identificación de los fragmentos, éstos son decelarados y detenidos en la región de frenado, situada a la salida del FRS. El dispositivo experimental empleado consta de un degrader homogéneo de espesor variable, dos centelleadores de *veto*, una matríz de tres detectores de silicio y el espectrómetro de rayos γ RISING. La colocación del sistema se puede apreciar en la figura 1. Los iones pesados, que han sido producidos a energías relativistas, son decelerados al atravesar el degrader homogéneo. Los centelleadores de veto permiten determinar el espesor que debe tener el degrader para implantar los núcleos pesados en la matriz de silicios. Cada detector de silicio (Double Sided Silicon Strip Detectors, DSSSD, $5 \times 5 \times 0.1$ cm^3), consta de 16 pistas frontales y traseras que proporcionan las posiciones x e y a través de 256 píxeles. Adicionalmente, los detectores DSSSD están unidos a unos pre-amplificadores logarítmicos, capaces de detectar un amplio rango de energías, desde el frenado de los fragmentos implantados (más de un GeV) hasta la emisión de un electrón (menos de 1 MeV). La alta pixelación de estos aparatos nos permite determinar las vidas medias de los núcleos ricos en neutrones a través de correlaciones espacio-temporales entre los iones implantados y las desintegraciones β. Circunvalando la matríz de DSSSD, se encuentra el espectrómetro RISING en su *configuración de haz parado*, que consta de 15 cúmulos de detectores de Ge, cada uno de ellos conteniendo siete cristales hexagonales hiper puros tipo n de Ge montados en un criostato común. Los cúmulos de Ge están dispuestos en tres anillos angulares de cinco detectores en ángulos de 51°, 90° y 129°. Así, utilizando correlaciones temporales entre fragmentos, partículas β y rayos γ, se puede investigar la estructura de niveles a baja energía de núcleos madre e hijo, por medio de espectroscopía γ isomérica y β-retrasada, respectivamente.

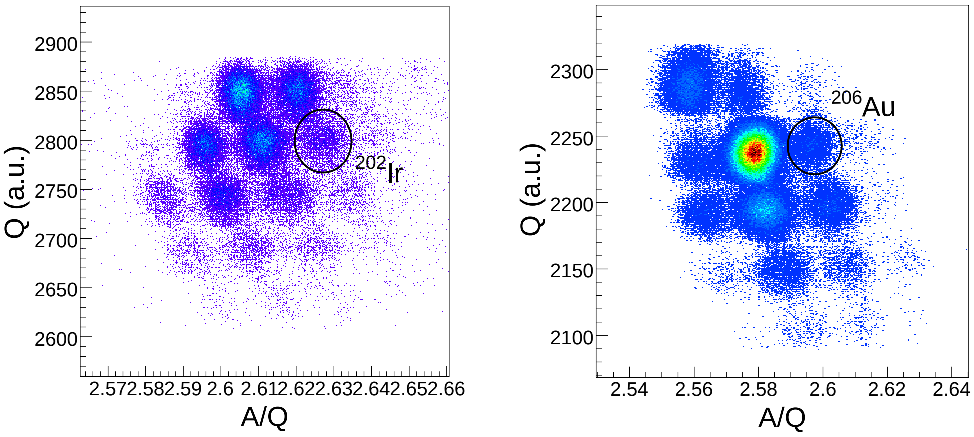

(a) *Configuración del FRS centrada en* ^{202}*Ir.*

(b) *Configuración del FRS centrada en* ^{206}*Au.*

Figure 2: Matrices de identificación isotópica.

Resultados

Identificación isotópica

La figura E.2(a) muestra la matriz de identificación de los isótopos producidos en una configuración del FRS centrada en ^{202}Ir, mientras que la figura E.2(b) muestra la matriz de identificación correspondiente a una configuración centrada en ^{206}Au. En ambos casos, cada cúmulo de puntos representa un un núcleo. La alta resolución obtenida con la técnica experimental descrita anteriormente ha permitido identificar sin ambigüedad las diferentes especies isotópicas producidas en el experimento.

En relación a la figura E.2(a), se han medido las vidas medias de los núcleos identificados y se ha estudiado la estructura a baja energía de los núcleos hijo. En la figura E.2(b), se han medido las secciones eficaces de producción por intercambio de carga (π,ν) de los isótonos con N=127.

Secciones eficaces de intercambio de carga

En este trabajo se han medido, por primera vez, las secciones eficaces de intercambio de carga de cuatro núcleos pertenecientes a la capa de neutrones N=127 (^{207}Hg, ^{206}Au, ^{205}Pt y ^{204}Ir). En la figura 3 se muestra con puntos negros la evolución de las secciones eficaces medidas en función del número de vacantes de protones respecto al proyectil ^{208}Pb. Por comparación, las

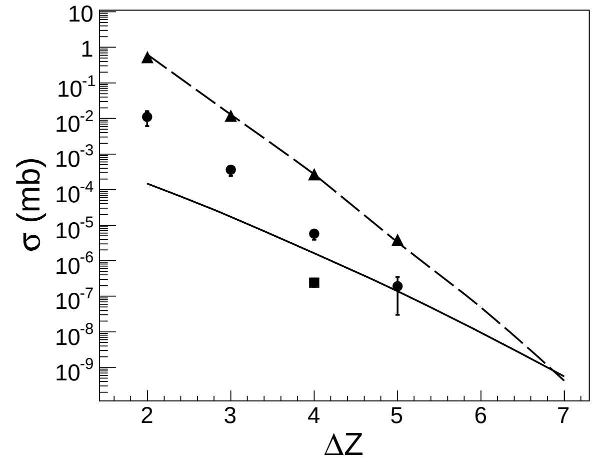

Figure 3: Secciones eficaces de los núcleos producidos por intercambio de carga en función del número de agujeros de protones relativos al núcleo proyectil ^{208}*Pb (puntos negros). En comparación, también se muestran las secciones eficaces de fragmentación fría de los núcleos con* $N = 126$ *[19] (triñgulos rojos) y una simulación de las secciones eficaces de fragmentación de* ^{238}*U para los núcleos con* $N = 127$ *(línea azul). El único dato experimental disponible en este último caso se muestra en el cuadrado verde.*

secciones eficaces de producción por fragmentación fría de los isótonos de la capa N=126 aparecen en triángulos, así como las secciones eficaces de fragmentación de ^{238}U para los núcleos de la capa N=127 (línea negra), simuladas con el código COFRA. La seccion eficaz de ^{205}Pt [116], la única medida experimental a partir de fragmentación de uranio, también se muestra. Finalmente, la línea punteada hace referencia a las secciones eficaces simuladas de los núcleos con N=126, producidos en fragmentación de plomo. En este último caso, la consistencia con los valores experimentales demuestra el gran poder predictivo de COFRA.

La figura 3 evidencia la idoneidad del intercambio de carga a energías relativistas para producir núcleos con N=127 y masas comprendidas entre A=205 y A=207. De esta manera, se podría estudiar la estructura nuclear de los isótonos con N=126 a través de su desintegración β.

Espectroscopía γ isomérica

En este trabajo se han reconocido transiciones isoméricas características de ^{204,203}Pt, previamente observadas [124, 125], que nos proporcionan un

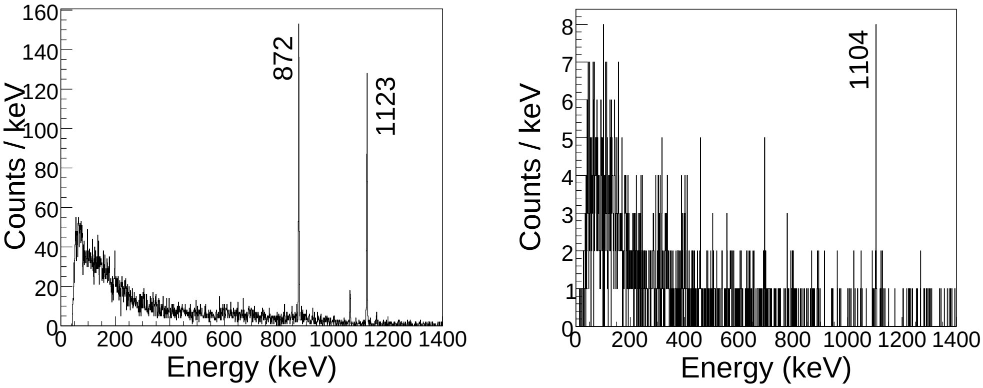

Figure 4: Espectros γ retrasados asociados a los núcleos ^{204}Pt (derecha) y ^{203}Pt (izquierda).

control interno del procedimiento de identificación isotópica. La figura 4 muestra los espectros γ de isómeros obtenidos en el presente análisis para estos núcleos.

Espectroscopía γ β-retrasada

Los espectros γ β-retrasados se obtienen a partir de correlaciones espacio-temporales entre los iones implantados en la matríz de detectores DSSSD y los electrones emitidos en su desintegración, así como de correlaciones temporales entre las partículas β y las transiciones γ registradas en el espectrómetro RISING. Los espectros resultantes presentan la superposición de tres componentes. En primer lugar, las transiciones γ características del núcleo estudiado. En segundo lugar, el fondo originado por la dispersión Compton, que constituye un continuo de energías. Y en tercer lugar, un fondo originado por transiciones características de otros isótopos, producto de correlaciones aleatorias entre el núcleo de interés y partículas β de otras especies presentes en los silicios, bien núcleos hijo de implantaciones colindantes o bien núcleos nieto. Este fondo es el más significativo, en tanto en cuanto las vidas medias de los iones implantados son del orden del ciclo temporal del haz primario.

Mientras el fondo Compton se puede reducir fácilmente aplicando una rutina de *addback*[1], el fondo conformado por transiciones características de otros núcleos es difícil de eliminar. Para ello, los fragmentos seleccionados sólo se correlacionan con la primera partícula β detectada en el píxel de implantación durante la pausa del haz. De acuerdo con las distribuciones de posición de los iones en la matríz de silicios, las correlaciones se realizan en el rango de strips X donde la implantación del núcleo de interés domina sobre el resto. La contaminación de fondo se reproduce en un nuevo espectro con la secuencia temporal inversa de correlaciones ion-β. Del espectro resultante se obtienen, sin ambigüedad, las transiciones magnéticas más intensas de cada núcleo. La información espectral se completa con el análisis de coincidencias γ-γ. La técnica de coincidencias supone una fuente de información muy importante a la hora de determinar la estructura nuclear de los isótopos estudiados, ya que la contaminación de fondo ligada a otras especies nucleares se suprime significativamente. Como consecuencia, es posible asignar a un núcleo dado las transiciones γ de menor intensidad, así como determinar la localización de los estados excitados en el esquema de niveles.

---

[1] La rutina de addback utilizada consiste en sumar las señales de energía de los cristales de Ge de un mismo cúmulo registradas simultáneamente, para así reconstruir la energía del rayo γ incidente. El umbral de energía tomado es de 25 keV.

El análisis de coincidencias γ-γ se realiza sobre un *espectro total de energías β-retrasado*, que incluye las transiciones γ de todas las partículas β detectadas durante las pausas del haz. El umbral para la detección de βs se fija en 150 KeV. La figura 5 muestra dicho espectro, en el que se indica el núcleo al que pertenece cada transición, en caso de ser conocida. En negro se muestran los rayos γ que fueron identificados en trabajos anteriores, mientras que las transiciones determinadas por primera vez en esta disertación aparecen en rojo. Los asteriscos denotan un origen incierto del rayo γ.

^{204}Pt → ^{204}Au

El esquema de niveles de ^{204}Au propuesto en este trabajo se muestra en la figura 6, junto con los cálculos de modelo de capas. En las predicciones de SM, el primer estado excitado queda muy bajo en energía, probablemente debido a una deficiencia en la interacción usada en los cálculos. La asignación de espines y paridades se ha hecho combinando las predicciones del modelo de capas y las reglas de selección de las transiciones FF en esta región de la carta de núcleos. Así, se espera observar principalmente transiciones (0^-), (1^-) decayendo del estado fundamental (0^+) en ^{204}Pt. Además, los cálculos de SM colocan dos estados (2^-) en el rango de energías del esquema de niveles experimental. Se han propuesto tres niveles como posibles candidatos a tener espín-paridad (2^-), por ser los que muestran un menor γ-feeding.

En conclusión, la consistencia en J^π y energía entre los niveles nucleares medidos y calculados evidencia la estructura de partícula única de este núcleo.

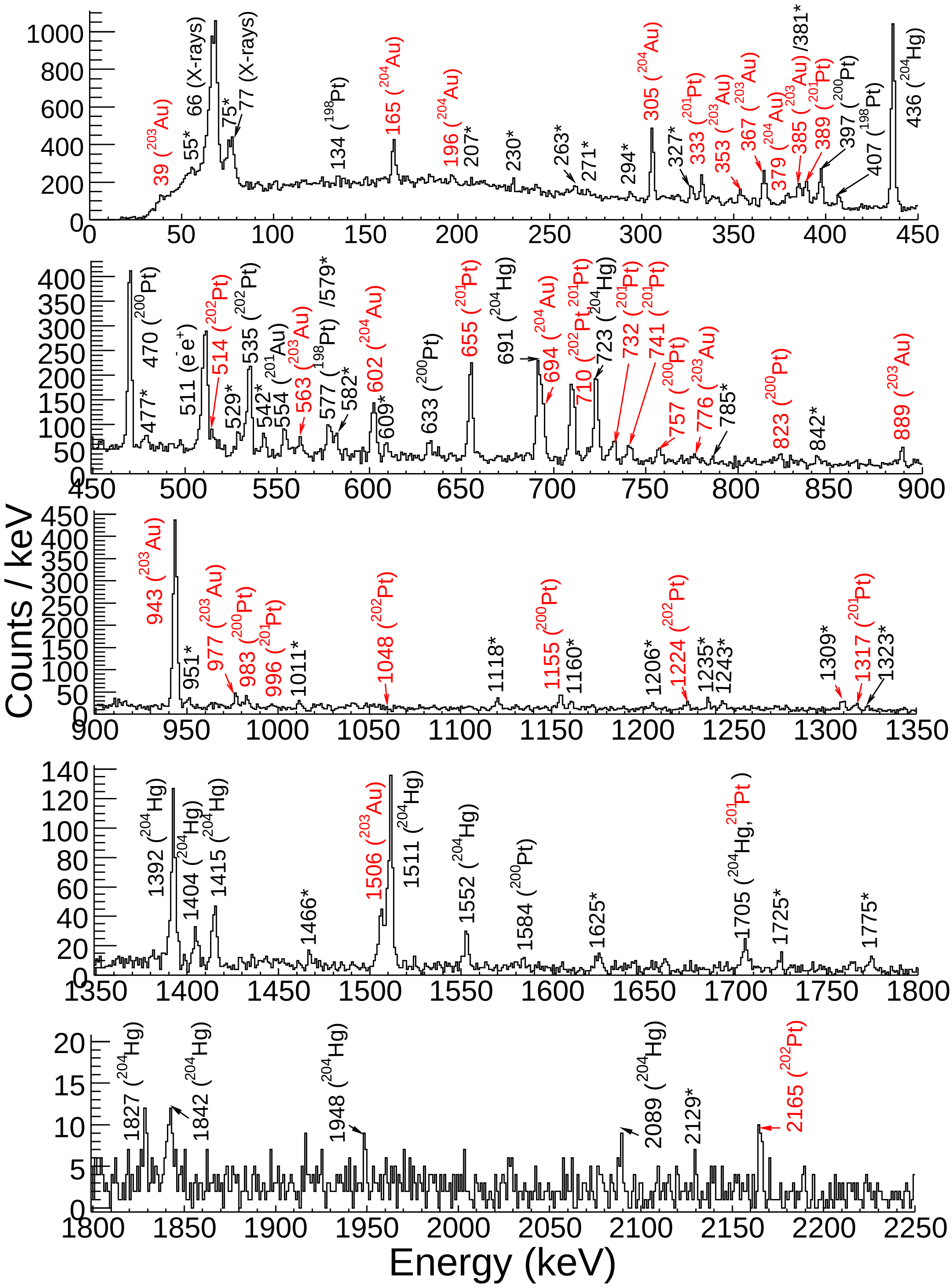

Figure 5: Espectro total de energías β-retrasado para una configuración del FRS centrada en ^{202}Ir. Al lado de cada transición se añade, en paréntesis, el núcleo al que pertenece. Las líneas γ marcadas con un asterisco tienen un origen incierto. Los rayos γ que fueron identificados en trabajos anteriores se muestran en negro, mientras que las transiciones determinadas por primera vez en este experimento aparecen en rojo.

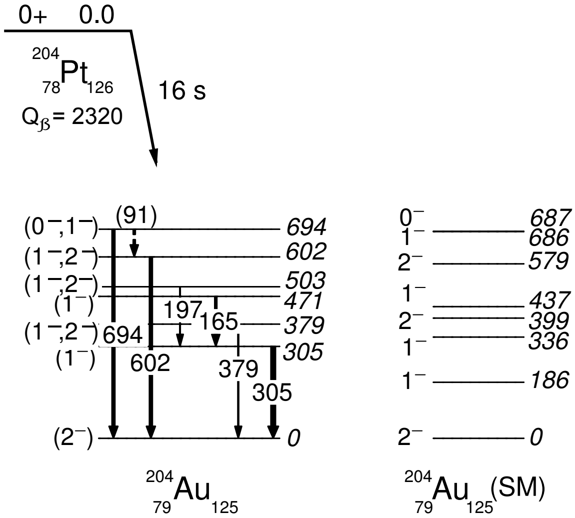

Figure 6: Esquema de niveles experimental de ^{204}Au. Por comparación, los cálculos de SM también se muestran.

^{203}Pt → ^{203}Au

El esquema de niveles de ^{203}Au medido en este trabajo se muestra en el centro de la figura 7. A su izquierda se encuentra el esquema experimental observado en investigaciones previas [139, 140], y a su derecha las predicciones del modelo de capas. Ligadas a este núcleo aparecen tres transiciones γ -353, 367 y 65 keV- cuyo origen es desconocido. Por una parte, tienen una vida media menor que las transiciones características de ^{203}Au ($T_{1/2}$=12(5)s frente a $T_{1/2}^{203Pt}$=22(4)s). Esta diferencia no puede ser justificada por la población de un estado isomérico en el núcleo padre, ya que éste sólo podría decaer al estado metaestable $11/2^-$ en ^{203}Au, ya observado a 641 keV [?]. Por otra parte, están inequívocamente relacionadas con la implantación de ^{203}Pt, tanto por presentar la misma distribución de posición en la matríz de silicios como por emerger de la contaminación de fondo en el espectro γ 3.12.

La asignación de espines y paridades se ha hecho en base a la información espectral previa y a las reglas de selección de transiciones FF. Los valores de espín dados entre paréntesis son consistentes con las predicciones del modelo de capas, aunque no se pueden determinar firmemente.

^{202}Ir → ^{202}Pt

La figura 8 muestra el esquema de niveles experimental de ^{202}Pt junto con los cálculos completos y truncados del modelo de capas. Los estados mar-

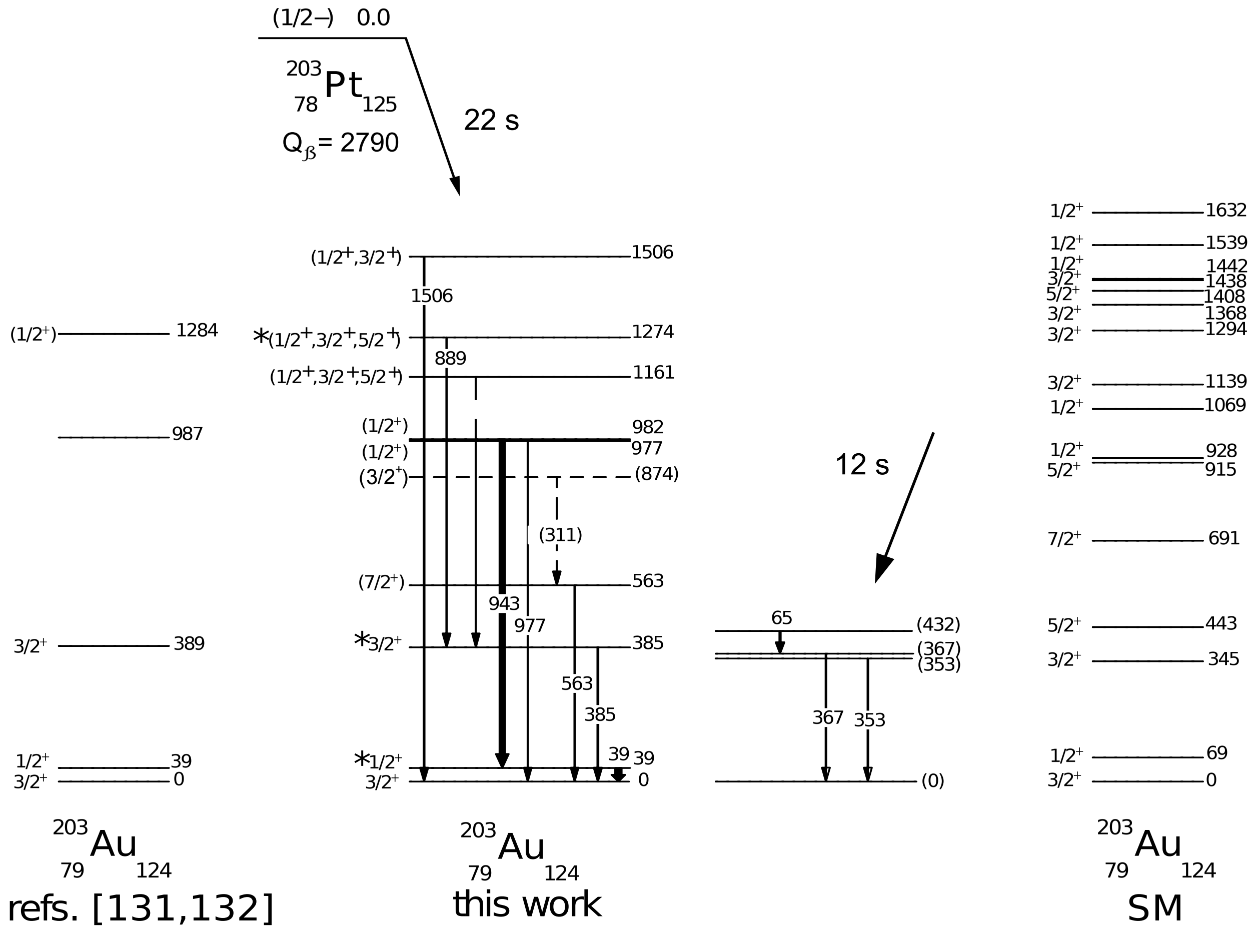
(1/2–) 0.0
$^{203}_{78}$Pt$_{125}$
Q_β= 2790
22 s
12 s
(1/2⁺) 1284
987
3/2⁺ 389
1/2⁺ 39
3/2⁺ 0
$^{203}_{79}$Au$_{124}$
refs. [131,132]
(1/2⁺,3/2⁺) 1506
*(1/2⁺,3/2⁺,5/2⁺) 1274
(1/2⁺,3/2⁺,5/2⁺) 1161
(1/2⁺) 982
(1/2⁺) 977
(3/2⁺) (874)
(7/2⁺) 563
*3/2⁺ 385
*1/2⁺ 39
3/2⁺ 0
1506
889
943
977
(311)
563
385
39
$^{203}_{79}$Au$_{124}$
this work
65
(432)
(367)
(353)
367
353
(0)
1/2⁺ 1632
1/2⁺ 1539
1/2⁺ 1442
3/2⁺ 1438
5/2⁺ 1408
3/2⁺ 1368
3/2⁺ 1294
3/2⁺ 1139
1/2⁺ 1069
1/2⁺ 928
5/2⁺ 915
7/2⁺ 691
5/2⁺ 443
3/2⁺ 345
1/2⁺ 69
3/2⁺ 0
$^{203}_{79}$Au$_{124}$
SM

Figure 7: Izquierda: niveles nucleares de ^{203}Au citados en la refs. [139, 140]. Centro: esquema de niveles experimental de ^{203}Au. Derecha: predicciones del modelo de capas.

cados con un asterisco fueron previamente asignados en un experimento de espectroscopía de isómeros [89]. Nótese que todos los rayos γ identificados en este análisis presentan coincidencia mutua con la línea a 535 keV. También hay que resaltar el estado excitado a 2700 keV. Dado su bajo γ-feeding y la gran diferencia de energía con el resto de niveles, se ha propuesto la existencia de una transición β permitida que decaiga desde el estado fundamental (1^-,2^-) en ^{202}Ir a este nivel. De acuerdo con esto, los espines y paridades propuestos son (2^-,3^-). Por otra parte, la aparición de una desintegración γ débil decayendo del estado (4^+) indica que el espín-paridad del estado fundamental de ^{202}Ir es (2^-).

En general, el margen de error de los niveles nucleares predicho por los cálculos del modelo de capas es de 160 keV, excepto para el primer estado (3^-), que se estima 600 keV por debajo de la energía experimental. En consecuencia, las asignaciones de J^π son sólo tentativas.

En los cálculos con el modelo truncado se suprime la contribución de los orbitales con espines altos. Como resultado, la energía del estado fundamental aumenta y la del resto de niveles se reduce.

^{201}Ir → ^{201}Pt

El esquema de niveles propuesto para ^{201}Pt se muestra en la figura 9 junto con los cálculos truncados de SM. Debido a las grandes diferencias de energía entre los niveles nucleares observados y calculados, no se ha realizado una asignación de espines y paridades. Sin embargo, las predicciones del modelo de capas indican que todos los estados a baja energía de este núcleo tienen valores de J^π de ($1/2^-$), ($3/2^-$) o ($5/2^-$). Sólo se ha mantenido la asignación del estado fundamental, ($5/2^-$), en base a la sistemática de los núcleos vecinos con N=123, aunque los espines ($1/2^-$,$3/2^-$) no se pueden excluir definitivamente. También de acuerdo con la sistemática de los isótonos vecinos con N=124, se ha propuesto un estado fundamental ($1/2^+$,$3/2^+$) para ^{202}Ir, no pudiéndose descartar tampoco un espín ($5/2^+$).

^{200}Ir → ^{200}Pt

La espectroscopía γ β-retrasada de ^{200}Pt proporciona el esquema de niveles experimental que se muestra en la figura 10. La localización de los estados excitados se basa tanto en el análisis de coincidencias γ-γ como en información previa sobre la estructura de este núcleo [146]. De las transiciones γ mostradas en la figura 10, siete se han identificado por primera vez en este experimento (294 keV, 652.3 keV, 757 keV, 822.9 keV, 982.9 keV, 1155 keV y 1260.3 keV), presentando todas ellas coincidencia mutua con la transición

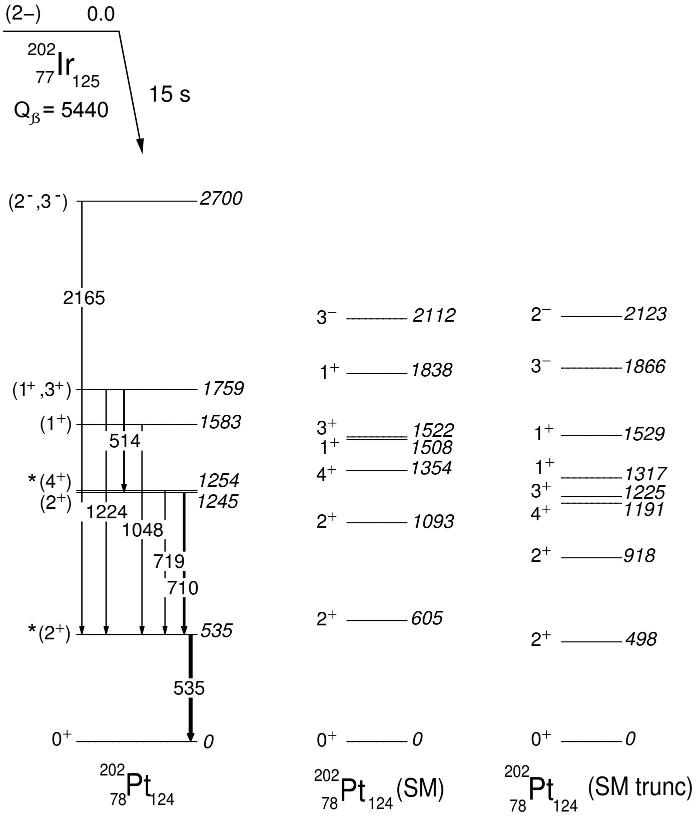
(2–) 0.0
$^{202}_{77}$Ir$_{125}$
Q$_β$= 5440
15 s
(2⁻,3⁻) 2700
2165
(1⁺,3⁺) 1759
(1⁺) 1583
514
*(4⁺) 1254
(2⁺) 1245
1224
1048
719
710
*(2⁺) 535
535
0⁺ 0
$^{202}_{78}$Pt$_{124}$
3⁻ 2112
1⁺ 1838
3⁺ 1522
1⁺ 1508
4⁺ 1354
2⁺ 1093
2⁺ 605
0⁺ 0
$^{202}_{78}$Pt$_{124}$(SM)
2⁻ 2123
3⁻ 1866
1⁺ 1529
1⁺ 1317
3⁺ 1225
4⁺ 1191
2⁺ 918
2⁺ 498
0⁺ 0
$^{202}_{78}$Pt$_{124}$ (SM trunc)

Figure 8: Izquierda: esquema de niveles experimental de ^{202}*Ir. Centro: predicciones del modelo de capas. Derecha: cálculos truncados de SM.*

del primer estado excitado a 470.1 keV.

El elevado número de nucleones de valencia de ^{200}Pt impide hacer cálculos de modelos de capas para este isótopo. Sin embargo, podemos obtener nueva información espectral combinando este trabajo con estudios previos. Así, se espera un estado fundamental (1^-,2^-) de ^{200}Ir de acuerdo con la sistemática de isótonos vecinos con N=122, aunque no se pueden excluir espines mayores. En los estudios de transferencia de dos neutrones [44, 46] se observaron los estados 4^+ a 1103 keV y 0^+ a 1583 keV, de los que sólo el 4^+ aparece en la desintegración β de ^{200}Ir. Por tanto, los espines (0^-,1^-) quedan descartados. La ausencia en la desintegración β de un estado tentativo $(5)^-$ a 1567 keV, observado en estudios isoméricos [89], excluye el espín (4^-). Tampoco se consideran espines mayores en base a la aparición de varios estados 2^+ con un γ-feeding no nulo. Así pues, el espín propuesto para el estado base de ^{200}Ir es (2^-,3^-).

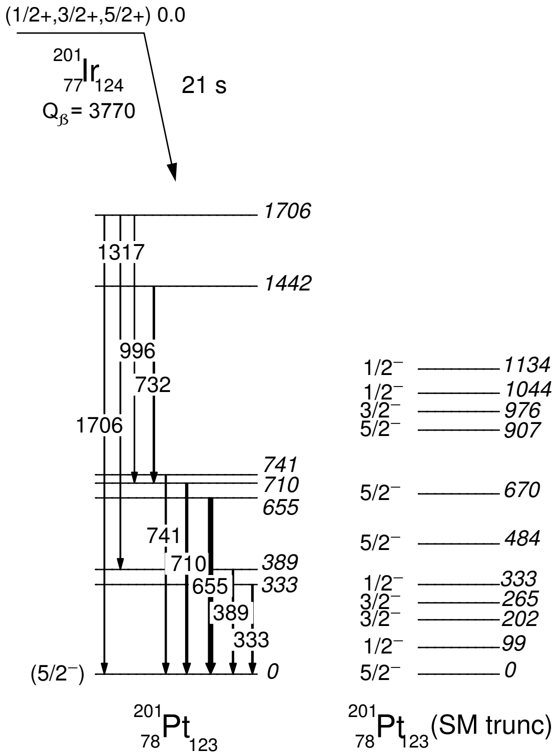
(1/2+,3/2+,5/2+) 0.0
$^{201}_{77}Ir_{124}$
Q_β= 3770
21 s
1706
1317
1442
996
732
1706
741
710
655
741
710
655
389
333
389
333
(5/2⁻)
0
$^{201}_{78}Pt_{123}$
1/2⁻ 1134
1/2⁻ 1044
3/2⁻ 976
5/2⁻ 907
5/2⁻ 670
5/2⁻ 484
1/2⁻ 333
3/2⁻ 265
3/2⁻ 202
1/2⁻ 99
5/2⁻ 0
$^{201}_{78}Pt_{123}$(SM trunc)

Figure 9: Izquierda: esquema de niveles experimental de ^{201}Pt. Derecha: Cálculos truncados del modelo de capas.

Conclusiones

En general, la interpretación en términos de partícula única de núcleos con varias vacantes de valencia fuera del core de ^{208}Pb es muy complicada a causa de la gran densidad de estados nucleares con mezclas fuertes de configuración. A pesar de esto, la consistencia entre los estados nucleares medidos y los calculados con el modelo de capas para los isótopos de Au confirma su estructura de partícula primaria y, por tanto, su forma esférica. Éste no es el caso de los núcleos de Pt, que muestran características propias de sistemas colectivos, como la cascada 0^+-2^+-2^+ con transiciones E2 fuertes. De hecho, algunos modelos colectivos, como el IBM [45], podrían describir apropiadamente las secuencias de transiciones γ observadas en ^{200}Pt.

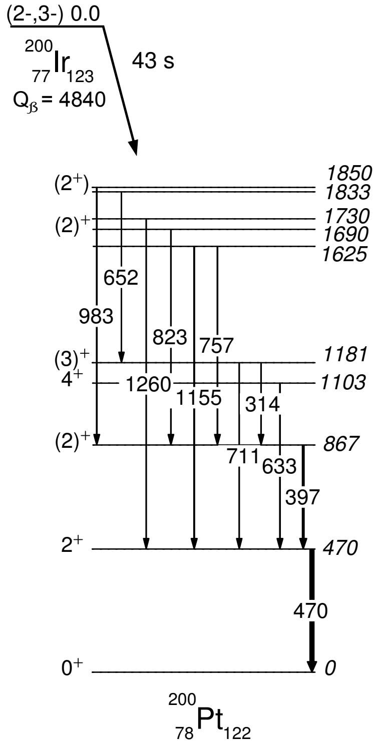

Figure 10: Esquema de niveles experimental de ^{200}Ir.

Vidas medias de desintegración β

Una vez identificadas las transiciones magnéticas de mayor intensidad para cada isótopo, se evalúa el período de desintegración del núcleo madre. Para ello, hemos implementado la técnica de evaluación de vidas medias desarrollada por T. Kurtukian en su tesis doctoral [19]. El procedimiento será descrito a continuación.

Las vidas medias experimentales se obtienen a partir de correlaciones espacio-temporales entre los fragmentos implantados y el primer electrón emitido durante la pausa del haz, siempre que sea registrado en coincidencia con el rayo γ característico del núcleo hijo. Así, es posible suprimir la contaminación inducida por partículas β provenientes tanto de otros fragmentos implantados en la matríz de silicios como de núcleos hijo.

Las curvas de desintegración β presentan la superposición de dos componentes. Por una parte, las correlaciones temporales resultantes de la desintegración radiactiva del ion estudiado. Por otra, un fondo correspondiente a las correlaciones aleatorias entre implantaciones y electrones, producto de la distribución cíclica del haz incidente. Este fondo se forma por dos fuentes independientes: un evento de implantación “falso” o un evento β “falso”. El primer caso se da cuando se correlaciona una partícula β con un fragmento distinto del que originó la desintegración radiactiva, ya se implantase antes (evento LTE) o después (evento MIE) en la misma celda. Un electrón falso, sin embargo, sólo se puede producir por una identificación incorrecta del píxel, debido a la multiplicidad de los silicios, o por una coincidencia γ-β falsa, inducida por el fondo Compton del espectro de rayos γ.

Para distinguir la curva de desintegración del fondo, es necesario caracterizar la forma de las correlaciones aleatorias. Esto se consigue midiendo el intervalo temporal entre una implantación dada y el último electrón que se emitió previamente, es decir, realizando correlaciones ion-β en una secuencia de tiempo inversa.

La información de las correlaciones ion-β verdaderas se extrae a partir del cociente entre las distribuciones temporales *hacia adelante* y *hacia atrás*. Debido a esta compleja estructura, las vidas medias de desintegración β se calculan a partir de un ajuste χ^2 entre los datos experimentales y una función numérica, generada con simulaciones Monte-Carlo que reproducen las correlaciones temporales ion-β, emulando las condiciones experimentales del FRS. Los parámetros de entrada del código Monte-Carlo son la secuencia del haz incidente, la tasa de detección de desintegraciones β durante la pausa del haz (sólo se consideran los electrones emitidos en coincidencia con el rayo γ característico del núcleo hijo), la probabilidad de detección de la transición γ asociada y la eficiencia de detección de partículas β. Como parámetro libre sólo se deja el período de desintegración β, τ.

El procedimiento de análisis se basa en aplicar el método de mínimos cuadrados a los cocientes experimental y simulado de correlaciones temporales, *hacia adelante* y *hacia atrás*. De esta manera, el parámetro τ responsable de minimizar el ajuste χ^2 será aquél más compatible con el espectro experimental de correlaciones temporales.

La tabla 1 muestra las vidas medias obtenidas en este trabajo, correspondientes a seis isótopos de Au, Pt e Ir próximos a la cerradura de capas N=126. A continuación, se muestran las *figuras de mérito F* [2] de cada núcleo y el máximo período de tiempo medible para un valor de F=3. Además, se incluyen algunas predicciones teóricas para estos isótopos, como los cálculos de *Gross-theory* [128], el modelo híbrido con transiciones GT en RPA y transiciones FF en *Gross-theory* [129] y la aproximación QRPA [130, 131], que incorpora las transiciones GT y las transiciones FF desde una perspectiva mi-

---

[2] F caracteriza el significado estadístico de las condiciones experimentales, y se define como el cociente entre el número de correlaciones temporales verdaderas y las fluctuaciones aleatorias de las correlaciones falsas.

Nuclide	$T_{1/2}$ (s)	F	T^{exp}_{max} (s) (F=3)	$T^{th}_{1/2}$ (s) Gr. Th.	$T^{th}_{1/2}$ (s) QRPA	$T^{th}_{1/2}$ (s) CQRPA
^{204}Au (*)	$37.2^{+0.8}_{-0.8}$	16.8	311			
^{204}Pt	16^{+6}_{-5}	13.3	153	6.8	321.8	7.4
^{203}Pt	22^{+4}_{-4}	13.2	193	41.1	564.0	12.7
^{202}Ir (*)	15^{+3}_{-3}	30.0	607	8.5	68.4	9.8
^{201}Ir	21^{+5}_{-5}	10.7	178	18.5	130.0	28.4
^{200}Ir	43^{+6}_{-6}	16.9	335	13.3	124.1	25

Table 1: Vidas medias de desintegración β medidas en este trabajo, junto con sus correspondientes valores de F, la máxima vida media experimentalmente medible si consideramos una figura de mérito F=3, y las predicciones de algunos modelos teóricos. Las vidas medias de los núcleos marcados con un asterisco fueron previamente medidas.

croscópica. Las vidas medias de los núcleos marcados con un asterisco (^{202}Ir y ^{204}Au) fueron previamente medidas [19, 135]. La consistencia entre los resultados actuales y los aportados en referencias anteriores nos proporciona un control interno del nuevo procedimiento de análisis.

En general, se observa que el modelo híbrido sobreestima las vidas medias en varios órdenes de magnitud, mientras que el modelo autoconsistente QRPA reproduce mejor los datos medidos, sobreestimando las vidas medias experimentales en un factor dos. Así pues, la introducción de las transiciones primeras prohibidas en la descripción de la desintegración β de núcleos cercanos a la capa N=126 supone un elemento clave para el entender el proceso r en esta región de la carta de núcleos.

Bibliography

[1] E. Haseltine. *Discover Magazine*, 23:2, 2002.

[2] E.M. Burbidge G.R. Burbidge W.A. Fowler and F. Hoyle. *Rev. Mod. Phys.*, 29:547, 1957.

[3] A.G.W. Cameron. Atomic Energy of Canada Report No. CRL-41, 1957.

[4] C.D. Coryell. *J. Chem. Educ.*, 38:67, 1961.

[5] S.E. Woosley and R.D. Hoffman. *ApJ*, 395:202, 1992.

[6] B.S. Meyer et al. *ApJ*, 399:656, 1992.

[7] K. Takahashi et al. *Astrom. Astrophys.*, 286:857, 1994.

[8] S.E. Woosley et al. *Astrophys. J.*, 433:229, 1994.

[9] E. Symbalisty and D.N. Schramm. *Astrophys. Lett.*, 22:143, 1982.

[10] S. Rosswog C. Freiburghaus and F.-K. Thielemann. *ApJ*, 525, 1999.

[11] Y.-Z. Qian. *ApJ*, 534, 2000.

[12] K.-L. Kratz et al. *Astro. Phys. J.*, 403:216, 1993.

[13] K. Langanke and G. Martinez Pinedo. *Rev. Mod. Phys.*, 75:819, 2003.

[14] E. Lund et al. *Phys. Scr.*, 34:614, 1986.

[15] R.L. Gill et al. *Phys. Rev. Lett.*, 56:1874, 1986.

[16] K.-L. Kratz et al. *Z Phys. A*, 325:489, 1986.

[17] J. Benlliure et al. *Nucl. Phys. A*, 660:87, 1999.

[18] C. Gaarde. *Annu. Rev. Nucl. Part. Sci.*, 41:187, 1991.

[19] T. Kurtukián. PhD Thesis. Universidad de Santiago de Compostela, 2006.

[20] R.F. Casten. *Nucl. Phys. A*, 443:1, 1985.

[21] R.F. Casten and N.V. Zamfir. *Phys. Rev. Lett.*, 70:402, 1993.

[22] P.H. Regan F.R. Xu P.M. Walker M. Oi A.K. Rath and P.D. Stevenson. *Phys. Rev. C*, 65:037302, 2002.

[23] P.D. Stevenson M.P. Brine Zs. Podolyák P.H. Regan P.M. Walker and J. Rikovska Stone. *Phys. Rev. C*, 72:047303, 2005.

[24] P. Sarriguren R. Rodríguez-Guzmán and L.M. Robledo. *Phys. Rev. C*, 77:064322, 2008.

[25] Z. Podolyák. *Phys. Lett. B*, 672:116, 2009.

[26] J. Jolie and A. Linneman. *Phys. Rev. C*, 68:031301, 2003.

[27] A. de Shalit and I. Talmi. *Nuclear Shell Theory.* Academic Press, New York, 1963.

[28] P.J. Brussard and P.W.M. Glaudemans. *Shell Model Applications in Nuclear Spectroscopy.* North-Holland, Amsterdam, first edition, 1977.

[29] R.F. Casten. *Nuclear Structure from a Simple Perspective.* Oxford University press, New York, second edition, 2000.

[30] F. Iachello and A. Arima. *The Interacting Boson Model.* Cambridge University Press, 1987.

[31] A. Arima and F. Iachello. 53, 1974.

[32] A. Arima and F. Iachello. *Phys. Rev. Lett.*, 35:1069, 1975.

[33] A. Arima and F. Iachello. *Phys. Rev. Lett.*, 40:385, 1975.

[34] J.A. Cizewski et al. *Phys. Rev. Lett.*, 40:167, 1978.

[35] R.F. Casten and J.A. Cizewski. *Phys. Lett. B*, 79:5, 1978.

[36] R.F. Casten H.G. Börner J.A. Pinston and W.F. Davidson. *Nucl. Phys. A*, 309:206, 1978.

[37] F. Todd Baker et al. *Nucl. Phys. A*, 371:68, 1981.

[38] P.T. Deason et al. *Phys. Rev. C*, 23:1414, 1981.

[39] W. Boeglin et al. *Nucl. Phys. A*, 477:399, 1988.

[40] A. Sethi et al. *Phys. Rev. C*, 44:700, 1991.

[41] C. Wheldon et al. *Phys. Rev. C*, 63:011304, 2001.

[42] F. Iachello and A. Arima. *Phys. Lett. B*, 53:309, 1974.

[43] J.A. Cizewski et al. *Nucl. Phys. A*, 323:349, 1979.

[44] J.A. Cizewski et al. *Phys. Rev. C*, 23:1453, 1981.

[45] A. Arima and F. Iachello. *Ann. Phys. (N.Y.)*, 123:468, 1979.

[46] S.W. Yates et al. *Phys. Rev. C*, 37:1889, 1988.

[47] M. Steiner et al. *Nucl. Instr. and Meth. A*, 312:420, 1992.

[48] K.-H. Schmidt et al. *Nucl. Instr. and Meth. A*, 260:287, 1987.

[49] S.J. Steer. PhD Thesis. University of Surrey, 2008.

[50] S. Pietri et al. *Nucl. Instr. and Meth. B*, 261:179, 2007.

[51] `http://www.gsi.de`.

[52] R. Serber. *Phys. Rev.*, 72:1114, 1947.

[53] Y. Eisenberg. *Phys. Rev. C*, 96:1378, 1954.

[54] J.-J. Gaimard and K.-H. Schmidt. *Nucl. Phys. A*, 531:709, 1991.

[55] J. Hüfner et al. *Phys. Rev. C*, 12:1888, 1975.

[56] J. Benlliure et al. Proceedings of the Third International Conference on Fission and Properties on Neutron-Rich Nuclei November 3-9, Sanibel Island, Florida, USA, 2002.

[57] K. Helariuta et al. *Eur. Phys. J. A*, 17:181, 2003.

[58] J. Benecke et al. *Phys. Rev.*, 188:2159, 1969.

[59] K. Sümerer et al. *Phys. Rev. C*, 42:2546, 1990.

[60] K. Sümmerer and B. Blank. *Phys. Rev. C*, 61:034607, 2000.

[61] D.J. Morrisey and B.M. Sherrill. *Lect. Notes Phys.*, 651:113, 2004.

[62] E. Hanelt B. Blank and K.-H. Schmidt. Simulation code LIESCHEN.

[63] O.B. Tarasov and D. Bazin. *Nucl. Instr. and Meth. B*, 204:174, 2003.

[64] N. Iwasa et al. *Nucl. Instr. and Meth. B*, 126:284, 1997.

[65] `http://www-w2k.gsi.de/charms/amadeus.htm`.

[66] `http://www.gsi.de/beschleuniger/index_e.html`.

[67] `http://fpsalmon.usc.es/genp/doc/nuclear/experiments/s312/settings.shtml`.

[68] H. Geissel et al. *Nucl. Instr. and Meth. B*, 70:286, 1992.

[69] J. Pereira. Diploma Thesis. Universidad de Santiago de Compostela, 1999.

[70] H. Stelzer. *Nucl. Instr. and Meth. A*, 310:103, 1991.

[71] B. Voss. Diploma Thesis, Institut für Kernphysik, TH Darmstadt, 1995.

[72] J. Pereira. PhD Thesis. Universidad de Santiago de Compostela, 2004.

[73] G.F. Knoll. *Radiation Detector and measurement.* John Wiley & sons, New York, second edition, 1989.

[74] M. Pfüzner et al. *Nucl. Instr. and Meth. B*, 86:213, 1994.

[75] A. Stolz and R. Schneider. Technical Manual Ionization Chamber MUSIC80, 2000.

[76] O. Frisch. British Atomic Energy Report BR-49, 1944.

[77] E. Casarejos et al. *Phys. Rev. C*, 74:044612, 2006.

[78] H. Geissel et al. *Nucl. Instr. and Meth. A*, 282:247, 1989.

[79] R. Kumar et al. *Nucl. Instr. and Meth. A*, 598:754, 2009.

[80] `http://www-linux.gsi.de/~wolle/EB_at_GSI/STOPPED_BEAMS/index.html`.

[81] `http://www.microsemiconductor.co.uk`.

[82] `http://www.mesytec.com`.

[83] `http://www.caen.it/nuclear/product.php?mod=V785`.

[84] J. Simpson. *Z Phys. A*, 358:139, 1997.

[85] W. Korten and S. Lunardi. Achievements with the Euroball spectrometer 1997-2003, 2003.

[86] R. Grzywacz et al. *Phys. Rev. C*, 55:1126, 1997.

[87] C. Chandler et al. *Phys. Rev. C*, 61:044309, 2000.

[88] Z. Podolyák et al. *Nucl. Phys. A*, 722:273, 2003.

[89] M. Caamano et al. *Eur. Phys. J.*, 23:201, 2005.

[90] Z. Podolyák et al. *Phys. Lett. B*, 633:203, 2006.

[91] P.H. Regan et al. Int. Jour. Mod. Phys. E 17-8, 2008.

[92] N. Alkhomashi et al. *Phys. Rev. C*, 80:064308, 2009.

[93] P. Detistov et al. *Acta Phys. Pol. B*, 38:1287, 2007.

[94] `http://www.xia.com/DGF-4C_download.html`.

[95] `http://www.caen.it/nuclear/product.php?mod=V767`.

[96] `http://www.nndc.bnl.gov/useroutput/AR_254357_1.html`.

[97] `http://radware.phy.ornl.gov/gf3/gf3.html#5.2.`

[98] `http://www.gsi.de/daq/`.

[99] `http://www.-linux.gsi.de/~mbs/v43/manual/gm_vme_trig.pdf`.

[100] J. Grebosz. *Comp. Phys. Comm.*, 176:251, 2007.

[101] J.J. Cowan et al. *Phys. Rep.*, 208:267, 1991.

[102] K. Sümmerer et al. *Phys. Rev. C*, 52:1106, 1995.

[103] M.F. Ordó nez. PhD Thesis. Universidad de Santiago de Compostela, 2007.

[104] C.A. Bertulani and D.S. Dolci. *Nucl. Phys. A*, 674:527, 2000.

[105] A. Kelić et al. *Phys. Rev. C*, 70:064608, 2004.

[106] C.A. Bertulani. *Nucl. Phys. A*, 554:493, 1993.

[107] C. Scheidenberger et al. *Nucl. Instr. and Meth. B*, 142:441, 1998.

[108] P.J. Karol. *Phys. Rev. C*, 11:1203, 1975.

[109] T. Motobayashi et al. *PLB*, 346, 1995.

[110] H. Sheit et al. *PRL*, 77, 1996.

[111] A. Prevost et al. *Eur. Phys. J. A*, 22, 2004.

[112] T. Rzaca-Urban W. Urban J.L. Durell A.G. Smith and I. Ahmad. *PRC*, 76, 2007.

[113] T. Kautzsch et al. *Eur. Phys. J. A*, 9, 2000.

[114] I. Dillmann et al. *PRL*, 91, 2003.

[115] A. Jungclaus et al. *PRL*, 99, 2007.

[116] H. Alvarez-Pol et al. *Eur. Phys. J. A*, 42:485, 2009.

[117] J. Meyer ter Vehn. *Nucl. Phys. A*, 249:11, 1975.

[118] V. Paar. *Problems of vibrational nuclei.* North Holland, 1975.

[119] J.L. Wood. *Interacting Bose-Fermi systems in nuclei.* Plenum Press, 1981.

[120] F. Iachello. *Phys. Rev. Lett.*, 44:772, 1980.

[121] `http://www.nndc.bnl.gov/ensdf/`.

[122] `http://www.nndc.bnl.gov/nudat2/`.

[123] S. Pietri et al. *Acta Phys. Pol. B*, 38:1255, 2007.

[124] S.J. Steer et al. *Acta Phys. Pol. B*, 38:1283, 2007.

[125] S.J. Steer et al. *Phys. Rev. C*, 78:061302, 2008.

[126] B.A. Brown A. Etchegoyen and W.D.M. Rae. The computer code OXBASH, MSU-NSCL report number 524.

[127] R. Peierls. *Proc. R. Soc. (London) A*, 149:467, 1935.

[128] T. Tachibana and M. Yamada. *Proc. Int. Conf. on exotic nuclei and atomic masses, Arles*, 660:763, 1995.

[129] B. Pfeiffer P. Moller and K.-L. Kraft. *Phys. Rev. C*, 67:055802, 2003.

[130] I.N. Borzov and S. Goriely. *PEPAN*, 34, 2003.

[131] I.N. Borzov. *Phys. Rev. C*, 67:025802, 2003.

[132] T.E. Ward H. Ihochi M. Karras and J.L. Meason. *Phys. Rev.*, 164:1545, 1967.

[133] G. Audi and A.H. Wapstra. *Nucl. Phys. A*, 565:1, 1993.

[134] A. Pakkanen T. Komppa and H. Helppi. *Nucl. Phys. A*, 184:157, 1972.

[135] D.A. Craig et al. *J. Phys. G: Nucl. Phys.*, 10:1133, 1984.

[136] `http://physics.anu.edu.au/nuclear/bricc/`.

[137] P. Möller J.R. Nix and K.-L. Kratz. *Atomic Data Nucl. Data Tables*, 66:131, 1997.

[138] Ch. Wenneman et al. *Z. Phys. A*, 347:185, 1994.

[139] E.R. Flynn Ronald E. Brown J.W. Sunier and J.M. Gursky. *Phys. Lett.*, 105, 1981.

[140] P. Grabmayr A. Mondry G.J. Wagner and P. Woldt. *Phys. Rev. C*, 49:2971, 1994.

[141] S. Shi W.D. Huang Y. Li D.Z. Yin J.H. Gu and J.Q. Tian. *Z. Phys. A*, 342:369, 1992.

[142] G. Audi A.H. Wapstra and C. Thibault. *Nucl. Phys. A*, 729:337, 2003.

[143] J. Facetti E. Trabal R. McClin and S. Torres. *Phys. Rev.*, 127:1690, 1962.

[144] K.P. Gopinathan M.C. Joshi and M. Radhamenon. *Nuovo Cimento*, 30:14, 1963.

[145] M. McMillan M. Kamen and S.Raben. *Phys. Rev.*, 52:375, 1937.

[146] `http://www1.nndc.bnl.gov/useroutput/AR_2314_4.html`.

[147] John C. Hill D.G.Shirk R.F. Petry and K.H. Wang. *Phys. Rev. C*, 13:2484, 1976.

[148] E. Fermi. *Z. Phys.*, 88:161, 1934.

[149] J. Damgaard et al. *Nucl. Phys. A*, 135:310, 1969.

[150] L. Rydström J. Blomqvist R.J. Liotta and C. Pomar. *NPA*, 512, 1990.

[151] B. Fornal et al. *PRL*, 87:21, 2001.

[152] I.N. Borzov. *Phys. of Atom. Nucl.*, 8, 2011.

[153] P. Bevington and D.K. Robinson. *Data Reduction and Error Analysis for the Physical Sciences.* McGraw Hill, second edition, 1992.

[154] D.N. Poenaru and W. Geiner. *Experimental Techniques in Nuclear Physics.* De Gruiter, New York, first edition, 1997.

[155] T. Kurtukián-Nieto et al. *Nucl. Phys. A*, 827:587, 2009.

[156] T. Kurtukián-Nieto et al. *Nucl. Instr. and Meth. A*, 589:472, 2008.

List of Figures

1 *Chart of nuclides showing the abundance patterns drawn from the r-process. The stable nuclides are marked by black boxes. The jagged black line denotes the limit of nuclear properties experimentally determined, whereas the magenta line indicates the r-process path. Colour-shading reveals the different (log) timescales for β-decay. Vertical and horizontal black lines represent the magic closed neutron and proton shells, respectively. Figure taken from [12].* 4

1.1 *Illustration of the two selections performed in the "in-flight" isotopic separation. a) First magnetic selection in A/Q. b) Second magnetic selection in Z/v. The corresponding production rates are on a logarithmic scale. The magnetic FRS setting is optimised to transmit ^{202}Ir.* 11

1.2 *Schematic view of the GSI accelerator facilities and experimental areas. The primary beams are delivered by the ion sources, pre-accelerated in the UNILAC and injected into the SIS18-synchrotron to be re-accelerated. Eventually, the projectile beam is forwarded to the desired experimental area.* 12

1.3 *Layout of the magnetic spectrometer FRS at GSI. Each dipole magnet can be adapted to fulfil the ion-optical conditions to the specific requirements of different experiments. Blue and red quadrupoles accomplish first-order focussing conditions at each image plane in the vertical and horizontal directions, respectively. Sextupoles correct second-order chromatic aberrations.* 15

1.4 *Schematic layout of the two FRS degraders. Upper panel: Achromatic mode. The resulting x-transversal position of the ions at F4 is independent from their momentum at the exit of the intermediate degrader. Lower panel: Monoenergetic mode. The final momentum distribution is independent from the horizontal position of the ions at the central focal plane. Note that the horizontal position distribution at F2 is preserved at F4.* . 19

1.5 *Schematic view of the FRagment Separator and the detection equipment used for the production, identification and β-delayed γ-ray spectroscopy of heavy neutron-rich nuclei.* 20

1.6 *Electronic scheme of the plastic scintillators.* 22

1.7 *Time-of-flight calibration for the present experiment. The linear fit allows to deduce the parameters d and T_0. See text for details.* 24

1.8 *Dependences of the energy loss signal in the chamber MUSIC42 for a magnetic setting of the FRS optimised to transmit ^{202}Ir.* 26

1.9 *Corrected energy loss signals in MUSIC42.* 26

1.10 *Correlation plot of the energy loss signals provided by the two MUSIC chambers used in the present experiment, for a setting centred in ^{202}Ir. The distribution corresponding to the iridium isotopes ($Z = 77$) is marked in the figure.* 28

1.11 *Corrected energy loss spectra of the MUSIC chambers. The figures correspond to a magnetic setting centred in ^{202}Ir.* 29

1.12 *Correlation plot between the energy loss in the aluminium intermediate degrader and the maximum ionic charge measured with the two MUSIC chambers for an FRS setting centred in ^{202}Ir. Each labelled distribution of clusters corresponds to a different charge state configuration along the FRS. See text for details.* 31

1.13 *Scatter plot of the maximum ionic charge measured in the MUSIC chambers in relation to the A/Q value of the fragments along the FRS for a setting centred in ^{202}Ir (marked).* 32

1.14 *Mass identification plot of the different iridium isotopes for an FRS setting centred in ^{202}Ir. The two-dimensional spectra show the A/Q ratio as a function of the position of the fragments at the central and final focal planes, respectively.* . . 32

1.15 *Schematic layout of the experimental configuration at the S4 region of the FRS. Selected fragments enter into the slowing-down system after being identified by their A/Q ratio and their ionic charge Q. The nuclei are decelerated in the homogeneous degrader and subsequently implanted into the active stopper. The three positions of the Si catcher occupied by DSSSD detectors are marked with black boxes. The scintillator system (SCI42 + SCI43) allows for the offline suppression of the ions destroyed in the slowing-down process.* 33

1.16 *Two-dimensional scatter plots of the energy loss in the scintillators located at S4 vs. the effective charge registered in the MUSIC chambers. The gates performed to select the implanted nuclei are shown.* 34

1.17 *Calibration of the S4 degrader thickness. The plot shows the ratio between the number of projectiles registered in SCI42 and the number of projectiles detected in SCI43 as a function of the degrader thickness. The linear fit performed to obtain the required thickness is displayed.* 35

1.18 *Photograph of the active stopper setup. The DSSSDs are contained in the light-tight box, which is placed in the middle of the RISING* γ*-ray array in its Stopped Beam configuration [80].* 37

1.19 *X-strips multiplicity distribution of the active stopper for the implantation of* ^{204}*Pt. The input shows the graphic in logarithmic scale. Multiplicity 1 indicates that only one pixel (X,Y) has been fired with an energy above the implantation threshold, and so on.* 38

1.20 *Corrected total energy spectrum of the active stopper for an FRS setting optimised to transmit* ^{202}*Ir. All x and y strips are included. Implantation events are triggered when at least one strip detects an energy loss above the limit marked with a dashed red line.* 40

1.21 *Two-dimensional cluster plots of identification for an FRS magnetic setting optimised to transmit* ^{202}*Ir. The left panel shows the total yield at the final focal plane of the FRS, whereas the right panel displays the corresponding heavy nuclei implanted in the active stopper.* 41

1.22 *Technical drawing of the RISING stopped beam setup. See text for details.* 43

1.23 *Isomeric energy-time matrix of the nuclide* ^{204}*Pt. The red line illustrates the prompt flash, whose time width profile is shown in the input figure.* 44

1.24 *Schematic layout of the RISING γ-ray array electronics.* . . . 45

1.25 *γ-ray energy spectrum of ^{152}Eu for one Ge crystal. The labelled photopeaks are used in the energy calibration of the RISING array.* . . . 46

1.26 *Efficiency calibration fit of the RISING spectrometer. The figure shows the range of energies of interest for the present work.* 49

1.27 *γ-ray energy spectra of the β-decay $^{202}Ir \rightarrow {}^{202}Pt$. Upper panel: Energy spectrum without addback correction. Lower panel: Energy spectrum with addback correction.* . . . 50

2.1 *Schematic representation of the two charge-exchange reaction mechanisms. a) quasielastic isospin-exchange scattering. b) inelastic isospin-exchange scattering.* . . . 55

2.2 *Region of the Segrè chart covered by the FRS setting optimised to transmit ^{206}Au. The red boxes indicate the nuclei produced by a single (π,ν) charge-exchange reaction, whereas the blue and green boxes illustrate the corresponding charge state contaminants $(A-3, Z)$ and $(A, Z+1)$, respectively.* . . . 56

2.3 *Matrices of a) the charge state distributions along the FRS, and b) the mass identification. The corresponding magnetic setting is optimised to transmit ^{206}Au, and it has been specifically performed to measure the single (π,ν) charge-exchange cross sections of nuclei with $N = 127$.* . . . 58

2.4 *Production cross sections as a function of the number of protons removed from the projectile ^{208}Pb. See text for details.* . 63

3.1 *Region of the chart of nuclei analysed in the present work through both isomeric and β-delayed γ-ray spectroscopic studies.* 66

3.2 *Delayed γ-ray spectra associated to the exotic nuclei ^{204}Pt (figure 3.2(a)) and ^{203}Pt (figure 3.2(b)). The γ-ray de-excitations depopulate the isomeric states observed in refs. [124, 125], thus confirming the isotopic identification.* . . . 68

3.3 *Position correlation between the x coordinate in the scintillator located in front of the active stopper and the x strip of the DSSSDs. The selected nuclide is ^{202}Ir.* . . . 70

3.4 *Multiplicity of the active stopper for β-like particle triggers in a setting centred in ^{205}Au. The inset shows the graphic in logarithmic scale. Multiplicity 1 indicates that only one pixel (x,y) has been fired with an energy above the β-particle detection threshold, and so on.* . . . 70

3.5 *Time signal of the β-decay trigger detector. The modulated spill structure is shown up.* 71

3.6 *(a) Transversal x-position distribution of the ions in the active stopper. (b) X-position distribution of the fragments in the scintillator SCI41.* 74

3.7 *β-delayed γ-ray energy spectrum of the decay ^{204}Pt to ^{204}Au. The red-labelled γ-ray transitions are tentatively assigned to the internal decay of ^{204}Au. The black-labelled transitions belong to background contamination. See text for details.* 77

3.8 *Background-subtracted β-delayed γ-ray energy spectrum of the decay ^{204}Pt to ^{204}Au. The red-labelled γ-ray transitions correspond to the internal decay of ^{204}Au. See text for details on the subtraction of background.* 78

3.9 *γ-γ coincident spectra of the transitions tentatively assigned to the decay of ^{204}Au.* 79

3.10 *Experimental level scheme of ^{204}Au. For comparison, the shell model approach is also shown. Q_β value taken from [137].* . . . 80

3.11 *β-delayed γ-ray energy spectrum of the decay ^{203}Pt to ^{203}Au. The red-labelled γ-ray transitions are tentatively assigned to the internal decay of ^{203}Au. The black-labelled transitions belong to background contamination. See text for details.* 82

3.12 *Background-subtracted β-delayed γ-ray energy spectrum of the decay ^{203}Pt to ^{203}Au. The red-labelled γ-ray transitions are tentatively assigned to the internal decay of ^{203}Au. See text for details on the subtraction of background.* 83

3.13 *γ-γ coincident spectra of the transitions tentatively assigned to the decay of ^{203}Au. A discussion on these spectra is developed in the text.* 84

3.14 *γ-γ coincident spectra of the transitions tentatively assigned to the decay of ^{203}Au. A discussion on these spectra is developed in the text.* 85

3.15 *Left: experimental level scheme of ^{203}Au determined by refs. [139, 140]. Centre: level scheme deduced in our β-decay studies. The states marked with an asterisk were previously identified in refs. [139, 140]. Right: Shell model approach shown for comparison. Q_β value taken from [137].* 86

3.16 *β-delayed γ-ray energy spectrum of the decay ^{202}Ir to ^{202}Pt. The red-labelled γ-ray transitions are tentatively assigned to the internal decay of ^{202}Pt. The black-labelled transitions belong to background contamination. See text for details.* 88

3.17 *Background-subtracted γ-ray energy spectrum of the decay ^{202}Ir to ^{202}Pt. The red-labelled γ-ray transitions are tentatively assigned to the internal decay of ^{202}Pt. See text for details on the subtraction of background.* 89

3.18 *γ-γ coincident spectra of the transitions tentatively assigned to the decay of ^{202}Pt. Red-labelled decays are thought to belong to the internal de-excitation of ^{202}Pt, whereas black-labelled transitions correspond to background contamination. A discussion on these spectra is developed in the text.* 90

3.19 *Left: Proposed level scheme of ^{202}Pt. The states marked with an asterisk were previously reported [89]. Centre: shell model approach calculated with the OXBASH code. Right: shell model approach calculated with a truncation of the OXBASH code. Q_β value taken from [137].* 91

3.20 *β-delayed γ-ray energy spectrum of the decay ^{201}Ir to ^{201}Pt. The red-labelled γ-ray transitions are tentatively assigned to the internal decay of this nucleus, whereas the green-labelled γ-ray peak was previously observed in the internal decay of ^{201}Au [145]. The black-labelled transitions belong to background contamination.* 93

3.21 *Black: γ-ray energy spectrum of the decay ^{201}Ir to ^{201}Pt. Green: Qualitative contribution of background related to ^{204,203}Au and ^{202}Pt. Red: Qualitative contribution of background related to ^{200}Pt. See text for details.* 94

3.22 *γ-γ coincident spectra of ^{201}Pt. Red-labelled decays are tentatively assigned to the internal de-excitation of ^{201}Pt. Black-labelled transitions correspond to background contamination, appeared due to the overlapping of the selected γ-peaks with other γ-ray decays of similar energy.* 95

3.23 *Right: Level scheme of ^{201}Pt proposed from this work. Right: structure of ^{201}Pt predicted with a truncation of the OXBASH code. Q_β value taken from [137].* 96

3.24 *β-delayed γ-ray energy spectrum of the decay ^{200}Ir to ^{200}Pt for all the ion-β time correlations registered in the active stopper.* 98

3.25 *β-delayed γ-ray energy spectrum of the decay ^{200}Ir to ^{200}Pt showing the forward ion-β time correlations registered in the pixel of implantation of the rear middle DSSSD.* 99

3.26 *γ-γ coincident spectra of ^{200}Pt.* 100

3.27 *Experimental level scheme of* ^{200}*Pt measured in the present work. Note that all the energy levels were previously reported [44], excluding the excited state at 1833 keV.* Q_β *value taken from [137].* 101
3.28 *Single-particle energies obtained using (a) the harmonic oscillator and (b) the harmonic oscillator and the spin-orbit interaction. The numbers in the circles are the magic numbers.* . . 104
3.29 *Angular dependence of the residual interaction strength for two particles in identical orbits and J=ODD. The* E_J *values are divided by the (2J+1)-weighted average matrix elements* $\mid \bar{E} \mid$ *to display the similarity in the J dependence (or* θ *dependence) of the various orbits.* 108

4.1 *Experimental* β*-decay curve of the nuclide* ^{204}*Pt. The figure reveals the suppression of time correlations between fragments and* β*-like particles during the spill time.* 113
4.2 *Contributions of background contamination events originated by the selection of a "false" fragment implantation.* 114
4.3 *Spatial distribution of the secondary nuclide* ^{203}*Pt as seen by the active stopper. The colour scale indicates the number of ions hit in a given pixel (X,Y).* 117
4.4 *(a) Measured ion-*β *time correlations in forward- (solid line) and backward-time (dashed red line) directions for the nucleus* ^{204}*Pt. (b) Simulated time distributions of the same fragment in forward- and backward-time directions for the value of* τ *(23 s) responsible of the* χ^2 *minimisation. The inset panel shows the measured ratios of the forward- and backward-time correlations (black line) with their error bars, as well as the Monte-Carlo simulated ratios for the lifetime that minimises the* χ^2 *fit (dashed red line). (c) and (d) Same figures for the nucleus* ^{202}*Ir, corresponding to a value of* $\tau = 22$ *s.* 121
4.5 *Left: hypersurface of* χ^2 *as a function of the detection efficiency* ϵ *and the lifetime* τ*. Right: contour plot of* χ^2 *as a function of the detection efficiency* ϵ *and the lifetime* τ*. The black solid line indicates the* $\Delta\chi^2 = 1$ *contour, whereas the cross points out the pair* $(\epsilon,\tau) = (40,22)$ *responsible of the* χ^2 *minimisation. Data corresponding to* ^{202}*Ir.* 122
4.6 *Left: Projection of* χ^2 *into the detection efficiency coordinate for a lifetime of* 22 *s. Right. Projection of* χ^2 *into the lifetime coordinate for a detection efficiency of* 40%*. Data corresponding to* ^{202}*Ir.* 122

4.7 *Forward- (red line) and backward-time (blue line) exponential fits of the time correlated distributions for* ^{202}*Ir (left) and* ^{204}*Au (right). See text for details.* 127

4.8 *Ratios between the experimental half lives and the theoretical calculations mentioned in the text.* 130

A.1 *Technical drawing of the FRS beam-line setup at the S2 region. The arrows indicate the distance in mm from the beginning of S2 to the corresponding device.* 136

B.1 *Technical drawing of the FRS beam-line setup at the S4 region. The arrows indicate the distance in mm from the beginning of S4 to the corresponding device.* 138

D.1 *Total* β*-delayed* γ*-ray energy spectrum for an FRS magnetic setting centred in* ^{202}*Ir. The nuclide to which every transition belongs, if known, is attached within parenthesis beside the energy of the photopeak, whereas an asterisk indicates that the origin of the* γ*-ray decay is uncertain. The transitions characterised for the first time in the present work are labelled in red in order to provide a general view of the spectroscopic results.* . 142

1 *Vista esquemática del FRS y el equipo de detección utilizado para producir, identificar y estudiar la desintegración* β *de los núcleos pesados ricos en neutrones.* 148

2 *Matrices de identificación isotópica.* 150

3 *Secciones eficaces de los núcleos producidos por intercambio de carga en función del número de agujeros de protones relativos al núcleo proyectil* ^{208}*Pb (puntos negros). En comparación, también se muestran las secciones eficaces de fragmentación fría de los núcleos con* $N = 126$ *[19] (trińgulos rojos) y una simulación de las secciones eficaces de fragmentación de* ^{238}*U para los núcleos con* $N = 127$ *(línea azul). El único dato experimental disponible en este último caso se muestra en el cuadrado verde.* 151

4 *Espectros* γ *retrasados asociados a los núcleos* ^{204}*Pt (derecha) y* ^{203}*Pt (izquierda).* 152

5 *Espectro total de energías β-retrasado para una configuración del FRS centrada en ^{202}Ir. Al lado de cada transición se añade, en paréntesis, el núcleo al que pertenece. Las líneas γ marcadas con un asterisco tienen un origen incierto. Los rayos γ que fueron identificados en trabajos anteriores se muestran en negro, mientras que las transiciones determinadas por primera vez en este experimento aparecen en rojo.* 154
6 *Esquema de niveles experimental de ^{204}Au. Por comparación, los cálculos de SM también se muestran.* 155
7 *Izquierda: niveles nucleares de ^{203}Au citados en la refs. [139, 140]. Centro: esquema de niveles experimental de ^{203}Au. Derecha: predicciones del modelo de capas.* 156
8 *Izquierda: esquema de niveles experimental de ^{202}Ir. Centro: predicciones del modelo de capas. Derecha: cálculos truncados de SM.* 158
9 *Izquierda: esquema de niveles experimental de ^{201}Pt. Derecha: Cálculos truncados del modelo de capas.* 159
10 *Esquema de niveles experimental de ^{200}Ir.* 160

List of Tables

1.1 *Charge state distributions and probability of nuclear reactions in the target for a setting centred in* ^{202}*Ir, predicted by the code AMADEUS [65].* 13

1.2 *Charge state distributions and probability of nuclear reactions in the intermediate degrader for a setting centred in* ^{202}*Ir. The selected degrader thickness is about half the range of the reference fragment (*^{202}*Ir).* 18

1.3 *Implanted nuclei in the present work. The production yields at F4 and the corresponding number of implanted fragments are shown.* 42

1.4 *Parameters involved in the efficiency calibration for the present experiment: photopeak energy, source activity, source intensity, number of* γ*-rays detected in the photopeak and efficiency of the array.* 48

2.1 *Charge state contaminants of the fragments produced by charge-exchange interactions. See text for details.* 59

2.2 *Single (*π*,*ν*) charge-exchange cross sections of the N=127 isotones synthesised for the first time in this experiment.* 61

3.1 *Energy levels,* γ*-ray energy transitions, relative intensities and apparent* β*-feeding associated to the decay* $^{204}Pt \rightarrow {}^{204}Au$*. The parameters related to the 91.6 keV peak have been calculated assuming an M1 character for this low-energy transition (*α_{tot} *= 9.5(4)).* 80

3.2 *Energy levels,* γ*-ray energy transitions, relative intensities and apparent* β*-feeding associated to the decay* $^{203}Pt \rightarrow {}^{203}Au$*. The measured parameters of the tentative M1 transition of 39 keV include the calculated internal conversion coefficient (*α_{tot} *= 20.5(3)).* 87

3.3 *Energy levels, γ-ray energy transitions, relative intensities, and apparent β-feeding of each state associated to the decay $^{202}Ir \rightarrow {}^{202}Pt$.* 91

3.4 *Energy levels, γ-ray energy transitions, relative intensities and apparent β-feeding of each state associated to the decay $^{201}Ir \rightarrow {}^{201}Pt$.* 94

3.5 *Energy levels, γ-ray energy transitions, relative intensities, and apparent β-feeding of each state associated to the decay $^{200}Ir \rightarrow {}^{200}Pt$.* 99

4.1 *Measured parameters associated with the experiment: number of fragments N_F, γ-ray energy transition of the first excited state of the daughter nucleus, number of γ-ray de-excitations N_γ, γ-ray detection efficiency ϵ_γ, and the corresponding value of the detection efficiency ϵ.* 116

4.2 *Parameters associated with each nucleus: number of fragments N_F, average fragment implantation rate ν_F, γ-labelled β-background frequency $\nu_{\gamma,\beta}^{back}$, and total detection efficiency ε. Recall that the β detection thresholds correspond to those pointed out in section 4.3.1.* 124

4.3 *Nuclei studied in the current work. The γ-ray transitions used to label the β-electrons are shown in the table, as well as the measured β-decay half lives, the time elapsed between two consecutive implantations, the figures of merit and the maximum half life experimentally measurable considering $F=3$. The half lives of the nuclei marked with an asterisk were previously reported (see text for details).* 126

4.4 *β-decay half lives measured in this work. For comparison, the half lives predicted by some theoretical models are also indicated. See text for details.* 129

C.1 List of layers of matter placed along the set-up line during the experiment. The degrader thicknesses of every setting can be perused in ref. [67]. 140

E.1 *Parameters associated to the measurement of the β-decay half life of each nuclide. The DSSSD configuration A refers to two independent central DSSSD, whereas B refers to a unique central DSSSD of double the thickness.* 144

1 *Vidas medias de desintegración β medidas en este trabajo, junto con sus correspondientes valores de F, la máxima vida media experimentalmente medible si consideramos una figura de mérito F=3, y las predicciones de algunos modelos teóricos. Las vidas medias de los núcleos marcados con un asterisco fueron previamente medidas.* 162